Quantification and Change Assessment of Debris-Covered Glaciers using Remote Sensing

Benjamin Aubrey Robson

Dissertation for the degree of philosophiae doctor (PhD)

at the University of Bergen

2016

Dissertation date: 31st October 2016

Year: 2016

Title: Quantification and Change Assessment of Debris-Covered Glaciers using Remote Sensing

Author: Benjamin Aubrey Robson

Print: AiT Bjerch AS / University of Bergen

Scientific environment

The work presented in this thesis was carried out at the Department of Geography, University of Bergen UiB) through a four-year scholarship and included a two-month research stay at the Department of Geoinformatics (Z_GIS) at the University of Salzburg, Austria. Time was also spent at other institutes for courses, most notably the Department of Geoscience, University of Oslo (UiO), for the course *GEO9520 - Remote Sensing and Image Analysis* in February 2013 as well as numerous trips for supervision from Christopher Nuth. Two summer schools were taken, the *Innsbruck Summer School of Alpine Research 2015: Close Range Sensing Techniques in Alpine Terrain, Obergurgl, Austria* and the 2016 *UAF Alaska Glaciology Summer school, McCarthy, USA*. Two trips were made to the Manaslu Region in 2013 and 2014. Lastly, a total of six international conferences were attended.

Acknowledgements

Writing a PhD is a lot more than just the process of writing publications, and the last four years in Bergen have been a fantastic and rewarding experience. There are many people that I am thankful to for their support and help over the last four years. Thanks to my two supervisors, Professor Svein Olaf Dahl and Dr. Christopher Nuth. Svein Olaf Dahl has also been brilliant at fuelling my dromomania and sending me all over the world for conferences, courses, and fieldwork and at going through my manuscripts over a cup of tea. Christopher Nuth has patiently walked me through all sorts of technical and processing problems I am encountered, and my PhD would not have been possible without his help. I am also very grateful to Daniel Hölbling who has helped with many aspects of Object-Based Image Analysis and helped facilitate a two month-long research visit to Salzburg.

Thanks also to my colleagues at the Department of Geography, especially Pål Ringkjøb Nielsen, Helge Tvedt, Max Koller, Sunniva Vatle and Henrik Jansen, as well as the many Master students who have helped occupy many potentially productive work hours with tea breaks, extended lunches and afternoon ciders. I would like to thank (and slightly apologise) to all those in the department that allowed me to be linguistically lazy and speak English when it suited me, and patiently speak slow Norwegian at other times. Takk! I also have a fantastic if eccentric group of friends in Bergen who I owe thanks to for filling these four years with all sorts of adventures and fun.

Thanks also to Asha Rai and his family and friends in Kathmandu that have made my three trips to the Himalayas run (mostly) smoothly. They were truly unforgettable trips.

I also would have struggled to complete my PhD in Bergen without the support, visits, and Marmite in the post from my family in the United Kingdom. Lastly, to my brother: I guess the title of "*most qualified Robson*" now passes to me!

Benjamin Robson Bergen, August 2016

Abstract

This thesis investigates how remote sensing data can be used to assess the changing state of debris-covered ice. The principal study areas are the Manaslu Region in Nepal (papers I and III) and the Hohe Tauern National Park, Austria (paper II).

Clean glacier ice is straightforward to semi-automatically classify using multi-spectral satellite imagery owing to the strong spectral signature of clean ice in the visible and near-infrared sections of the electromagnetic spectrum. Since the ablation zones of clean ice glaciers are at the pressure melting point, a change in terminus position or glacier area can be directly linked to a change in climate. Debris-covered ice is however more complicated to map and to interpret temporal change. Supraglacial debris is spectrally indistinguishable from the surrounding paraglacial terrain, and requires auxiliary data such as a Digital Elevation Model (DEM), thermal band data, or flow data. Object-Based Image Analysis (OBIA) provides a framework for combining multiple datasets in one analysis, while additionally allowing shape, contextual, hierarchical and textural criteria to be used to classify imagery.

Paper I combines optical (Landsat-8), topographic (void-filled SRTM) and SAR coherence (ALOS PALSAR) data within an OBIA workflow to semi-automatically classify both clean ice and debris-covered ice in the challenging area surrounding Mount Manaslu in Nepal. When compared with manually delineated outlines, the classification achieved an accuracy of 91% (93% for clean ice and 83% for debris-covered ice). The classification was affected by seasonal snow and shadows while the debris-covered ice mapping was influenced by the datasets being temporally inconsistent, and the mountainous topography causing inconsistencies in the SAR coherence data. The method compares well with other automated techniques for classifying debris-covered ice, but has two additional advantages: firstly, that SAR coherence data can distinguish active ice from stagnant ice based on whether motion or significant downwasting has occured, and secondly, that the method is applicable over a large study area using just space-borne data.

Paper II explores the potential of using high-resolution (10 m) topographic data and an edge detection algorithm to morphologically map the extent of debris-covered ice. The method was applied in the Hohe Tauern National Park, Austria, using a 10 m DEM derived from airborne *Light Detection and Radar* (LiDAR) acquisitions. Additionally, the end-of-summer transient snowline (TSL) was also mapped, which approximates the annual Equilibrium Line Altitude (ELA).

Our classification was applied on three Landsat satellite images from 1985, 2003 and 2013 and compared the results to the Austrian Glacier Inventories from 1969 and 1998 to derive decadal-scale glacial changes. A mean rate of glacier area reduction of 1.4 km^2a^{-1} was calculated between 1969 and 2013 with a total reduction in area of 33%. The TSL rose by 92 m between 1985 and 2013 to an altitude of 3005 m. By comparing our results with manually delineated outlines an accuracy of 97.5% was determined. When a confusion matrix was calculated it could be seen that the results contained few false positives but some false negatives which were attributed to seasonal snow, shadows and misclassified debris. Our results correspond broadly with those found in other areas of the European Alps although a heterogeneity in glacier change is observable. We recommend that future glacier mapping investigations should utilise a combination of both SAR coherence data and high-resolution topographic data in order to delineate the extent of both active and stagnant glacier ice.

Paper III investigates decadal scale changes in glacier area, velocity and volume in the previously undocumented Manaslu Region, Nepal. Between 2001 and 2013 the glacier area reduced by 8.2% (-0.68% a^{-1}). Simultaneously, the glaciers lowered by -0.21 ± 0.08 m a^{-1} and had a slightly negative specific mass balance of -0.05 ± 016 m w.e a^{-1} although mass balances ranged -2.49 ± 2.24 to +0.27 ± 0.30 m w.e a^{-1} throughout the region. The geodetic mass balance for select glaciers covered by a Corona DEM between 1970 and 2013 was -0.24 ± 0.12 m w.e a^{-1} which became more negative (-0.51 ± 0.12 m w.e. a^{-1}) between 2005 and 2013. Rates of surface lowering over debris-covered ice increasing by 168% between 1970 – 2000 (0.40 ± 0.18 m a^{-1}) and 2005 – 2013 (1.07 ±0.48 m a^{-1}). The rate of glacier melt varies due to presumed increases in debris thickness at the upper and lower boundaries of the ablation zone, while an area

of enhanced glacier downwasting corresponds to the presence of supraglacial lakes and exposed ice.

The glacier velocity varies across the region. Many glaciers have stagnant sections towards the glacier termini, and a trend of ongoing stagnation is observable. No relationship exists between trends in glacier area and glacier volume or velocity, although a weak relationship exists between trends in the changes of volume and velocity. The rates of glacier area and velocity change appear to be similar, although the number of glaciers that had records of area, velocity, and volume was few. Our results are comparable to studies looking at mean surface lowerings and geodetic mass balances in other areas of the Himalayas, and point towards heterogeneous yet pronounced mass losses across the Himalaya region.

Abbreviations

ASTER	Advanced Spaceborne Thermal Emission and Reflection Radiometer
DEM	Digital Elevation Model
DGPS	Differential Global Positioning System
DInSAR	Differential Interferometric Synthetic Aperture Radar
ELA	Equilibrium Line Altitude
ESA	European Space Agency
GCP	Ground Control Point
GIS	Geographic Information System
GLIMS	Global Land Ice Measurements from Space
GLOF	Glacial Lake Outburst Flood
HEP	Hydroelectric Power
HTNP	Hohe Tauern National Park
ICIMOD	International Centre for Integrated Mountain Development
InSAR	Interferometric Synthetic Aperture Radar
LiDAR	Light Detection And Ranging
NASA	National Aeronautics and Space Administration
NCC O (or OC)	Normalised Cross Correlation Orientation (or Orientation Correlation)
NCC	Normalised Cross Correlation
NDSI	Normalised Difference Snow Index
NDVI	Normalised Difference Vegetation Index
NIR	Near Infrared
NDWI	Normalised Difference Water Index
OBIA	Object-Based Image Analysis
PBIA	Pixel-Based Image Analysis
RGB	Red Green Blue; false composite image made up from three spectral bands
SAR	Synthetic Aperture Radar
SETSM	Surface Extraction with TIN-based Search-space Minimization
SNR	Signal to Noise Ratio
SRTM	Shuttle Radar Topography Mission
SWIR	Shortwave Infrared
TSL	Transient Snowline

List of publications

Paper I:

Robson, B.A., Nuth, C., Dahl, S.O., Hölbling, D., Strozzi, T. and Nielsen, P.R., 2015. Automated classification of debris-covered glaciers combining optical, SAR and topographic data in an object-based environment. *Remote Sensing of Environment*, 170, pp.372-387.

Paper II:

Robson, B.A., Hölbling, D., Nuth, C., Strozzi, T. and Dahl, S.O., 2016. Decadal Scale Changes in Glacier Area in the Hohe Tauern National Park (Austria) Determined by Object-Based Image Analysis. *Remote Sensing,* 8(1), pp.67-90.

Paper III:

Robson, B.A., Nuth, C., Nielsen, P.R., Girod, L., Hendricks, M., and Dahl, S.O., 2016. Decadal Scale Glacier Surface Lowering and Stagnation in the Manaslu Region of Nepal. Manuscript in preparation for being submitted to *Frontiers of Earth Science*

Contents

1. Introduction

The Himalayas contain the largest concentration of ice outside of the Polar Regions. The water balance of Asia is highly dependent on the seasonal melting of glaciers and seasonal snow, feeding rivers such as the Ganges, Indus and Yangtze which indirectly support over one billion people (Immerzeel et al., 2010). The magnitude of climate change in high mountain environments such as the Himalayas is expected to be greater than the global average, which will have direct consequences for the Himalayan cryosphere (Eriksson et al., 2009, Shrestha and Aryal, 2011). Changes in the state of the glaciers can impact the local population in two ways. First, a change in the seasonality of Himalayan hydrology will influence the irrigation and use of water resources in the greater High Asia region (Immerzeel et al., 2010, Bolch et al., 2012). Second, the downwasting of glaciers can lead to the formation and growth of pro-glacial lakes. Continued glacier melt can cause these lakes to expand to the point where they can breach; causing a Glacial Lake Outburst Flood (GLOF) (Bolch et al., 2008a, Schwanghart et al., 2014). Previous GLOF events in the Himalayas have destroyed hydro-electric power (HEP) plants, local villages, hiking paths, and transportation infrastructure (Richardson and Reynolds, 2000, Mool, 2011). In total over 6300 people are estimated to have been killed by GLOFs in central Asia since the 1500s (Carrivick and Tweed, 2016).

The status of glaciers in the Himalayas is therefore of great importance. Our understanding of the Himalayan cryosphere has for a large time been severely limited by a lack of data. The inaccessibility and remoteness of Himalayan glaciers have resulted in very few glaciers being directly studied. Between 1977 and 1999 only 6.8 km^2 of 30,000 km^2 of ice was sampled directly (Berthier et al., 2007). The lack of data is one of the causes of the now infamous *glaciergate* in which the 2007 Intergovernmental Panel on Climate Change (IPCC) incorrectly stated that the majority of Himalayan glaciers would disappear by 2035 (Cogley et al., 2010). Although the number of direct measurements has subsequently grown due to an increase in interest in the Himalayan cryosphere (Bolch et al., 2012), the majority of measurements are still biased towards small, debris-free, and easily-accessible glaciers (Gardelle et al.,

2013). Remote sensing has increasingly been used to study Himalayan glaciers. While some studies have addressed the entire mountain chain (Bajracharya and Shrestha, 2011, Kääb et al., 2012, Dehecq et al., 2015), those that study glacier changes over longer time-spans are typically restricted specific catchments in the Everest Region (Bolch et al., 2011), the Tian Shan (Shangguan et al., 2015), and the Indian Himalayas (Bhattacharya et al., 2016)with a noticeable lack of research in the Central Himalayas.

Ten percent of Himalayan glaciers are covered by supraglacial debris (Gardelle et al., 2013), although this proportion varies across the Himalayas. A clear distinction can be observed between the northwards flowing glaciers on the Tibetan Plateau that are clean ice glaciers, and the southwards flowing glaciers in the Himalayas that are covered by supraglacial debris in their ablation zones. Supraglacial debris is derived from debris flow and rock avalanche material that accumulated in the ablation zones of the glaciers. Nagai et al. (2013) suggested that more effective diurnal freeze-thaw action on slopes located south of the mountain divide causes an abundance of weathered and mobile material. The mountain slopes on the north of the mountain divide are on the other hand characterised by a more continental climate. The winter temperatures are far below freezing point which impedes freeze-thaw processes., thus limiting the amount of mobile debris.

1.1 Remote Sensing as a tool within glaciology

Remotely sensed data, such as satellite imagery has increasingly been used to increase our understanding of glaciers over varying spatial and temporal scales. Multispectral imagery, such as Landsat, ASTER or Sentinel-2 can be robustly and efficiently used to extract glacier outlines for clean ice glaciers, allowing inventories to be created with minimal manual correction necessary. Snow and ice have very low reflectance values in the shortwave infrared spectrum and very high reflectance values in the visible spectrum (Figure 1). This characteristic is the basis for distinguishing glacier ice from the surrounding terrain using methods such as supervised and unsupervised methods (Li et al., 1998, Sidjak, 1999), band ratios (Andreassen et al., 2008, Bolch et al., 2010) and object-based classifications (Bajracharya et al., 2014a, Rastner et al., 2014). A list

of commonly used band ratios and indices used for classification is given in Table 1. This has permitted mostly automated analysis of glaciers in clean ice regions such as Norway (Andreassen et al., 2012), western Canada (Bolch et al., 2010) and Patagonia (Paul and Mölg, 2014).

In regions that lack *in-situ* data, archives of remote sensing data can be used to quantify glacier change over several decades. Remote sensing has allowed spatially extensive monitoring of glacier parameters such as area , volume change, and velocity across the entire Himalayas (Bajracharya and Shrestha, 2011, Kääb et al., 2012, Dehecq et al., 2015, Kääb et al., 2015, Nuimura et al., 2015). Data from many sensors is freely available, such as Landsat, Advanced Spaceborne Thermal Emission and Reflection Radiometer (ASTER), and most recently the European Space Agency (ESA) Sentinel missions. When archives of remote sensing data are combined it is possible to assess glacier changes over the last 60 years (Figure 3). The Landsat series in particular provides a valuable resource, with 30 m resolution imagery over much of the planet back to 1982 and coarser 60 m imagery back to 1972 (Wulder et al., 2012). Since the Landsat archive was made freely available in 2008, the amount of scientific work using Landsat satellite imagery has rapidly increased (Wulder et al., 2012).

Clean glacier ice is spectrally distinct from the surrounding terrain (Figure 1 and 2) and can thereby be classified in a robust and efficient manner (Paul et al., 2015). Debris-covered is however spectrally similar to the surrounding terrain (Figure 2), such as paraglacial material or moraines, and is therefore more complicated to delineate.

Table 1: Commonly used spectral custom indices used in the classification of glacier ice.

Index Acronym	Custom Index Name	Band Formula
NDVI	Normalised Difference Vegetation Index	(NIR − Red) / (NIR + Red)
NDSI	Normalised Difference Snow Index	(Green − (SWIR) / (Green + SWIR)
NDWI	Normalised Difference Water Index	(Green − NIR) / (Green + NIR)
LWM	Land and Water Mask	(SWIR / Green + 0.001) × 100
NIR/SWIR	Commonly referred to as TM4/TM5	NIR/SWIR1
Red/SWIR	Commonly referred to as TM3/TM5	Red/SWIR1

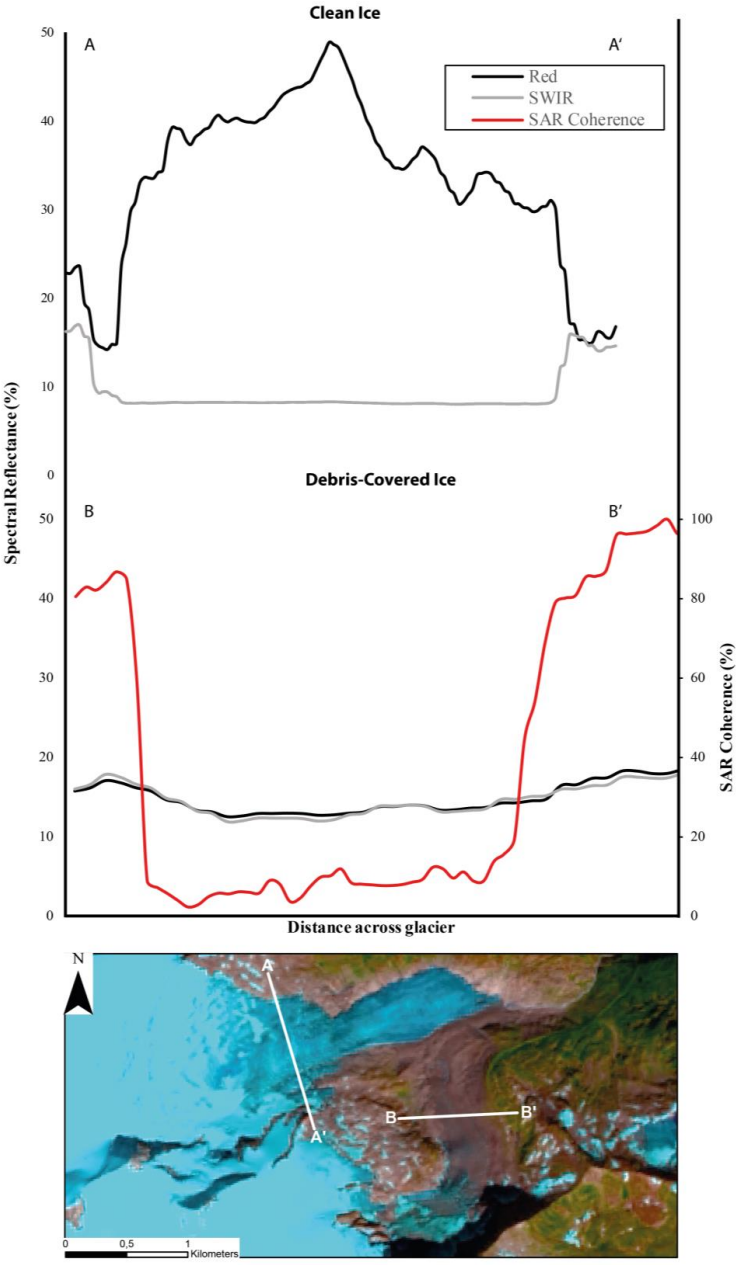

Figure 1: Spectral profiles across clean ice and debris-covered ice on Schlaten Kees, Hohe Tauern National Park, Austria. Note that across clean ice (A – A') there is a high degree of spectral difference between the red and shortwave infrared bands allowing band ratios or indices to differentiate clean ice from the surrounding terrain. There is essentially no spectral difference over debris-covered ice (B – B') where debris-covered ice is spectrally similar to the surrounding terrain. SAR coherence is capable of distinguishing debris-covered ice however, with flowing ice resulting in a loss of coherence (red line). Background image is a 2013 Landsat false colour composite.

Figure 2: Supraglacial debris is spectrally similar to the surrounding terrain and paraglacial material an can therefore be complicated to differentiate between using optical imagery. Photo: Jeff Kargel.

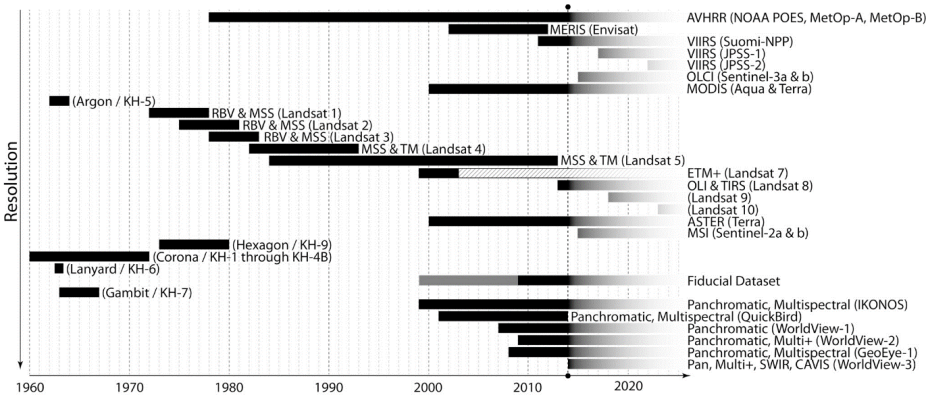

Figure 3: Past, present, and future optical satellite sensors. The exploitation of remote sensing archives allows time-series of data spanning more than 60 years. (Pope et al., 2014). (Repreinted under the Creative Commons Attribution-Non Commercial-No Derivatives License (CC BY NC ND).

1.2 Supraglacial debris and glacier mass balance

Debris-covered ice is known to complicate the relationship between glaciers and climate (Scherler et al., 2011, Benn et al., 2012). Many studies have found that when supraglacial debris reaches a given thickness then the debris acts to insulate the glacier ice as opposed to amplifying melting (Table 2). Reznichenko et al. (2010) ran experiments on how debris-cover influences ice melt rates within a laboratory and found that a debris-thickness of 50 mm would offset melting for > 12 hours. Given diurnal temperature variations however, debris that is 50 mm thick will never reach a steady state heat flux and the underlying ice will be completely insulated. These findings however fail to account for the fact that debris-cover thickness is spatially variable and frequently punctuated by exposed ice and can contain supraglacial lakes and ice cliffs (Figure 4).

Zhang et al. (2011) assessed the influence of debris-cover on a Tibetan glacier using both in-situ surveys and ASTER imagery and found that for 67% of the ablation area the debris-cover increased glacier melting, for 19% of the area the debris-cover insulated the underlying ice and for 14% of the area the melt-rate on the debris-covered ice equalled that on the clean ice. Some studies report that exposed ice can augment rates of ablation by an order of magnitude and that 20% of the total glacier ablation occurs through exposed ice and supraglacial lakes (Sakai et al., 2002, Immerzeel et al., 2014).

Additionally, the response of debris-covered glaciers varies from catchment to catchment with many glacier termini remaining stationary in recent years despite ongoing glacier downwasting (Scherler et al., 2011, Benn et al., 2012). Shukla and Qadir (2016) found areal shrinkages of 14 - 21% for glaciers in the Zanskar basin in the Ladakh Himalayas between 1977 and 2013 despite minimal terminus retreats (~2.5 ma^{-1}) using Landsat and ASTER imagery.

Table 2: Measured critical thicknesses on glaciers; critical thickness is thickness at which the debris insulates the underlying ice from melting. Source: Reznichenko et al. (2010)

Glacier	Country	Latitude (°N)	Elevation (m a. s. l.)	Critical thickness (mm)	Source
Khumbu	Nepal	27.57	5400	50	Kayastha and others (2000)
Lirung	Nepal	28.13	4400	80	Tangborn and Rana (2000)
Rakhiot	Pakistan	35.21	3400	30	Mattson and Gardner (1989)
Barpu	Pakistan	36.11	4000	25	Khan (1989)
Kuldgilga	Kagyzstan	39.30	5000	115	Demchenko and Sokolov (1982)
Djankuat	Russia	42.12	2700	70	Popovnin and Rozova (2002)
Eliot	USA	45.23	2200	40	Lundstrom and others (1993)
Peyto	Canada	51.41	2600	15	Nakawo and Young (1981)
Dome	Canada	52.12	2200	20	Mattson (2000)
Athabasca	Canada	52.12	2200	20	Mattson (2000)
Bilchenok	Russia	56.10	700	40	Yamaguchi and others (2000, 2007)
Kaskawulsh	Canada	60.46	1000	35	Loomis (1970)
Isfallsglaciaren	Sweden	67.54	1200	30	Østrem (1965)

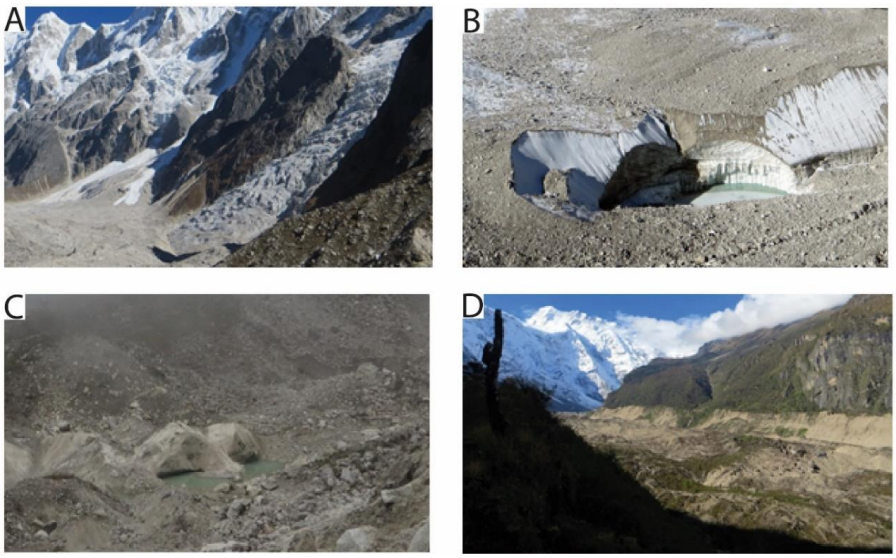

*Figure 4: Typical features of debris-covered glaciers. **(A)** Steep sections of ice (>40°) that meet shallower portions of the glacier (<25°) causing supraglacial debris to build-up and become entrained. **(B)** Exposed ice cliffs. **(C)** A supraglacial lake. **(D)** Stagnant lower reaches of a debris-covered glacier with vegetation growing. Photos: Benjamin Aubrey Robson and Pål Ringkjøb Nielsen.*

Bolch et al. (2008b) found that the debris-covered area on glaciers in the Everest Region have remained stable, leading to small overall area reductions, while Benn et al. (2012) claimed that Himalayan debris-covered glaciers primarily lose mass through melting of clean ice close to the ELA, vertical downwasting beneath debris, melt around ice-cliffs and ponds, and calving. It may therefore not be sufficient to solely measure glacier area change in order to properly assess the health of glaciers. Despite this some authors have used stationary termini positions to conclude that debris-covered glaciers in the Himalayas are in a balance and not losing mass (Ren et al., 2006, Bahuguna et al., 2007, Mehta et al., 2011, Bahuguna et al., 2014, Bajracharya et al., 2014b). Both changes in glacier velocity and glacier volume can be used as more direct indications of glacier mass balance and are measurable with remote sensing techniques (Heid and Kääb, 2012b, Paul et al., 2015). There is therefore a need to assess glacier response across the Himalayas in order to understand the heterogeneity of glacier change.

1.3 Mapping of debris-covered ice

The presence of supraglacial debris poses a problem for glacier mapping. As already mentioned, supraglacial debris is spectrally similar to the surrounding terrain and paraglacial material (Figures 1 and 2) which prevents simple band ratio techniques from being able to spectrally identify the ice. Instead auxiliary data and additional analysis tools must be used to map the extent of the debris-covered ice. Many authors opt to use morphological parameters such as the slope or curvature derived from a DEM or thermal band data in combination with optical data to map debris-covered ice (Paul et al., 2004, Ranzi et al., 2004, Shukla et al., 2010, Bhambri et al., 2011a, Racoviteanu and Williams, 2012, Bhardwaj et al., 2014, Alifu et al., 2015). This can be problematic for two reasons. Firstly, in some glaciated areas of the world, such as the Himalayas, it can be very costly to obtain an up-to-date and high-resolution DEM (Bolch et al., 2007). Secondly, the thermal signature of the underlying ice is entirely dependable on the distribution, composition, and thickness of the debris-cover (Takeuchi et al., 2000, Reznichenko et al., 2010), and may not always provide a reliable

means for mapping glacier ice. Many automated techniques for glacier mapping have been put forward, but the majority of them have been trailed over small study areas. There is therefore a need for a transferable method for classifying debris-covered ice over large areas.

This has led some authors to utilise flow data for mapping debris-covered ice based on the assumption that debris-covered ice will flow under its own weight. Smith et al. (2015) included velocity fields from Landsat 8 imagery in a workflow to map debris-covered ice, while Atwood et al. (2010) and Frey et al. (2012) used Synthetic Aperture Radar (SAR) coherence data.

SAR coherence data is produced by using two SAR scenes with a time-interval of approximately one month. Anything in the scene that has not changed, deformed or moved between the scenes maintains coherence, while anything that has moved or changed (such as a glacier flowing or melting beneath debris-cover) results in a loss of coherence. A strong contrast is therefore visible between active and flowing ice, and the surrounding terrain. SAR coherence data is therefore also capable of distinguishing stagnant glacier ice from active, flowing glacier ice. One problem associated with this is that glacier flow is not the sole cause for a loss of coherence. Vegetation change, surface water, landslides and mass movements can also result in a loss of SAR coherence. SAR coherence data cannot therefore be used solely to classify debris-covered ice without the use of other data sources, such as optical satellite imagery, or a DEM (Frey et al., 2012).

2. Research Objectives

This thesis addresses current research gaps concerning the study of debris-covered ice with the aim of improving our understanding of how debris-covered glaciers are responding to a changing climate, and the repercussions this will have on the population in the vicinity of the Himalayas. More specifically, this thesis assesses how remote sensing data can be used to identify and map debris-covered ice, and quantify its change over decadal scale time spans. The following research questions were focused on:

1. What is the potential for using satellite imagery within OBIA to accurately and efficiently classify clean and debris-covered ice components over a large area without auxiliary ground data?
2. How can OBIA be used to automate glacier change detection using multi-temporal satellite imagery?
3. What advantages does OBIA have for automated glacier mapping over traditional pixel-based techniques?
4. How have the glaciers in the Manaslu Region responded to changes to the climate on decadal scales, and how do these changes compare with other areas of the Himalayas?
5. How do trends in debris-covered glacier area relate to glacier velocity and volume trends? What implications does this have on glacier monitoring?

3. Study Areas

In this thesis, debris-covered and clean ice glaciers were investigated in two different geographical regions (Figure 5). The study area for two of the publications (**Paper I** and **Paper III**) was the Manaslu Region of Nepal while **Paper II** was conducted in the Hohe Tauern National Park in Austria. Both of these study areas contain supraglacial debris. The debris-covered glaciers in the Manaslu Region are important for water resources, with meltwater from the glaciers eventually flowing into the Gandaki River, a tributary for the River Ganges. The Manaslu Region also contains Thulagi Glacier which formerly-terminated in Dona Lake. The lake is currently dammed by an ice-cored moraine (Pant and Reynolds, 2000). Dona Lake has been identified as one of the most potentially dangerous glacier lakes in Nepal in the event of a GLOF event (Mool, 2011).

The debris-covered glaciers in the Austrian Alps are less numerous and less critical in terms of geohazards or water resources when compared to the Himalayas. Unlike the Manaslu Region however, high-resolution elevation products are available based on airborne LiDAR data acquired over the entire Austrian Alps by the federal governments of Austria. This provides an excellent opportunity to test how high-resolution elevation data roughly comparable to the TanDEM WorldDEM, which will soon be globally available at a resolution of 12 m, can be used in automated classifications of debris-covered ice based on the surface morphology. This will have implications for global-scale monitoring of debris-covered ice.

3.1 Manaslu Region, Nepal

The Manaslu Region of Nepal, in the Central Himalaya (Figure 5, and Figure 1; Paper I), covers 2350 km^2 in total, 33% (788 km^2) of which is covered by glaciers. The region contains a mixture of clean, debris-covered, stagnant, and lake terminating glaciers. The study area is located on both sides of the Nepali-Tibetan border, which is also the divide between the humid, monsoon-driven climate of the Himalayas to the south, and the more arid and continental climate of the Tibetan plateau to the north. The glaciers

flowing north onto the Tibetan plateau are generally clean ice, while the Himalayan glaciers flowing to the south are debris-covered in their ablation areas. The glaciers range in area from 5.6 to 32.0 km^2, are typically 0.5 km to 1 km wide, 5 – 15 km long, and range in elevation from 3000 m a.s.l. to over 7000 m a.s.l. Climate data in the region is limited, yet the Nepali Department of Hydrology and Meteorology estimate maximum and minimum annual temperatures of 26.7 °C and 12.8°C with 1066 mm of annual precipitation at the Larke Samdo weather station, 84°38E, 28°39N, 3650 m a.s.l. (Department of Hydrology and Meteorology (Government of Nepal), 2014). Glaciers in the Himalayas typically receive up to 80% of their annual accumulation during the summer monsoon meaning that rates of glacier accumulation and ablation are simultaneously at their highest between June and September (Benn and Owen, 1998). Himalayan glaciers are therefore sensitive to small perturbations in the intensity of the summer monsoon temperature which can influence both rates of ablation and the proportion of rain to snow (Benn and Owen, 1998). Tibetan glaciers in contrast respond more to the ablation season temperature (Owen and Benn, 2005).

3.2 The Hohe Tauern National Park, Austria

The Hohe Tauern National Park (HTNP) covers approximately 1800 km^2 between the federal states of Carinthia, Salzburg, and Taol in western Austria (Figure 5, and Figure 1; Paper II). Approximately 10% of the HTNP is ice-covered, with glaciers ranging in altitude from 2000 to 3600 m a.s.l. with the majority of glaciers being found between altitudes of 2700 and 3100 m. The glaciers in the HTNP are a mixture of clean ice and debris-covered ice which includes Pasterze Glacier (17.6 km^2), the largest glacier in the Austrian Alps. About 1.2 km^2 of Pasterze Glacier is covered in supraglacial debris cover, which reaches a thickness of 47 cm towards the glacier terminus (Kellerer-Pirklbauer, 2008). The majority of Austrian glaciers are less than 1 km^2 and only five glaciers in the country are larger than 10 km^2 (Paul et al., 2014). The climate in the Alps has changed considerably over the past decades and has warmed at a rate of approximately double the global average (Auer et al., 2007, Gobiet et al., 2014). This has led to a rapid retreat in small Alpine glaciers.

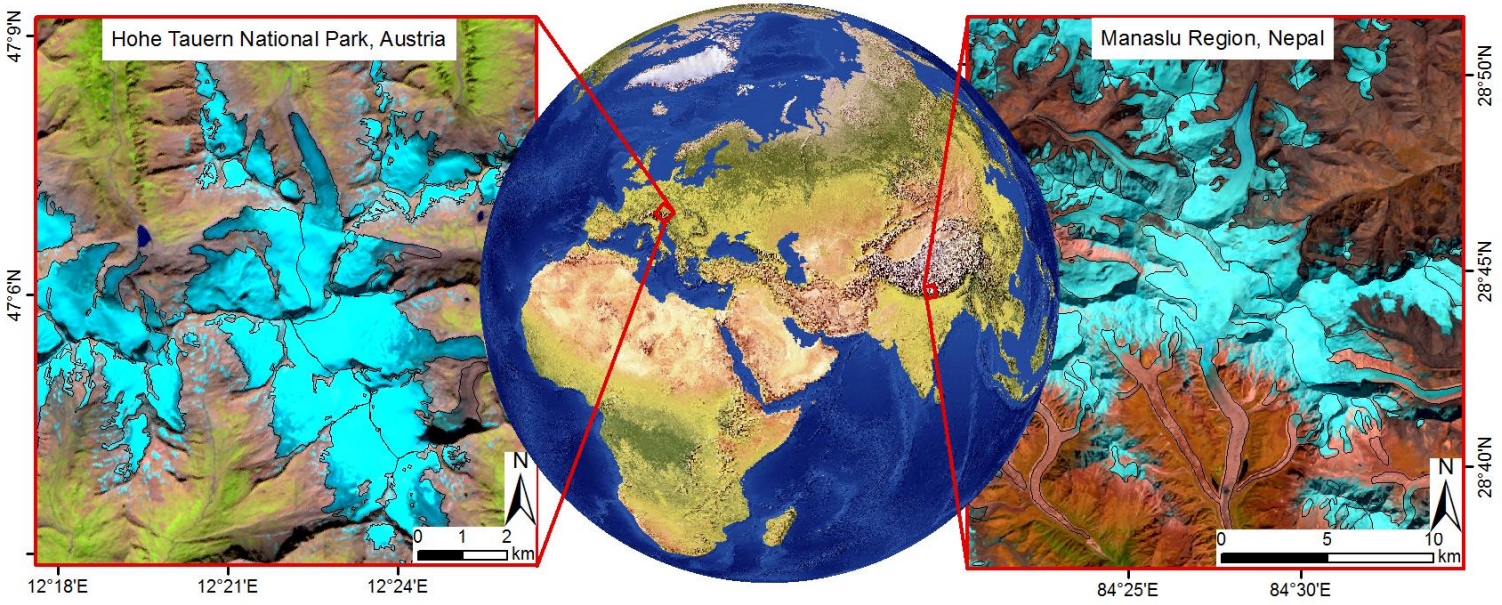

Figure 5: The location of the two study areas in this thesis. The Manaslu Region, Nepal was the study area for papers I and III. The Hohe Tauern National Park, Austria was the study area for paper II. For more extensive maps showing the study areas in their entirety, see figure (paper I) and figure 1 (paper II). The background satellite images on the subsets are false colour Landsat composites overlaid with glacier outlines from the Randolf Glacier Inventory v5.0 (RGI). The land cover satellite mosaic shown on the world map is derived from NASA MODIS data and downloaded from NaturalEarthData.com.

4. Background Methods

4.1 Object-Based Image Analysis (OBIA)

Object Based Image Analysis (OBIA) provides a framework for combining data sources as well as extracting information from imagery in a way that mimics our own perception of reality (Blaschke et al., 2014). OBIA is an emerging technology within remote sensing and image processing made possible by advances in computational power, and an increase in the resolution of imagery. As the spatial resolution of satellite imagery has increased, the relationship between the objects to be classified and the pixel sizes has changed (Figure 6). Objects (such as glaciers) are now represented by groups of pixels instead of individual pixels.

The initial stage in OBIA is the segmentation of the image pixels into near-homogenous objects that resemble real world features. In many ways this is the most crucial (and time consuming) step in OBIA (Dragut et al., 2014, Rastner et al., 2014). Analysis conducted at the object level is thereby not affected by the 'salt and pepper effect' that often impacts traditional pixel-based image analysis (PBIA) techniques that arise due to pixel-base noise and variation.

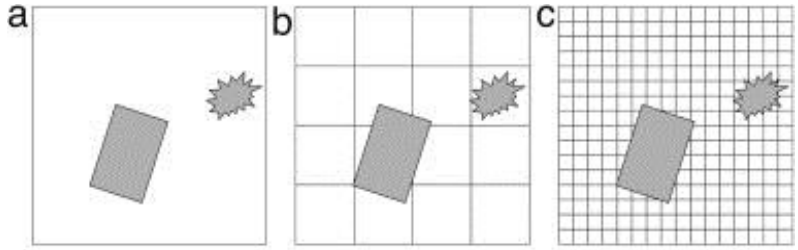

Figure 6: Relationship between objects under consideration and spatial resolution: (a) low resolution: pixels significantly larger than objects, sub-pixel techniques needed. (b) medium resolution: pixel and objects sizes are of the same order; pixel-by-pixel techniques are appropriate. (c) high resolution: pixels are significantly smaller than object, segmentation of pixels into groups of pixels and finally objects is needed (Blaschke, 2010). (Repreinted under the Creative Commons Attribution-Non Commercial-No Derivatives License (CC BY NC ND).

OBIA provides a methodological framework for computer-based interpretation of complex classes that are defined by a range of spatial, spectral, textual, and contextual properties derived from multiple data sources (Lang, 2008). This allows the image to be classified in a way that more mimics how the human eye interprets an image. For example, OBIA could understand that an iceberg is surrounded by water, that a lake is flat and surrounded by steeper slopes, or that a snow patch is less than 0.1 km^2 and should not be mapped as a glacier. OBIA also includes many processing algorithms, such as edge detection and otsu automatic thresholding which can be implemented directly into the classification workflow. OBIA allows more robust image classifications and is therefore more suitable for classifying complex natural phenomena, such as glaciers.

OBIA has to date been relatively underutilised within glaciology. Rastner et al. (2014) compared OBIA and PBIA in a selection of glacierised regions and found that OBIA outperformed PBIA by 3% for clean ice and by 12% for debris-covered ice. The International Centre for Integrated Mountain Development (ICIMOD) used Landsat TM data and the Shuttle Radar Topography Mission (SRTM) DEM to semi-automatically map all glaciers across the Himalayas (Bajracharya and Shrestha, 2011, Bajracharya et al., 2014a). Robb et al. (2015) used OBIA to map glacial geomorphology in Iceland based on a LiDAR DEM, and by using a mixture of textural, spatial and spectral rulesets they obtained results with an accuracy of 77%. It is clear that given the advantages that OBIA offers in image processing and classification there is potential for further automation of glacier mapping. This thesis includes two publications that deal with different approaches for classifying debris-covered glaciers within OBIA employing auxiliary data.

4.2 DEM generation from declassified Corona imagery

Corona and *Hexagon* were American reconnaissance missions that operated between 1960 - 1972 and 1973 – 1984 respectively. They were declassified in three stages in 1995, 2002 and 2011 (Fowler, 2013, Maurer and Rupper, 2015), and are now an invaluable asset to glaciologists, allowing surface lowerings and geodetic mass

balances to be calculated over time-periods of more than 60 years. Processing these data are however time consuming. Corona imagery in particular contains severe panoramic distortions that must be corrected (Altmaier and Kany, 2002) and has little calibration information available and no fiducial marks, which makes triangulation and DEM generation difficult. The interior orientation must be mathematically determined by using several hundred tie points, while the exterior orientation can be set using Ground-Control Points (GCPs) to link the images to a geographic co-ordinate system. Corona and Hexagon imagery has found increasing use in assessing geodetic mass balances for glaciers (Bolch et al., 2011, Pieczonka et al., 2013, Maurer and Rupper, 2015, Pieczonka and Bolch, 2015) as well as area changes across the Himalayas (Narama et al., 2010, Bhambri et al., 2011b, Schmidt and Nüsser, 2012, Chand et al., 2016).

4.3 Glacier Volume Change from DEM Differencing

The change in glacier volume or surface elevation can be determined by comparing DEMs from different points in time. If assumptions are made about the density of snow and ice then the geodetic mass balance can be calculated (Cogley et al., 2011). Assumptions commonly made are that Sorge's law applies; that density does not vary with depth (Bader, 1954) and that the ice that ablates or accumulates has a certain density. This is either a fixed density, normally between 850 – 900 kg m^{-3} (e.g. Bolch et al. (2011)) or different densities for the accumulation and ablation zones, with the accumulation zone commonly having lower densities of ~490 - 650 kg m^{-3} (Schiefer et al., 2007, Huss, 2013, Pellicciotti et al., 2015).

DEMs can be derived from many sources such as airborne and space-borne optical imagery using photogrammetry (Bolch et al., 2011), inferometric SAR (InSAR) data (Pandey et al., 2016), LiDAR scanning (terrestrial, airborne or spaceborne) (Abermann et al., 2009) and topographic maps (Aizen et al., 2007, Bauder et al., 2007). Each data source has limitations associated with it. Optical data for example requires good visual contrast, which can be problematic over snow covered terrain. InSAR data is dependent on coherence between images, and certain radar bands can penetrate snow and ice by

up to 10 m (Rignot et al., 2001). LiDAR data can have problems with waveform saturation as well as range restrictions (Paul et al., 2015) while topographic maps, particularly old maps can be subjective, inaccurate, or surveyed at low scales (Bauder et al., 2007).

4.3.1 DEM Co-registration

Before DEMs can be compared they must be co-registered to ensure that observed elevation differences are not a result of poorly aligned elevation products. There are many methods available for the co-registration of DEMs, yet Paul et al. (2015) suggest the method by Nuth and Kääb (2011) to be most computationally efficient. This method compares elevation bias (dH) divided by the tangent of the slope (tanα) against the aspect (ψ), as shown in Eq (1):

$$\frac{dh}{\tan\alpha} = a.\cos(b - \psi) + c \quad (1)$$

where *a* and *b* are the magnitude and direction of the co-registration shift, respectively, and *c* is the mean elevation bias between the DEMs divided by the mean surface slope. While this method removes planimetric elevation biases, many satellite derived DEMs contain along track and cross track elevation biases. These can be removed by fitting a polynomial equation to elevation differences over stable terrain.

4.3.2 Calculating surface lowerings, volume changes, and geodetic mass balances

The co-registered DEMs can be subtracted from one another to calculate changes in surface elevation. Inaccuracies in one or both DEMs in the differencing can however cause erroneous elevation values. To avoid surface and volume change results being adversely affected, elevation changes are often filtered. Many authors opt to exclude elevation differences that exceed the value of two or three times the standard deviation of elevation changes on stable terrain (Gardelle et al., 2013, Pellicciotti et al., 2015), or elevation differences that exceed known or realistic thinning or thickening rates (Wang and Kaab, 2015, Berthier et al., 2016). To avoid a systematic bias due to data coverage,

data voids can be filled. Bolch et al. (2011) filled voids that were smaller than 10 pixels using a spline interpolation, while Gardelle et al. (2013) filled voids based on the mean elevation change by elevation bands.

Mean rates of surface lowering can then be determined for each glacier. Changes in volume can be worked out by summing up the elevation changes at each pixel (SL) and multiplying by the pixel size (PS) squared:

$$\Delta V = \sum SL \times PS^2 \quad (2)$$

A change in volume is converted to a geodetic mass balance (*B*) by assuming a constant density of glacier ice (see *4.3*), ρ_i and wate,r ρ_i (999.972 kgm^{-3}) and dividing by the glacier area (S) (Cogley et al., 2011, Pieczonka and Bolch, 2015):

$$B = \frac{\rho_i}{\rho_w} \times \frac{\Delta V}{S} \quad (3)$$

4.4 Glacier velocity

The velocity of a glacier is an important parameter which controls the flow of mass between the accumulation and ablation zones of the glacier, and both governs, and is governed by the glacier geometry (Kääb, 2005).

The glacier discharge (Q_x) through a cross section at a given distance (x) from the highest point on a glacier can be expressed as:

$$Q_x = \sum_{i=1}^{x} b_i w_i \quad (4)$$

where b_i is the net balance rate and w_i is the width at successive portions of the glacier surface (Benn and Evans, 2010). When Q_x is divided by the cross sectional area, A_x then the average velocity, $\bar{u}_x$ is derived. Measuring the long-term change in glacier velocity is therefore an appropriate means for assessing a change in glacier mass balance.

4.4.1 Determining glacier velocities with remote sensing

Glacier velocity can be determined by measuring the displacement of surface features between successive imagery, commonly referred to as feature tracking. Optical satellite imagery such as from the Landsat or ASTER sensors have been extensively used to calculate velocities (Kääb, 2005, Heid and Kääb, 2012b, Sam et al., 2015). Feature tracking methods identify features such as crevasses, debris or dirty ice and calculate the displacement between them. Berthier et al. (2005) tracked features between SPOT5 satellite images and found an accuracy of 1/5 of a pixel when compared to DGPS measurements. Although variations in the altitude of the Landsat sensor cause sub-pixel noise, the larger spatial and temporal coverage of Landsat imagery compared to other sensors means it has been widely used in velocity calculations (Quincey et al., 2011, Heid and Kääb, 2012a, Fahnestock et al., 2015). Lee et al. (2004) found that Landsat-7 imagery had image to image registrations accuracies of ~5 m, while Landsat 8 and Sentinel 2 imagery can map displacements to a precision of 1-2 m (Fahnestock et al., 2015, Kääb et al., 2016).

Pre-processing of images can help extract additional image matches. Heid and Kääb (2012a) evaluated different matching techniques for different glacierised regions and found that using orientation correlation (OC) enhanced the number of correct matches that could be extracted when working on debris-covered glaciers in the Himalayas. Using OC (also known as Normalised Cross Correlation Orientation, or NCC O) enhances the differences in pixel values and creates a normalised image of the gradient of pixel values. Unlike NCC, which operates in the spatial domain (using a reference window and searching for the same features in the second image), NCC O operates in the frequency domain (phase differences across the reference window are correlated). NCC O is more sensitive to the change in pixel values rather than the pixel values themselves and is hence not prone to mismatches due to changes in scene illumination.

Feature tracking is sensitive to the spectral and spatial resolution of the data used (Sam et al., 2015), the temporal interval between acquisitions (Paul et al., 2015) and the accuracy of the image orthorectification (Kääb, 2005). Additionally, the size of the

reference template, i.e. the number of pixels that is considered a discrete "feature" to be tracked is also important. The template must be large enough that the features being matched are not noise artefacts but small enough to limit displacement gradients within the window (Heid and Kääb, 2012a). Some authors have developed methods that mitigate this problem. For example, Debella-Gilo and Kääb (2012) created an algorithm that compares the template size to the signal to noise ratio (SNR) to determine an optimum template size for maximum cross correlation coefficients while Ahn and Howat (2011) applied feature tracking to many input image derivatives such as gradients and principle components with many template sizes and found the most probable displacement based on stacking the data.

Problems can arise if the DEMs used in orthorectification of satellite images by NASA or ESA before the images are distributed are of poor quality. If two satellite images are acquired from different positions, then poor orthorectification can lead to artificial horizontal displacements (Kääb, 2005). This bias is cancelled out of if the satellite images are acquired from the same row and path.

In this thesis the NCC O algorithm was implemented within the open source software *CIAS* (Kääb and Vollmer, 2000).

4.5 Uncertainty estimation

The uncertainty of the results in this thesis is a key component since the first two papers deal with the accuracy of automated mapping of debris-covered ice and the third with decadal scale glacier changes and whether the observed changes are significant. We assessed the glacier mapping accuracies in two ways, percentage deviations from reference glacier outlines, and by computing a confusion matrix. The former is useful in comparing different classification methods but is influenced by the size of the glaciers and the total sample size. As the number of glaciers increases, the percentage deviation becomes a random error and not a systematic error (Nuth et al., 2013). A confusion matrix has the advantage of being able to differentiate between false

positives (objects mapped as glacier ice that in actuality were not), and false negatives (glacier ice that was not mapped).

The accuracy of the volume and velocity results were determined by assessing the values over terrain that was assumed to be stable. In the absence of *in-situ* velocity measurements the velocity measurements over stable terrain can be used as a measure for uncertainty, with the assumption that the displacements should be zero. The standard deviation of these displacements can then be used for setting error budgets. The High Himalayas in reality does not have terrain that is completely stable and is frequently effected by rockfalls, debris flows, and other mass movements. When longer time-intervals are used for feature tracking the likelihood of displacements being registered on stable ground increases, making uncertainty estimates more troublesome.

5. Presentation of Papers

This thesis includes three articles. The first two articles address different approaches of automated mapping of debris-covered ice within OBIA. In **Paper I,** SAR coherence data is combined with optical and elevation data to map debris-covered ice in the Manaslu Region of Nepal based on whether the surface has moved or changed between two acquisitions. **Paper II** uses high-resolution elevation data to map debris-covered ice based on the surface morphology in the High Tauern National Park, Austria. Decadal changes in glacier area were determined by classifying Landsat images from 2013, 2003, and 1985 and comparing the results with the first two Austrian Glacier Inventories from 1969 and 1998. **Paper III** investigates how debris-covered glaciers in the Manaslu Himalaya have responded to climate in the last decades in terms of glacier area, velocity, and volume and how these changes fit into the broader picture of Himalayan glacier change.

5.1 Paper I: Automated classification of debris-covered glaciers combining optical, SAR and topographic data in an object-based environment

In **paper I** we mapped debris-covered glaciers by integrating SAR coherence data (ALOS PALSAR) with optical (Landsat 8) and topographic (void-filled SRTM) data. This has some distinct advantages. Notably that only satellite-borne data is required allowing the method to be applied anywhere on the planet without the need for high-resolution elevation data which often must often be derived from airborne or terrestrially surveyed data. Additionally, since SAR coherence data is sensitive to movement, it is possible to differentiate between active and stagnant ice, something that Bolch et al. (2007) and Ghosh et al. (2014) have previously highlighted is missing from other classification methods.

Two classifications were performed, one based solely on the optical and topographic data (OBIA_OT), while the second classification used in addition the SAR coherence data (OBIA_OTS). Figure 2 (paper I) shows the entire methodology employed to classify debris-covered ice, clean ice and glacial lakes. Both OBIA classification outlines were then compared to each other, to manually delineated outlines, and to the

reference glacier inventory (the 2010 ICIMOD glacier inventory). We mapped 788 km^2 of glacier ice in the Manaslu Region, 15% (113 km^2) of which is debris-covered. The OBIA_OTS method had an accuracy of 91% for mapping the entire glaciers, or when broken down, 93% accuracy for clean ice and 83% for debris-covered ice. When the SAR data was excluded from the classification procedure (OBIA_OT), the accuracy of the classification of debris-covered ice fell to 72%.

The results show that the inclusion of SAR coherence data is clearly advantageous for mapping debris-covered glaciers. The OBIA_OTS method was able to classify debris-covered glaciers even when the debris lithology varied considerably over the glacier surface (Figure 6; Paper I). There were some areas where the SAR coherence signal of glacier ice was indistinguishable from the surrounding terrain. For example a loss of coherence or little return to the sensor occurred at the termini of glaciers if vegetation or water were present, additionally no data was returned from some north-facing valleys. Both methods struggled with some of the steep tributary glaciers where the clean ice met the debris-covered ice.

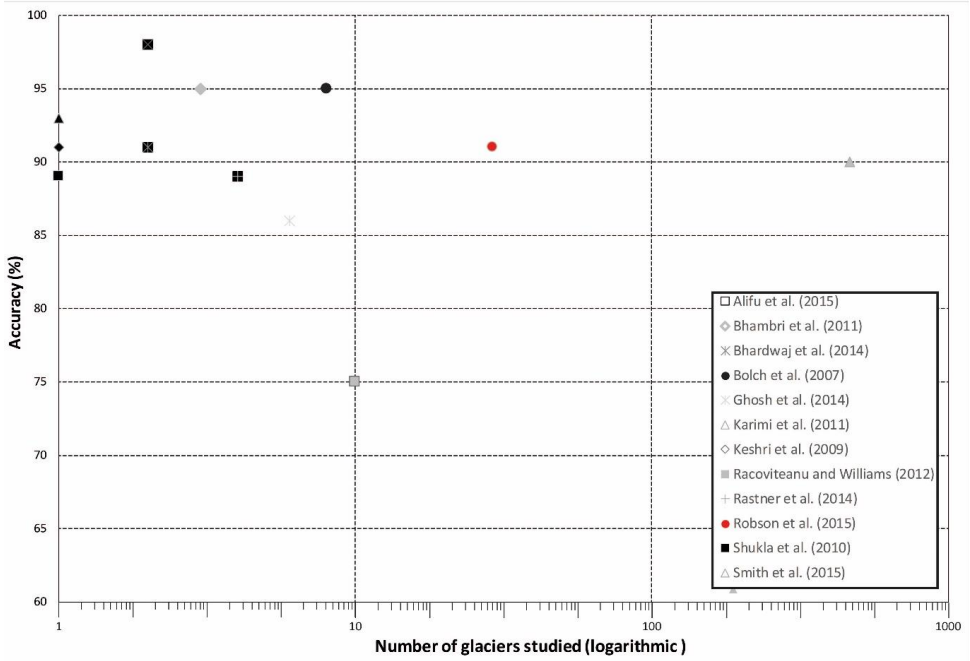

Figure 7: A comparison of other methods used to semi-automatically classify debris-covered ice. Note that the x-axis is logarithmic. The results from paper I are highlighted in red

The OBIA_OTS outlines compare well with the work of others Figure 7 shows how the accuracy of other methods compare to our OBIA classification. It can be seen that there are two methods that managed to classify a larger number of debris-covered glaciers with a high accuracy, Smith et al. (2015) and our OBIA method. Both methods utilised flow information. Our method used SAR coherence data to detect where ice had flowed or changed, while Smith et al. (2015) used Landsat derived velocity fields. This highlights that velocity or flow data is a transferable and reliable method for identifying debris-covered ice.

5.2 Paper II: Decadal Scale Changes in Glacier Area in the Hohe Tauern National Park (Austria) Determined by Object-Based Image Analysis

The upcoming *TanDEM World DEM* will provide 12 m resolution elevation data near-globally. In order to assess how this can be used in debris-covered glacier classifications the glaciers in the HTNP, Austria, were classified relying on Landsat data and a 10 m DEM derived from airborne LiDAR data. An edge detection filter was applied on the DEM to segment the image into objects based on where a sudden change in surface slope occurred, assuming that this would correspond to the marginal and terminal moraines of the glacier. The objects were then classified as clean ice and debris-covered ice using *fuzzy logic* where objects are classified without exact Boolean thresholds (Benz et al., 2004). For example, if a given object met 4 out of 5 criteria to be classified for debris-covered ice, but had a value that was below the value of the fifth criterion, it could still be classified as debris-covered ice. Clean ice was classified using the band ratio between the NIR and SWIR1 bands and the NDSI with constraints on the altitude and slope. Pro-glacial lakes were excluded using the NDWI. Clean ice objects were then split further into two sub-classes (snow and bare ice) using a *spectral difference segmentation* on an intensity image of a RGB of the SWIR1, NIR and Red bands. The boundary between these snow and bare ice was interpreted as the Transient Snowline (TSL) which can be used as a proxy for the ELA (Chinn et al., 2005).

Unlike for the Himalayas, it was found that the debris-covered ice in the Austrian Alps exhibited a thermal signature. Thermal band data was therefore used in conjunction with the NDVI, slope and red spectral band to classify debris-covered ice. Contextual properties were used to include nearby, spectrally similar objects, and then objects classified as glacier ice that were smaller than 0.1 km^2 or with very irregular shapes (compactness of objects ≥2.5) were assumed to be snow patches and subsequently removed. We applied this analysis on three Landsat satellite images, from 1985, 2003 and 2013 and compared the results with the Austrian Glacier Inventories from 1969 and 1998.

In total, the glacier area reduced by 33% between 1969 and 2013 at a mean rate of 1.4 $km^2\ a^{-1}$ (Figures 6 and 7; Paper II). The rate of glacier loss has varied over the 44-year period, with the period between 1998 and 2003 having the highest ice losses per year, at 8.9 $km^2\ a^{-1}$. The proportion of glaciers smaller than 1 km^2 increased from 69% in 1969 to 80% in 2013 (Figure 6, Paper II). The five glaciers that have supraglacial debris underwent less change in glacier area than the regional average, indicating the insulating effect of debris-cover on the underlying ice. The change in debris-covered glacier area is mixed, with the debris-cover of some glaciers increasing, while others lost debris cover. Between 1985 and 2013 the TSL rose by 92 m to an altitude of 3005 m (Figures 13 and 15; Paper II).

The results correspond well with the work of others working the European Alps (Paul et al., 2011, Carturan et al., 2013). Pronounced glacier losses across the European Alps are evident although the glacier response across the mountain chain is heterogeneous.

The accuracy of the study was assessed by comparing the OBIA_2003 results with reference data from the Global Land Ice Measurements from Space (GLIMS) project (Paul et al., 2011) and by comparing the OBIA_2013 outlines to a set of manually corrected outlines (Man_2013). The percentage accuracies gave values for the OBIA_2003 and OBIA_2013 classifications of 93.9% and 97.5% respectively, which is in line, or exceeding the levels of accuracy obtained by others who classified clean glacier ice (Albert, 2002, Paul et al., 2002, Paul et al., 2013) . We obtained a user's

accuracy of 94.1% which shows that there were few false positives (objects misclassified as glacier ice), but the producer's accuracy (81.6%) shows that there were some false negatives (glacier ice that was not mapped). The false negatives are most likely caused by seasonal snow, shadows and misclassified debris-covered ice and show the importance of time of image acquisition and satellite azimuth. When we determined the percentage accuracy over the debris-covered ice, an accuracy of 86.6% was calculated. Although the sample size was considerably smaller than the debris-covered ice studied in the Himalayas in paper I this shows that using high-resolution elevation data can produce results comparable to outlines generated from SAR coherence data.

It has been demonstrated that our automated OBIA analysis is suitable for determining glacier change over decadal scales and that the methods are transferable between different satellite images. This shows great potential for future glacier inventories being semi-automated.

5.3 Paper III: Decadal Scale Glacier Surface Lowering and Stagnation in the Manaslu Region of Nepal

Paper III attempts to understand how glacier area, volume and velocity relate to each other by using remote sensing data while also quantifying glacier changes in a previously undocumented region of the Himalayas over decadal scales.

A 1.8 m declassified *Corona* imagery from 1970 was compared to an ASTER DEM from 2005, the SRTM1 from 2000 and the 2013 SETSM (Surface Extraction with TIN-based Search-space Minimization) DEM. Co-registrations were applied to the DEMs as outlined in *4.4.1*. Glacier surface velocities were determined by feature tracking Landsat images from 2013/2014, 1999/2000 and 1993/1994 for 11 glaciers. Glacier areas were measured for 2013, 2005, 2001 and for select glaciers for 1970.

Between 2000 and 2013 we found a mean surface lowering of -0.21 ± 0.08 m a^{-1}, with the debris-covered ablation zones lowering at a mean rate of -0.35 ± 0.03. Over the entire study area, the geodetic mass balance was only slightly negative (-0.05 ± 0.16),

although the region contains a high degree of heterogeneity (Figure 4; Paper III), with geodetic mass balances ranging from -2.49 ± 2.24 to +0.27 ± 0.30 m w.e a^{-1}.

Our analysis shows evidence of increased mass losses. The geodetic mass balance between 1970 and 2013 for the three glaciers covered by the Corona DEM was -0.24 ± 0.12 m w.e a^{-1} which became -0.51 ± 0.12 between 2005 and 2013. Similarly, rates of surface lowering over debris-covered ice increased by 168% between 1970 – 2000 (-0.40 ± 0.18 m a^{-1}) and 2005 – 2013 (-1.07 ± 0.48 m a^{-1}). In many cases the lowermost few kilometres of glacier tongue downwasted less. We interpret changes in the rates of melting beneath debris due to the build-up supraglacial debris and the presence of surface ponds and exposed ice (Figures 10 and 11; Paper 3).

The glaciers that were covered by the Corona image shrank by -0.33% a^{-1} between 1970 and 2013. Between 2001 and 2013 all the glaciers in the study area reduced in area by 8.2% (-0.68% a^{-1}). Twelve percent of the glaciers areas did not change by more than 1% between 2000 and 2013. The clean ice glaciers in Tibet and the clean-ice components of debris-covered glaciers lost a greater proportion of area than the debris-covered glaciers (-0.58% a^{-1} and -0.80% a^{-1} respectively as opposed to -0.09% a^{-1}) and 52% of debris-covered glaciers had an increase in the debris-cover between 2001 and 2013. In many cases the losses that occurred for the debris-covered glaciers happened at the glacier margins while the glacier termini remained relatively stationary. The exception to this is Thulagi Glacier, a former lake-terminating glacier, that retreated ~1.4 km between 1970 and 2013 and now terminates on land.

When the glacier velocity is examined, it can be seen how there is also a large spatial variability across the Manaslu region (Figure 8; Paper 3). Over the whole region there was little change between 1993/1994 (34.9 ± 5.6 m a^{-1}) and 1999/2000 (31.3 ± 3.2 m a^{-1}), however between 1999/2000 and 2013/2014 there was a 1.2% a^{-1} reduction in measured velocity. The termini of many glaciers have become progressively less active (Figure 9; Paper 3). This corresponds to the same areas where the rates of surface lowering drop, suggesting an ongoing trend of glacier stagnation.

When just the glaciers that had velocities measured (excluding the two near-stagnant glaciers: G084516E28729N and G084695E28384N) are examined, it can be seen that both the velocity and the glacier area have been reducing at approximately the same rate (-0.9% a^{-1} and -0.8% a^{-1} respectively) between 2000 and 2013. The same glaciers lowered by a mean of 0.59 ± 0.08 m a^{-1}. There is no relationship between a change in area and the mean surface change (R^2 = 0.002) or glacier area change and velocity change (R^2 = 0.22). A weak relationship (R^2 = 0.47) exists between glacier velocity change and mean surface lowering. Both the glacier area and mean surface lowering show increased rates of glacier losses between 2005-2000 compared with 2013-2005 and 2013-2000.

When we compare our results to the work of others it can be seen that our mean geodetic mass balance is in line with results from Langtang valley and the Everest Region (Bolch et al., 2011, Pellicciotti et al., 2015) while our regional downwasting of -0.21 ± 0.08 m a^{-1} between 2000 and 2013 agrees with the mean average for the entire Himalaya of -0.21 ± 0.05 m a^{-1} found by Kääb et al. (2012). The velocity results are comparable to findings from the Everest Region (Quincey et al., 2009), however our decadal area changes far exceed those found in the Everest Region by Bolch et al. (2008b) It appears that the glaciers covered by the Corona data in this study are not wholly reprehensive of the entire study area, and seem to be losing mass and shrinking at a faster rate than the regional average. Paper III demonstrates how different glacier parameters can lead to different interpretations, over half of the debris-covered glaciers underwent an increase in debris-covered area and 12% did not change in total area by >1%. Despite this, mass losses and velocity changes are negative, highlighting the complicated nature of how debris-covered ice responds to climate.

6. Conclusions and Future Perspectives

This thesis has demonstrated that OBIA can be used effectively to quantify debris-covered ice and determine its change over time. OBIA can exploit multiple data sources in one classification. Given that debris-covered ice is spectrally similar to the surrounding terrain, auxiliary data must be used in order to delineate its extent. Paper I has shown how SAR coherence data can be used to classify debris-covered ice based on whether objects have flowed or changed over an approximate one-month time-interval. The method was applied to a sizable area (2350 km^2) in the Himalayas and classified a selection of debris-covered and clean ice glaciers to an accuracy of 91%. However, SAR data is complex to process and is sensitive to the quality of the DEM used in phase unwrapping, which can be a problem in areas such as the Himalayas that typically lack high-quality elevation products. Additionally, mountainous terrain causes problems with shadow, layover, and foreshortening. Paper II classified debris-covered glaciers using a LiDAR derived DEM to outline debris-covered ice using the surface morphology. The classification was applied to three Landsat images from 1985, 2003, and 2013, which were compared to two Austrian Glacier Inventories from 1969 and 1998 to derive decadal glacier area changes.

Both methods achieved high accuracies and show promise for future application, yet one important difference distinguishes the classification that included SAR coherence data and that that did relied only on optical and topographic data. Methods that utilise SAR coherence data or motion data (such as Landsat velocity fields as in Smith et al. (2015)) measures ice that has flowed or changes (such as melting beneath the debris-cover) and classifies it as debris-covered ice. Although stagnant ice continues to downwaste, the annual rates of this (< 1 m a^{-1}) are much less than the surface velocities (> 10 m a^{-1}) causing stagnant ice to not be classified. Using morphological parameters such as the slope and curvature on the other hand will classify ice that is not necessarily flowing or downwasting, meaning that the active ice and the stagnant ice are classified.

For the Austrian Alps this is not a significant difference, given that only five of the one hundred and forty-five glaciers in the HTNP that were classified had debris-cover,

however for areas such as the Himalayas or parts of the Andes then the distinction between active and stagnant ice can have large implications. Sub-debris melt in stagnant ice still contributes to water resources. In the case of lake-terminating glaciers such as Thulagi glacier, melt of stagnating ice can also lead to expanding moraine-dammed lakes, increasing GLOF risk. A combination of both methods could be utilised to classify both the active and stagnant ice. ESA's recent Sentinel program makes it is possible to access up-to-date and high-resolution SAR (Sentinel-1) and optical (Sentinel-2) data. Additionally, ESA provide a set of tools and tutorials to allow users to generate SAR coherence data (and other interferometric results) without the need of expensive specialist software. This increases the potential for combining both high-resolution topographic data *and* SAR coherence data in one analysis to map the extent of both active ice and stagnant glacier ice. The use of multi-temporal SAR coherence data could be used to determine the ongoing stagnation of glacier termini.

OBIA has many advantages over traditional pixel based approaches when it comes to glacier mapping. As well as efficiently combining data sources within one classification, OBIA allows the computation of many image-processing algorithms such as edge detection, *otsu* automatic thresholding and texture analysis. This means workflows can be automated and transferred between different data-sources and different study areas. The contextual and spatial characteristics of OBIA allow a degree of post-processing to be included semi-automatically in the workflow, for example removing small or irregularly shaped objects. OBIA also removes the 'salt and pepper effect' that is present in pixel-based classifications. Manual corrections will still be needed, but the amount of editing necessary is significantly reduced. OBIA has been shown to achieve higher accuracies working with both clean ice and debris-covered ice and the classification procedure is very adjustable on a step-by-step process (Rastner et al., 2014).

OBIA does however have some disadvantages associated with it. It is more computationally expensive than pixel-based methods. In particular, image segmentation can take a considerable time to complete, and must often be repeated many times until a suitable segmentation is found since the overall results are highly

dependent on the initial segmentation. Most OBIA software requires training and is also expensive (such as eCognition, ERDAS Imagine Objective, and ENVI Feature Tracking) although open-source alternatives are now available such as Interimage (www.lvc.ele.puc-rio.br/projects/interimage/) or Orfeo Toolbox (www.orfeo-toolbox.org).

This thesis also investigated decadal area, volume, and velocity changes in the previously undocumented Manaslu Region of the Nepali Himalayas. Climate and topography vary across the Himalayas causing a heterogeneous trend in glacier change. Paper III shows that glacier change within the Manaslu region is inharmonious. Glacier area changes between 2001 and 2013 varied from -40.0% to +10.5%, glacier velocities changes from -84.2% to +29.7 and glacier surface lowerings from -1.39 m a^{-1} to +0.29 m a^{-1}. The regional averages compare well with work carried out in the Everest Region as well as the Langtang valley although our results show a less negative mass balance. The regional mean surface lowering between 2000 and 2013 (-0.21 ± 0.08 m a^{-1}) conform well with the mean lowering between 2003 and 2008 of −0.21 ± 0.05 m a^{-1} found by (Kääb et al., 2012). This suggests that the glaciers in the Manaslu Region are not downwasting as much as other areas in the Central Himalayas, yet conform to the regional trend of ongoing surface lowering and mass loss.

Given the large archives of remote sensing data available, future work should focus on automating glacier velocity and volume measurements. Dehecq et al. (2015) created an automated pipeline calculating velocities over the entire Pamir-Karakoram-Himalaya. Similarly, Altena et al. (2015) used a knowledge based routine where glacier displacements were filtered based on if a continuous velocity was measurable between three images. Glacier volume change measurements can also be automated. Maurer and Rupper (2015) developed an automated pipeline for DEM extraction and image orthorectification of declassified Hexagon imagery called *HEXIMAP* which could lead to an increase in the usage of declassified imagery. When combined with near-global DEM products such as the SRTM, ASTER GDEM and ALOS 3D World then large-scale glacier volume change analysis becomes possible.

It can be concluded that the glacier area, velocity, and volume all respond in different ways to climate. There was a weak relationship between trends in glacier velocity changes and glacier volume changes and the rates of reduction in glacier area and glacier velocity corresponded well. More work is however needed to assess the relationships between different parameters for debris-covered glaciers, both over a larger number of glaciers, and over a higher temporal resolution. Future change analysis of debris-covered glaciers should complement area change assessment by also including velocity or volume data.

7. References

ABERMANN, J., LAMBRECHT, A., FISCHER, A. & KUHN, M. 2009. Quantifying changes and trends in glacier area and volume in the Austrian Ötztal Alps (1969–1997–2006). *The Cryosphere Discussions,* 3**,** 415-441.

AHN, Y. & HOWAT, I. M. 2011. Efficient automated glacier surface velocity measurement from repeat images using multi-image/multichip and null exclusion feature tracking. *IEEE Transactions on Geoscience and Remote Sensing,* 49**,** 2838-2846.

AIZEN, V. B., KUZMICHENOK, V. A., SURAZAKOV, A. B. & AIZEN, E. M. 2007. Glacier changes in the Tien Shan as determined from topographic and remotely sensed data. *Global and Planetary Change,* 56**,** 328-340.

ALBERT, T. H. 2002. Evaluation of remote sensing techniques for ice-area classification applied to the tropical Quelccaya Ice Cap, Peru. *Polar Geography,* 26**,** 210-226.

ALIFU, H., TATEISHI, R. & JOHNSON, B. 2015. A new band ratio technique for mapping debris-covered glaciers using Landsat imagery and a digital elevation model. *International Journal of Remote Sensing,* 36**,** 2063-2075.

ALTENA, B., KÄÄB, A. & NUTH, C. Robust glacier displacements using knowledge-based image matching. Analysis of Multitemporal Remote Sensing Images (Multi-Temp), 2015 8th International Workshop on the, 2015. IEEE, 1-4.

ALTMAIER, A. & KANY, C. 2002. Digital surface model generation from CORONA satellite images. *ISPRS Journal of Photogrammetry and Remote Sensing,* 56**,** 221-235.

ANDREASSEN, L., PAUL, F., KÄÄB, A. & HAUSBERG, J. 2008. Landsat-derived glacier inventory for Jotunheimen, Norway, and deduced glacier changes since the 1930s. *The Cryosphere,* 2**,** 131-145.

ANDREASSEN, L., WINSVOLD, S., PAUL, F. & HAUSBERG, J. 2012. Inventory of Norwegian glaciers. Oslo: Norges Vassdrags- og energidirektorat.

ATWOOD, D. K., MEYER, F. & ARENDT, A. 2010. Using L-band SAR coherence to delineate glacier extent. *Canadian Journal of Remote Sensing,* 36**,** S186-S195.

AUER, I., BOHM, R., JURKOVIC, A., LIPA, W., ORLIK, A., POTZMANN, R., SCHONER, W., UNGERSBOCK, M., MATULLA, C. & BRIFFA, K. 2007. HISTALP-historical instrumental climatological surface time series of the Greater Alpine Region. *International Journal of Climatology,* 27**,** 17-46.

BADER, H. 1954. Sorge's Law of densification of snow on high polar glaciers. *J. Glaciol,* 2**,** 319-323.

BAHUGUNA, I., KULKARNI, A., NAYAK, S., RATHORE, B., NEGI, H. & MATHUR, P. 2007. Himalayan glacier retreat using IRS 1C PAN stereo data. *International Journal of Remote Sensing,* 28**,** 437-442.

BAHUGUNA, I., RATHORE, B., BRAHMBHATT, R., SHARMA, M., DHAR, S., RANDHAWA, S., KUMAR, K., ROMSHOO, S., SHAH, R. & GANJOO, R. 2014. Are the Himalayan glaciers retreating? *Current Science,* 106**,** 1008-1013.

BAJRACHARYA, S. R., MAHARJAN, S. B. & SHRESTHA, F. 2014a. The status and decadal change of glaciers in Bhutan from the 1980s to 2010 based on satellite data. *Annals of Glaciology,* 55**,** 159-166.

BAJRACHARYA, S. R., MAHARJAN, S. B., SHRESTHA, F., BAJRACHARYA, O. R. & BAIDYA, S. 2014b. *Glacier Status in Nepal and Decadal Change from 1980 to 2010 Based on Landsat Data*.

BAJRACHARYA, S. R. & SHRESTHA, B. 2011. *The status of glaciers in the Hindu Kush-Himalayan region*, International Centre for Integrated Mountain Development (ICIMOD).

BAUDER, A., FUNK, M. & HUSS, M. 2007. Ice-volume changes of selected glaciers in the Swiss Alps since the end of the 19th century. *Annals of Glaciology,* 46**,** 145-149.

BENN, D. I., BOLCH, T., HANDS, K., GULLEY, J., LUCKMAN, A., NICHOLSON, L. I., QUINCEY, D., THOMPSON, S., TOUMI, R. & WISEMAN, S. 2012. Response of debris-covered glaciers in the Mount Everest region to recent warming, and implications for outburst flood hazards. *Earth-Science Reviews,* 114**,** 156-174.

BENN, D. I. & EVANS, D. J. A. 2010. *Glaciers & glaciation,* London, Hodder Education.

BENN, D. I. & OWEN, L. A. 1998. The role of the Indian summer monsoon and the mid-latitude westerlies in Himalayan glaciation: review and speculative discussion. *Journal of the Geological Society,* 155**,** 353-363.

BENZ, U. C., HOFMANN, P., WILLHAUCK, G., LINGENFELDER, I. & HEYNEN, M. 2004. Multi-resolution, object-oriented fuzzy analysis of remote sensing data for GIS-ready information. *ISPRS Journal of Photogrammetry and Remote Sensing,* 58**,** 239-258.

BERTHIER, E., ARNAUD, Y., KUMAR, R., AHMAD, S., WAGNON, P. & CHEVALLIER, P. 2007. Remote sensing estimates of glacier mass balances in the Himachal Pradesh (Western Himalaya, India). *Remote Sensing of Environment,* 108**,** 327-338.

BERTHIER, E., CABOT, V., VINCENT, C. & SIX, D. 2016. Decadal region-wide and glacier-wide mass balances derived from multi-temporal ASTER satellite digital elevation models. Validation over the Mont-Blanc area. *Frontiers in Earth Science,* 4**,** 63.

BERTHIER, E., VADON, H., BARATOUX, D., ARNAUD, Y., VINCENT, C., FEIGL, K. L., RÉMY, F. & LEGRÉSY, B. 2005. Surface motion of mountain glaciers derived from satellite optical imagery. *Remote Sensing of Environment,* 95**,** 14-28.

BHAMBRI, R., BOLCH, T. & CHAUJAR, R. K. 2011a. Mapping of debris-covered glaciers in the Garhwal Himalayas using ASTER DEMs and thermal data. *International Journal of Remote Sensing,* 32**,** 8095-8119.

BHAMBRI, R., BOLCH, T., CHAUJAR, R. K. & KULSHRESHTHA, S. C. 2011b. Glacier changes in the Garhwal Himalaya, India, from 1968 to 2006 based on remote sensing. *Journal of Glaciology,* 57**,** 543-556.

BHARDWAJ, A., JOSHI, P. K., SNEHMANI, SINGH, M. K., SAM, L. & GUPTA, R. D. 2014. Mapping debris-covered glaciers and identifying factors affecting the accuracy. *Cold Regions Science and Technology,* 106–107**,** 161-174.

BHATTACHARYA, A., BOLCH, T., MUKHERJESS, K., PIECZONKA, T., KROPACEK, J. & BUCHROITHNER, M. 2016. Overall recession and mass budget of Gangotri Glacier, Garhwal Himalayas, from 1965-2015 using remote sensing data. *Journal of Glaciology*.

BLASCHKE, T. 2010. Object based image analysis for remote sensing. *ISPRS Journal of Photogrammetry and Remote Sensing,* 65**,** 2-16.

BLASCHKE, T., HAY, G. J., KELLY, M., LANG, S., HOFMANN, P., ADDINK, E., FEITOSA, R. Q., VAN DER MEER, F., VAN DER WERFF, H. & VAN COILLIE, F. 2014. Geographic object-based image analysis–towards a new paradigm. *ISPRS Journal of Photogrammetry and Remote Sensing,* 87**,** 180-191.

BOLCH, T., BUCHROITHNER, M., PETERS, J., BAESSLER, M. & BAJRACHARYA, S. 2008a. Identification of glacier motion and potentially dangerous glacial lakes in the

Mt. Everest region/Nepal using spaceborne imagery. *Natural Hazards and Earth System Science,* 8**,** 1329-1340.

BOLCH, T., BUCHROITHNER, M., PIECZONKA, T. & KUNERT, A. 2008b. Planimetric and volumetric glacier changes in the Khumbu Himal, Nepal, since 1962 using Corona, Landsat TM and ASTER data. *Journal of Glaciology,* 54**,** 592-600.

BOLCH, T., BUCHROITHNER, M. F., KUNERT, A. & KAMP, U. Automated delineation of debris-covered glaciers based on ASTER data. Geoinformation in Europe. proceedings of the 27th EARSeL Symposium, 2007. 4-6.

BOLCH, T., KULKARNI, A., KAAB, A., HUGGEL, C., PAUL, F., COGLEY, J. G., FREY, H., KARGEL, J. S., FUJITA, K., SCHEEL, M., BAJRACHARYA, S. & STOFFEL, M. 2012. The State and Fate of Himalayan Glaciers. *Science,* 336**,** 310-314.

BOLCH, T., MENOUNOS, B. & WHEATE, R. 2010. Landsat-based inventory of glaciers in western Canada, 1985-2005. *Remote Sensing of Environment,* 114**,** 127-137.

BOLCH, T., PIECZONKA, T. & BENN, D. 2011. Multi-decadal mass loss of glaciers in the Everest area (Nepal Himalaya) derived from stereo imagery. *The Cryosphere,* 5**,** 349-358.

CARRIVICK, J. L. & TWEED, F. S. 2016. A global assessment of the societal impacts of glacier outburst floods. *Global and Planetary Change,* 144**,** 1-16.

CARTURAN, L., FILIPPI, R., SEPPI, R., GABRIELLI, P., NOTARNICOLA, C., BERTOLDI, L., PAUL, F., RASTNER, P., CAZORZI, F., DINALE, R. & DALLA FONTANA, G. 2013. Area and volume loss of the glaciers in the Ortles-Cevedale group (Eastern Italian Alps): controls and imbalance of the remaining glaciers. *Cryosphere,* 7**,** 1339-1359.

CHAND, P., SHARMA, M. C. & PRASAD, R. N. 2016. Heterogeneity in Fluctuations of Glacier with Clean Ice-Covered, Debris-Covered and Proglacial Lake in the Upper Ravi Basin, Himachal Himalaya (India), During the Past Four Decades (1971–2013). *In:* SINGH, R. B., SCHICKHOFF, U. & MAL, S. (eds.) *Climate Change, Glacier Response, and Vegetation Dynamics in the Himalaya: Contributions Toward Future Earth Initiatives.* Cham: Springer International Publishing.

CHINN, T. J., HEYDENRYCH, C. & SALINGER, M. J. 2005. Use of the ELA as a practical method of monitoring glacier response to climate in New Zealand's Southern Alps. *Journal of Glaciology,* 51**,** 85-95.

COGLEY, J. G., HOCK, R., RASMUSSES, L. A., ARENDT, A., BAUDER, A., BRAITHWAITE, R. J., JANSSON, P., KASER, G., MÖLLER, M., NICHOLSON, L. I. & ZEMP, M. 2011. Glossary of Glacier Mass Balance and Related Terms. *IHP-VII Technical Documents in Hydrology No. 86.* Paris: UNESCO-IHP.

COGLEY, J. G., KARGEL, J. S., KASER, G. & VAN DER VEEN, C. 2010. Tracking the source of glacier misinformation. *Science,* 327**,** 522.

DEBELLA-GILO, M. & KÄÄB, A. 2012. Locally adaptive template sizes for matching repeat images of Earth surface mass movements. *ISPRS journal of photogrammetry and remote sensing,* 69**,** 10-28.

DEHECQ, A., GOURMELEN, N. & TROUVE, E. 2015. Deriving large-scale glacier velocities from a complete satellite archive: Application to the Pamir–Karakoram–Himalaya. *Remote Sensing of Environment,* 162**,** 55-66.

DEPARTMENT OF HYDROLOGY AND METEOROLOGY (GOVERNMENT OF NEPAL). 2014. *Interpolated 12 km temperature and rainfall mean annual data (1970–2010)* [Online]. Kathmandu, Nepal. Available: http://dhm.gov.np/dpc.

DRAGUT, L., CSILLIK, O., EISANK, C. & TIEDE, D. 2014. Automated parameterisation for multi-scale image segmentation on multiple layers. *Isprs Journal of Photogrammetry and Remote Sensing,* 88**,** 119-127.

ERIKSSON, M., XU, J., SHRESTHA, A. B., VAIDYA, R. A., SANTOSH, N. & SANDSTRÖM, K. 2009. The changing Himalayas: impact of climate change on water resources and livelihoods in the greater Himalayas. Kathmandu: International Centre for Integrated Mountain Development (ICIMOD).

FAHNESTOCK, M., SCAMBOS, T., MOON, T., GARDNER, A., HARAN, T. & KLINGER, M. 2015. Rapid large-area mapping of ice flow using Landsat 8. *Remote Sensing of Environment*.

FOWLER, M. J. F. 2013. Declassified Intelligence Satellite Photographs. *In:* HANSON, S. W. & OLTEAN, A. I. (eds.) *Archaeology from Historical Aerial and Satellite Archives.* New York, NY: Springer New York.

FREY, H., PAUL, F. & STROZZI, T. 2012. Compilation of a glacier inventory for the western Himalayas from satellite data: methods, challenges, and results. *Remote Sensing of Environment,* 124**,** 832-843.

GARDELLE, J., BERTHIER, E., ARNAUD, Y. & KAAB, A. 2013. Region-wide glacier mass balances over the Pamir-Karakoram-Himalaya during 1999-2011. *Cryosphere,* 7**,** 1263-1286.

GHOSH, S., PANDEY, A. C. & NATHAWAT, M. S. 2014. Mapping of debris-covered glaciers in parts of the Greater Himalaya Range, Ladakh, western Himalaya, using remote sensing and GIS. *Journal of Applied Remote Sensing,* 8.

GOBIET, A., KOTLARSKI, S., BENISTON, M., HEINRICH, G., RAJCZAK, J. & STOFFEL, M. 2014. 21st century climate change in the European Alps—a review. *Science of the Total Environment,* 493**,** 1138-1151.

HEID, T. & KÄÄB, A. 2012a. Evaluation of existing image matching methods for deriving glacier surface displacements globally from optical satellite imagery. *Remote Sensing of Environment,* 118**,** 339-355.

HEID, T. & KÄÄB, A. 2012b. Repeat optical satellite images reveal widespread and long term decrease in land-terminating glacier speeds. *The Cryosphere,* 6**,** 467-478.

HUSS, M. 2013. Density assumptions for converting geodetic glacier volume change to mass change. *The Cryosphere,* 7**,** 877-887.

IMMERZEEL, W. W., KRAAIJENBRINK, P. D. A., SHEA, J. M., SHRESTHA, A. B., PELLICCIOTTI, F., BIERKENS, M. F. P. & DE JONG, S. M. 2014. High-resolution monitoring of Himalayan glacier dynamics using unmanned aerial vehicles. *Remote Sensing of Environment,* 150**,** 93-103.

IMMERZEEL, W. W., VAN BEEK, L. P. H. & BIERKENS, M. F. P. 2010. Climate Change Will Affect the Asian Water Towers. *Science,* 328**,** 1382-1385.

KELLERER-PIRKLBAUER, A. 2008. The Supraglacial Debris System at the Pasterze Glacier, Austria: Spatial Distribution, Characteristics and Transport of Debris. *Zeitschrift für Geomorphologie, Supplementary Issues,* 52**,** 3-25.

KÄÄB, A. 2005. Combination of SRTM3 and repeat ASTER data for deriving alpine glacier flow velocities in the Bhutan Himalaya. *Remote Sensing of Environment,* 94**,** 463-474.

KÄÄB, A., BERTHIER, E., NUTH, C., GARDELLE, J. & ARNAUD, Y. 2012. Contrasting patterns of early twenty-first-century glacier mass change in the Himalayas. *Nature,* 488**,** 495-498.

KÄÄB, A., TREICHLER, D., NUTH, C. & BERTHIER, E. 2015. Brief Communication: Contending estimates of 2003–2008 glacier mass balance over the Pamir–Karakoram–Himalaya. *The Cryosphere,* 9**,** 557-564.

KÄÄB, A. & VOLLMER, M. 2000. Surface geometry, thickness changes and flow fields on creeping mountain permafrost: Automatic extraction by digital image analysis. *Permafrost and Periglacial Processes,* 11**,** 315-326.

KÄÄB, A., WINSVOLD, H. S., ALTENA, B., NUTH, C., NAGLER, T. & WUITE, J. 2016. Glacier Remote Sensing Using Sentinel-2. Part I: Radiometric and Geometric Performance, and Application to Ice Velocity. *Remote Sensing,* 8.

LANG, S. 2008. Object-based image analysis for remote sensing applications: modeling reality – dealing with complexity. *In:* BLASCHKE, T., LANG, S. & HAY, G. J. (eds.) *Object-Based Image Analysis: Spatial Concepts for Knowledge-Driven Remote Sensing Applications.* Berlin, Heidelberg: Springer Berlin Heidelberg.

LEE, D. S., STOREY, J. C., CHOATE, M. J. & HAYES, R. W. 2004. Four years of Landsat-7 on-orbit geometric calibration and performance. *IEEE Transactions on Geoscience and Remote Sensing,* 42**,** 2786-2795.

LI, Z., SUN, W. & ZENG, Q. 1998. Measurements of Glacier Variation in the Tibetan Plateau Using Landsat Data. *Remote Sensing of Environment,* 63**,** 258-264.

MAURER, J. & RUPPER, S. 2015. Tapping into the Hexagon spy imagery database: A new automated pipeline for geomorphic change detection. *ISPRS Journal of Photogrammetry and Remote Sensing,* 108**,** 113-127.

MEHTA, M., DOBHAL, D. & BISHT, M. 2011. Change of Tipra glacier in the Garhwal Himalaya, India, between 1962 and 2008. *Progress in Physical Geography,* 35**,** 721-738.

MOOL, P. K. 2011. *Glacial lakes and glacial lake outburst floods in Nepal*, International Centre for Integrated Mountain Development.

NAGAI, H., FUJITA, K., NUIMURA, T. & SAKAI, A. 2013. Southwest-facing slopes control the formation of debris-covered glaciers in the Bhutan Himalaya. *Cryosphere,* 7**,** 1303-1314.

NARAMA, C., KAAB, A., DUISHONAKUNOV, M. & ABDRAKHMATOV, K. 2010. Spatial variability of recent glacier area changes in the Tien Shan Mountains, Central Asia, using Corona (similar to 1970), Landsat (similar to 2000), and ALOS (similar to 2007) satellite data. *Global and Planetary Change,* 71**,** 42-54.

NUIMURA, T., SAKAI, A., TANIGUCHI, K., NAGAI, H., LAMSAL, D., TSUTAKI, S., KOZAWA, A., HOSHINA, Y., TAKENAKA, S., OMIYA, S., TSUNEMATSU, K., TSHERING, P. & FUJITA, K. 2015. The GAMDAM glacier inventory: a quality-controlled inventory of Asian glaciers. *The Cryosphere,* 9**,** 849-864.

NUTH, C., KOHLER, J., KÖNIG, M., VON DESCHWANDEN, A., HAGEN, J. O., KÄÄB, A., MOHOLDT, G. & PETTERSSON, R. 2013. Decadal changes from a multi-temporal glacier inventory of Svalbard. *The Cryosphere,* 7**,** 1603-1621.

NUTH, C. & KÄÄB, A. 2011. Co-registration and bias corrections of satellite elevation data sets for quantifying glacier thickness change. *The Cryosphere,* 5**,** 271.

OWEN, L. A. & BENN, D. I. 2005. Equilibrium-line altitudes of the Last Glacial Maximum for the Himalaya and Tibet: an assessment and evaluation of results. *Quaternary International,* 138–139**,** 55-78.

PANDEY, P., MANICKAM, S., BHATTACHARYA, A., RAMANATHAN, A. L., SINGH, G. & VENKATARAMAN, G. 2016. Qualitative and quantitative assessment of TanDEM-X DEM over western Himalayan glaciated terrain. *Geocarto International***,** 1-13.

PANT, S. R. & REYNOLDS, J. M. 2000. Application of electrical imaging techniques for the investigation of natural dams: an example from the Thulagi Glacier Lake, Nepal. *Journal of the Nepal Geological Society,* 22**,** 211-218.

PAUL, F., ARNAUD, Y., RANZI, R. & ROTT, H. 2014. European Alps. *In:* KARGEL, J. S., LEONARD, G. J., BISHOP, M. P., KÄÄB, A. & RAUP, B. H. (eds.) *Global Land Ice Measurements from Space.* Springer Berlin Heidelberg.

PAUL, F., BARRAND, N. E., BAUMANN, S., BERTHIER, E., BOLCH, T., CASEY, K., FREY, H., JOSHI, S. P., KONOVALOV, V., BRIS, R. L., MÖLG, N., NOSENKO, G., NUTH, C., POPE, A., RACOVITEANU, A., RASTNER, P., RAUP, B., SCHARRER, K., STEFFEN, S. & WINSVOLD, S. 2013. On the accuracy of glacier outlines derived from remote-sensing data. *Annals of Glaciology,* 54**,** 171-182.

PAUL, F., BOLCH, T., KAAB, A., NAGLER, T., NUTH, C., SCHARRER, K., SHEPHERD, A., STROZZI, T., TICCONI, F., BHAMBRI, R., BERTHIER, E., BEVAN, S., GOURMELEN, N., HEID, T., JEONG, S., KUNZ, M., LAUKNES, T. R., LUCKMAN, A., BONCORI, J. P. M., MOHOLDT, G., MUIR, A., NEELMEIJER, J., RANKL, M., VANLOOY, J. & VAN NIEL, T. 2015. The glaciers climate change initiative: Methods for creating glacier area, elevation change and velocity products. *Remote Sensing of Environment,* 162**,** 408-426.

PAUL, F., FREY, H. & LE BRIS, R. 2011. A new glacier inventory for the European Alps from Landsat TM scenes of 2003: challenges and results. *Annals of Glaciology,* 52**,** 144-152.

PAUL, F., HUGGEL, C. & KAAB, A. 2004. Combining satellite multispectral image data and a digital elevation model for mapping debris-covered glaciers. *Remote Sensing of Environment,* 89**,** 510-518.

PAUL, F., KAAB, A., MAISCH, M., KELLENBERGER, T. & HAEBERLI, W. 2002. The new remote-sensing-derived swiss glacier inventory: I. Methods. *Annals of Glaciology, Vol 34, 2002,* 34**,** 355-361.

PAUL, F. & MÖLG, N. 2014. Hasty retreat of glaciers in northern Patagonia from 1985 to 2011. *Journal of Glaciology,* 60**,** 1033-1043.

PELLICCIOTTI, F., STEPHAN, C., MILES, E., HERREID, S., IMMERZEEL, W. W. & BOLCH, T. 2015. Mass-balance changes of the debris-covered glaciers in the Langtang Himal, Nepal, from 1974 to 1999. *Journal of Glaciology,* 61**,** 373-386.

PIECZONKA, T. & BOLCH, T. 2015. Region-wide glacier mass budgets and area changes for the Central Tien Shan between ~ 1975 and 1999 using Hexagon KH-9 imagery. *Global and Planetary Change,* 128**,** 1-13.

PIECZONKA, T., BOLCH, T., JUNFENG, W. & SHIYIN, L. 2013. Heterogeneous mass loss of glaciers in the Aksu-Tarim Catchment (Central Tien Shan) revealed by 1976 KH-9 Hexagon and 2009 SPOT-5 stereo imagery. *Remote Sensing of Environment,* 130**,** 233-244.

POPE, A., REES, W., FOX, A. & FLEMING, A. 2014. Open Access Data in Polar and Cryospheric Remote Sensing. *Remote Sensing,* 6**,** 6183.

QUINCEY, D., LUCKMAN, A. & BENN, D. 2009. Quantification of Everest region glacier velocities between 1992 and 2002, using satellite radar interferometry and feature tracking. *Journal of Glaciology,* 55**,** 596-606.

QUINCEY, D. J., BRAUN, M., GLASSER, N. F., BISHOP, M. P., HEWITT, K. & LUCKMAN, A. 2011. Karakoram glacier surge dynamics. *Geophysical Research Letters,* 38.

RACOVITEANU, A. & WILLIAMS, M. W. 2012. Decision Tree and Texture Analysis for Mapping Debris-Covered Glaciers in the Kangchenjunga Area, Eastern Himalaya. *Remote Sensing,* 4**,** 3078-3109.

RANZI, R., GROSSI, G., IACOVELLI, L. & TASCHNER, S. Use of multispectral ASTER images for mapping debris-covered glaciers within the GLIMS Project. Geoscience

and Remote Sensing Symposium, 2004. IGARSS'04. Proceedings. 2004 IEEE International, 2004. IEEE, 1144-1147.

RASTNER, P., BOLCH, T., NOTARNICOLA, C. & PAUL, F. 2014. A Comparison of Pixel- and Object-Based Glacier Classification With Optical Satellite Images. *Ieee Journal of Selected Topics in Applied Earth Observations and Remote Sensing,* 7**,** 853-862.

REN, J., JING, Z., PU, J. & QIN, X. 2006. Glacier variations and climate change in the central Himalaya over the past few decades. *Annals of Glaciology,* 43**,** 218-222.

REZNICHENKO, N., DAVIES, T., SHULMEISTER, J. & MCSAVENEY, M. 2010. Effects of debris on ice-surface melting rates: an experimental study. *Journal of Glaciology,* 56**,** 384-394.

RICHARDSON, S. D. & REYNOLDS, J. M. 2000. An overview of glacial hazards in the Himalayas. *Quaternary International,* 65–66**,** 31-47.

RIGNOT, E., ECHELMEYER, K. & KRABILL, W. 2001. Penetration depth of interferometric synthetic-aperture radar signals in snow and ice. *Geophysical Research Letters,* 28**,** 3501-3504.

ROBB, C., WILLIS, I., ARNOLD, N. & GUÐMUNDSSON, S. 2015. A semi-automated method for mapping glacial geomorphology tested at Breiðamerkurjökull, Iceland. *Remote Sensing of Environment,* 163**,** 80-90.

SAKAI, A., NAKAWO, M. & FUJITA, K. 2002. Distribution Characteristics and Energy Balance of Ice Cliffs on Debris-Covered Glaciers, Nepal Himalaya. *Arctic, Antarctic, and Alpine Research,* 34**,** 12-19.

SAM, L., BHARDWAJ, A., SINGH, S. & KUMAR, R. 2015. Remote sensing flow velocity of debris-covered glaciers using Landsat 8 data. *Progress in Physical Geography***,** 0309133315593894.

SCHERLER, D., BOOKHAGEN, B. & STRECKER, M. R. 2011. Spatially variable response of Himalayan glaciers to climate change affected by debris cover. *Nature Geoscience,* 4**,** 156-159.

SCHIEFER, E., MENOUNOS, B. & WHEATE, R. 2007. Recent volume loss of British Columbian glaciers, Canada. *Geophysical Research Letters,* 34.

SCHMIDT, S. & NÜSSER, M. 2012. Changes of High Altitude Glaciers from 1969 to 2010 in the Trans-Himalayan Kang Yatze Massif, Ladakh, Northwest India. *Arctic, Antarctic, and Alpine Research,* 44**,** 107-121.

SCHWANGHART, W., WORNI, R., HUGGEL, C., STOFFEL, M. & KORUP, O. 21st century Himalayan hydropower: Growing exposure to glacial lake outburst floods? EGU General Assembly Conference Abstracts, 2014. 15824.

SHANGGUAN, D., BOLCH, T., DING, Y., KRÖHNERT, M., PIECZONKA, T., WETZEL, H.-U. & LIU, S. 2015. Mass changes of Southern and Northern Inylchek Glacier, Central Tian Shan, Kyrgyzstan, during~ 1975 and 2007 derived from remote sensing data. *The Cryosphere,* 9**,** 703-717.

SHRESTHA, A. B. & ARYAL, R. 2011. Climate change in Nepal and its impact on Himalayan glaciers. *Regional Environmental Change,* 11**,** 65-77.

SHUKLA, A., ARORA, M. K. & GUPTA, R. P. 2010. Synergistic approach for mapping debris-covered glaciers using optical–thermal remote sensing data with inputs from geomorphometric parameters. *Remote Sensing of Environment,* 114**,** 1378-1387.

SHUKLA, A. & QADIR, J. 2016. Differential response of glaciers with varying debris cover extent: evidence from changing glacier parameters. *International Journal of Remote Sensing,* 37**,** 2453-2479.

SIDJAK, R. 1999. Glacier mapping of the Illecillewaet icefield, British Columbia, Canada, using Landsat TM and digital elevation data. *International Journal of Remote Sensing,* 20**,** 273-284.

SMITH, T., BOOKHAGEN, B. & CANNON, F. 2015. Improving semi-automated glacier mapping with a multi-method approach: applications in central Asia. *The Cryosphere,* 9**,** 1747-1759.

TAKEUCHI, Y., KAYASTHA, R. B. & NAKAWO, M. 2000. Characteristics of ablation and heat balance in debris-free and debris-covered areas on Khumbu Glacier, Nepal Himalayas, in the pre-monsoon season. *IAHS PUBLICATION***,** 53-62.

WANG, D. & KAAB, A. 2015. Modeling Glacier Elevation Change from DEM Time Series. *Remote Sensing,* 7**,** 10117-10142.

WULDER, M. A., MASEK, J. G., COHEN, W. B., LOVELAND, T. R. & WOODCOCK, C. E. 2012. Opening the archive: How free data has enabled the science and monitoring promise of Landsat. *Remote Sensing of Environment,* 122**,** 2-10.

ZHANG, Y., FUJITA, K., LIU, S., LIU, Q. & NUIMURA, T. 2011. Distribution of debris thickness and its effect on ice melt at Hailuogou glacier, southeastern Tibetan Plateau, using in situ surveys and ASTER imagery. *Journal of Glaciology,* 57**,** 1147-1157.

Paper I

Crossing the Larke Pass at sunrise. Photo: Pål Ringkjøb Nielsen

Remote Sensing of Environment 170 (2015) 372–387

Contents lists available at ScienceDirect

Remote Sensing of Environment

journal homepage: www.elsevier.com/locate/rse

Automated classification of debris-covered glaciers combining optical, SAR and topographic data in an object-based environment

Benjamin Aubrey Robson [a,*], Christopher Nuth [b], Svein Olaf Dahl [a], Daniel Hölbling [c], Tazio Strozzi [d], Pål Ringkjøb Nielsen [a]

[a] Department of Geography, University of Bergen, Fosswinckelsgate 6, 5007 Bergen, Norway
[b] Department of Geosciences, University of Oslo, Postboks 1047 Blindern, Oslo 0316, Norway
[c] Department of Geoinfomatics-Z_GIS, University of Salzburg, Schillerstrasse 30, 5020 Salzburg, Austria
[d] GAMMA Remote Sensing, Worbstr. 225, Gümligen 3073, Switzerland

ARTICLE INFO

Article history:
Received 19 January 2015
Received in revised form 8 September 2015
Accepted 5 October 2015
Available online 22 October 2015

Keywords:
Debris-covered glacier
Object-based image analysis
Landsat 8
SAR coherence
Semi-automatic classification
Himalayas

ABSTRACT

Satellite imagery is increasingly used to monitor glacier area changes and create glacier inventories. Robust and efficient pixel-based band ratios have proven to be accurate for automatically delineating clean glacier ice, however such classifications are restricted on debris-covered ice due to its spectral similarity with surrounding terrain. Object-Based Image Analysis (OBIA) has emerged as a new analysis technique within remote sensing. It offers many advantages over pixel-based classification techniques due to the ability to work with multiple data sources and handle data contextually and hierarchically. By making use of OBIA capabilities we automatically classify clean ice and debris-covered ice in the challenging area surrounding Mount Manaslu in Nepal using optical (Landsat 8), topographic (void-filled SRTM) and SAR coherence (ALOS PALSAR) data. Clean ice was classified with a mean accuracy of 93% whilst debris-covered ice was classified with an accuracy of 83% when compared to manually corrected outlines, providing a total glacier accuracy of 91%. With further developments in the classification, steep tributary sections of ice could be contextually included, raising the accuracy to over 94%. One prominent advantage of OBIA is that it allows some post-processing and correction of the glacier outlines automatically, reducing the amount of manual correction needed. OBIA incorporating SAR coherence data is recommended for future mapping of debris-covered ice.

1. Introduction

Current and accurate glacier outlines are required for many applications within glaciology, such as glacier area change analysis (Bajracharya, Maharjan, & Shrestha, 2014; Nuth et al., 2013; Shangguan et al., 2014), masks when determining glacier velocity (Berthier et al., 2005; Kääb, 2005; Quincey, Luckman, & Benn, 2009) and volume change estimations (Berthier, Schiefer, Clarke, Menounos, & Remy, 2010; Gardelle, Berthier, Arnaud, & Kääb, 2013), as well as input and validation data within glacier modelling (Pradhananga et al., 2014; Racoviteanu, Armstrong, & Williams, 2013; Rees & Collins, 2006).

The status of glaciers within the Himalayas is of great importance. Due to their remote location, many glacierised areas, such as the Himalayas, are under-sampled when it comes to direct in-situ glacier observation data (Berthier et al., 2007). Existing in-situ data is often biased towards small to medium sized and debris-free glaciers (Gardelle et al., 2013). Mass balance measurements are relatively sparse with few records extending more than 10 years, (Bolch et al., 2012; Pratap, Dobhal, Bhambri, Mehta, & Tewari, 2015a).

Changes in glacierised area have implications on the amount of ice area exposed to melt, this influencing the discharge of many rivers originating in the Himalayas that are important for irrigation and hydro-electric power production (Bolch et al., 2012; Immerzeel, Van Beek, & Bierkens, 2010). Additionally, the continued down-wasting and retreat of debris-covered glaciers in the Himalayas can lead to the development of moraine-dammed lakes, which can breach catastrophically producing glacial lake outburst floods (GLOFs) that disrupt downstream populations and infrastructure (Richardson & Reynolds, 2000).

Remotely sensed data provide a means of increasing our understanding of these remote regions by permitting analysis at the regional scale (Paul, Bolch, et al., 2013; Nuimura et al., 2014). Satellite imagery has been widely used in the last decades for delineating glacier outlines over large areas, often using automated or semi-automated methodologies such as band ratios and supervised classifications, with reported accuracies of over 95% (Albert, 2002; Paul & Andreassen, 2009; Paul, Barrand, et al., 2013). Global glacier inventories such as the GLIMS

* Corresponding author.
E-mail addresses: benjamin.robson@uib.no (B.A. Robson), christopher.nuth@geo.uio.no (C. Nuth), Svein.Dahl@uib.no (S.O. Dahl), daniel.hoelbling@sbg.ac.at (D. Hölbling), strozzi@gamma-rs.ch (T. Strozzi), Pal.R.Nielsen@uib.no (P.R. Nielsen).

http://dx.doi.org/10.1016/j.rse.2015.10.001
0034-4257/

(Global Land Ice Measurements from Space) initiative and the Randolph Glacier Inventory aim to map land glaciers globally using optical satellite imagery and assess their changes over time (Ranzi, Grossi, Iacovelli, & Taschner, 2004; Pfeffer et al., 2014). The application of these techniques has allowed glaciers to be mapped and analysed over large areas of the Himalayas (Scherler, Bookhagen, & Strecker, 2011; Frey, Paul, & Strozzi, 2012; Bajracharya, Maharjan, Shrestha, Bajracharya and Baidya, 2014; Nuimura et al., 2014).

Many glaciers within the Himalayas are heavily covered in debris. Debris-cover on glacier-ice is an important component in glacier mass balance and is known to complicate the response of the ice to climate (Scherler et al., 2011; Zhang, Fujita, Liu, Liu, & Nuimura, 2011; Benn et al., 2012; Pratap, Dobhal, Mehta, & Bhambri, 2015b), yet the relationship is poorly understood. Debris cover can either insulate or amplify glacial melting, depending on variables such as the debris thickness, composition and the amount of precipitation (Takeuchi, Kayastha, & Nakawo, 2000; Reznichenko, Davies, Shulmeister, & Mcsaveney, 2010; Bhardwaj, Joshi, Snehmani, Sam, & Gupta, 2014b). For example Bolch, Buchroithner, Pieczonka, and Kunert (2008a) reported that the debris coverage on Khumbu Glacier increased as the total glacier area reduced. The spatial distribution of debris over the glacier and the presence of supraglacial lakes and exposed ice cliffs are therefore important factors affecting how the glacier responds to changes in climate. In some cases, debris cover may cause rates of ablation to increase by up to an order of magnitude (Benn et al., 2012; Immerzeel et al., 2014; Juen, Mayer, Lambrecht, Han, & Liu, 2014).

Although the delineation of clean ice is a robust and accurate procedure, the automated classification of debris-covered glacier ice is not so straightforward, due to the spectral similarity of glacier debris cover to the surrounding terrain of rock or glacial moraines (Paul, Bolch, et al., 2013; Huang, Li, Tian, Zhou, & Chen, 2014). Several methods have been implemented to aid delineation of debris-covered ice. Morphological parameters such as the slope and curvature, as well as thermal satellite data have been used in both automatic and semi-automatic classification methods (Paul, Huggel, & Kaab, 2004; Ranzi et al., 2004; Bolch, Buchroithner, Kunert, & Kamp, 2007a; Shukla, Arora, & Gupta, 2010; Bhambri, Bolch, & Chaujar, 2011; Racoviteanu & Williams, 2012; Tiwari, Arora, & Gupta, 2014). To date however, most of these automated studies have not focused on large-scale regions (>200 km^2) but a small number of glaciers (<5 glaciers) are analysed e.g. (Bolch et al., 2007a; Bhambri et al., 2011; Racoviteanu & Williams, 2012; Bhardwaj, Joshi, Snehmani, Sam, & Gupta, 2014a). A high resolution Digital Elevation Model (DEM) significantly aids the automated delineations of debris-covered ice through parameters such as curvature or slope (Tiwari et al., 2014), yet DEMs over many mountainous areas often have high uncertainty, with high-resolution DEMs often only available at great expense (Bolch et al., 2007a). The majority of studies that delineate debris-covered glaciers therefore have relied on some degree of manual interpretation (Bajracharya & Shrestha, 2011; Sharma, Singh, Kulkarni, & Ajai, 2013; Bhardwaj et al., 2014a; Nuimura et al., 2014; Shangguan et al., 2014; Kääb et al., 2015). Paul, Barrand, et al. (2013) had 20 participants manually map 24 glaciers and found differences in interpretation of up to 30% over heavily debris-covered glaciers. One reason for this is the high variability in the spatial coverage and composition of glacial debris cover, which makes spectral and topographic delineations difficult (Racoviteanu, Paul, Raup, Khalsa, & Armstrong, 2009).

Some recent studies have exploited the coherence pattern between two Synthetic Aperture Radar (SAR) images in order to differentiate debris-covered ice from surrounding terrain (Zongli, Shiyin, Xin, Jian, & Sichun, 2011; Frey et al., 2012; Saraswat et al., 2013; Snehmani, Gupta, Bhardwaj, & Joshi, 2014). Change over time or movement result in a loss of coherence over the glacier, which can then be used as a guide for the digitisation of debris-covered ice (Frey et al., 2012). Atwood, Meyer, and Arendt (2010) automatically mapped debris-covered ice in the Wrangell Mountains and the Juneau Ice Field in Alaska, relying solely on SAR coherence data. Complicated mountain topography however makes this unfeasible in regions such as the Himalayas where layover and foreshortening can cause no signal return to the sensor over sizable areas (Frey et al., 2012).

Object-Based Image Analysis (OBIA) is a promising methodology where near-homogenous objects are the basis of classifications instead of pixels. This allows more possibilities when defining classification rules, e.g. considering spatial characteristics or contextual information. OBIA also permits multi-data integration meaning that it is possible to fully exploit a combination of data sources, (e.g. optical satellite imagery, SAR data, DEM). OBIA can therefore be used to semi-automatically classify glaciers and distinguish between different surface types and characteristics.

1.1. Objectives

The main objective of this study is to test OBIA for accurately delineating debris-covered glaciers by combining SAR coherence data with optical and topographic data. The accuracy of the classification technique is assessed by comparing the automatic outlines against both manually delineated outlines and the most recent published glacier outlines available at the time of study. For most of the study area the International Centre for Integrated Mountain Development (ICIMOD) glacier inventory was used. This inventory was based on images acquired between 2007 and 2009 for glaciers in Nepal. The glacier outlines in Tibet are from the Chinese Glacier Inventory (CGI) based on aerial photography from the 1970s. Both glacier inventories were incorporated into the Randolf Glacier Inventory 3.2 and downloaded through the GLIMS database. (ICIMOD, 2010; Pfeffer et al., 2014). For simplicity we refer to both glacier inventories as the reference outlines for the duration of the paper.

1.2. Study area

We tested our classification in the Manaslu region of Nepal. The Manaslu Region contains an assortment and range of glaciers found and surfaces including (clean ice, heavily debris-covered, stagnant ice and lake terminating ice. The region covers 2350 km^2 in total. The glaciers in the study area range in elevation from 3000 m.a.s.l. to over 7000 m.a.s.l and cover a total area of 788 km^2. They are typically 0.5–1 km in width and 5–15 km in length with areas that vary from 5.6 km^2 to 32.0 km^2. The glaciers on the southern side of the topographic divide are heavily debris-covered, while those north of the divide are clean type glaciers, with minimal or no debris cover. Nineteen debris-covered glaciers are analysed in the vicinity of Mount Manaslu (8163 m), which lies between the districts of Gorkha and Manang in Central Nepal, (Fig. 1). Ten clean-ice glaciers on the northern slopes of Himlung, Ratna Chuli and Lugula Himal were also investigated. The Manaslu Region is situated at the boundary between the maritime, monsoon-driven climate found in Nepal, and the drier, more continental climate of the Tibetan plateau (Benn & Owen, 1998). Although climate data is limited, the Nepali Department of Hydrology and Meteorology estimate maximum and minimum temperatures of 26.7 °C and 12.8 °C with 1066 mm of precipitation a year at the weather station *Larke Samdo*, 84°38E, 28°39N, 3650 m.a.s.l. (Government of Nepal, D. O. H. a. M, 2014). Glaciers in Nepal receive up to 80% of their annual accumulation during the summer monsoon between June and September (Ageta & Higuchi, 1984; Benn & Owen, 1998). Rates of both accumulation and ablation are highest simultaneously during the summer monsoon; small changes in temperature can therefore strongly affect the balance between accumulation and ablation (Benn & Owen, 1998). Glaciers on the northern side of the mountain divide receive much less precipitation, and as such respond primarily to changes in ablation season temperature (Owen & Benn, 2005). A combination of warmer summer temperatures and reduced precipitation over the last few decades have caused increased rain and reduced snow, (Benn et al., 2012) leading to a marked retreat of many glaciers within the Himalayas (Bajracharya, Maharjan and Shrestha, 2014).

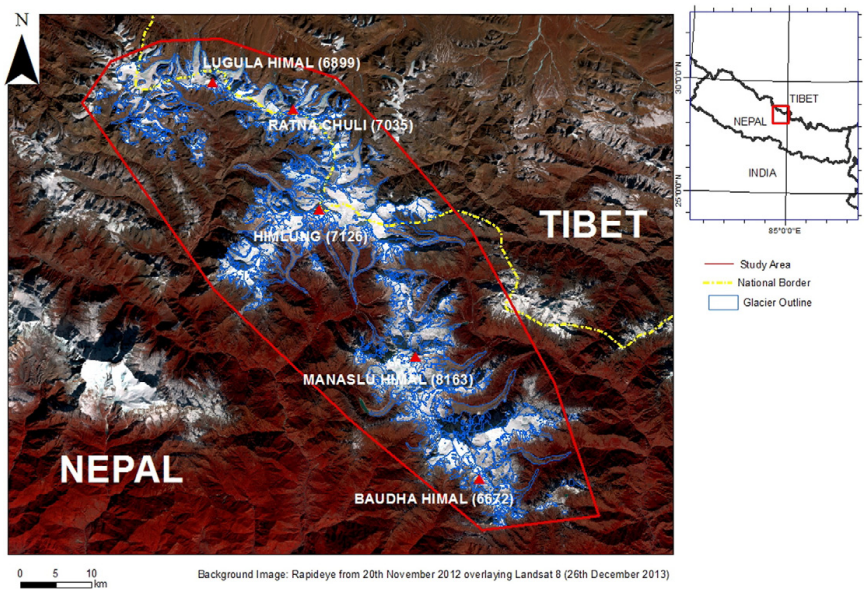

Fig. 1. Location of the glaciers studied (outlines derived from this study) within the Manaslu Region (28°N, 84°E), and the location of the Manaslu Region within Nepal.

The study area also contains Thulagi Lake (0.9 km^2), (also referred to as Dona Lake) situated in front of Thulagi Glacier (G084538E28524N); which has been identified as one of the most potentially hazardous glacial lakes in Nepal (Mool et al., 2011). An outburst flood could affect 160,000 people in the Marsyangdi river basin, damaging or destroying infrastructure relating to hydroelectric power generation as well as sections of the Annapurna and Manaslu hiking circuits (Mool et al., 2011).

2. Background

2.1. Object-based image analysis

Object-based image analysis (OBIA) is a spatially explicit information extraction workflow, combining image processing and GIS functionalities (Blaschke, 2010). Traditional pixel-based methods only consider the spectral characteristics of single pixels, often resulting in a salt-and-pepper effect within the classification, thus requiring post-processing or cleaning. This reduces the robustness of pixel-based methods to adequately depict complex natural phenomena such as glaciers. In addition, pixels may not always be clearly assignable to one land cover type since each pixel can contain reflectance values from multiple land classes. OBIA instead segments pixels into near-homogenous objects, on which the analysis is conducted.

OBIA provides a methodological framework for computer-based interpretation of complex classes that are defined by a range of spatial, spectral and contextual properties derived from multiple data sources (Lang, 2008). Today, OBIA or GEOBIA (geographic object-based image analysis) is a relatively new and evolving methodology in remote sensing and GIScience (Blaschke et al., 2014). Working on the object-level as opposed to the pixel-level facilitates the combined use of spectral, spatial, textural, hierarchical and contextual properties. Unlike single pixels, image objects are defined by a large number of properties in addition to just spectral values, such as shape, compactness and area that can be applied during classification. This is especially useful when working with high resolution (HR) imagery (spatial resolution <30 m) or very high resolution (VHR) imagery (spatial resolution <4 m), (Hoersch & Amans, 2012) where objects of interest are usually larger than the pixel size, or when performing combined analysis of data from various sources (e.g. optical, DEM, SAR, vector data) as the most appropriate properties of image objects derived from multiple datasets can be used for classification. This makes object-based approaches more intricate, especially when performing knowledge-based analysis. The process of how scene complexity is broken down into meaningful image primitives with object-based approaches is closely related to how humans perceive an image (Blaschke & Strobl, 2001). Extracting useful information from individual pixels can be significantly influenced by the signals of surrounding pixels (Townshend et al., 2000). This effect can be almost neglected when working with image objects because of the reduced relevance of radiometric information of single pixels. For the same reason, atmospheric and radiometric correction of images appears to be less important for object-based mapping tasks (Hölbling, Friedl, & Eisank, 2015). A number of studies have shown that OBIA outperforms pixel-based approaches within various applications such as land use mapping and landslide delineation (Gao, Mas, Maathuis, Zhang, & Van Dijk, 2006; Myint, Gober, Brazel, Grossman-Clarke, & Weng, 2011; Moosavi, Talebi, & Shirmohammadi, 2014).

2.2. Classifying glaciers with OBIA

Initial studies have been conducted delineating debris-covered ice within an object-based classification. Rastner, Bolch, Notarnicola, and Paul (2014), for example compared pixel-based and object-based classification techniques with high reliance on slope and surface temperature parameters over different clean and debris-covered conditions. They found object-based classifications delivered marginally more accurate results when classifying clean ice, but significantly more accurate results when working on debris-covered ice. The International Centre for Integrated Mountain Development (ICIMOD) used Landsat TM and SRTM elevation data within OBIA to classify glaciers over the entire Himalayas (ICIMOD, 2010; Bajracharya & Shrestha, 2011; Bajracharya, Maharjan and Shrestha, 2014; Bajracharya, Maharjan, Shrestha, Bajracharya et al., 2014), although the amount of manual correction required is not known.

2.3. Use of remote sensing data to classify glaciers

This study uses optical, topographic and SAR coherence data.

Due to the high spectral contrast between clean ice and the surrounding terrain, optical images provide a reliable means of automatically classifying clean ice. Band ratios have been found to be the most consistently accurate way of classifying clean ice (Albert, 2002), with a threshold applied to ratios of the Landsat TM bands TM4/TM5 or TM3/TM5 being the most accurate and robust (Paul, Bolch, et al., 2013). Much work has been done mapping debris-covered ice using optical data. Band ratios such as the Normalised Difference Vegetation Index (NDVI), Land and Snow Mask (LWM) and Normalised Difference Snow Index (NDSI) (explained Table 2.) have been used to debris-covered glaciers (Keshri, Shukla, & Gupta, 2009; Bajracharya, Maharjan, Shrestha, Bajracharya et al., 2014; Bajracharya et al., 2015). Brenning, Pena, Long, and Soliman (2012) on the other hand used the diurnal variation in thermal data to map glaciers. Most authors however have combined SWIR, NIR and thermal band data for mapping debris-covered ice (Shukla et al., 2010; Casey, Kaab, & Benn, 2012; Karimi et al., 2012; Bhardwaj et al., 2014a; Tiwari et al., 2014; Alifu, Tateishi, & Johnson, 2015). We investigated the potential of including thermal data in our study; however the thermal signature was not consistently visible over the study area. While some debris-covered glaciers exhibited a clear difference in temperature, for many of the debris-covered glaciers there was no thermal signature visible through the glacier debris. We therefore did not include thermal data in the classification.

As mentioned above, breaks in topographic data such as surface slope and curvature can be used to distinguish the debris-covered glacier tongue morphologically (Bolch et al., 2007a), while elevation can constrain the altitudinal extent of classifications to exclude false positives, such as declassifying any objects classified as glacier ice found at low elevations.

The exploitation of interferometric coherence information between two SAR images separated by a time interval provides a means of identifying features that have changed in a landscape, and as such is applicable to the study of features such as glaciers and landslides (Catani, Farina, Moretti, Nico, & Strozzi, 2005; Atwood et al., 2010; Strozzi, Ambrosi, & Raetzo, 2013; Joyce, Samsonov, Levick, Engelbrecht, & Belliss, 2014). De-coherence can relate to either motion occurring between when the images were taken, or to changing surface conditions. It is therefore important to distinguish glaciers from changing surface conditions, such as snowfall, rock slides and vegetation changes (Snehmani et al., 2014). The use of SAR coherence data is therefore appealing as it provides a way to distinguish moving debris-covered glacier areas that are optically similar to the surrounding non-glacier terrain. The integration of SAR data with optical images and topographic data in OBIA can provide valuable information for classification.

Optical or topographic data are incapable of differentiating between active glacier-ice and stagnant glacier ice, something that Bolch et al. (2007a) and Ghosh, Pandey, and Nathawat (2014) state as a weakness in current methods for classifying debris-covered ice. SAR coherence data allow the identification of active ice based on whether motion or a change in surface conditions has occurred. There is some discussion however whether stagnant glacier tongues should be included in glacier mapping. Many definitions of what constitutes a glacier specifically mention that glaciers must be actively flowing (Benn & Evans, 2010; Cuffey & Paterson, 2010). However if one is interested in GLOF hazards, then the identification and downwasting of stagnant ice is very important (Richardson & Reynolds, 2000; Bolch, Buchroithner, Peters, Baessler, & Bajracharya, 2008b). It is beyond the scope of this paper to speculate whether stagnant glacier-ice should be included or not in glacier mapping; however in this study we only consider debris-covered ice that is active and has flowed or undergone a change in surface conditions, and is therefore detectable on SAR coherence data.

3. Data and methods

3.1. Data

Optical imagery from Landsat 8 (Green, Red, NIR and SWIR-1 bands) acquired in October and December 2013 was used. One Landsat 8 scene from October was used for debris-covered glaciers, while a second scene from late December was used on the higher elevation, clean-ice and the glaciers in the north of the study area which were affected by seasonal snow in the October scene. In addition, a RapidEye image (5 m resolution) was used to manually correct the glacier outlines in order to later assess the accuracy of the classification.

The elevation data used in the classification is a version of the SRTM DEM that was void-filled with the 1:50,000 Finnmap topographic maps of Nepal (available pre-processed online (De Ferranti, 2012)). The ASTER GDEM was not used as it is considerably noisy; contains large striping artefacts (Tachikawa et al., 2011; Rexer & Hirt, 2014) and lacks a consistent timestamp that would have led to problems when classifying with topographic derivatives.

Two coherence images were generated from four ALOS PALSAR images acquired in 2007 with a time separation of 46 days. All the data used in this study is shown in Table 1.

3.2. Methods

Two OBIA classifications were performed within Trimble eCognition 9.0: one based solely on the optical and topographic data (OBIA_OT), while the second classification used in addition the SAR coherence images (OBIA_OTS).

The workflow consists of three steps:

1. Pre-processing: The SRTM was bi-linearly resampled to 30 m resolution to match the resolution of the Landsat 8 image and a slope raster generated. Custom indices and band ratios were created Table 2.) within ArcGIS. The ALOS PALSAR images were processed in order to create the SAR Coherence data. First, the interferometric processing combined the pairs of Single Look Complex (SLC) images at HH-polarization into interferograms using GAMMA Remote Sensing software. Because of rugged topography in some areas, a simulated phase image, which corresponds to the topographic phase was computed from the void-filled SRTM DEM and then subtracted from the interferometric phase. For coherence estimation an adaptive window size varying between 3×3 and 9×9 pixels for a 1 range $\times$ 4 azimuth looks interferogram was used (Frey et al., 2012). The resulting terrain-corrected and geocoded coherence images were combined with a mask considering regions with layover and radar shadow as well as the SRTM voids. The two coherence images were mosaicked into one file for input into OBIA. All data was projected to UTM zone 45N.
2. Image segmentation: The initial image segmentation into near-homogeneous objects is one of the most critical stages within OBIA (Drăguţ, Csillik, Eisank, & Tiede, 2014). Image segmentation is a bottom-up process that begins by grouping pixels into objects. Additional object hierarchical levels can be created where individual objects are merged. Different datasets (individual spectral bands, topographic derivatives, etc.) can be used to segment the image, and different weighting factors based on their importance in the segmentation can be assigned. As pointed out by Rastner et al. (2014), the performance of OBIA is strongly influenced by the initial choice of parameters during image segmentation. A trade-off had to be reached when choosing a scale parameter for creating either too large and too small objects The former can cause multiple classes to be grouped into single objects, resulting in misclassifications, while the latter reduces the functionality of using shape and contextual constraints in the classification. In both classifications, image objects were created using the multi-resolution segmentation algorithm in eCognition based on three hierarchical levels on the blue, green, NIR, panchromatic, red and

Table 1
Data used in this study.

Date	Sensor	Scene ID	Spatial resolution (m)
08.10.2013	Landsat 8	LC81420402013281LGN00	30 (15 pan-sharp)
26.12.2013	Landsat 8	LC81420402013361LGN00	30 (15 pan-sharp)
20.11.2012	RapidEYE	11240644	5
11.02.2000	SRTM	SRTM3N28E084V2	90
19.08.2007	ALOS PALSAR	Coherence image from pair: ALOS_511560560_20070704_20070819.cc	16 m × 13 m, geocoded to 1 arc-sec (~30 m)
05.09.2007	ALOS PALSAR	Coherence image from pair: ALOS_512560560_20070721_20070905.cc	16 m × 13 m, geocoded to 1 arc-sec (~30 m)

shortwave infrared bands, as well as the slope. It was found that having multiple image object levels helped group non-glacier features together, making it easier to exclude them from the classification. For the classification that incorporated SAR data, the SAR coherence data was also included and the weights of the optical and topographic data were reduced. The scale parameter, which dictates the size of objects, was chosen with assistance from the Estimation of Scale Parameter 2 (ESP 2) tool (Drăguţ et al., 2014). The weighting factors in segmentation are important so that one data source does not dominate the creation of objects. We applied higher weightings to the slope (×4), to SWIR1, SWIR2 (×3) as well as the SAR coherence data, green, NIR, panchromatic and red channels (×2). The scale parameter, shape and compactness criterions used are displayed in Fig. 2.

3. Rule based classifications: Fig. 2 shows the workflow for the classification procedure, including all parameters and thresholds that were used, as well as the post-classification filtering. Various parameters and parameter combinations (band ratios and indices, topographic derivatives, spatial properties, etc.) were tested to determine the most appropriate thresholds and parameters for classification. Some thresholds were acquired from the literature (for example the SWIR/NIR ratio, NDVI and slope) (Paul, Bolch, et al., 2013, Bajracharya, Maharjan, Shrestha, 2014) while others were determined through trial and error. Fuzzy logic classifications were used to identify lakes, clean ice and debris-covered ice. Fuzzy logic relies on assigning membership functions to different criteria ranging from 0 (non-member) to 1 (member) thereby allowing an upper or lower threshold to accommodate a range of values (Benz, Hofmann, Willhauck, Lingenfelder, & Heynen, 2004). In addition, each classification rule could have a weighting factor assigned, i.e. a higher weighting factor increases the significance of that particular rule set in the classification.

The following classification procedure was applied:

3a. Mapping of water bodies and clean ice

Lakes and clean ice were delineated first as they were easiest to classify and therefore could be masked out for the rest of the analysis. Water bodies were classified using the NDWI, slope and elevation. Clean ice was classified using the Landsat NIR/SWIR1 ratio, slope and elevation.

3b. Mapping of debris-covered ice

A third segmentation level was applied to all unclassified objects. This was found to help group non-glacier objects. The following two classifications were then performed.

Table 2
Custom indices used in the glacier classifications.

Index Acronym	Custom Index Name	Band formula
NDVI	Normalised Difference Vegetation Index	(NIR − Red) / (NIR + Red)
NDSI	Normalised Difference Snow Index	(Green − (SWIR) / (Green + SWIR)
NDWI	Normalised Difference Water Index	(Green − NIR) / (Green + NIR)
LWM	Land and Water Mask	(SWIR / Green + 0.001) × 100
SWIR/NIR	Commonly referred to as TM4/TM5	SWIR/NIR

i. Classification using only optical and elevation data (OBIA_OT)

Debris-covered ice was classified with equal weights applied to the NDVI, NDSI and slope. The NDVI was sensitive to vegetation growth at the glacier terminus, the NDSI as such was used to include patches of dirty ice protruding through the debris. The NDSI was found to be more effective for this than the NIR/SWIR ratio, which was less able to delineate dirty ice. Similar to Bajracharya, Maharjan, Shrestha (2014), the elevation was used to limit the altitudinal range where glaciers could be classified, reducing false positives. The LWM was also included in the classification.

ii. Classification using SAR coherence data (OBIA_OTS)

The second OBIA classification procedure included SAR coherence data and applied lower weights assigned to the NDVI (40%) and NDSI (30%).

4. Classification refinement: The image objects classified as glacier ice (both clean ice and debris-covered ice) were merged together, and then objects were filtered by area and by the distance from the clean ice. The image objects were then expanded into neighbouring objects with similar spectral, topographic or SAR coherence characteristics (as shown in Fig. 2). Some problems were caused by very elongated but narrow objects that resulted in overestimations of the glacier width, thus a criterion was set (Fig. 2) to exclude objects that were adjacent to the debris-covered ice and had a high length/width ratio. Lastly, object boundaries were smoothed by using the pixel-based growing and shrinking commands within eCognition. The classifications were then exported to shapefile (.shp) format.
5. Manual correction of glacier outlines: The shapefiles were divided into drainage areas using the SRTM DEM. Due to the coarse resolution of the DEM, some manual correction was necessary for the drainage divides. The OBIA_OTS outlines were manually corrected with reference to high resolution Google Earth imagery, a RapidEye image from 2012, photographs from the field, and the SAR coherence images. Both the classifications outlines were then compared to each other, to the manually delineated outlines, and to the reference glacier inventory.
6. Comparison of glacier outlines and accuracy assessment: Originally it was planned to compare the OBIA outlines only against the reference glacier inventory for data verification, however such comparisons were not straightforward due to the range in years that were used when the reference inventory was produced. To assess the spatial overlap between the reference and the classification, our OBIA outlines were therefore compared against both the reference outlines as well as OBIA outlines that we manually corrected (OBIA_Man). For comparison purposes the reference outlines were manually split into clean ice and debris-ice by overlaying them on the Landsat images. Unlike the reference glacier outlines; our manual outlines used the SAR coherence data in addition to Google Earth and RapidEye imagery in order to determine the extent of the glacier ice beneath the debris cover. We mapped only active glacier ice that had undergone motion or a change in surface conditions and was therefore visible as a loss of SAR coherence, or when signs of glacier motion such as a rough texture were visible on the higher resolution images (Bhambri et al., 2011). We therefore consider our manually corrected outlines to be "truth" in this study. The OBIA outlines, both from optical and topographic data (OBIA_OT), as well as those from optical, topographic

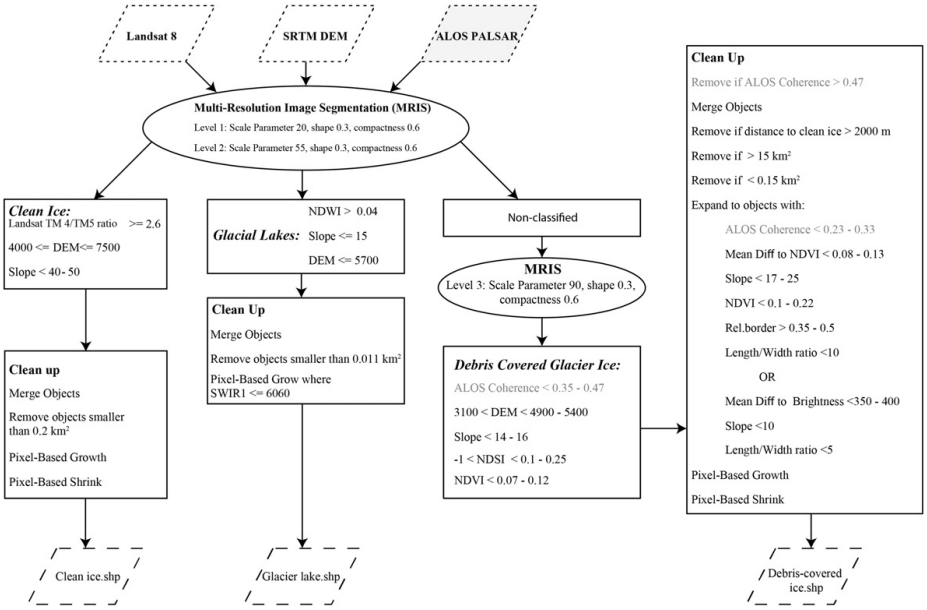

Fig. 2. Flowchart showing the procedure followed to classify clean ice, glacial lakes and debris-covered ice. Rule sets that are in grey were used in the classification that used ALOS PALSAR coherence data in addition to Landsat 8 optical and SRTM elevation data, while the other classification relied solely on the optical and elevation data. An explanation of the processing steps is given in Section 3.2.

and SAR coherence data (OBIA_OTS) were compared with the manually corrected outlines (OBIA_Man) and the reference glacier inventory (REF) and percentages of deviation were used to assess the accuracy. OBIA_Man and REF were also compared.

4. Results

A total of 19 debris-covered and 10 clean-ice glaciers were classified, comprising in total 788 km^2 of ice, 15% (113 km^2) of which is debris-covered. Fig. 3 and Table A.1 show the reference glacier inventory areas (REF), the OBIA outlines using optical and terrain data (OBIA_OT), the OBIA outlines using optical, terrain and SAR coherence data (OBIA_OTS) and the manually corrected outlines (OBIA_Man). It is apparent from Fig. 3 that the OBIA_OT method has the greatest variance of the 3 methods for mapping debris-covered ice. It also appears that the OBIA_OT mapping becomes less reliable for the larger debris-covered glaciers. Fig. 4 compares both the clean ice and debris-covered ice areas derived from the OBIA method, the manual delineations and the reference glacier inventory.

In terms of total glacier area (clean ice and debris-covered ice), our method achieved an accuracy of 91% over the 788 km^2 of glacier ice. Of the 27 glaciers classified, 14 of which were mapped with accuracy of 95% of more. While most comparable studies (for example Bolch, Buchroithner, Kunert, and Kamp (2007b); Bhambri et al. (2011); Rastner et al. (2014); Alifu et al. (2015)) assess accuracy over the entire glacier due to the difficulty of classifying debris-covered ice as opposed to clean ice, we present separate results and discussion for both clean ice and debris-covered ice to quantify the difference between classification techniques used in this study.

4.1. Delineation of clean ice

Due to the high spectral contrast between ice and rock, the SAR coherence was not necessary when classifying clean ice. Comparison of the outlines from this study revealed that the clean ice areas were mapped with an accuracy of 85% against the reference data, and an accuracy of 93% against the manually corrected outlines. This is approximately in line with the accuracies found by other studies (Paul, Bolch, et al., 2013). Visual inspection of the automatic outlines revealed an accuracy of within ±30 m to individual outlines in most cases. Errors arose due to shadow covering portions of the glacier and in some cases narrow strips of rock surrounded by ice were classified as glacier.

Large disparities were found when comparing with the automated clean ice outlines to the reference outlines north of the mountain divide (Fig. 5). This can be explained as they were created using aerial imagery from the 1970s. On average the agreement with the reference outlines

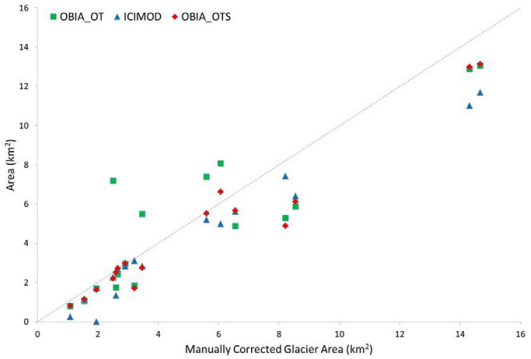

Fig. 3. Scatter plot comparing the manually corrected glacier outlines (OBIA_Man) against the OBIA outlines using optical and topographic data (OBIA_OT), the OBIA outlines using optical, topographic and SAR coherence data (OBIA_OTS) as well as the ICIMOD glacier outlines (ICIMOD) for the debris covered portions of the glaciers in the Manaslu Region. The total glacier area (clean and debris-covered ice) is shown, the clean ice was measured using the OBIA_OT method only.

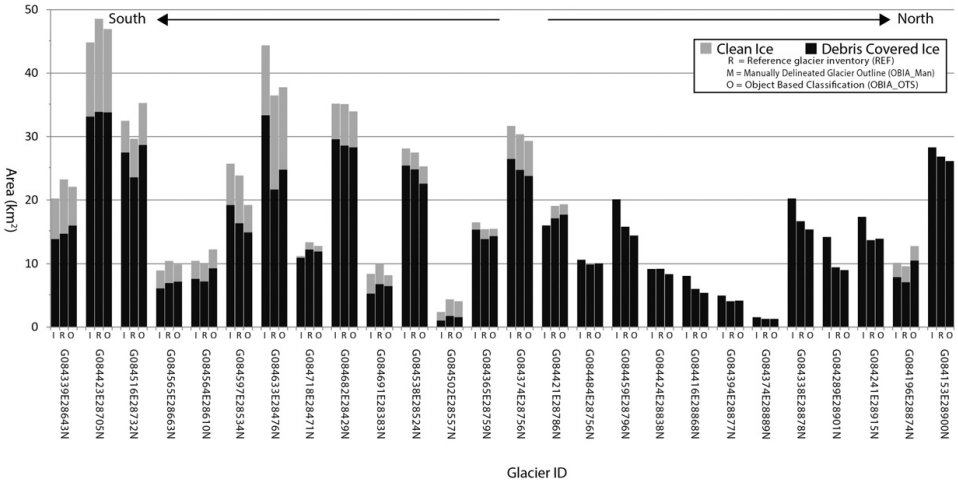

Fig. 4. A comparison between the measured clean ice areas and debris-covered areas of the glaciers of the Manaslu Region, Nepal. Three areas for each glacier are shown; the reference glacier outlines (REF), OBIA_Man outlines, and the OBIA outlines. The debris covered outlines shown are OBIA_OTS areas while the clean ice areas are OBIA_OT outlines. Clean ice is easier to map automatically and as such OBIA_Man and OBIA_OTS agree well with each other for the debris-free glaciers in the north, it is also noticeable how the ICIMOD data is out of date and show consistently larger glacier areas. The debris-covered portions of glaciers are harder to map and as such there was more variation between the areas measured by the ICIMOD, OBIA_Man and OBIA_OTS.

was 74% for these glaciers. Differences of glacier extent by between 500 and 1000 m at the glacier terminus are common.

4.2. Delineation of debris-covered ice

Debris-covered ice remains one of the most troublesome aspects of remote sensing glaciology (Kääb et al., 2015). For debris-covered glaciers, OBIA_OTS classification mapped to an accuracy of 83% against the manually delineated outlines. The OBIA_OT classification is considerably less accurate, and in particular is sensitive to lithological changes in glacier debris, occasionally mapping individual glaciers as multiple entities (Fig. 6). The mean accuracy falls to 72% when compared to the manual delineations. This is a sizable error term, and shall be explored in the following section.

Both OBIA_OT and OBIA_OTS fail to detect debris-covered ice in some situations. Neither method fully classifies the steep tributaries of clean ice that flow down gullies towards the glacier. The steepness of these sections, often 25–50°, is greater than the threshold of 14–16° used for debris-covered ice, this excluding them from the classification. When the slope threshold was increased to accommodate these steep sections, the classification included non-glacial debris adjacent to the glacier terminus. If these steep tributaries of ice are not considered and the accuracy assessment is carried out solely over the glacier margins and termini, then the accuracy of mapping debris-covered ice rises to 91% (Table A.2), over the entire glacier this increases to 94%.

On occasion there are areas where the reference outlines fail to map debris-covered ice, for example the glacier termini are often not fully mapped (as visible in Fig. 6D and Fig. 7). highlighting problems caused

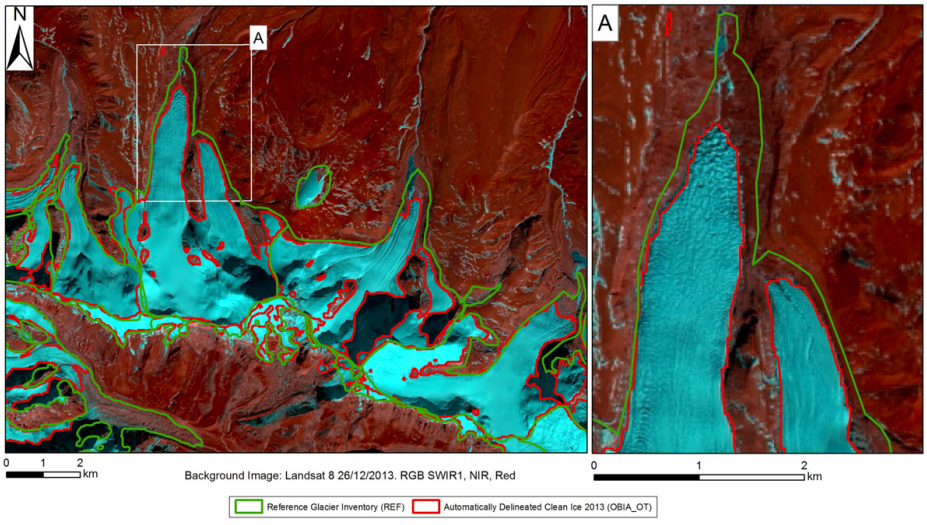

Fig. 5. Comparison between the OBIA mapping of clean glacier ice and the 2010 ICIMOD Glacier inventory.

by the spectral similarity of debris-covered ice to the surrounding terrain for mapping debris-covered ice without additional data. Moreover, some steep marginal moraines or paraglacial slopes are misclassified as debris-covered ice (Fig. 6) by both classification techniques, although glacier ice can extend into valley slopes by up to 100 m (Bernard et al. (2014)).

4.3. Comparison of SAR coherence based classification (OBIA_OTS) to spectral based classification (OBIA_OT)

The OBIA_OTS outperforms the OBIA_OT classification in most cases, especially on the glacier termini, where the glacier debris often becomes more lithologically similar to the surrounding bedrock (Kääb et al., 2015). When the OBIA_OT outperforms the OBIA_OTS classification it does so by a mean of only 3.2% compared to the 18.2% that OBIA_OTS outperforms the OBIA_OT. The SAR based classification occasionally delineated what appeared to be avalanche or debris flow deposits which flow out onto the glacier. Similarly, in a few situations (for example on glacier G084374E28756N) the OBIA_OT classification was able to differentiate between the debris-covered ice and paraglacial slopes better than the OBIA_OTS classification. This is most likely explained by the paraglacial slopes and glacier debris being more lithologically distinct in the optical imagery compared with in the SAR coherence data.

The OBIA_OTS classification however was able to classify the glacier on relative motion and not just based on the debris lithology. Even in situations where the lithology was sufficiently distinct between the debris and rock, the heterogeneity of image objects based on optical data still occasionally caused misclassifications towards the glacier margins.

There were some areas where the SAR coherence data had problems, for example a loss of coherence over water (Fig. 8A), steep north-facing valleys (Fig. 8B), or areas where no data was received back at the sensor (Fig. 8C). Problems can arise through orthorectification of the SAR data, or areas with non-uniform patterns of SAR coherence, typically found near the glacier terminus caused by vegetation or surface water.

5. Discussion

5.1. Use of SAR coherence data to classify debris-covered ice

SAR coherence data requires expertise knowledge and expensive software in order to be processed (Frey et al., 2012). Therefore, it was attempted to classify debris-covered ice based on optical and topographic data alone, especially since the data used for this (Landsat 8 and the SRTM DEM) are both freely available. When the SAR coherence data is excluded from the OBIA, the accuracy of the classification falls by 12%. The spectrally based classification was sufficient on several of the larger debris-covered glaciers, where prominent shifts in lithology or vegetation represented the shift from debris-covered ice to stagnant ice, moraine or rock. In some cases however, the termini of glaciers were overestimated, with avalanche and debris flow deposits (Fig. 9) as well as surface water leading to misclassifications of debris-covered ice. In many cases the delineations of debris-covered ice from the spectral classification varied by 30% or more when compared to the manually corrected outlines as a result of similar spectral signatures of the glacier debris and surrounding bedrock. The SAR coherence data also permits the distinction between active ice from stagnant ice when combined with optical and topographic data, something stated as a weakness in methods that only use optical and topographic data (Bolch et al., 2007a; Ghosh et al., 2014). Although SAR coherence data has not been used within OBIA to map debris-covered ice, it has been used without additional data to automatically map ice in Alaska (Atwood et al., 2010), in combination with optical data for manual delineations. For example Frey et al. (2012) used SAR coherence data as a guide for manual delineation over 9310 km^2 of ice in the Western Himalayas. Zongli et al.

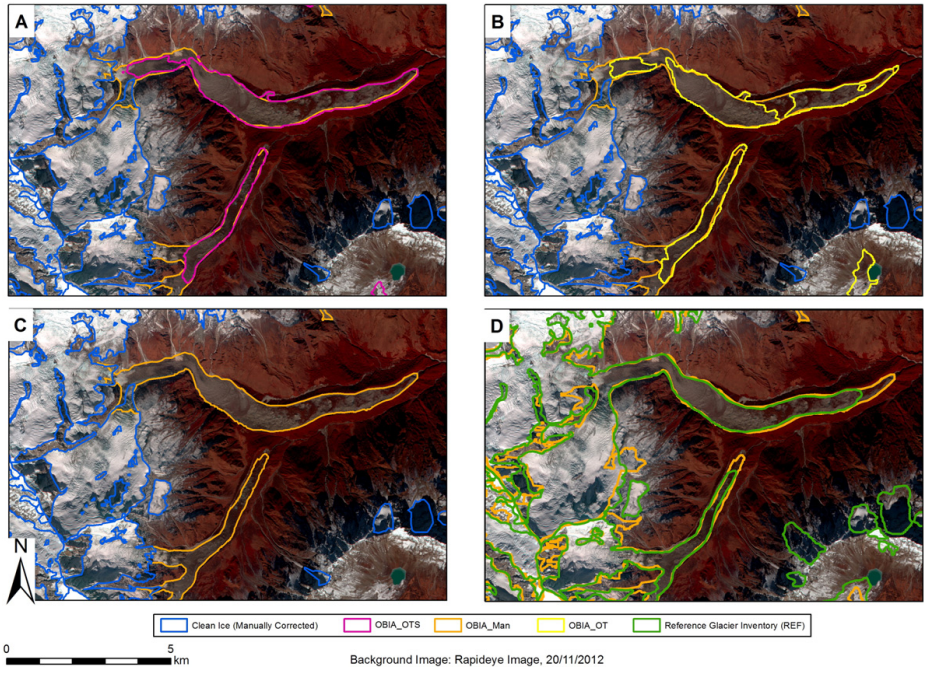

Fig. 6. Comparison of the mapping of debris-covered glacier ice. The manually corrected outlines are compared with the OBIA_OTS classification (A), the OBIA_OT classification (B), and the 2010 ICIMOD glacier inventory (C). In addition the OBIA_OTS classification is compared with the 2010 ICIMOD glacier inventory (D). Notice how due the OBIA_OT classification is sensitive to the debris lithology, and depicts the glacier as three sections.

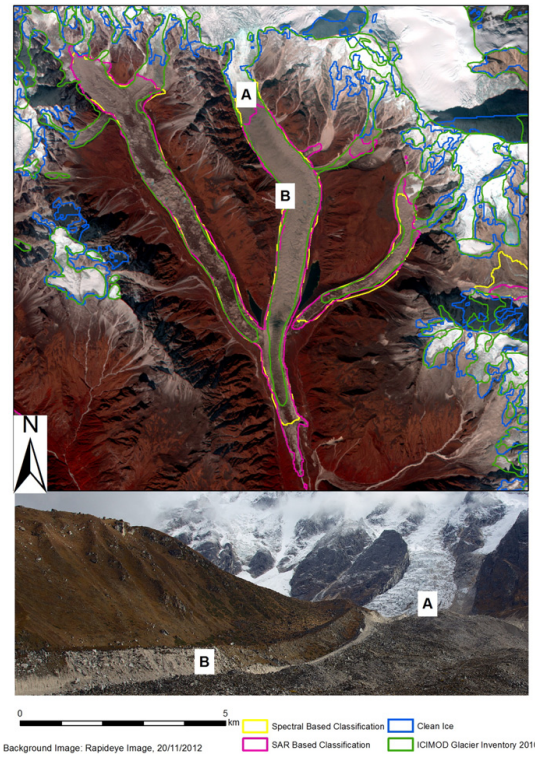

Fig. 7. The OBIA method struggles most with the steep tributaries (A) where clean ice met debris-covered ice, as well as the extent of the glacier termini. In some cases paraglacial slopes or lateral moraines were also misclassified as debris-covered ice (B). Note in addition the large disparity between the extent of the right hand branch of Ponkar glacier in the OBIA classifications and the ICIMOD glacier inventory.
Photo: Pål Ringkjøb Nielsen.

(2011) used SAR coherence data within a Maximum Likelihood classification in China and pointed out problems of surface water also having low coherence values. Huang et al. (2014) used both a backscatter coefficient threshold (89.16% accuracy) and multi-polarimetric analysis within a support-vector-machine (SVM) learning strategy. The latter achieved accuracies of 98.29% although the method is more complicated and was applied on only 1 glacier (83.6 km^2).From the work conducted in this study, it is clear that the inclusion of SAR coherence data within OBIA greatly improves the automatic delineation for debris-covered ice. In particular the lowermost portions of the debris-covered tongues are often spectrally similar to stagnant ice and surrounding bedrock, and therefore indistinguishable if solely using optical data.

It is important to note that despite the improvement that the coherence data brings to the overall classification, it is not possible to classify debris-covered ice based solely on SAR coherence data as was done in Alaska by Atwood et al. (2010). This is because greater amounts of vegetation, steeper topography with unstable slopes and inactive debris-covered ice, all of which contribute to a loss of SAR coherence, are more widespread in the Himalayas than in Alaska (Frey et al., 2012). Optical data can be used to exclude glacial lakes, vegetation growing in the proximity of the glacier or on stagnant ice, while slope data can exclude steep gullies and paraglacial slopes. There are some areas, however, where SAR data was not received at the sensor due to the effects of steep topography on the radar image, namely layover and shadow, as well as problems in orthorectification in the absence of a high quality DEM. In areas where no SAR coherence data was available, the classification relied solely on optical and topographic data, an additional advantage of using multiple data sources with OBIA. The use of SAR data acquired by a descending orbit would reduce the areas of missing information, but the ALOS operation strategy was to operate the SAR sensor only at night and therefore along ascending orbits. Other SAR sensors with short repeat intervals and high spatial resolution, such as TerraSAR-X and Sentinel-1, could be also considered for future studies.

5.2. Comparison with other debris-covered ice classifications

The accuracy of a glacier outline is dependent upon a number of factors, for example the presence of seasonal snow and shadows, the identification of topographic drainage divides and the presence of supraglacial debris (Paul, Barrand, et al., 2013). Often the accuracy is provided as a percentage of the total glacier area as this is one of the only measures from which to compare various studies on various glaciers. However, the relative accuracy is dependent significantly on the size of the glacier or study area, and thus comparisons to other studies must also consider this. As the study area or number of glaciers mapped increases, the error term becomes more random and less systematic (Nuth et al., 2013). Care must therefore be taken then when comparing accuacy assessments between studies, especially for studies that worked on a few large glaciers.

There are very few studies that have used OBIA to directly map glacier ice. Rastner et al. (2014) mapped glaciers in Everest Region of Nepal and similarly found that OBIA mapped debris-covered ice 11.9% more accurately than pixel based methods, with an overall accuracy of 88.5%, however no separate accuracy is provided for clean and debris-covered ice. ICIMOD have performed OBIA over large regions of the Himalayas, including Bhutan (Bajracharya, Maharjan, Shrestha, 2014), Nepal (Bajracharya, Maharjan, Shrestha, Bajracharya et al., 2014) and the entire Hindu Kush Himalayas (HKH) (Bajracharya & Shrestha, 2011, Bajracharya et al., 2015), however these classifications do not include SAR data, nor do they include information on the amount of manual corrections that were necessary.

By comparing to manually corrected outlines, we found an accuracy of 91% for 29 glaciers over the entire glacier area, including an accuracy of 83% over debris-covered ice.

Many studies of debris-covered ice mapping within the Himalayas have used other semi-automatic methodologies and found accuracies higher than those found in our investigation, yet these studies all mapped considerably less than the 788 km^2 of ice mapped in this study. For example Alifu et al. (2015) found an accuracy of >98% over two glaciers, Bolch et al. (2007a) obtained an accuracy of 95% over less than 10 glaciers while Bhambri et al. (2011) also achieved 95% over 3 glaciers (226 km^2). Our study achieved higher total accuracies than Bajracharya, Maharjan, Shrestha (2014) who obtained an accuracy of 91% over 2 glaciers while Shukla et al. (2010) mapped one glacier (65 km^2 (Kulkarni, Dhar, Rathore, & Raj, 2006)) to an accuracy of 89.35%. Racoviteanu and Williams (2012) had errors of up to 25%. Although some studies obtained higher accuracies than us, their study areas were considerably smaller, and any automatic method for mapping debris-covered ice should function over large areas. We therefore consider our method as favourable and more robust due to its inclusion of SAR data which can be used to distinguish active-ice from stagnant-ice and the surrounding terrain and its application over a large study area.

5.3. Importance of image segmentation and classification parameters

Two of the most critical steps in the classification were the assigning weights to the input data, and the parameters used in the image segmentation. Assigning weights of importance for image classification of the coherence data, optical data and topographic data had to be selected carefully in order to exploit each dataset fully. Assigning a higher weight to the optical data could cause a reliance on the lithological composition of the debris cover at the expense of the SAR coherence or topographic data, while weighing the topographic data higher could cause problems

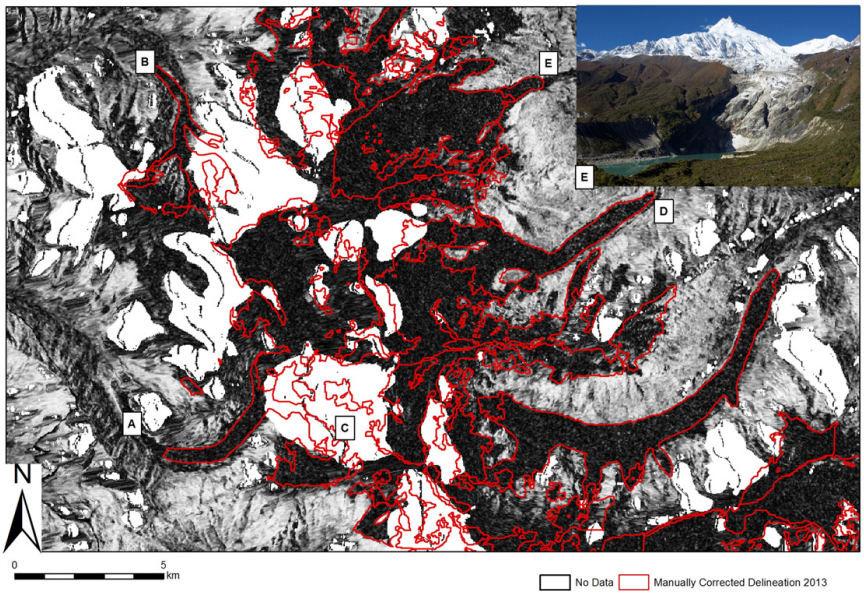

Fig. 8. An illustration of where the SAR coherence signal struggled. Dark shades illustrate a loss of coherence, and therefore that motion has occurred or the ground conditions have changed. (A) The loss of coherence over water was indistinguishable from that of glaciers, (B) some steep valleys facing north showed a loss of coherence over the entire valley, making it hard to depict glaciers, (C) some areas no data at all was returned (shown in white) due to the steep topography (D). Many glacier termini however were easy to distinguish based on loss of coherence. Panel E shows Manaslu Glacier, where the loss of coherence data couldn't differentiate between clean ice, very steep proglacial rock and water.

when the newer, optical data conflicted with the topographic data. The end result varied considerably depending on the weighting factors, and much time was spent trying to balance the data weight assignments as well as possible.

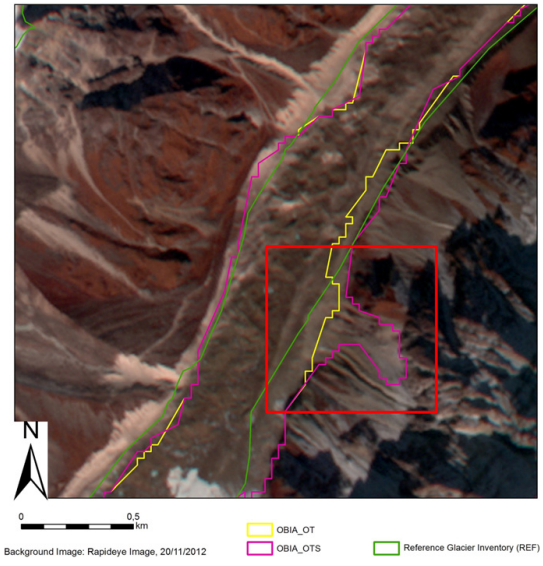

Fig. 9. An example from Syancha Glacier (G084564E28610N) of a debris flow flowing onto the glacier (shown in red square). Due to the spectral similarity of the debris-covered ice and the debris flow, as well as a loss of coherence or no SAR data received, the debris flow deposit was misclassified as glacier ice.

Care is required to decide which parameter sets (such as slope or NDVI) should be used in the classification. The Himalayas are a very heterogeneous region, thus a parameter threshold in one area may not be transferable to another area, as has been found by others (Bhambri et al., 2011; Scherler et al., 2011). As few parameters as possible were chosen in order to make the classification more transferable between the different conditions in the Manaslu region. The parameters were limited to a few initial band ratios and indices before the delineations were expanded using contextual and relational properties.

Three segmentations were used in this study; a higher weighting factor on the slope helped to create larger objects over the gently sloping debris-covered glacier tongues, and smaller objects over the surrounding bedrock. This however caused some of the steeper glacier tributaries to be fragmented between objects, making it more difficult to include them in the classification. In particular some elongated features such as narrow nunataks were too small to be adequately depicted by segmentation and were therefore misclassified as clean ice. The classification procedure was made simpler by using multiple hierarchical segmentations to build large yet homogenous objects while minimising objects that included multiple classes. This made the subsequent classification procedure simpler.

5.4. Use of topographic parameters for classifying debris-covered ice

Several studies pointed to the importance of topographic parameters in the classification. Rastner et al. (2014) and Bajracharya, Maharjan, Shrestha (2014) both used the slope within OBIA to separate debris-covered ice and the surrounding valley sides, while the slope and curvature have been used in other methods such as cluster analysis or supervised classifications to map debris-covered ice based on its morphology (Paul et al., 2004; Ranzi et al., 2004; Bolch et al., 2007a; Bhambri et al., 2011; Racoviteanu & Williams, 2012, Bhardwaj et al., 2014a; Tiwari et al., 2014). The slope was especially useful in separating debris-covered ice from the surrounding bedrock, whilst the elevation

was used in separating glacial lakes from clean ice, and eliminating spectrally similar objects such as scree slopes that were found in lower valleys. There is a large potential to gain information by using the surface curvature and the surface roughness to demarcate the debris-covered portion of the glacier, as has been done in other studies (Paul et al., 2004; Bolch et al., 2007a; Shukla et al., 2010; Bhambri et al., 2011; Bhardwaj et al., 2014a). Such information has not been included as part of an object-based classification of glacier ice before, and in particular could be useful for including the steep glacier tributaries that were missed from the classification. Edge detection of a break in slope or curvature could be used in creating image objects depicting the debris-covered glacier tongue. In this study the resolution of the SRTM DEM was not sufficient to use either the curvature or the surface roughness; however the future release of higher resolution DEMs such as the TanDEM-X Global DEM could increase the ability of an automated OBIA classification.

5.5. Comparison between OBIA and pixel based methods

The use of OBIA has many advantages over standard pixel based methods. The ability to include contextual information permits the removal and subsequent reclassification of cloud and shadows that are surrounded by glacier ice. This reduces the amount of manual correction that is necessary. OBIA can efficiently break down an object into its components, while the ability to assign classes within a hierarchy allows sub- and supraclasses. This allows a "glacier" to be made up of "clean ice" and "debris-covered ice", or "glacial lakes" to be made up of "proglacial lakes", "supra-glacial lakes" and "marginal-glacier lakes". Hierarchical ordering of classifications also enables temporary classifications that can be used to expand classifications into troublesome areas.

Additionally, as OBIA permits the handling of optical, SAR and DEM data simultaneously, classifications can use a combination of remotely sensed data in order to determine a class, allowing an improvement of the classification of debris-covered ice when compared to pixel based methods. It should be noted though that pixel based methods are simpler to perform than OBIA, both in terms of steps and technical knowledge needed when classifying, as well as computational power. Nonetheless, OBIA is recommended for future work on glacier inventories and glacier areas estimations, but mostly with either debris-covered ice or when working on very large areas in order to reduce the amount of manual correction necessary. The power of OBIA is to increase the robustness of generating glacier outlines and provide the potential to distinguish various subclasses of glaciers.

5.6. Future directions

Future studies could also explore the possibility of using the NIR or Red spectral channels to separate clean ice from snow-covered ice, thereby mapping the transient snow line (TSL). The highest altitude of the TSL during an ablation season can be considered a proxy for the equilibrium line altitude (ELA) of a glacier (Racoviteanu, Williams, & Barry, 2008, Bishop et al., 2014). Kääb et al. (2015).

The disparity found between the various glacier outlines compared in this study highlight the need for frequent, up to date glacier inventories. Large differences were found for the glaciers north of the mountain divide as a result of the 40 year difference between the creation of the two inventories. Remote sensing and GIS technologies, such as OBIA, facilitate the automatic or semi-automatic creation of regular glacier inventories, however differences in arbitrary thresholds such as the upper elevation and upper slope threshold cause significant differences in the upper boundaries of glaciers. This study used shallower slope thresholds than the ICIMOD inventory in order to exclude false positives; thresholds selected depend on the specific datasets used and also vary by location. Nonetheless, if multiple glacier inventories are used to assess glacier area changes over time, problems can arise. For example, there is no clear consensus on the upper bounds of the accumulation area, nor whether steep terrain that contributes snow and ice to the glacier through avalanching should be considered as a part of the glacier. It is interesting that some changes between the reference glacier inventory and the outlines derived in this study were due to differences in these upper delineations, and could cause noise when assessing glacier area change between multiple inventories. Through initiatives such as GLIMS and the Randolph Glacier Inventory, a defined outline for the use of OBIA could be used to streamline the creation and maintenance of glacier outlines.

6. Conclusions

Remote sensing glaciology, and in particular large scale glacier mapping is hampered by glacier debris being spectrally indistinguishable from the surrounding terrain. This study has shown that OBIA can be used effectively for automated and robust mapping of glaciers; both clean ice and debris-covered ice, and has many advantages over traditional pixel-based methods. OBIA permits the handling of multiple data types including optical, SAR and elevation data, while hierarchical and contextual capabilities allow rule sets such as excluding debris-covered ice not adjacent to clean ice, including neighbouring objects that are spectrally similar or determining an object's class by its shape or area. These capabilities of OBIA reduce the amount of post-processing required while enhancing the potential to enhance glacier mapping to the various types of glacier surfaces (i.e. snow lines, debris-cover type, lake detection etc.…).

We have shown that by combining SAR coherence data with optical satellite imagery and topographic data in an OBIA, it is possible to accurately map clean ice and debris-covered ice, even with course-resolution elevation data, such as the 90 m SRTM DEM. However using SAR coherence data within OBIA only classifies ice that has undergone motion or a change in surface conditions, thereby excluding stagnant glacier ice. Stagnant ice may not part of the active glacier, but is still important when considering GLOF hazards.

This OBIA however has some restrictions when it comes to steep, unstable valley slopes, rock slides, flowing surface water, and vegetation. In addition, the mountainous terrain in our study area results in SAR data not always being retrievable due to shadowing and layover effects. Nevertheless, over a large (788 km^2) study area we semi-automatically mapped the clean ice with an accuracy of 93% (7% error) and the debris-covered portions to an accuracy of 83% (17% error) given an accuracy over the entire glacier of 91%. This accuracy can be improved using a higher resolution DEM, and/or by using temporally consistent data within the classification, while if steep, tributary sections of ice can be contextually included then the accuracy will rise to over 94%. We can recommend the use of OBIA incorporating SAR coherence data with optical imagery and topographic data for future studies in order to robustly map heavily debris-covered glacierised regions at a large spatial scale.

Acknowledgements

First and foremost the authors would like to thank Asha Badadur Rai (www.adventurousnepal.com) and his family for organising all the logistics and practicalities of our fieldwork trekking around the Manaslu Conservation Area in both 2013 and 2014 and making us very welcome in Nepal. Thanks also to Tommy Robson and Ingrid Lycke Austbø for proof reading this manuscript. Thanks to the three reviewers who had many helpful comments and suggestions and vastly improved the quality of this paper. We are also very grateful to both ResClim and Meltzer for the additional funding received for this project. Christopher Nuth acknowledges support by the European Research Council under the European Union's Seventh Framework Programme (FP/2007-2013)/ERC grant agreement no. 320816. This study is also a contribution from the ESA project Glaciers_cci (4000109873/14/I-NB) that supported the production of ALOS PALSAR coherence images. We are very grateful to NASA and the USGS for free provision of Landsat 8 and SRTM data. Daniel Hölbling has been partly supported by the Austrian Science Fund (FWF) through the project iSLIDE under Grant P 25446-N29.

Appendix

Table A.1
ICIMOD Glacier inventory, manual delineation, a spectrally based OBIA and a SAR based OBIA.

Glacier GLIMS ID	Colloquial name (if available)	Clean ice area (km^2)					Debris covered ice area (km^2)				
		REF	OBIA_Man	OBIA_OT	% difference OBIA_OT − REF	% difference OBIA_OT − Manual	REF	OBIA_Man	OBIA_OTS	% difference OBIA_OTS − REF	% difference OBIA_OTS − OBIA_Man
G084339E28643N	Suti Glacier	13.82	14.68	15.95	−14.51	−8.65	6.40	8.55	6.12	3.27	28.42
G084423E28705N	Kechakyu Khola Glacier	33.16	33.90	33.82	-1.95	0.24	11.68	14.67	13.13	-9.88	10.50
G084455E28727N	Ponkar Glacier										
G084486E28664N	Salpudanda Glacier										
G084516E28732N	Fukang Glacier North	15.25	13.59	17.47	−16.34	−28.55	4.98	6.07	6.62	-27.02	-9.06
G084518E28703N	Fukang Glacier South	12.24	9.98	11.20	10.42	−12.22					
G084565E28663N	Larkya Glacier	1.41	1.50	1.81	−26.39	−20.60	2.82	3.47	2.73	2.47	21.20
G084564E28610N	Manaslu Glacier	7.63	7.21	9.29	−23.02	−28.85	2.82	2.91	2.96	−4.81	−1.72
G084597E28534N	Punggen Glacier	19.19	16.33	14.89	26.33	8.82	7.41	8.22	4.88	30.78	40.63
G084633E28476N	Hinang Glacier	33.36	21.66	24.79	39.57	−14.45	11.01	14.31	12.98	−13.77	9.30
G084718E28471N		10.95	12.24	11.93	−8.01	2.53	0.25	1.08	0.81	−51.85	25.00
G084682E28429N	Himal Chuli Glacier	29.57	28.57	28.30	4.45	0.95	5.62	6.55	5.66	−0.61	13.59
G084691E28383N	Bhauda Himal Glacier	5.30	6.77	6.48	−17.43	4.28	3.10	3.21	1.71	43.30	46.73
G084538E28524N	Thulagi Glacier	25.43	24.82	22.57	11.52	9.07	2.68	2.66	2.71	−1.13	−1.88
G084502E28557N	Changli Glacier	1.05	1.78	1.59	−30.34	10.67	1.34	2.60	2.50	−44.62	3.85
G084365E28759N		15.33	13.82	14.29	7.53	−3.40	1.13	1.55	1.15	−1.29	25.81
G084374E28756N		26.48	24.84	23.80	10.79	4.19	5.19	5.60	5.51	−5.71	1.61
G084421E28786N		15.98	17.10	17.69	−10.00	−3.45	0.00	1.95	1.63	−83.59	16.41
G084484E28756N		10.62	9.88	10.05	5.77	−1.72	n/a	n/a	n/a	n/a	n/a
G084459E28796N		20.09	15.76	14.37	36.29	8.82	n/a	n/a	n/a	n/a	n/a
G084424E28838N		9.17	9.19	8.34	9.03	9.25	n/a	n/a	n/a	n/a	n/a
G084416E28868N		8.08	6.01	5.40	44.59	10.15	n/a	n/a	n/a	n/a	n/a
G084394E28877N		4.97	4.08	4.17	19.61	−2.21	n/a	n/a	n/a	n/a	n/a
G084374E28889N		1.56	1.30	1.29	20.77	0.77	n/a	n/a	n/a	n/a	n/a
G084338E28878N		20.22	16.64	15.34	29.33	7.81	n/a	n/a	n/a	n/a	n/a
G084289E28901N		14.15	9.43	8.99	54.72	4.67	n/a	n/a	n/a	n/a	n/a
G084241E28915N		17.32	13.66	13.88	25.18	−1.61	n/a	n/a	n/a	n/a	n/a
G084196E28874N		7.89	7.09	10.50	−36.81	0.00	2.26	2.51	2.21	1.99	11.95
G084153E28900N		28.28	26.83	26.13	8.01	2.61	n/a	n/a	n/a	n/a	n/a
Total deviation		408.50	368.66	374.33	15.26	6.67	68.69	85.91	73.31	15.48	16.18

(*continued on next page*)

Table A.1 *(continued)*

Glacier GLIMS ID	Debris covered ice area (km^2)				Total glacier (km^2)							
	OBIA_OT	% difference OBIA_OT − REF	% difference OBIA_OT − OBIA_Man	% difference OBIA OT − OBIA OTS	REF	OBIA_Man	OBIA_OTS	% difference OBIA_OTS − REF	% difference OBIA_OTS − OBIA_Man	OBIA_OT	% difference OBIA_OT − REF	% difference OBIA_OT − OBIA_Man
G084339E28643N	5.87	6.20	31.35	4.08	20.22	23.23	22.07	−9.15	4.99	21.82	−7.91	−6.07
G084423E28705N	13.06	-9.41	10.97	0.53	44.84	48.57	46.95	-4.71	3.34	46.88	-4.55	-3.48
G084455E28727N												
G084486E28664N												
G084516E28732N	8.06	-50.74	-32.78	−21.75	32.47	29.64	35.29	-8.68	-19.06	36.73	-13.12	23.92
G084518E28703N												
G084565E28663N	5.48	−76.66	−57.93	−100.42	4.23	4.97	4.54	−7.33	8.65	7.29	−72.34	46.68
G084564E28610N	2.93	−3.78	−0.69	1.01	10.45	10.12	12.25	−17.22	−21.05	12.22	−16.94	20.75
G084597E28534N	5.27	26.03	35.89	−7.99	26.60	24.55	19.77	25.68	19.47	20.16	24.21	−17.88
G084633E28476N	12.88	−13.07	10.00	0.77	44.37	35.97	37.77	14.87	−5.00	37.67	15.10	4.73
G084718E28471N	0.79	−50.00	26.85	2.47	11.20	13.32	12.74	−13.75	4.35	12.72	−13.57	−4.50
G084682E28429N	4.87	11.45	25.65	13.96	35.19	35.12	33.96	3.50	3.30	33.17	5.74	−5.55
G084691E28383N	1.84	39.25	42.68	−7.60	8.40	9.98	8.19	2.50	17.94	8.32	0.95	−16.63
G084538E28524N	2.42	9.77	9.02	10.70	28.11	27.48	25.28	10.07	8.01	24.99	11.10	−9.06
G084502E28557N	1.74	−15.38	33.08	30.40	2.39	4.38	4.09	−71.13	6.62	3.33	−39.33	−23.97
G084365E28759N	1.06	4.52	31.61	7.83	16.46	15.37	15.44	6.20	−0.46	15.35	6.74	−0.13
G084374E28756N	7.39	−39.29	−31.96	−34.12	31.67	30.44	29.31	7.45	3.71	31.19	1.52	2.46
G084421E28786N	1.69	−86.67	13.33	−3.68	15.98	19.05	19.32	−20.90	−1.42	19.38	−21.28	1.73
G084484E28756N	n/a	n/a	n/a	n/a	10.62	9.88	10.05	5.37	−1.72	10.05	5.37	1.72
G084459E28796N	n/a	n/a	n/a	n/a	20.09	15.76	14.37	28.47	8.82	14.37	28.47	−8.82
G084424E28838N	n/a	n/a	n/a	n/a	9.17	9.19	8.34	9.05	9.25	8.34	9.05	−9.25
G084416E28868N	n/a	n/a	n/a	n/a	8.08	6.01	5.40	33.17	10.15	5.40	33.17	−10.15
G084394E28877N	n/a	n/a	n/a	n/a	4.97	4.08	4.17	16.10	−2.21	4.17	16.10	2.21
G084374E28889N	n/a	n/a	n/a	n/a	1.56	1.30	1.29	17.31	0.77	1.29	17.31	−0.77
G084338E28878N	n/a	n/a	n/a	n/a	20.22	16.64	15.34	24.13	7.81	15.34	24.13	−7.81
G084289E28901N	n/a	n/a	n/a	n/a	14.15	9.43	8.99	36.47	4.67	8.99	36.47	−4.67
G084241E28915N	n/a	n/a	n/a	n/a	17.32	13.66	13.88	19.86	−1.61	13.88	19.86	1.61
G084196E28874N	7.18	−196.02	−186.06	−224.89	10.15	9.60	12.71	−25.22	−32.40	17.68	−74.19	84.17
G084153E28900N	n/a	n/a	n/a	n/a	28.28	26.83	26.13	7.60	2.61	26.13	7.60	−2.61
Total deviation	82.53	27.77	28.33	−12.62	477.19	454.57	447.64	13.75	8.99	456.86	19.47	10.05

Table A.2
Comparison between the manually delineated outline and the OBIA_OTS classifications when steep tributaries of the glaciers are excluded.

GLIMS glacier ID	Debris covered ice (clipped) (km^2)					Total glacier (clipped) (km^2)				
	OBIA_Man	OBIA_OTS	% difference OBIA_OTS − OBIA_Man	OBIA_OT	% difference OBIA_OT − OBIA_Man	OBIA_Man	OBIA_OTS	% difference OBIA_OTS − OBIA_Man	OBIA_OT	% difference OBIA_OT − OBIA_Man
G084339E28643N	6.21	6.12	1.46	5.87	5.44	20.89	22.07	−5.65	21.82	−4.46
G084423E28705N	12.55	13.13	−4.64	13.06	−4.10	46.45	46.95	−1.08	46.88	−0.93
G084455E28727N										
G084486E28664N										
G084516E28732N	5.80	6.62	−14.05	8.06	−38.89	19.39	24.09	−24.21	25.53	−31.64
G084518E28703N										
G084565E28663N	2.60	2.70	−3.94	5.48	−111.13	4.10	4.51	−10.06	7.29	−78.01
G084564E28610N	2.82	2.96	−5.03	2.93	−3.95	10.03	12.25	−22.15	12.22	−21.85
G084597E28534N	4.24	4.88	−15.05	5.27	−24.27	20.57	19.77	3.90	20.16	2.00
G084633E28476N	11.50	12.98	−12.92	12.88	−12.02	33.16	37.77	−13.92	37.67	−13.61
G084718E28471N	0.98	0.81	17.53	0.79	19.37	13.22	12.74	3.64	12.72	3.78
G084682E28429N	5.77	5.66	1.88	4.87	15.58	34.34	33.96	1.10	33.17	3.40
G084691E28383N	1.64	1.71	−4.43	1.84	−12.01	8.41	8.19	2.58	8.32	1.11
G084538E28524N	2.31	2.71	−17.45	2.42	−4.77	27.13	25.28	6.81	24.99	7.89
G084502E28557N	1.68	2.50	−48.96	1.74	−3.37	3.46	4.09	−18.28	3.33	3.86
G084365E28759N	1.23	1.15	6.38	1.06	14.10	15.05	15.44	−2.60	15.35	−1.97
G084374E28756N	5.04	5.51	−9.29	7.39	−46.70	29.88	29.31	1.91	31.19	−4.40
G084421E28786N	1.85	1.63	11.78	1.69	8.52	18.95	19.32	−1.96	19.38	−2.28
G084196E28874N	2.14	2.21	−3.29	7.18	−235.54	12.02	12.26	−2.00	17.23	−43.35
Total	68.36	73.29	9.17	82.53	25.89	327.03	339.21	5.98	348.45	8.90

References

Ageta, Y., & Higuchi, K. (1984). Estimation of mass balance components of a summer-accumulation type glacier in the Nepal Himalaya. *Geografiska Annaler Series a-Physical Geography*, *66*, 249–255.

Albert, T. H. (2002). Evaluation of remote sensing techniques for ice-area classification applied to the tropical Quelccaya Ice Cap, Peru. *Polar Geography*, *26*, 210–226.

Alifu, H., Tateishi, R., & Johnson, B. (2015). A new band ratio technique for mapping debris-covered glaciers using Landsat imagery and a digital elevation model. *International Journal of Remote Sensing*, *36*, 2063–2075.

Atwood, D. K., Meyer, F., & Arendt, A. (2010). Using L-band SAR coherence to delineate glacier extent. *Canadian Journal of Remote Sensing*, *36*, S186–S195.

Bajracharya, S., & Shrestha, B. (2011). *The status of glaciers in the Hindu Kush-Himalayan region*. Kathmandu: ICIMOD.

Bajracharya, S. R., Maharjan, S. B., & Shrestha, F. (2014a). The status and decadal change of glaciers in Bhutan from the 1980s to 2010 based on satellite data. *Annals of Glaciology*, *55*, 159–166.

Bajracharya, S. R., Maharjan, S. B., Shrestha, F., Bajracharya, O. R., & Baidya, S. (2014b). *Glacier status in Nepal and decadal change from 1980 to 2010 based on Landsat data*. Kathmandu: ICIMOD.

Bajracharya, S. R., Maharjan, S. B., Shrestha, F., Guo, W., Liu, S., Immerzeel, W., & Shrestha, B. (2015). The glaciers of the Hindu Kush Himalayas: current status and observed changes from the 1980s to 2010. *International Journal of Water Resources Development*, *31*, 161–173.

Benn, D. I., & Evans, D. J. (2010). *Glaciers and glaciation*. Hodder Education.

Benn, D. I., & Owen, L. A. (1998). The role of the Indian summer monsoon and the mid-latitude westerlies in Himalayan glaciation: review and speculative discussion. *Journal of the Geological Society*, *155*, 353–363.

Benn, D. I., Bolch, T., Hands, K., Gulley, J., Luckman, A., Nicholson, L. I., ... Wiseman, S. (2012). Response of debris-covered glaciers in the Mount Everest region to recent warming, and implications for outburst flood hazards. *Earth-Science Reviews*, *114*, 156–174.

Benz, U. C., Hofmann, P., Willhauck, G., Lingenfelder, I., & Heynen, M. (2004). Multi-resolution, object-oriented fuzzy analysis of remote sensing data for GIS-ready information. *ISPRS Journal of Photogrammetry and Remote Sensing*, *58*, 239–258.

Bernard, É, et al. (2014). Where does a glacier end? GPR measurements to identify the limits between valley slopes and actual glacier body. Application to the Austre Lovénbreen, Spitsbergen. *International Journal of Applied Earth Observation and Geoinformation*, *27*, 100–108.

Berthier, E., Vadon, H., Baratoux, D., Arnaud, Y., Vincent, C., Feigl, K. L., ... Legresy, B. (2005). Surface motion of mountain glaciers derived from satellite optical imagery. *Remote Sensing of Environment*, *95*, 14–28.

Berthier, E., Arnaud, Y., Kumar, R., Ahmad, S., Wagnon, P., & Chevallier, P. (2007). Remote sensing estimates of glacier mass balances in the Himachal Pradesh (Western Himalaya, India). *Remote Sensing of Environment*, *108*, 327–338.

Berthier, E., Schiefer, E., Clarke, G. K. C., Menounos, B., & Remy, F. (2010). Contribution of Alaskan glaciers to sea-level rise derived from satellite imagery. *Nature Geoscience*, *3*, 92–95.

Bhambri, R., Bolch, T., & Chaujar, R. K. (2011). Mapping of debris-covered glaciers in the Garhwal Himalayas using ASTER DEMs and thermal data. *International Journal of Remote Sensing*, *32*, 8095–8119.

Bhardwaj, A., Joshi, P. K., Snehmani, S.,. M. K., Sam, L., & Gupta, R. D. (2014a). Mapping debris-covered glaciers and identifying factors affecting the accuracy. *Cold Regions Science and Technology*, *106–107*, 161–174.

Bhardwaj, A., Joshi, P. K., Snehmani, S.,. M. K., Sam, L., & Gupta, R. D. (2014b). Mapping debris-covered glaciers and identifying factors affecting the accuracy. *Cold Regions Science and Technology*, *106*, 161–174.

Bishop, M., Bush, A. G., Furfaro, R., Gillespie, A., Hall, D., Haritashya, U., & Shroder, J., Jr. (2014). Theoretical foundations of remote sensing for glacier assessment and mapping. In J. S. KARGEL, G. J. LEONARD, M. P. BISHOP, A. KÄÄB, & B. H. RAUP (Eds.), *Global land ice measurements from space*. Springer Berlin Heidelberg.

Blaschke, T. (2010). Object based image analysis for remote sensing. *ISPRS Journal of Photogrammetry and Remote Sensing*, *65*, 2–16.

Blaschke, T., & Strobl, J. (2001). What's wrong with pixels? Some recent developments interfacing remote sensing and GIS. *GIS - Zeitschrift für Geoinformationssysteme*, *6*, 12–17.

Blaschke, T., Hay, G. J., Kelly, M., Lang, S., Hofmann, P., Addink, E., Feitosa, R. Q., Van Der Meer, F., Van Der Werff, H., Van Coillie, F., et al. (2014). Geographic object-based image analysis – towards a new paradigm. *ISPRS Journal of Photogrammetry and Remote Sensing*, *87*, 180–191.

Bolch, T., Buchroithner, M. F., Kunert, A., & Kamp, U. (2007a). Automated delineation of debris-covered glaciers based on ASTER data. *Geoinformation in Europe (Proc. of 27th EARSel Symposium, 04–07 June 2007)* (pp. 403–410). Italy: Bozen.

Bolch, T., Buchroithner, M. F., Kunert, A., & Kamp, U. (2007b). Automated delineation of debris-covered glaciers based on ASTER data. *Geoinformation in Europe. proceedings of the 27th EARSeL Symposium* (pp. 4–6).

Bolch, T., Buchroithner, M., Pieczonka, T., & Kunert, A. (2008a). Planimetric and volumetric glacier changes in the Khumbu Himal, Nepal, since 1962 using Corona, Landsat TM and ASTER data. *Journal of Glaciology*, *54*, 592–600.

Bolch, T., Buchroithner, M. F., Peters, J., Baessler, M., & Bajracharya, S. (2008b). Identification of glacier motion and potentially dangerous glacial lakes in the Mt. Everest region/Nepal using spaceborne imagery. *Natural Hazards and Earth System Sciences*, *8*, 1329–1340.

Bolch, T., Kulkarni, A., Kaab, A., Huggel, C., Paul, F., Cogley, J. G., Frey, H., Kargel, J. S., Fujita, K., Scheel, M., et al. (2012). The state and fate of Himalayan glaciers. *Science*, *336*, 310–314.

Brenning, A., Pena, M. A., Long, S., & Soliman, A. (2012). Thermal remote sensing of ice-debris landforms using ASTER: an example from the Chilean Andes. *The Cryosphere*, *6*, 367–382.

Casey, K. A., Kaab, A., & Benn, D. I. (2012). Geochemical characterization of supraglacial debris via in situ and optical remote sensing methods: a case study in Khumbu Himalaya, Nepal. *The Cryosphere*, *6*, 85–100.

Catani, F., Farina, P., Moretti, S., Nico, G., & Strozzi, T. (2005). On the application of SAR interferometry to geomorphological studies: estimation of landform attributes and mass movements. *Geomorphology*, *66*, 119–131.

Cuffey, K. M., & Paterson, W. S. B. (2010). *The physics of glaciers.* Academic Press.

De Ferranti, J. (2012). Viewfinder panoramas [Online]. Available: http://www.viewfinderpanoramas.org/ [Accessed 15/06/2013]

Drăguț, L., Csillik, O., Eisank, C., & Tiede, D. (2014). Automated parameterisation for multi-scale image segmentation on multiple layers. *ISPRS Journal of Photogrammetry and Remote Sensing*, *88*, 119–127.

Frey, H., Paul, F., & Strozzi, T. (2012). Compilation of a glacier inventory for the western Himalayas from satellite data: methods, challenges, and results. *Remote Sensing of Environment*, *124*, 832–843.

Gao, Y., Mas, J. F., Maathuis, B. H. P., Zhang, X. M., & Van Dijk, P. M. (2006). Comparison of pixel-based and object-oriented image classification approaches - a case study in a coal fire area, Wuda, Inner Mongolia, China. *International Journal of Remote Sensing*, *27*, 4039–4055.

Gardelle, J., Berthier, E., Arnaud, Y., & Kääb, A. (2013). Region-wide glacier mass balances over the Pamir–Karakoram–Himalaya during 1999–2011. *The Cryosphere*, *7*, 1263–1286.

Ghosh, S., Pandey, A. C., & Nathawat, M. S. (2014). Mapping of debris-covered glaciers in parts of the Greater Himalaya Range, Ladakh, western Himalaya, using remote sensing and GIS. *Journal of Applied Remote Sensing*, *8* (083579–083579).

Government of Nepal, D. O. H. a. M (2014). *Interpolated 12 km temperature and rainfall mean annual data (1970–2010) [online].* Nepal: Kathmandu (Available: http://dhm.gov.np/dpc).

Hoersch, B., & Amans, V. (2012). *GMES space component data access portfolio: data warehouse 2011–2014.* Frascati, Italy: European Space Agency.

Hölbling, D., Friedl, B., & Eisank, C. (2015). An object-based approach for semi-automated landslide change detection and attribution of changes to landslide classes in northern Taiwan. *Earth Science Informatics*, *1-9*.

Huang, L., Li, Z., Tian, B. S., Zhou, J. M., & Chen, Q. (2014). Recognition of supraglacial debris in the Tianshan Mountains on polarimetric SAR images. *Remote Sensing of Environment*, *145*, 47–54.

Icimod (2010). In S. R. Bajracharya, & P. MOOL (Eds.), *Glacier mapping and monitoring tools and techniques.* ICIMOD.

Immerzeel, W. W., Van Beek, L. P. H., & Bierkens, M. F. P. (2010). Climate change will affect the Asian water towers. *Science*, *328*, 1382–1385.

Immerzeel, W. W., Kraaijenbrink, P. D. A., Shea, J. M., Shrestha, A. B., Pellicciotti, F., Bierkens, M. F. P., & De Jong, S. M. (2014). High-resolution monitoring of Himalayan glacier dynamics using unmanned aerial vehicles. *Remote Sensing of Environment*, *150*, 93–103.

Joyce, K. E., Samsonov, S. V., Levick, S. R., Engelbrecht, J., & Belliss, S. (2014). Mapping and monitoring geological hazards using optical, LiDAR, and synthetic aperture RADAR image data. *Natural Hazards*, *73*, 137–163.

Juen, M., Mayer, C., Lambrecht, A., Han, H., & Liu, S. (2014). Impact of varying debris cover thickness on ablation: a case study for Koxkar Glacier in the Tien Shan. *The Cryosphere*, *8*, 377–386.

Kääb, A. (2005). Combination of SRTM3 and repeat ASTER data for deriving alpine glacier flow velocities in the Bhutan Himalaya. *Remote Sensing of Environment*, *94*, 463–474.

Kääb, A., Bolch, T., Casey, K., Heid, T., Kargel, J., Leonard, G., ... Raup, B. (2015). Glacier mapping and monitoring using multispectral data. In J. S. KARGEL, G. J. LEONARD, M. P. BISHOP, A. KÄÄB, & B. H. RAUP (Eds.), *Global land ice measurements from space*. Springer Berlin Heidelberg.

Karimi, N., Farokhnia, A., Shishangosht, S., Elmi, M., Eftekhari, M., & Ghalkhani, H. (2012). Elevation changes of Alamkouh glacier in Iran since 1955, based on remote sensing data. *International Journal of Applied Earth Observation and Geoinformation*, *19*, 45–58.

Keshri, A. K., Shukla, A., & Gupta, R. P. (2009). ASTER ratio indices for supraglacial terrain mapping. *International Journal of Remote Sensing*, *30*, 519–524.

Kulkarni, A., Dhar, S., Rathore, B. P., Raj, K. B., & Kalia, R. (2006). Recession of Samudra Tapu glacier, Chandra river basin, Himachal Pradesh. *Journal of the Indian Society of Remote Sensing*, *34*, 39–46.

Lang, S. (2008). Object-based image analysis for remote sensing applications: modeling reality — dealing with complexity. In T. BLASCHKE, S. LANG, & G. HAY (Eds.), *Object-based image analysis*. Springer Berlin Heidelberg.

Mool, P., Maskey, P. R., Koirala, A., Joshi, S. P., Lizong, W., Shrestha, A. B., Eriksson, M., Gurung, B., Pokharel, B., Khanal, N. R., et al. (2011). *Glacial lakes and glacial lake outburst floods in Nepal.* Kathmandu: ICIMOD.

Moosavi, V., Talebi, A., & Shirmohammadi, B. (2014). Producing a landslide inventory map using pixel-based and object-oriented approaches optimized by Taguchi method. *Geomorphology*, *204*, 646–656.

Myint, S. W., Gober, P., Brazel, A., Grossman-Clarke, S., & Weng, Q. H. (2011). Per-pixel vs. object-based classification of urban land cover extraction using high spatial resolution imagery. *Remote Sensing of Environment*, *115*, 1145–1161.

Nuimura, T., Sakai, A., Taniguchi, K., Nagai, H., Lamsal, D., Tsutaki, S., Kozawa, A., Hoshina, Y., Takenaka, S., Omiya, S., et al. (2014). The GAMDAM Glacier Inventory: a quality controlled inventory of Asian glaciers. *The Cryosphere Discuss*, *8*, 2799–2829.

Nuth, C., Kohler, J., König, M., Von Deschwanden, A., Hagen, J. O., Kääb, A., ... Pettersson, R. (2013). Decadal changes from a multi-temporal glacier inventory of Svalbard. *The Cryosphere*, *7*, 1603–1621.

Owen, L. A., & Benn, D. I. (2005). Equilibrium-line altitudes of the Last Glacial Maximum for the Himalaya and Tibet: an assessment and evaluation of results. *Quaternary International*, *138–139*, 55–78.

Paul, F., & Andreassen, L. M. (2009). A new glacier inventory for the Svartisen region, Norway, from Landsat ETM+ data: challenges and change assessment. *Journal of Glaciology*, *55*, 607–618.

Paul, F., Huggel, C., & Kaab, A. (2004). Combining satellite multispectral image data and a digital elevation model for mapping debris-covered glaciers. *Remote Sensing of Environment*, *89*, 510–518.

Paul, F., Barrand, N., Baumann, S., Berthier, E., Bolch, T., Casey, K., ... Bris, R. L. (2013a). On the accuracy of glacier outlines derived from remote-sensing data. *Annals of Glaciology*, *54*, 171–182.

Paul, F., Bolch, T., Kääb, A., Nagler, T., Nuth, C., Scharrer, K., Shepherd, A., Strozzi, T., Ticconi, F., Bhambri, R., et al. (2013b). The glaciers climate change initiative: methods for creating glacier area, elevation change and velocity products. *Remote Sensing of Environment*, *162*, 408–426.

Pfeffer, W. T., Arendt, A. A., Bliss, A., Bolch, T., Cogley, J. G., Gardner, A. S., Hagen, J. O., Hock, R., Kaser, G., Kienholz, C., et al. (2014). The Randolph Glacier Inventory: a globally complete inventory of glaciers. *Journal of Glaciology*, *60*, 537–552.

Pradhananga, N. S., Kayastha, R. B., Bhattarai, B. C., Adhikari, T. R., Pradhan, S. C., Devkota, L. P., ... Mool, P. K. (2014). Estimation of discharge from Langtang River basin, Rasuwa, Nepal, using a glacio-hydrological model. *Annals of Glaciology*, *55*, 223–230.

Pratap, B., Dobhal, D., Bhambri, R., Mehta, M., & Tewari, V. (2015a). Four decades of glacier mass balance observations in the Indian Himalaya. *Regional Environmental Change*, *1-16*.

Pratap, B., Dobhal, D., Mehta, M., & Bhambri, R. (2015b). Influence of debris cover and altitude on glacier surface melting: a case study on Dokriani Glacier, central Himalaya, India. *Annals of Glaciology*, *56*, 9.

Quincey, D. J., Luckman, A., & Benn, D. (2009). Quantification of Everest region glacier velocities between 1992 and 2002, using satellite radar interferometry and feature tracking. *Journal of Glaciology*, *55*, 596–606.

Racoviteanu, A., & Williams, M. W. (2012). Decision tree and texture analysis for mapping debris-covered glaciers in the Kangchenjunga area, eastern Himalaya. *Remote Sensing*, *4*, 3078–3109.

Racoviteanu, A. E., Williams, M. W., & Barry, R. G. (2008). Optical remote sensing of glacier characteristics: a review with focus on the Himalaya. *Sensors*, *8*, 3355–3383.

Racoviteanu, A. E., Paul, F., Raup, B., Khalsa, S. J. S., & Armstrong, R. (2009). Challenges and recommendations in mapping of glacier parameters from space: results of the 2008 global land ice measurements from space (GLIMS) workshop, Boulder, Colorado, USA. *Annals of Glaciology*, *50*, 53–69.

Racoviteanu, A. E., Armstrong, R., & Williams, M. W. (2013). Evaluation of an ice ablation model to estimate the contribution of melting glacier ice to annual discharge in the Nepal Himalaya. *Water Resources Research*, *49*, 5117–5133.

Ranzi, R., Grossi, G., Iacovelli, L., & Taschner, S. (2004). Use of multispectral ASTER images for mapping debris-covered glaciers within the GLIMS project. *Igarss 2004: IEEE international geoscience and remote sensing symposium proceedings. Vols 1-7*. (pp. 1144–1147).

Rastner, P., Bolch, T., Notarnicola, C., & Paul, F. (2014). A comparison of pixel- and object-based glacier classification with optical satellite images. *Ieee Journal of Selected Topics in Applied Earth Observations and Remote Sensing*, *7*, 853–862.

Rees, H. G., & Collins, D. N. (2006). Regional differences in response of flow in glacier-fed Himalayan rivers to climatic warming. *Hydrological Processes*, *20*, 2157–2169.

Rexer, M., & Hirt, C. (2014). Comparison of free high resolution digital elevation data sets (ASTER GDEM2, SRTM v2.1/v4.1) and validation against accurate heights from the Australian National Gravity database. *Australian Journal of Earth Sciences*, *61*, 213–226.

Reznichenko, N., Davies, T., Shulmeister, J., & Mcsaveney, M. (2010). Effects of debris on ice-surface melting rates: an experimental study. *Journal of Glaciology*, *56*, 384–394.

Richardson, S. D., & Reynolds, J. M. (2000). An overview of glacial hazards in the Himalayas. *Quaternary International*, *65-6*, 31–47.

Saraswat, P., Syed, T. H., Famiglietti, J. S., Fielding, E. J., Crippen, R., & Gupta, N. (2013). Recent changes in the snout position and surface velocity of Gangotri glacier observed from space. *International Journal of Remote Sensing*, *34*, 8653–8668.

Scherler, D., Bookhagen, B., & Strecker, M. R. (2011). Spatially variable response of Himalayan glaciers to climate change affected by debris cover. *Nature Geoscience*, *4*, 156–159.

Shangguan, D., Liu, S., Ding, Y., Wu, L., Deng, W., Guo, W., ... Guo, Z. (2014). Glacier changes in the Koshi River basin, central Himalaya, from 1976 to 2009, derived from remote-sensing imagery. *Annals of Glaciology*, *55*, 61.

Sharma, A. K., Singh, S. K., Kulkarni, A. V., & Ajai (2013). Glacier inventory in Indus, Ganga and Brahmaputra Basins of the Himalaya. *National Academy Science Letters (India)*, *36*, 497–505.

Shukla, A., Arora, M., & Gupta, R. (2010). Synergistic approach for mapping debris-covered glaciers using optical–thermal remote sensing data with inputs from geomorphometric parameters. *Remote Sensing of Environment*, *114*, 1378–1387.

Snehmani, S.,. M. k., Gupta, R., Bhardwaj, A., & Joshi, P. K. (2014). *Geocarto International*, *1–27*.

Strozzi, T., Ambrosi, C., & Raetzo, H. (2013). Interpretation of aerial photographs and satellite SAR interferometry for the inventory of landslides. *Remote Sensing*, *5*, 2554–2570.

Tachikawa, T., Kaku, M., Iwasaki, A., Gegch, D., Oimoen, M., Zhang, Z., Danielson, J., Krieger, T., Curtis, B., Haase, J., et al. (2011). ASTER global digital elevation model version 2 — summary of validation results. In D. MEYER (Ed.), *Earth Remote Sensing Data Analysis Center (ERSDAC)*.

Takeuchi, Y., Kayastha, R. B., & Nakawo, M. (2000). Characteristics of ablation and heat balance in debris-free and debris-covered areas on Khumbu Glacier, Nepal Himalayas, in the pre-monsoon season. *IAHS Publication*, *53-62*.

Tiwari, R. K., Arora, M. K., & Gupta, R. P. (2014). Comparison of maximum likelihood and knowledge-based classifications of debris cover of glaciers using aster optical-thermal imagery. *Remote Sensing of Environment*. http://dx.doi.org/10.1016/j.rse.2014.10.026.

Townshend, J., Huang, C., Kalluri, S., Defries, R., Liang, S., & Yang, K. (2000). Beware of per-pixel characterization of land cover. *International Journal of Remote Sensing, 21*, 839–843.

Zhang, Y., Fujita, K., Liu, S. Y., Liu, Q., & Nuimura, T. (2011). Distribution of debris thickness and its effect on ice melt at Hailuogou glacier, southeastern Tibetan Plateau, using in situ surveys and ASTER imagery. *Journal of Glaciology, 57*, 1147–1157.

Zongli, J., Shiyin, L., Xin, W., Jian, L., & Sichun, L. (2011). Applying SAR interferometric coherence to outline debris-covered glacier. *Geoinformatics, 2011 19th international conference on, 24–26 June 2011* (pp. 1–4).

Paper II

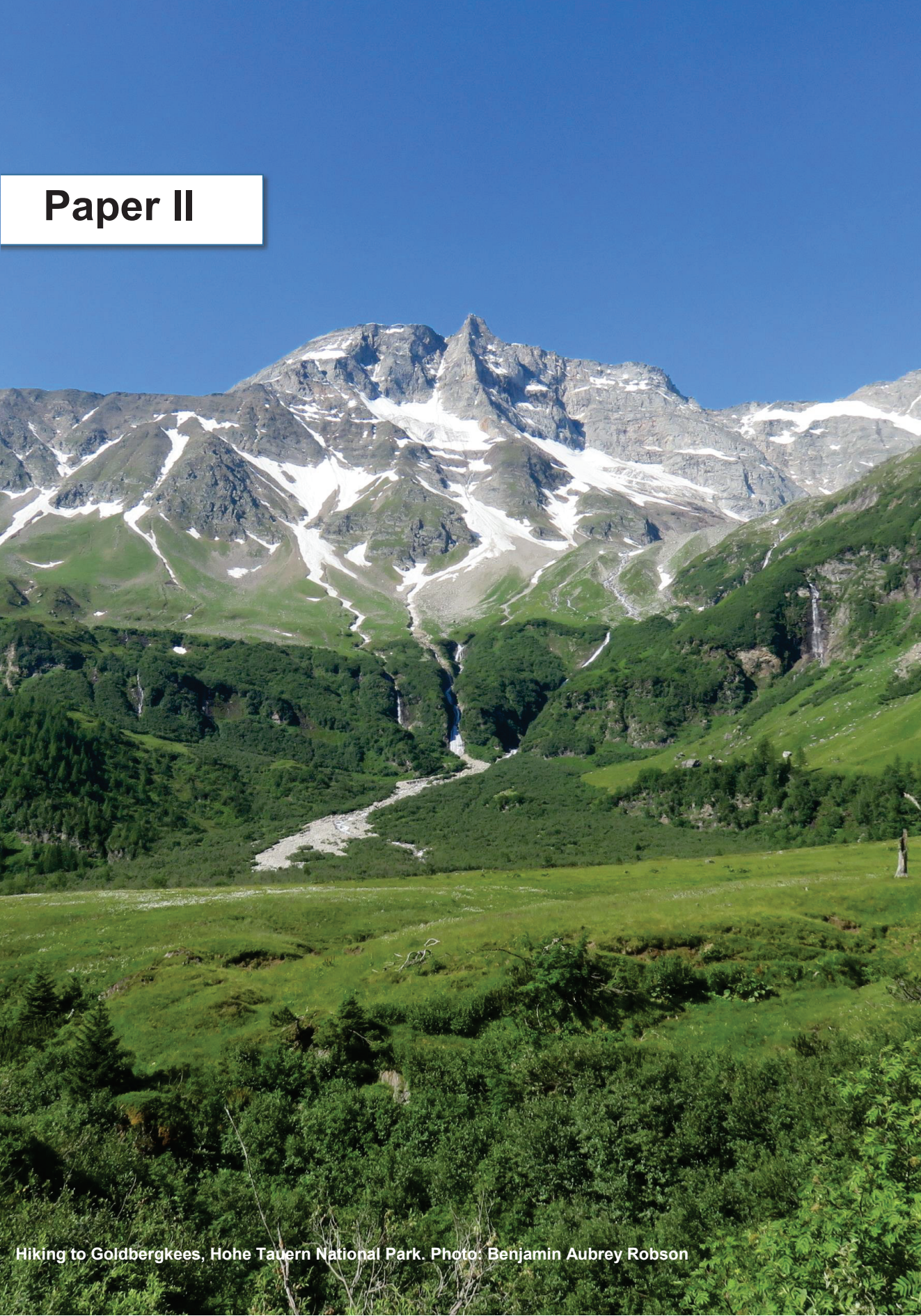

Hiking to Goldbergkees, Hohe Tauern National Park. Photo: Benjamin Aubrey Robson

remote sensing

MDPI

Article

Decadal Scale Changes in Glacier Area in the Hohe Tauern National Park (Austria) Determined by Object-Based Image Analysis

Benjamin Aubrey Robson [1,*], Daniel Hölbling [2], Christopher Nuth [3], Tazio Strozzi [4] and Svein Olaf Dahl [1]

Received: 14 October 2015; Accepted: 12 January 2016; Published: 15 January 2016
Academic Editors: Magaly Koch and Prasad S. Thenkabail

1 Department of Geography, University of Bergen, Fosswinckelsgate 6, Bergen 5007, Norway; svein.dahl@uib.no
2 Department of Geoinfomatics-Z_GIS, University of Salzburg, Schillerstrasse 30, Salzburg 5020, Austria; daniel.hoelbling@sbg.ac.at
3 Department of Geosciences, University of Oslo, Postboks 1047 Blindern, Oslo 0316, Norway; christopher.nuth@geo.uio.no
4 GAMMA Remote Sensing, Worbstr. 225, Gümligen 3073, Switzerland; strozzi@gamma-rs.ch
* Correspondence: benjamin.robson@uib.no; Tel.: +47-5558-3077

Abstract: In this paper, we semi-automatically classify clean and debris-covered ice for 145 glaciers within Hohe Tauern National Park in the Austrian Alps for the years 1985, 2003, and 2013. We also map the end-summer transient snowline (TSL), which approximates the annual Equilibrium Line Altitude (ELA). By comparing our results with the Austrian Glacier Inventories from 1969 and 1998, we calculate a mean reduction in glacier area of 33% between 1969 and 2013. The total ice area reduced at a mean rate of 1.4 km^2 per year. This TSL rose by 92 m between 1985 and 2013 to an altitude of 3005 m. Despite some limitations, such as some seasonal snow being present at higher elevations, as well as uncertainties related to the range of years that the LiDAR DEM was collected, our results show that the glaciers within Hohe Tauern National Park conform to the heavy shrinkage experienced in other areas of the European Alps. Moreover, we believe that Object-Based Image Analysis (OBIA) is a promising methodology for future glacier mapping.

Keywords: glacier mapping; OBIA; landsat; change detection; Alps; snowline; classification

1. Introduction

Glacier change is among the best natural indicators of climate change [1]. The European Alps have undergone a sharp decline in glacier area in recent decades [2–4] which can impact runoff [5], hydro-electric power production [6], hazards such as rockfalls and debris flows [7], and tourism [8]. Due to the time-consuming nature of carrying out *in situ* glacier measurements, many recent studies have opted for remotely sensed data to assess changes in glacier area [9], volume [10], and velocity [11] over various portions of the European Alps. Remote sensing data, such as satellite images, allow glacier area changes to be quantified at the regional scale, often using semi-automated methods. The strong spectral signature of clean ice makes it easy to identify in the Near-Infrared (NIR) and Shortwave-Infrared (SWIR) portions of the electromagnetic spectrum [12]. Band ratios and spectral indices that use the NIR and SWIR spectral bands, such as the Normalized Difference Snow Index (NDSI), are therefore well suited for semi-automatic mapping of clean ice, and have been used extensively in the European Alps [4,13,14]. Clean ice reflects 25%–35% less visible radiation than fresh snow, thereby allowing the end-of-season snowline or transient snowline (TSL) to be mapped [15].

The TSL can be used as an approximation of the equilibrium line altitude (ELA), the altitude on the glacier where the rate of accumulation equals the rate of ablation. The ELA is often used as a proxy for glacier mass balance, so by mapping the TSL on a regional scale, information about the health of the glaciers can be extracted [16]. The Global Land Ice Measurements from Space (GLIMS) initiative aims to provide a framework for assessing glacier changes using remotely sensed data, and to construct a global glacier inventory containing, among other information, data about the glacier size, the elevation of the TSL and the presence of supraglacial debris.

Debris-covered ice (rockfall and avalanche material overlaying the glacier ice) remains a problem in automated glacier mappings. The spectral similarity of supraglacial debris to the surrounding terrain inhibits mapping debris-covered ice automatically by using only spectral information. Auxiliary data such as thermal [17], morphological, [18] or coherence images between two Synthetic Aperture Radar (SAR) images (henceforth referred to as SAR coherence data) [19,20] must therefore be used in classifications. The mapping of debris-covered ice mostly requires manual mapping or correction and, as such, takes up a significant amount of time and effort in glacier mapping. Object-Based Image Analysis (OBIA) is a relatively new and emerging methodology within Geographic Information Systems Science or GIScience [21]. By working at the object level instead of the pixel level (PBIA or Pixel-Based Image Analysis), additional information such as spatial, contextual, hierarchical or textural information can be used to assign objects to classes. OBIA also permits the handling of multiple datasets (for example optical, topographic, SAR, vector) for classifying objects.

Little work to date has been done using OBIA to map glaciers. Rastner *et al.* [22] obtained very high (94.5% and 98.6%) accuracies working in the clean ice regions of the Canadian Coast Mountains and Greenland, respectively. The authors concluded that OBIA offered more advantages for applications on debris-covered glaciers than on clean ice. The studies that have used OBIA for glacier mapping have often focused on the delineation of debris-covered glaciers. Rastner *et al.* [22] obtained an accuracy of 88.5% in the Everest Region of Nepal. Robson *et al.* [20] used SAR coherence data in combination with optical and topographic data to map glaciers in the Manaslu Region of Nepal to an accuracy of 91%. The International Centre for Integrated Mountain Development (ICIMOD) used OBIA to assess decadal changes in Nepal [23] and Bhutan [24], as well as to map glaciers over the entire Himalayas [25]. The only time OBIA has been used in the European Alps was by Eisank *et al.* [26], who solely used the surface curvature to delineate cirque glaciers. To date, no work has been conducted performing multi-temporal OBIA classifications to assess glacier change over time.

Two glacier inventories have been conducted in Austria, both based on aerial photography from 1969 (henceforth referred to as AGI_1969) and 1996–2002 (with most images acquired in 1997 and 1998, henceforth referred to as AGI_1998) [27]. A 17% decrease in glacier area occurred between the two inventories [9]. LiDAR campaigns over the Austrian Alps were conducted between 2006 and 2013 by the regional governments [28–30]. The LiDAR dataset covers a range of years that has been collated together. This is clearly a source of error and is discussed in Section 5.3.

Several authors have calculated glacier area changes by using the Austrian Glacier Inventories, LiDAR data, or additional data. A change in glacier area of 8.2% was found for glaciers in the Ötztal Alps between the LiDAR data (acquired in this case in 2006) and AGI_1998 [31] while Schicker [32] used Landsat Thematic Mapper (TM) data to find an accelerating shrinkage of glaciers (13.3% between 1969 and 1985 and 21.8% between 1997 and 2003) for the Stubai Alps. Paul *et al.* [4] used 10 Landsat TM scenes to map glacier ice over the entire European Alps which was then submitted to GLIMS. Due to inconsistencies such as the interpretation of snow patches, no change assessment with the two previous Austrian Glacier Inventories could be conducted; however, a difference of 30% or 2% per year was found when the 2003 data were compared to the World Glacier Inventory (WGI) data from 1970 $\pm$ 15 years.

In this paper, we combine Landsat 5 and Landsat 8 imagery with a LiDAR-based DEM to map glacier outlines and transient snowlines in the Hohe Tauern National Park, Austria, for the years 1985, 2003, and 2013 and assess the change. The Austrian Glacier Inventories from 1969 and 1998 were

also used for comparison. We evaluate the potential of using high-resolution topographic data within OBIA to semi-automatically delineate debris-covered ice based on breaks in the surface morphology. Lastly, we create manually corrected glacier outlines with reference to the LiDAR DEM, SAR coherence data, and the change in surface elevation between the LiDAR DEM and the SRTM (Shuttle Radar Topography Mission). The SRTM DEM is a near-global (56° S to 60° N) elevation model acquired using the Space Shuttle Endeavour in February 2000 [33]. The SRTM1 product can be downloaded for free from the USGS Earth Explorer (earthexplorer.usgs.gov) and offers a spatial resolution of 1 arc-second (approximately 30 m).

The objectives of this paper are two-fold:

(1) To semi-automatically assess the changes in glacier area in Hohe Tauern National Park in the Austrian Alps by using Object-Based Image Analysis (OBIA).

(2) To assess the potential of using high resolution topographic data to detect debris-covered ice by using edge detection of the surface slope. Although debris-covered ice is not of a major concern in the Austrian Alps, other glacierized regions such as the Himalayas contain considerable amounts of debris-covered ice and, as such, any semi-automatic methods would be beneficial for estimating ice reserves and assessing glacier change.

2. Study Area and Data Used

Hohe Tauern National Park (HTNP) covers approximately 1800 km^2 between the federal states of Carinthia, Salzburg and Tyrol in western Austria (Figure 1). Approximately 10% (125 km^2) of HTNP is covered by glaciers [3], ranging in altitude from 2000 to 3600 m with the majority of glaciers situated between 2700 and 3100 m. The glaciers present are a mixture of clean ice and debris-covered glaciers. HTNP includes the Pasterze Glacier (17.6 km^2) (Figure 2), the largest glacier in the Austrian Alps; 1.2 km^2 of the Pasterzr Glacier is covered by supraglacial debris which reaches 47 cm in thickness towards the glacier terminus [34]. The majority of Austrian glaciers are less than 1 km^2 and only five glaciers in the country are larger than 10 km^2 [27]. Glaciers in the Austrian Alps can exist above ~2080 m, and sometimes at lower elevations due to higher-than-average accumulation primarily because of leeward accumulation caused by wind, or due to supraglacial debris insulating the underlying ice [8].

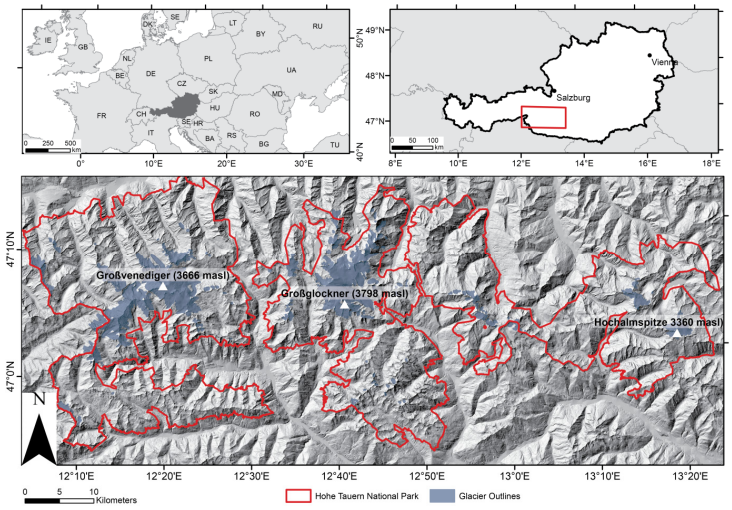

Figure 1. Location map of Hohe Tauern National Park (HTNP) within Austria.

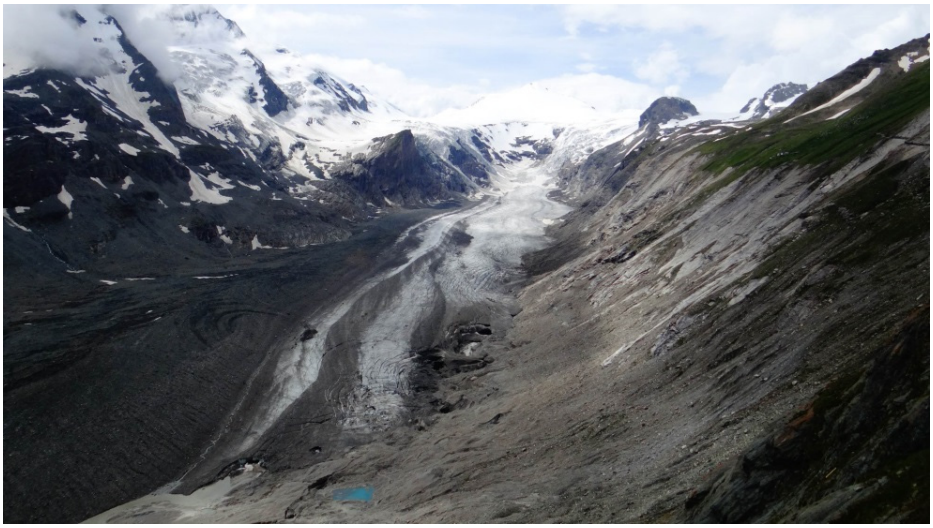

Figure 2. Pasterze Glacier, the largest glacier in Austria. Pasterze Glacier contains significant debris cover on the southern part of the glacier tongue. Photo: Hanna Siiki.

The climate in the Alps has changed considerably over the past decades [35]. The annual mean temperatures in the Greater Alpine Region have risen by about twice as much compared to average global warming or the average rise in the northern hemisphere since the late 19th century [36]. For example, the Sonnblick Observatory (3106 m a.s.l.) in the HTNP, which is the highest observatory in the world that is operated throughout the year, recorded an increase of approximately 2 °C since 1887 [37]. A major indicator of climate change in the Alps is the shrinkage and loss of volume of alpine glaciers with short response times [38].

One hundred and forty-five glaciers in HTNP were selected from the 1969 Austrian Glacier Inventory to assess glacier change; this was done to exclude snow patches and very small glaciers that were found in the AGI_1969. In total this represented 181 km^2 of the 207 km^2 (88%) of ice present in HTNP in 1969.

The data used in this study (Table 1) comprise three Landsat scenes from the end of the ablation season (late August/early September) of 1985, 2003, and 2013 as well as a LiDAR-derived DEM from between 2006 and 2013 resampled to 10 m resolution, which is freely available from the geodata portal of Austria (www.geoland.at). Although it could have been possible to obtain a 1 m DEM from this data, it is uncertain whether this large amount of data would have been stable within the eCognition software and it was unlikely to produce significantly better results. Ideally, DEM data from each time period would have been used in the classification. The SRTM DEM was available from February 2000, but it was found that the morphology of the glacier termini was not sufficiently prominent in the elevation model. This is suggested to be the result of the coarser 30 m resolution, meaning that a glacier of 500–600 m width would be only ~15 pixels, as well as the acquisition being in the accumulation season, when the glacier is more likely covered by snow. The LiDAR-derived DEM was therefore used as the elevation source for all three classifications as well as for generating the topographic derivatives (slope, curvature and aspect). The implications of this are discussed in Section 5.3. The change in elevation between the LiDAR DEM and the SRTM was used as a reference when manually correcting the 2013 outlines, along with an ALOS PALSAR coherence image (see Section 3.3). InSAR coherence data (commonly referred to in the literature simply as SAR coherence data) is an image generated from a pair of SAR images with a short interval between acquisitions. In our case we used two ALOS PALSAR images separated by approximately two weeks. The interferometric coherence between the

image pairs is used to determine which areas have undergone a change in surface conditions or motion, and which areas have been stable. This has been used by others to delineate where debris-covered ice is found [19,20].

Table 1. Data used in this study.

Scene ID	Date	Sensor	Resolution (m)
LC81920272013247LGN00	4 September 2013	Landsat 8	30 (15 pan-sharp)
LT51920272003236MTI01	24 August 2003	Landsat 5	30
LT51920271985234KIS00	22 August 1985	Landsat 5	30
	2006–2013	LiDAR	10
SRTM1N47E012V3	11 February 2000	SRTM	30
Track 637 Frame 930	01 July 2007	ALOS PALSAR	16 m × 13 m, geo-coded to 1 arc-second (~30 m)
Track 637 Frame 930	16 August 2007	ALOS PALSAR	16 m × 13 m, geo-coded to 1 arc-second (~30 m)

We used the SAR coherence data from 2007 only for data verification for two reasons: (1) because the size of glaciers in the Austrian Alps compared to the Himalayas makes SAR coherence data less suitable; and (2) we wanted to focus on assessing the potential of solely using high-resolution topographic data to classify debris covered ice based on the surface morphology.

3. Methods

Three classifications were performed within Trimble eCognition 9.0 for the years 1985, 2003 and 2013. Before analysis, all data were re-projected to UTM zone 33N. Image segmentation is one of the most critical stages in OBIA. As such, time was taken to find suitable segmentation parameters based on statistical pre-evaluations; this was done with the help of the Estimation of Scale Parameter 2 (ESP 2) tool [39]. In addition to choosing what datasets should be used to segment the data and create objects, scale, shape and compactness parameters are also specified. Within the multiresolution segmentation in eCognition, the scale parameter determines the size of the segmented image objects, the shape parameter dictates the relative importance of the shape versus the color/pixel values (calculated from the perimeter divided by four times the square root of the area) while the compactness decides how compact or smooth the final objects should be. eCognition calculates the compactness as the length and width divided by the area [40].

Running multiple hierarchical multiresolution segmentations was found to help group non-glacier objects together (Figure 3). Two segmentations were run before clean ice was classified, while an additional segmentation to create larger objects was performed before classifying debris-covered ice (see Table 2). The transient snowline (TSL) was mapped using a spectral difference segmentation performed on the second segmentation level (Table 2). A compact ruleset was applied that assigned objects to the classes of snow, clean ice or debris-covered ice. In order to account for the differences in bit depth between the Landsat 5 (8 bit–256 values) and Landsat 8 images (16 bit–65536 values), the thresholds for classifications had to be altered slightly. This was particularly important for thresholds for singular spectral bands, such as the red channel being used to map debris-covered ice. Fuzzy thresholds help alleviate this problem. Following image segmentation, objects were classified. This was done by assigning thresholds and fuzzy thresholds to the different classes, as detailed below.

Table 2. Parameters used in image segmentation. The clean ice was classified at level 2, the TSL was classified at level 2B, debris-covered ice was classified at level 3.

Segmentation Level	Scale Parameter	Shape	Compactness	Bands Used	Purpose
1	3 (5 *)	0.3	0.6	Blue, Green, NIR, Red, Slope, SWIR 1, SWIR 2, Thermal	Input for level 2
2	5 (8 *)	0.8	0.6	Blue, Green, NIR, Red, Slope, SWIR 1, SWIR 2, Thermal	Classifying clean Ice
2B	Maximum spectral difference = 10	n/a	n/a	NIR	Classifying transient snowline
3	10 (12 *)	0.25	0.5	NIR, Red, Slope, NDVI, canny edge detection (slope) **	Classifying debris covered Ice

*—Due to the increased bit depth, the scale parameter had to be increased for Landsat 8; **—As the topographic data did not correspond well to the 1985 data, the edge detection was not included in this classification.

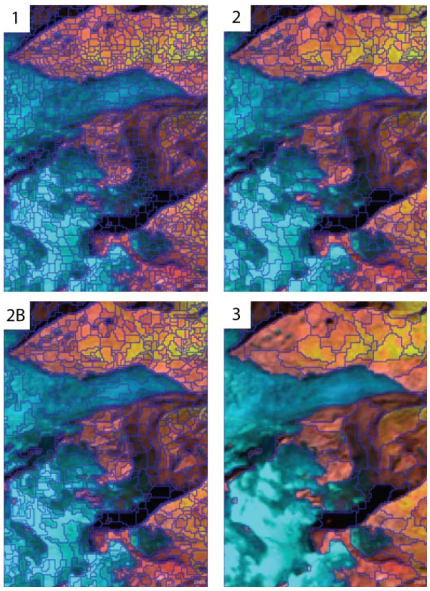

Figure 3. An illustration of the four segmentation levels within eCognition that were used within the classification procedure. An overview of each level and what it was used for is given in Table 2.

3.1. Clean Ice and Transient Snowline (TSL)

Clean ice was classified based on the following rules outlined below. Literature was used to select thresholds and is given when applicable; in other cases, the thresholds were found by trial and error. Note that many thresholds are fuzzy thresholds, and therefore contain a range of values (denoted with a dash). For example ⩾1.4–2 means objects were classified if they had values greater than 2, although if other criteria were met, objects with values between 2 and 1.4 were also considered. This allowed a degree of flexibility with the classification procedure.

- NIR/SWIR1 ratio ⩾1.4–2 (after [41,42])
- The Normalized Difference Snow Index (NDSI) with a threshold of ⩾−0.05–0.1 (after [43])

- The Normalized Difference Water Index (NDWI) with a threshold <0.15–0.4. It has been highlighted by others that turbid proglacial meltwater can be misclassified as clean ice (for example [4]), and the NDWI was therefore used to exclude proglacial lakes.
- Constraints of altitude of ⩾2000 m and an upper threshold for the slope between 40° and 60°.

    - The classified image objects that bordered each other were then merged and clean ice smaller than 0.02 km^2 was removed from the classification.

Before the TSL could be classified, a spectral difference segmentation was performed. In this process, image objects already classified as clean ice were merged based on the similarity in spectral values (in this case the NIR spectral band), provided that neighboring objects did not vary in NIR reflectance by more than 10 (or 1000 for Landsat 8). The image objects then roughly corresponded to the boundary between snow and clean ice. It was found that the boundary between snow and ice was clearly visible using a false color composite image of the SWIR1, NIR and Red bands. An intensity image for these three bands was therefore generated with values ranging from 0 to 1. A threshold of 0.5 (or 0.38 for Landsat 8) was used to separate snow from clean ice.

3.2. Debris-Covered Ice

Due to the spectral similarity of debris-covered ice to the surrounding terrain, the classification procedure could not rely solely on spectral information. Instead, a combination of topographic parameters from the LiDAR DEM as well as the thermal band was used to delineate debris-covered ice. A canny edge detection process was used on the surface slope (Figure 4), which helped highlight where a break in the surface morphology occurred. This edge detection layer was then used in the segmentation when creating object level 3. The resulting image objects were then classified with a combination of fixed thresholds and fuzzy thresholds.

- −0.05–0 ⩽ NDVI values ⩽0.01–0.03. The NDVI has been used by others to take advantage of the fact that debris-covered ice typically has less vegetation than the surrounding non-glacierized terrain (for example [24]).
- Red channel ⩽59 (in the case of Landsat 8, 11000 was used). This was found to be useful in excluding some paraglacial slopes.
- An upper threshold of the slope between 12° and 20°. Surface slope has been extensively used to delineate debris-covered ice, with a threshold of 20° being used previously in the European Alps (for example, see [18])
- Thermal band ⩽12 °C. The thermal signature has often been used to differentiate debris-covered ice (for example, see [17]). The strength of the thermal signature is, however, highly dependent on the thickness and distribution of the glacier debris [44] and care should be taken to not overly rely on the thermal signature. For this reason it was an advantage to include the thermal band as a fuzzy membership function. That way objects that met all other criteria yet did not have a distinct thermal signature could still be considered debris-covered ice.
- Normalized Difference Water Index (NDWI) ⩾−0.03. A threshold in the NDWI was included to exclude marginal glacial lakes from the classification.

The classification was then expanded into neighboring objects (⩾80% shared border) that had a temperature of ⩽10 °C, or objects within 50 m of clean ice and 800 m from debris-covered ice that were spectrally similar and that had slopes of 20°–30°. Image objects that were initially classified as debris-covered ice but that did not border clean ice were then removed. Clean ice and debris-covered ice were finally combined into one class and any objects smaller than 0.1 km^2 or with very irregular shapes (compactness of objects ⩾2.5) were removed, although during manual corrections some small glaciers that were present in the reference datasets were included.

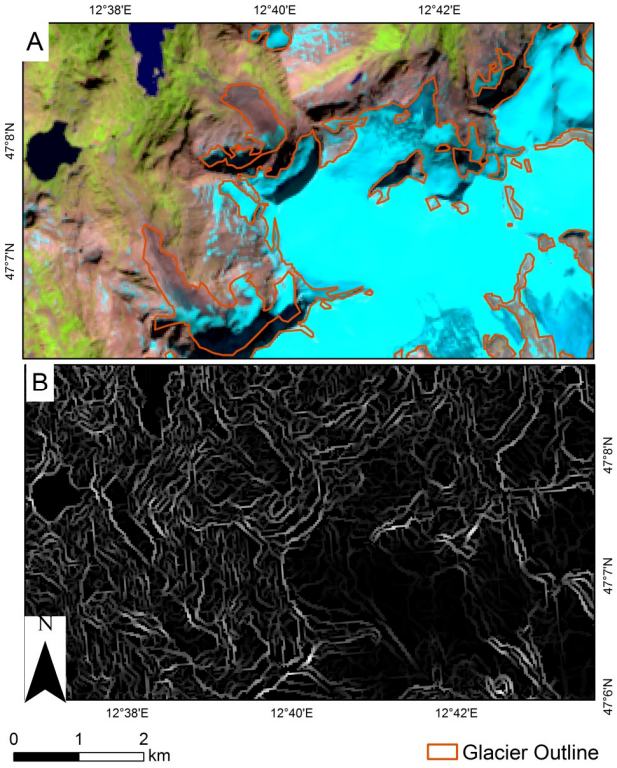

Figure 4. Edge detection on the LiDAR-derived DEM was effective for identifying debris-covered termini based on a break in surface morphology. (**A**) Shows the Landsat 2013 image with glacier outlines overlaid; (**B**) shows the edge detection dataset. It can be seen that the edge detection can be used in helping delineate the extent of debris-covered ice. The glacier outlines shown are the manually corrected 2013 outlines (2013_Man).

3.3. Post-Processing

The glacier outlines were smoothed using pixel-based growing and shrinking tools within eCognition before being exported as shapefiles. The glacier outlines were then divided by their drainage divides; the same drainage divides as the AGI were used to maintain consistency. Individual glacier shapefiles from the three OBIA classifications (1985_OBIA, 2003_OBIA and 2013_OBIA) were then compared with the AGI data from 1969 and 1998.

3.4. Manual Delineation and Accuracy Assessment

The reference glacier outlines available through GLIMS were dated from images acquired in 2003. Hence, in order to assess the accuracy of the OBIA_2013 outlines, it was necessary to create a set of manually corrected outlines (2013_Man) that were assumed to be "truth." These outlines were created with the aid of different data sources (Figure 5), namely Google Earth imagery, SAR coherence data, the profile curvature and hillshade models from the LiDAR DEM, and the difference in elevation between the LiDAR DEM and the SRTM DEM (henceforth referred to as difference in elevation, or ΔH). The comparison between these two DEMs meant that the spatial resolution of the LiDAR DEM (10 m) had to be reduced to the spatial resolution of the SRTM (30 m). This understandably results in a loss of information; however, since ΔH was only used for visual analysis and not quantitatively,

we do not consider this a particular problem. The reason for using ΔH was that glacier ice, even if debris-covered, is recognizable from the surrounding terrain by a change in surface elevation [42].

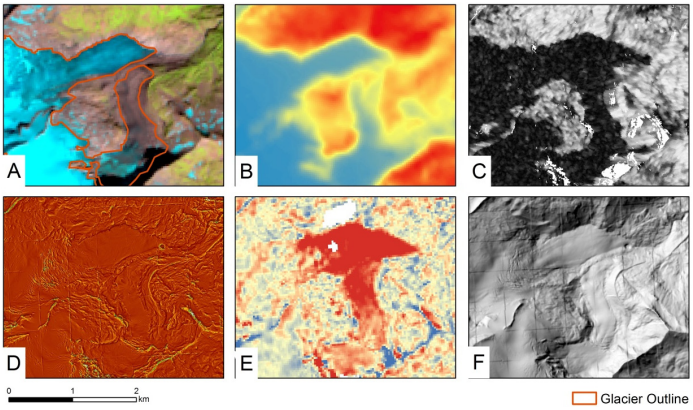

Figure 5. The glacier outlines (**A**) were manually corrected with reference to thermal data (**B**); SAR coherence data (**C**); the profile curvature (**D**); difference in elevation between 2000 and 2006 (**E**); and a hillshade model (**F**).

We evaluated the accuracy of our classifications in two ways. Firstly, we calculated simple percentage deviations (between OBIA_2003 and 2003_GLIMS, and OBIA_2013 and Man_2013 respectively). Although this is not a highly sophisticated method for assessing the accuracy of an image classification, it is widely used within the field of glaciology (for example [18,45]). In addition we assessed the accuracy using a confusion matrix following the methodology described by [46]. Ten thousand random points were generated within the HTNP and were assigned to either be "glacier" or "non-glacier" using the 2013_Man outlines. These points were then compared with the OBIA_2013 results and the following error terms were determined:

- User's accuracy—This is an error of commission and shows the percentage of the final classification that was a glacier.
- Producer's accuracy—This is an error of omission and describes the percentage of actual glacier area that was successfully classified.
- Overall accuracy—This considers both the user's accuracy and the producer's accuracy and shows the percentage of points that were correctly classified.
- Kappa coefficient—This is a measure of agreement between the classifications and the ground truth pixels, and of the classification not being due to random chance [47].

4. Results of Glacier Mapping

A total of 145 glaciers were mapped, representing 88% of the ice within HTNP in 1969. The results of the mapping are shown in Table S1. The most recent classification (OBIA_2013) contains 120 km^2 of ice. The average glacier size was 0.22 km^2 with 33 glaciers (23% of total) being larger than 1 km^2 and three glaciers (2%) being larger than 5 km^2. Supraglacial debris is present on four glaciers, most prominently on the Pasterze Glacier (1.1 km^2) and Schlaten Kees Glacier (0.95 km^2).

4.1. Decadal-Scale Changes in Glacier Area

Between AGI_1969 and OBIA_1985 there was a 3% decrease in glacier area from 181 km^2 to 175 km^2 with a mean loss of 0.4 $km^2 \cdot a^{-1}$. This rate of glacier loss increased to 1.2 $km^2 \cdot a^{-1}$ between OBIA_1985 and AGI_1998 as the total glacier area decreased by a further 9% to 160 km^2. An increase

in the rate of glacier shrinkage happened between AGI_1998 and OBIA_2003, when the glacier area was reduced by a further 28% to 115 km^2 at a rate of 8.9 km$^2 \cdot$ a^{-1}. In total this accounts for a loss in glaciated area of 36% since 1969. Between OBIA_2003 and OBIA_2013, a growth of 5% (9 km^2) was observed at a rate of 0.6 km$^2 \cdot$ a^{-1}. This is discussed in Section 5.1. In 1969, 69% of glaciers were smaller than 1 km^2, and this had increased to 80% by 2013 (Figure 6). Between 1969 and 2013, the glaciers in the HTNP lost a total of 60.4 km^2 (33%) of the glacier area at a mean rate of 1.4 km^2 per year within the HTNP. Between 1985 and 2013, the glacier area reduced by 54.6 km^2 (31%) (Figures 7–10).

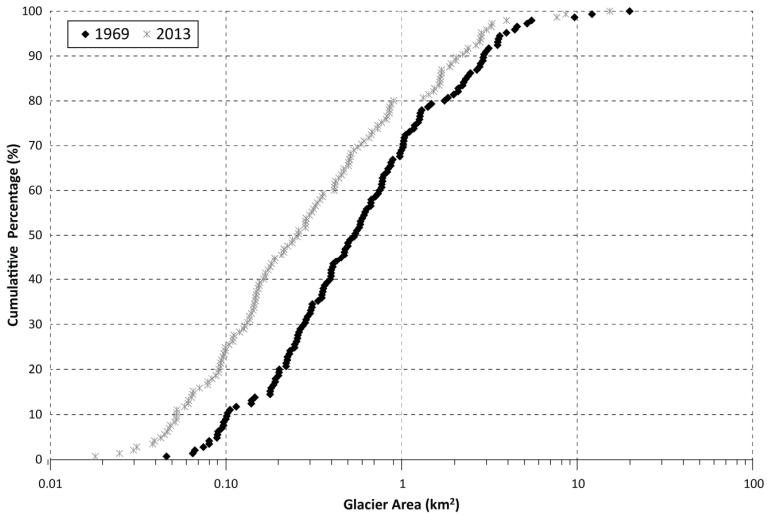

Figure 6. A cumulative distribution graph of the total glacier area against the size of individual glaciers in 1969 and 2013. Note that the x-axis is logarithmic.

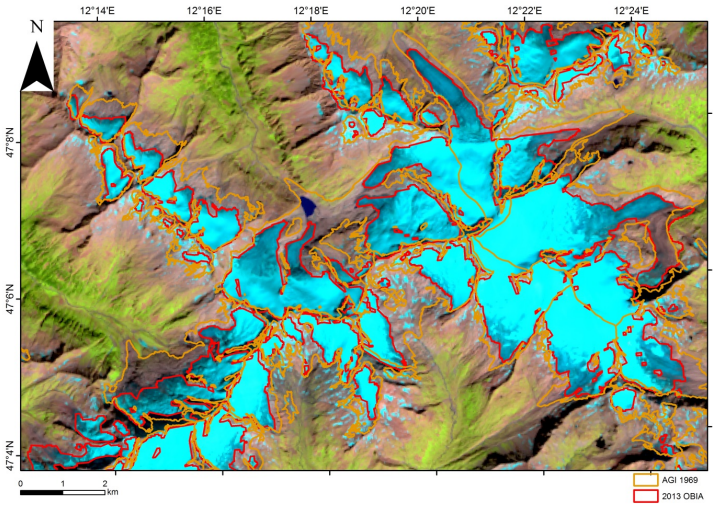

Figure 7. Total glacier area change between 1969 and 2013 over Schlaten Kees, Untersulzbach Kees, Viltragen Kees and Obersulzbach Kees. The background image is a false color (SWIR1, NIR, Red) Landsat image in order to help highlight snow and ice.

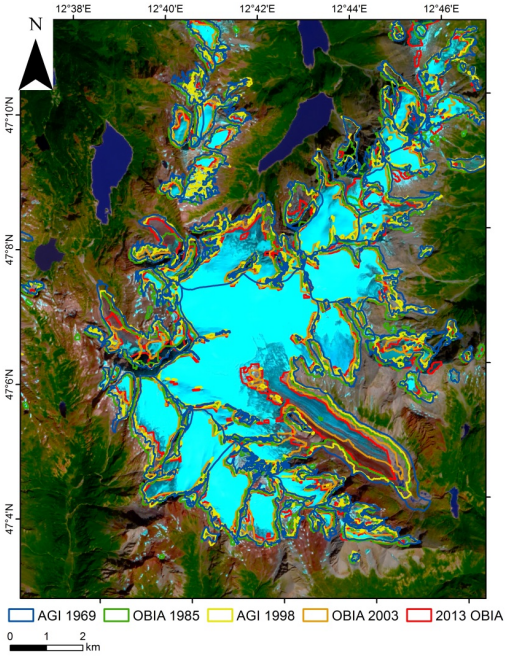

Figure 8. Decadal changes around Großglockner, including the largest glacier in Austria, the Pasterze Glacier, which includes a heavily debris-covered glacier tongue. The background image is a false color (SWIR1, NIR, Red) Landsat image in order to help highlight snow and ice.

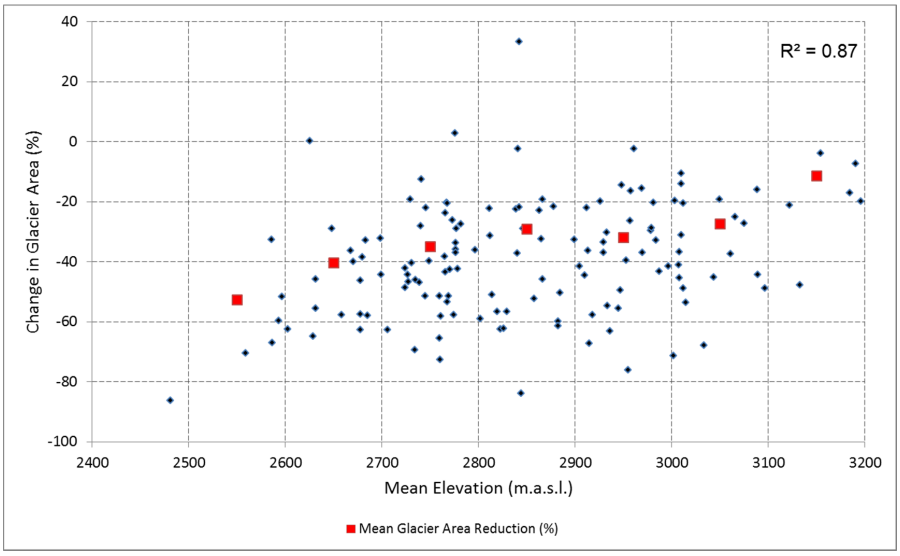

Figure 9. Percentage change in glacier area between 1969 and 2013 against mean glacier elevation.

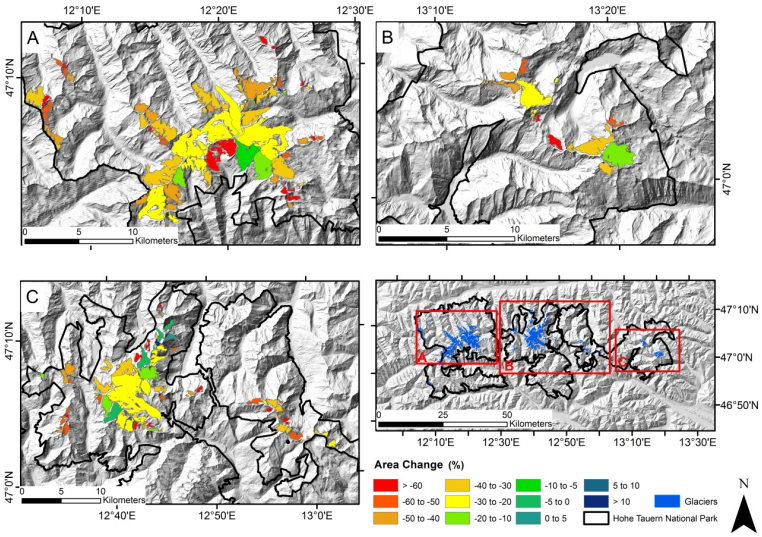

Figure 10. Percentage area change between 1969 and 2013 for individual glaciers within Western (**A**); Central (**B**); and Eastern (**C**) portions of the Hohe Tauern National Park.

Some relationship exists between mean glacier altitude and the change in glacier area (R^2 = 0.87), with glaciers at lower altitudes losing larger proportions of their area than glaciers lying at higher altitudes (as shown in Table S2 and Figure 9). The 16 glaciers with mean altitudes of <2600 m lost, on average, 53% of their area between 1969 and 2013, compared to the 29 glaciers between 3000 and 3100 m or the six glaciers higher than 3100 m which lost, respectively, 27% and 12% of their area. Three of these glaciers appeared to have grown in size. These snow patches (<0.08 km^2) are, however, located at relatively high altitudes, indicating that these area growths are most likely artefacts of seasonal snow. Smaller glaciers lost, on average, a greater proportion of area relative to their size than larger glaciers (R^2 = 0.60) (see Table S3 and Figure 11). The 69 glaciers with sizes <0.5 km^2 lost, on average, 55% of their area between 1969 and 2013, although there is a large spread in the data. Three glaciers lost >75% of their area (IDs: 5070 (Klockerin Kees), 6063 (Mailfrosnitz Kees) and 6052 (Dorfer Kees)). One glacier remained at a constant area (5058 (Walcher Kees)), while three underwent expansions of between 3% and 33% (IDs: 5056 (Sandboden Kees), 5068 (Kaindl Kees) and 6082)). Glaciers that were between 5 and 10 km^2 and >10 km^2, in contrast, lost an average of 25% and 24% of their areas, respectively. Glaciers which had a mean aspect towards the west-northwest (WNW) and south-southeast (SSE) lost slightly more area than glaciers facing in other directions (Table S4 and Figure 12). The difference, however, is not especially prominent at the regional level where glacier losses are more apparent on smaller glaciers, regardless of aspect (Figure 10).

It is hard to assign any general trends to how the debris-covered portions of glaciers have changed (Table S5), especially given that the classifications relied partly on one DEM from between 2006 and 2013. Nevertheless, changes to the spectral properties of the debris cover allowed the classification procedure to map some changes in the area of the debris cover. The reliability of these changes is discussed in Section 5.3. Information about the proportion of supraglacial debris is available from the three OBIA classifications, but not from the two AGIs. The five glaciers that have debris cover shrank by a mean of 22%, although the amount of debris cover varied. This is less than the mean reduction of 32% that occurred to glaciers within HTNP. While the amount of debris-covered ice on Ödenwinkel Kees was reduced by 42%, and Obersulzbach Kees lost all of its supraglacial debris, and three glaciers (Schlaten Kees, Unterer Riffl Kees and Pasterze Glacier) experienced an increase in debris-covered ice of 39%, 45% and 22%, respectively. Figures 7, 8 and 10 show the decadal-scale changes.

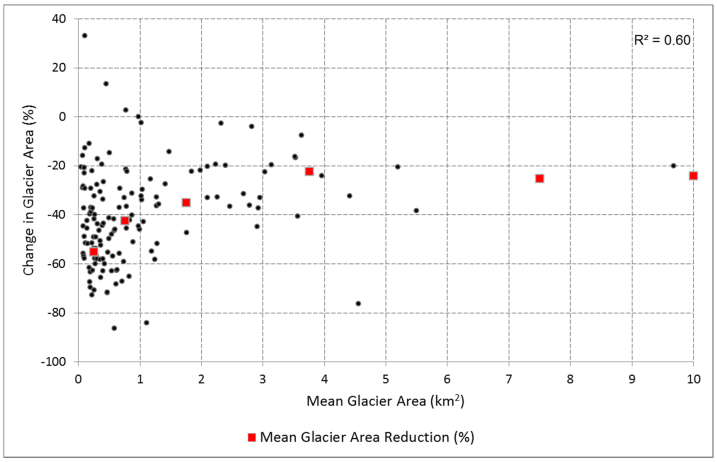

Figure 11. Percentage change in glacier area between 1969 and 2013 against glacier area as of 1969. Note that the two largest glaciers are excluded.

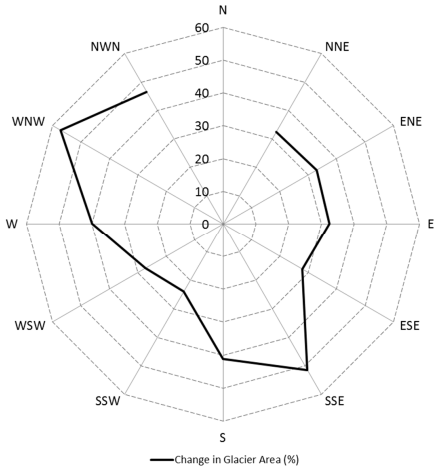

Figure 12. Percentage change in glacier area between 1969 and 2013 against mean glacier aspect. Note that no glaciers had a mean aspect towards the north (345°–15°).

4.2. Change in Transient Snowline Elevation (TSL)

Fifty-seven glaciers were larger than 0.2 km^2 and had the TSL mapped in both the 1985 and 2013 images, 47 of which also had the TSL mapped in the 2003 image. The TSL itself varies considerably over the region (Table S7 and Figure 13). The TSL varies by up to 199 m in elevation across the glaciers on the 1985 image, and up to 108 m on the 2013 image (Figure 14). Glaciers with the highest TSLs are those located on southerly exposed slopes (Table S8 and Figure 14), with glaciers facing the south and south-southwest having mean TSL altitudes in 1985 of 2910 and 2900 m compared with glaciers facing north-northeast (NNE) and north-northwest (NNW) which had altitudes of 2774 and 2814 m, respectively. Note that there is a lack of data on glaciers with a northerly aspect due to shadows. This is further discussed in Section 4.3. Given the variation of TSL elevation within HTNP it is not

straightforward to report changes over the entire region between the three classifications. However, the average altitude of the TSL in 1985 was 2913 m. This increased by an average of 159 m to 3071 m in 2003, leaving very little snow on most of the glaciers before decreasing by 66 m to 3005 m in 2013. In total, this represents a rise of 92 m between 1985 and 2013.

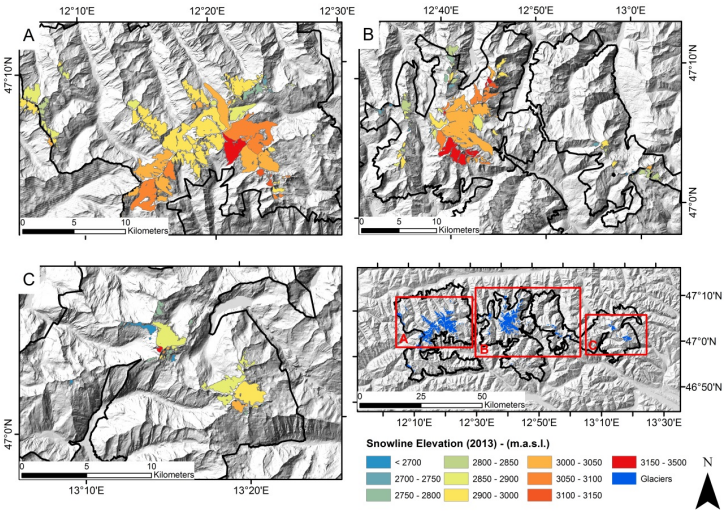

Figure 13. Snowline elevation as mapped for individual glaciers in 2013 within within Western (**A**); Central (**B**); and Eastern (**C**) portions of the Hohe Tauern National Park.

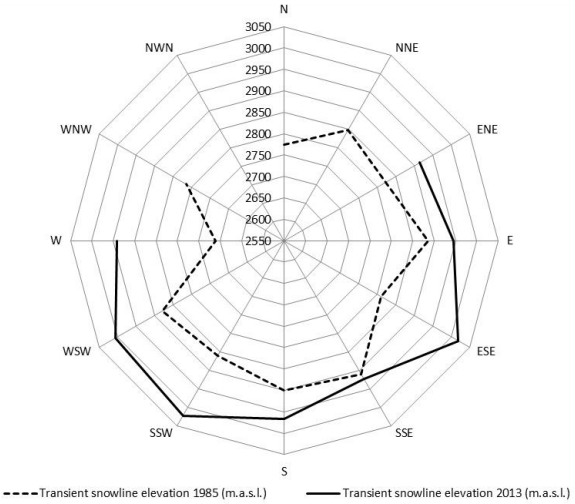

Figure 14. Mapped transient snowlines (TSLs) from 1985 and 2013 against aspect. Note that no snowlines were mapped with NWN aspects in 1985 or NWN and WNW in 1985, and these glaciers were more effected by shadows which masked the TSL.

4.3. Accuracy Assessment

In order to determine the accuracy of our OBIA classifications, we compare our glacier outlines with reference data (Table S6). Our OBIA_2003 outlines were compared with the GLIMS outlines [4], referred to henceforth as GLIMS_2003. OBIA_2013 outlines were compared with manually corrected outlines (2013_Man, Section 3.3). Although in many cases there is no alternative measure to assess classification accuracies, care needs to be taken when basing accuracy assessments on percentage differences to reference data, particularly between different studies that focus on different samples of glaciers. The relative accuracy is dependent on both the size of the glaciers and the total study area. As the study area or number of glaciers being mapped increases, the error term becomes more random and less systematic [45].

By comparing the total mapped ice for the 145 glaciers within HTNP, the OBIA_2003 classifications had an accuracy of 94% compared with GLIMS_2003. Among these, 62% of the glaciers were mapped with an accuracy of >90%, 39% of which were mapped with an accuracy of >95%. There were some glaciers identified in GLIMS_2003 that were not mapped in our classification. This was either due to the glaciers being smaller than the area threshold specified within the OBIA classification procedure, or because of shadows. The OBIA_2013 glacier outlines were mapped to a mean accuracy of 98%, 51% of the glaciers were mapped with an accuracy of >90% and 33% were mapped with an accuracy of >95%. The errors associated with the mapping of these glaciers are mainly caused by shadows and seasonal snow. In these cases these errors could mask changes in glacier area, and manual correction is necessary. For many of the glaciers, though, especially the larger glaciers, the glacier outlines were sufficiently accurate to see changes in glacier area over a decadal scale. It could be, however, that for annual changes in glacier area it is necessary to manually correct glacier outlines for shadow, snow and debris.

We also computed a confusion matrix for assessing the accuracy of OBIA_2013 (Table 3). The high kappa value shows that the classification did not happen due to chance. The user's accuracy shows that there were few false positives (objects mapped as glacier ice that in actuality were not), but the producer's accuracy shows that the classification was affected by false negatives (*i.e.*, glacier ice that was not mapped). This is mostly due to problems such as shadows, seasonal snow, and the difficulty of mapping debris-covered ice.

Table 3. User's accuracy, producer's value and overall accuracy from a confusion matrix. The values were determined for the OBIA classifications of glaciers in 2013, assessed against the manually delineated outlines (Man_2013).

User's Accuracy	Producer's Accuracy	Overall Accuracy	Kappa
94.1	81.6	0.98	0.9

The reference data contained no information that distinguished between clean ice and debris-covered ice. The entire region contained only 2.2 km^2 of glacial debris (1.8% of the total glacierized area). Nevertheless, if 2013_Man is compared to OBIA_2013 for just the debris-covered portions of the glaciers, then a total accuracy of 86.6% can be stated. Although given that just four glaciers had supraglacial debris, we maintain that it is more appropriate to consider the mapping of glacier accuracy over the entire glacier rather than report separate accuracies for clean ice and debris-covered ice. The accuracy of the debris-covered mapping for the 2003 and 1985 classifications is most likely lower than for the 2013 classification, given that the input data (Landsat data and LiDAR DEM) were not temporally consistent. This most likely explains the variations in the depicted debris cover between the three classifications (Table S5). We therefore consider our mapping of glacier debris in 2013 to be a fairly accurate assessment, but have less faith in the temporal trends in the supraglacial debris depicted.

In terms of the accuracy of our time series of decadal-scale change, several error terms must be considered in addition to the classification accuracy. The 2013 image is slightly affected by seasonal snow at higher elevations, which can cause an exaggeration of the glacier extent. Additionally, the 1998 glacier inventory (AGI_1998) is based on images from 1996 to 2002, making it harder to compare to the other results.

The extraction of the TSL altitude relies on the accuracy of the DEM used in extracting the snowline altitude. We used a 10 m DEM derived from LiDAR campaigns between 2006 and 2013 for extracting the snowline elevation for all three classifications. Although it can be assumed since the snowline approximately equals the annual equilibrium line, elevation changes here should be less than in the ablation area, and this needs to be kept in mind when interpreting results. The choice of satellite imagery also impacts the mapping of the TSL. Although the images we used were mostly snow-free, some northern-facing glaciers were obscured by shadows, making it impossible to map the TSL. Without *in situ* data (such as that used by [48] when working on changing snow and ice faces), it is difficult to thoroughly assess the accuracy of the TSL mappings, also if considering the high variability of TSL altitude within HTNP.

5. Discussion

5.1. Area Loss Compared with Other Areas in the European Alps

The glacier losses that we mapped within HTNP have been compared to other studies in the European Alps. It should be noted that small-scale glacier advances have been reported between the 1960s and 1980s [1,49]. It may have been possible to better assess such glacier variations; however, between the available datasets of 1969 and 1985, only a modest reduction in glacier area is visible. Paul *et al.*, (2011) found an approximate reduction in glacier area of 33% over the Austrian, French, Italian and Swiss Alps between 1970 $\pm$ 15 years and 2003. This corresponds well with our results of a decrease in 33% between 1969 and 2003 or 31% between 1985 and 2013. Carturan *et al.* (2013) found a 23.4% $\pm$ 3% reduction in glacier area between 1987 and 2009 in the Ortles-Cevedale Alps of Italy, while Gardent *et al.* (2014) found a 25% reduction in area between the late 1960s and the late 2000s in the French Alps. This is less than the 31% we found between 1985 and 2013.

Abermann *et al.* (2009) found an 8.2% reduction in area between 1997 and 2006 in the Austrian Ötztal Alps, considerably less than the 24% reduction we found between 1998 and 2003. Paul *et al.* (2011) found a reduction of 18% in area for glaciers in the Swiss Alps between 1985 and 1999 [50], double the 9% reduction within HTNP between 1985 and 1998. This shows that there is a large spatial heterogeneity in glacier area response to climate across the European Alps, although an evident trend of a clear reduction in glacier size over the last decades is dominant.

A 5% increase in glacier area is found between 2003 and 2013. We have two explanations for this apparent anomaly. The 2013 image contained some seasonal snow at higher altitudes, and optical satellite imagery struggles to differentiate between snow and ice, so if seasonal snow obscures the glacier margin, automatic methods are prone to misclassify this as glacier growth. Additionally, the summer of 2003 was abnormally hot. The European heatwave of 2003 caused extreme glacier melt in the European Alps at a rate of eight times the long-term average (1960–2000), and double the rate experienced in the 1998 heatwave [51,52].

Pasterze Glacier, the largest glacier in Austria, contains two components, a northern, debris-free part, and a southern, debris-covered part [53]. Our results showed that between 1985 and 2013, the amount of debris cover on the Pasterze Glacier increased by 22% to 1.1 km^2. It should, however, be noted (as discussed in Section 5.3) that without corresponding elevation data, delineating debris-covered ice is difficult. This can lead to some erroneous results, such as the amount of debris in 2003 being less than in 1985 and 2013. Nevertheless, Kellerer-Pirklbauer (2008) found a 40% increase in the amount of debris between 1970 and 2008, which is in line with our findings.

5.2. Use of OBIA for Glacier Mapping

By using OBIA we were able to map 120 km^2 (as of 2013) of glacier ice, including both debris-covered ice and clean ice, semi-automatically. OBIA offered many advantages over PBIA techniques when applied to glacier mapping. Rastner *et al.* [22] highlight how OBIA provides marginally higher (~3%) accuracies for mapping clean ice when compared to PBIA. Accuracy is, however, not the only advantage of OBIA. OBIA allows classes to be defined by multiple characteristics, and this allows, for example, proglacial lakes to be separated from glacier ice (a problem identified by Andreassen *et al.* [54]) by including a classification threshold based on the NDWI in the ruleset. Working at the object level additionally allows some post-processing to be included in the workflow, for example smoothing object boundaries or eliminating some false-positive objects. This allowed snow patches to be removed by size, mean elevation and shape, as well as removing debris-covered ice that is not attached to clean ice. Snow patches can be a problem when comparing classification results with old glacier inventories. OBIA allows the inclusion of vector data, allowing only ice masses that were present in the glacier inventory to be delineated in the classification. This can help reduce the amount of false positives that need to be removed with opportune post-processing.

OBIA offers significantly more advantages when applied to mapping debris-covered ice. Debris-covered ice is difficult to identify based solely on spectral information [55,56], thereby additional data sources such as a DEM or SAR coherence data should be used. OBIA allows these data sources to be combined in the classification procedure. In this study we used the surface morphology, spectral values and thermal properties to identify debris-covered ice. The morphology was used by performing an edge extraction on the surface slope; this edge detection was then used in the segmentation of image objects. This analysis could have been done using PBIA, but edge detection could have only been used as a guide to manual interpretation as opposed to being a component in a semi-automated workflow. Once the ruleset was generated for one scene, it could be applied to other imagery from different dates, although due to changes in the sensor (Landsat 8 *vs.* Landsat 5) or differences in the time of acquisition or scene illumination, small adjustments had to be made to the thresholds used in the classification. The transferability of rulesets highlights the potential for OBIA being used for creating more frequent and consistent glacier inventories.

The accuracy of semi-automated mappings of glacier ice is affected by a number of factors, such as the presence of seasonal snow, shadows or the presence of supraglacial debris [57]. Additionally, given the reported rapid shrinkage of glaciers in the European Alps, the range of years which the LiDAR data were gathered (2006 to 2013) contributes to the uncertainty of mapping the debris-covered glaciers.

The transient snowline proved relatively easy to map due to the spectral difference between bare ice and snow. Distinguishing between bare ice and snow is an established technique [48,58,59]. Our analysis, however, was limited by having just three years' worth of data. Although an overall rise in TSL is observable between 1985 and 2013, three TSL measurements are not sufficient to establish a temporal trend, given the large variability within each image. The 2003 dataset shows almost no snow being left on the glaciers. Although this makes it harder to infer a trend from the three datasets, this augmentation in TSL altitude most likely reflects the unusually hot summer of 2003 where extensive ablation occurred for a prolonged period of time [51]. The snowline varies spatially within HTNP, with glaciers that have a more southern aspect and therefore a higher radiation receipt being characterized by higher snowlines [60]. Care needs to be taken when interpreting snowlines mapped from optical imagery and interpreting them as a proxy for ELA. The mapped snowline is highly affected by the image acquisition date, seasonal snowfalls and shadow [15,58]. It is therefore of great importance that the satellite acquisition occurs as close as possible to the end of the ablation season in order for multiple images to be comparable. The images we used were acquired from the end of August or start of September, so it is likely that further ablation occurred between these dates and the period of first snowfall.

When snowlines are mapped over decadal timescales, then the snowline altitude can be used as a proxy for the ELA or glacier mass balance [61,62]. We, however, do not consider our snowline

time series to be sufficiently long to infer any changes in glacier mass balance. We instead consider our snowline mapping results to demonstrate the potential for semi-automatically delineating the transient snowline from time series of optical satellite images using OBIA.

We believe that OBIA is, therefore, a suitable methodology for semi-automated mapping of glaciers, including the delineation of debris-covered ice and the TSL. Once the classification rulesets had been created in eCognition, it took less than 5 min to fully classify the entire study area. The adjustments needed to adapt the rulesets for the different Landsat sensors took approximately 45 min before the classification could be run again on a different image. The results had an accuracy of 92%, meaning that only minor portions had to be manually edited. Once the classification ruleset has been generated, OBIA offers a method for relatively efficient transferability to other images.

5.3. Topographic Data for Debris-Covered Ice

Topographic data have been widely used to map debris-covered ice by interpreting a change in morphology at the glacier terminus [18,63,64]. To date, however, edge detection has not been used as a processing step within a classification of debris-covered ice. Although the morphology can be used to depict the glacier terminus edge, there is some discussion needed whether what can be detected as a break of topography is active glacier ice, or whether it is stagnant ice. Stagnant ice can become decoupled from the active flowing glacier ice [65]. However, it can still contribute to water resources through melting. There is no clear consensus on whether stagnant glacier ice should be mapped as part of the glacier, although with the exception of perhaps the Pasterze Glacier this is not of major concern in the HTNP, it must be considered when working in areas of significant supraglacial debris such as the Himalayas [66].

Edge detection proved a reliable method to extract the terminus position of debris-covered glacier tongues. Only one DEM dataset derived from LiDAR data acquired between 2007 and 2013 was available, meaning that a change in surface morphology could not be used to delineate changes in debris cover. The DEM was used to assist creating image objects for OBIA_2003 and OBIA_2013, but no DEM was available to correspond with OBIA_1985. This most likely explains the slightly dubious results obtained for the debris-cover mapping, for example the Pasterze Glacier experiencing a decrease and subsequent increase in debris cover. The classification procedure managed to depict changes in supraglacial debris by variations in the spectral values, although ideally each OBIA classification would have had a corresponding DEM in order to map changes in morphology at the glacier terminus. Future LiDAR acquisitions could be used to accurately determine the shrinkage of debris-covered glacier tongues on a multi-temporal basis by incorporating edge detection algorithms within the analysis. It is not possible, however, to differentiate between debris-covered ice and ice-cored moraines by solely using topographic data. It would therefore be advantageous for future work to incorporate either SAR coherence data or surface displacement data derived from feature tracking of multi-temporal satellite images [67].

6. Conclusions

We have demonstrated the use of Object-Based Image Analysis (OBIA) for robust mapping of clean and debris-covered ice within Hohe Tauern National Park, Austria. By comparing our three classifications (OBIA_1985, OBIA_2003 and OBIA_2013) with the two Austrian Glacier Inventories (AGI_1969 and AGI_1998) we have determined the total loss and rate of glacier terminus retreat for 145 glaciers. Mean rates of glacier loss appear to have increased from a mean of 0.4 $km^2 \cdot a^{-1}$ between 1969 and 1985 up to a rate of 8.9 $km^2 \cdot a^{-1}$ between 1998 and 2003, although given the time intervals we are working with, it is difficult to speculate that this represents an acceleration in glacier loss. Our analysis contained only five time periods over a 44-year period, one of which was hampered by seasonal snow. Care therefore needs to be taken in interpreting how the rate of glacier loss has changed over this time. It can be stated, however, that the total area of ice reduced by 33% from 181 km^2 in 1969 to 120 km^2 in 2013. The year 2003 is showed as having a total ice area of 5% less than in 2013 at

115 km^2. We explain this as being due to a combination of some seasonal snow at higher altitudes in the 2013 satellite image and the extreme heat of the summer of 2003.

While clean ice can already be robustly classified using PBIA methods, the inclusion of spatial and contextual information helps remove false positives (such as snow patches or turbid-water) and semi-automatizes post-processing procedures, thereby reducing the amount of manual corrections needed. Additionally, the transferability of rulesets could further the development of semi-automated glacier mapping procedures in other regions of the world.

The mapping of debris-covered ice can be greatly improved by using OBIA. Working at the object level allows topographic as well as spectral and thermal data to be used in combination to delineate debris-covered ice. Contextual and spatial information can be used to remove debris not connected to clean ice, or expand the classification into spectrally similar objects. Additionally, the inclusion of algorithms such as edge detection allow debris-covered ice to be mapped using breaks in surface morphology, building on the work of others [18,63,68].

The future availability of relatively high resolution DEMs, such as the TanDEM-X Global DEM or Sentinel-2 photogrammetric DEMs, could provide possibilities of using more up-to-date topographic data to map debris-covered ice [69,70]. In particular, the use of multi-temporal high-resolution stereo imagery, providing optical imagery and a DEM from the same acquisition, should be explored. Additionally, although we have demonstrated that the use of OBIA in classifying clean ice is efficient and accurate, the process still requires the careful selection of thresholds for band ratios and spectral indices. OBIA allows the use of "automatic thresholds" where a threshold is determined that divides a histogram into two subsets [71,72]. Such an approach has not been utilized within the field of remote sensing glaciology, and has the potential to facilitate a fully automatic workflow for the classification of clean ice. Given the prominent spectral signature of clean ice as opposed to fresh snow, future studies could also map the TSL using automatic thresholds over a long timescale, providing an automatically generated time series of transient snowline fluctuations.

Acknowledgments: Benjamin Robson is especially grateful to Pål Ringkjøb and Henrik Løseth Jansen for many helpful discussions and opinions on different aspects of this paper. Thanks also to the Department of Z_GIS, University of Salzburg who facilitated much of this work. This study was funded by the University of Bergen. This work was partly supported by the Austrian Science Fund (FWF) through the project iSLIDE (FWF-P25446-N29). We are very grateful to NASA and the USGS for free provision of Landsat and SRTM data. We are thankful to the four anonymous reviewers for helpful criticism and guidance that improved this paper significantly.

Author Contributions: Benjamin Robson wrote the manuscript with contributions and feedback from all co-authors. The OBIA Analysis was carried out by Benjamin Robson and Daniel Hölbling with advice and guidance from Christopher Nuth. Tazio Strozzi obtained and processed the ALOS coherence data.

Conflicts of Interest: The authors declare no conflict of interest.

References

1. Zemp, M.; Paul, F.; Hoelze, M.; Haeberli, W. Glacier fluctuations in the European Alps, 1850–2000. *Darkening Peaks Glacier Retreat Sci. Soc.* **2008**. [CrossRef]
2. Fischer, A. Glaciers and climate change: Interpretation of 50 years of direct mass balance of Hintereisferner. *Glob. Planet Chang.* **2010**, *71*, 13–26. [CrossRef]
3. Fischer, M.; Huss, M.; Barboux, C.; Hoelzle, M. The new Swiss Glacier Inventory SGI2010: Relevance of using high-resolution source data in areas dominated by very small glaciers. *Arct. Antarct Alp. Res.* **2014**, *46*, 933–945. [CrossRef]
4. Paul, F.; Frey, H.; le Bris, R. A new glacier inventory for the European Alps from Landsat TM scenes of 2003: Challenges and results. *Ann. Glaciol.* **2011**, *52*, 144–152. [CrossRef]
5. Koboltschnig, G.R.; Schöner, W. The relevance of glacier melt in the water cycle of the Alps: The example of Austria. *Hydrol. Earth Syst. Sci.* **2011**, *15*, 2039–2048. [CrossRef]

6. Schaefli, B.; Hingray, B.; Musy, A. Climate change and hydropower production in the Swiss Alps: Quantification of potential impacts and related modelling uncertainties. *Hydrol. Earth Syst. Sci. Discuss.* **2007**, *11*, 1191–1205. [CrossRef]
7. Chiarle, M.; Iannotti, S.; Mortara, G.; Deline, P. Recent debris flow occurrences associated with glaciers in the Alps. *Glob. Planet Chang.* **2007**, *56*, 123–136. [CrossRef]
8. Abermann, J.; Kuhn, M.; Fischer, A. Climatic controls of glacier distribution and glacier changes in Austria. *Ann. Glaciol.* **2011**, *52*, 83–90. [CrossRef]
9. Lambrecht, A.; Kuhn, M. Glacier changes in the Austrian Alps during the last three decades, derived from the new Austrian glacier inventory. *Ann. Glaciol.* **2007**, *46*, 177–184. [CrossRef]
10. Paul, F.; Haeberli, W. Spatial variability of glacier elevation changes in the Swiss Alps obtained from two digital elevation models. *Geophys. Res. Lett.* **2008**, *35*. [CrossRef]
11. Berthier, E.; Vincent, C. Relative contribution of surface mass-balance and ice-flux changes to the accelerated thinning of Mer de Glace, French Alps, over 1979–2008. *J. Glaciol.* **2012**, *58*, 501–512. [CrossRef]
12. Kääb, A.; Huggel, C.; Paul, F.; Wessels, R.; Raup, B.; Kieffer, H.; Kargel, J. Glacier Monitoring from ASTER Imagery: Accuracy and Applications. In Proceedings of the EARSeL-LISSIG-Workshop Observing Our Cryosphere from Space, Bern, Switzerland, 11–13 March 2002; pp. 43–53.
13. Gardent, M.; Rabatel, A.; Dedieu, J.-P.; Deline, P. Multitemporal glacier inventory of the French Alps from the late 1960s to the late 2000s. *Glob. Planet Chang.* **2014**, *120*, 24–37. [CrossRef]
14. Carturan, L.; Filippi, R.; Seppi, R.; Gabrielli, P.; Notarnicola, C.; Bertoldi, L.; Paul, F.; Rastner, P.; Cazorzi, F.; Dinale, R.; *et al*. Area and volume loss of the glaciers in the Ortles-Cevedale group (Eastern Italian Alps): Controls and imbalance of the remaining glaciers. *Cryosphere* **2013**, *7*, 1339–1359. [CrossRef]
15. Mathieu, R.; Chinn, T.; Fitzharris, B. Detecting the equilibrium-line altitudes of New Zealand glaciers using ASTER satellite images. *N. Z. J. Geol. Geophys.* **2009**, *52*, 209–222. [CrossRef]
16. Chinn, T.J.; Heydenrych, C.; Salinger, M.J. Use of the ELA as a practical method of monitoring glacier response to climate in New Zealand's Southern Alps. *J. Glaciol.* **2005**, *51*, 85–95. [CrossRef]
17. Taschner, S.; Ranzi, R. Comparing the opportunities of Landsat-TM and Aster data for monitoring a debris covered glacier in the Italian Alps within the GLIMS project. In Proceedings of the 2002 IEEE International Geoscience and Remote Sensing Symposium, Toronto, ON, Canada, 24–28 June 2002; pp. 1044–1046.
18. Paul, F.; Huggel, C.; Kaab, A. Combining satellite multispectral image data and a digital elevation model for mapping debris-covered glaciers. *Remote Sens. Environ.* **2004**, *89*, 510–518. [CrossRef]
19. Frey, H.; Paul, F.; Strozzi, T. Compilation of a glacier inventory for the western Himalayas from satellite data: Methods, challenges, and results. *Remote Sens. Environ.* **2012**, *124*, 832–843. [CrossRef]
20. Robson, B.A.; Nuth, C.; Dahl, S.O.; Hölbling, D.; Strozzi, T.; Nielsen, P.R. Automated classification of debris-covered glaciers combining optical, SAR and topographic data in an object-based environment. *Remote Sens. Environ.* **2015**, *170*, 372–387. [CrossRef]
21. Blaschke, T.; Hay, G.J.; Kelly, M.; Lang, S.; Hofmann, P.; Addink, E.; Feitosa, R.Q.; van der Meer, F.; van der Werff, H.; van Coillie, F. Geographic object-based image analysis-towards a new paradigm. *ISPRS J. Photogramm. Remote Sens.* **2014**, *87*, 180–191. [CrossRef] [PubMed]
22. Rastner, P.; Bolch, T.; Notarnicola, C.; Paul, F. A Comparison of Pixel- and Object-Based Glacier Classification With Optical Satellite Images. *IEEE J. STARS* **2014**, *7*, 853–862. [CrossRef]
23. Bajracharya, S.R.; Maharjan, S.B.; Shrestha, F.; Bajracharya, O.R.; Baidya, S. *Glacier Status in Nepal and Decadal Change from 1980 to 2010 Based on Landsat Data*; International Centre for Integrated Mountain Development: Kathmandu, Nepal, 2014.
24. Bajracharya, S.R.; Maharjan, S.B.; Shrestha, F. The status and decadal change of glaciers in Bhutan from the 1980s to 2010 based on satellite data. *Ann. Glaciol.* **2014**, *55*, 159–166. [CrossRef]
25. Bajracharya, S.R.; Shrestha, B. *The Status of Glaciers in the Hindu Kush-Himalayan Region*; International Centre for Integrated Mountain Development (ICIMOD): Kathmandu, Nepal, 2011.
26. Eisank, C.; Drăguţ, L.; Götz, J.; Blaschke, T. Developing a semantic model of glacial landforms for object-based terrain classification—The example of glacial cirques. *GEOBIA* **2010**, *XXXVIII-4/C7*, 1682–1777.
27. Paul, F.; Arnaud, Y.; Ranzi, R.; Rott, H. European Alps. In *Global Land Ice Measurements from Space*; Kargel, J.S., Leonard, G.J., Bishop, M.P., Kääb, A., Raup, B.H., Eds.; Springer: Berlin, Germany; Heidelberg, Germany, 2014; pp. 439–463.

28. Carinthia Regional Government. Digitales Geländemodell (10 m) Kärnten. Available online: http://data.ktn.gv.at/package/digitales-gelaendemodell-10m-kaernten/ (accessed on 14 October 2015).
29. Tirol Regional Government. Digitales Geländemodell Tirol. Available online: https://www.tirol.gv.at/data/datenkatalog/geographie-und-planung/digitales-gelaendemodell-tirol/ (accessed on 28 March 2015).
30. Salzburg Regional Goverment. Status Laserscan Befliegung im Bundesland Salzburg. Available online: http://www.salzburg.gv.at/als-status-jahr_2014_09_05.pdf (accessed on 28 March 2015).
31. Abermann, J.; Lambrecht, A.; Fischer, A.; Kuhn, M. Quantifying changes and trends in glacier area and volume in the Austrian Ötztal Alps (1969–1997–2006). *Cryosphere Discuss.* **2009**, *3*, 415–441. [CrossRef]
32. Schicker, I. *Changes in Area of Stubai Glaciers analysed by means of Satellite Data for the GLIMS Project*; University of Innsbruck: Innsbruck, Austria, 2006.
33. Van Zyl, J.J. The Shuttle Radar Topography Mission (SRTM): A breakthrough in remote sensing of topography. *Acta Astronaut.* **2001**, *48*, 559–565. [CrossRef]
34. Kellerer-Pirklbauer, A. The Supraglacial Debris System at the Pasterze Glacier, Austria: Spatial Distribution, Characteristics and Transport of Debris. *Z. Geomorphol. Suppl. Issues* **2008**, *52*, 3–25. [CrossRef]
35. Gobiet, A.; Kotlarski, S.; Beniston, M.; Heinrich, G.; Rajczak, J.; Stoffel, M. 21st century climate change in the European Alps—A review. *Sci. Total Environ.* **2014**, *493*, 1138–1151. [CrossRef] [PubMed]
36. Auer, I.; Bohm, R.; Jurkovic, A.; Lipa, W.; Orlik, A.; Potzmann, R.; Schoner, W.; Ungersbock, M.; Matulla, C.; Briffa, K. HISTALP-historical instrumental climatological surface time series of the Greater Alpine Region. *Int. J. Climatol.* **2007**, *27*, 17–46. [CrossRef]
37. Behm, M.; Raffeiner, G.; Schöner, W. Climate change and possible impacts on alpinism: A case study on the Nationalpark Hohe Tauern. In Proceedings of the 3rd Symposium of the Hohe Tauern National Park for Research in Protected Areas, Kaprun, Austria, 15–17 September 2005; pp. 21–24.
38. Schrott, L.; Otto, J.-C.; Keller, F. Modelling alpine permafrost distribution in the Hohe Tauern region, Austria. *Austrian J. Earth Sci.* **2012**, *105*, 169–183.
39. Dragut, L.; Csillik, O.; Eisank, C.; Tiede, D. Automated parameterisation for multi-scale image segmentation on multiple layers. *Isprs J. Photogramm. Remote Sens.* **2014**, *88*, 119–127. [CrossRef] [PubMed]
40. Trimble. *eCognition Developer Reference Book 9.0*; Trimble: Munich, Germany, 2014.
41. Racoviteanu, A.E.; Paul, F.; Raup, B.; Khalsa, S.J.S.; Armstrong, R. Challenges and recommendations in mapping of glacier parameters from space: Results of the 2008 Global Land Ice Measurements from Space (GLIMS) workshop, Boulder, Colorado, USA. *Ann. Glaciol.* **2009**, *50*, 53–69. [CrossRef]
42. Kääb, A.; Bolch, T.; Casey, K.; Heid, T.; Kargel, J.; Leonard, G.; Paul, F.; Raup, B. Glacier Mapping and Monitoring Using Multispectral Data. In *Global Land Ice Measurements from Space*; Kargel, J.S., Leonard, G.J., Bishop, M.P., Kääb, A., Raup, B.H., Eds.; Springer: Berlin, Germany; Heidelberg, Germany, 2014; pp. 75–112.
43. Silverio, W.; Jaquet, J.-M. Glacial cover mapping (1987–1996) of the Cordillera Blanca (Peru) using satellite imagery. *Remote Sens. Environ.* **2005**, *95*, 342–350. [CrossRef]
44. Mihalcea, C.; Brock, B.W.; Diolaiuti, G.; D'Agata, C.; Citterio, M.; Kirkbride, M.P.; Cutler, M.E.J.; Smiraglia, C. Using ASTER satellite and ground-based surface temperature measurements to derive supraglacial debris cover and thickness patterns on Miage Glacier (Mont Blanc Massif, Italy). *Cold Reg. Sci. Technol.* **2008**, *52*, 341–354. [CrossRef]
45. Nuth, C.; Kohler, J.; König, M.; von Deschwanden, A.; Hagen, J.O.; Kääb, A.; Moholdt, G.; Pettersson, R. Decadal changes from a multi-temporal glacier inventory of Svalbard. *Cryosphere* **2013**, *7*, 1603–1621. [CrossRef]
46. Beck, M.W.; Vondracek, B.; Hatch, L.K.; Vinje, J. Semi-automated analysis of high-resolution aerial images to quantify docks in glacial lakes. *ISPRS J. Photogramm. Remote Sens.* **2013**, *81*, 60–69. [CrossRef]
47. Congalton, R.G. A review of assessing the accuracy of classifications of remotely sensed data. *Remote Sens. Environ.* **1991**, *37*, 35–46. [CrossRef]
48. Bayr, K.J.; Hall, D.K.; Kovalick, W.M. Observations on glaciers in the eastern Austrian Alps using satellite data. *Int. J. Remote Sens.* **1994**, *15*, 1733–1742. [CrossRef]
49. Patzelt, G. The period of glacier advances in the Alps, 1965 to 1980. *Z. Gletsch. Glazialgeol.* **1985**, *21*, 403–407.

50. Paul, F.; Kaab, A.; Maisch, M.; Kellenberger, T.; Haeberli, W. Rapid disintegration of Alpine glaciers observed with satellite data. *Geophys. Res. Lett.* **2004**, *31*. [CrossRef]
51. Paul, F.; Machguth, H.; Kääb, A. On the impact of glacier albedo under conditions of extreme glacier melt: The summer of 2003 in the Alps. *EARSeL eProc.* **2005**, *4*, 139–149.
52. De Bono, A.; Peduzzi, P.; Kluser, S.; Giuliani, G. Impacts of Summer 2003 Heat Wave in Europe. Available online: http://www.unisdr.org/files/1145_ewheatwave.en.pdf (accessed on 14 October 2015).
53. Avian, M.; Kellerer-Pirklbauer, A.; Proske, H.; Wack, R.; Bauer, A. Assessment of Landscape Changes using High Resolution LiDAR data: The Proglacial Area of Pasterze Glacier and the DGSD of Zintlwald as Recent Examples in the Eastern Alps. Available online: https://www.researchgate.net/profile/Michael_Avian/publication/228954263_Assessment_of_Landscape_Changes_using_High_Resolution_LiDAR_data_The_Proglacial_Area_of_Pasterze_Glacier_and_the_DGSD_of_Zintlwald_as_Recent_/links/09e415114f5c646a66000000.pdf (accessed on 14 October 2015).
54. Andreassen, L.; Paul, F.; Kääb, A.; Hausberg, J. Landsat-derived glacier inventory for Jotunheimen, Norway, and deduced glacier changes since the 1930s. *Cryosphere* **2008**, *2*, 131–145. [CrossRef]
55. Bolch, T.; Kamp, U. Glacier mapping in high mountains using DEMs, Landsat and ASTER data. *Grazer Schr. Geogr. Raumforsch.* **2006**, *41*, 37–48.
56. Paul, F.; Bolch, T.; Kaab, A.; Nagler, T.; Nuth, C.; Scharrer, K.; Shepherd, A.; Strozzi, T.; Ticconi, F.; Bhambri, R.; *et al*. The glaciers climate change initiative: Methods for creating glacier area, elevation change and velocity products. *Remote Sens. Environ.* **2015**, *162*, 408–426. [CrossRef]
57. Paul, F.; Barrand, N.E.; Baumann, S.; Berthier, E.; Bolch, T.; Casey, K.; Frey, H.; Joshi, S.P.; Konovalov, V.; Bris, R.L.; *et al*. On the accuracy of glacier outlines derived from remote-sensing data. *Ann. Glaciol.* **2013**, *54*, 171–182. [CrossRef]
58. Pelto, M. Utility of late summer transient snowline migration rate on Taku Glacier, Alaska. *Cryosphere* **2011**, *5*, 1127–1133. [CrossRef]
59. Klein, A.G.; Isacks, B.L. Spectral mixture analysis of Landsat thematic mapper images applied to the detection of the transient snowline on tropical Andean glaciers. *Glob. Planet Chang.* **1999**, *22*, 139–154. [CrossRef]
60. Evans, I.S. Local aspect asymmetry of mountain glaciation: A global survey of consistency of favoured directions for glacier numbers and altitudes. *Geomorphology* **2006**, *73*, 166–184. [CrossRef]
61. Chinn, T. Glacier fluctuations in the Southern Alps of New Zealand determined from snowline elevations. *Arct. Alp. Res.* **1995**, 187–198. [CrossRef]
62. Rabatel, A.; Dedieu, J.-P.; Thibert, E.; Letréguilly, A.; Vincent, C. 25 years (1981–2005) of equilibrium-line altitude and mass-balance reconstruction on Glacier Blanc, French Alps, using remote-sensing methods and meteorological data. *J. Glaciol.* **2008**, *54*, 307–314. [CrossRef]
63. Bhardwaj, A.; Joshi, P.K.; Snehmani; Singh, M.K.; Sam, L.; Gupta, R.D. Mapping debris-covered glaciers and identifying factors affecting the accuracy. *Cold Reg. Sci. Technol.* **2014**, *106–107*, 161–174. [CrossRef]
64. Alifu, H.; Tateishi, R.; Johnson, B. A new band ratio technique for mapping debris-covered glaciers using Landsat imagery and a digital elevation model. *Int. J. Remote Sens.* **2015**, *36*, 2063–2075. [CrossRef]
65. Quincey, D.J.; Luckman, A.; Benn, D. Quantification of Everest region glacier velocities between 1992 and 2002, using satellite radar interferometry and feature tracking. *J. Glaciol.* **2009**, *55*, 596–606. [CrossRef]
66. Scherler, D.; Bookhagen, B.; Strecker, M.R. Spatially variable response of Himalayan glaciers to climate change affected by debris cover. *Nat. Geosci.* **2011**, *4*, 156–159. [CrossRef]
67. Smith, T.; Bookhagen, B.; Cannon, F. Improving semi-automated glacier mapping with a multi-method approach: Applications in central Asia. *Cryosphere* **2015**, *9*, 1747–1759. [CrossRef]
68. Shukla, A.; Arora, M.K.; Gupta, R.P. Synergistic approach for mapping debris-covered glaciers using optical-thermal remote sensing data with inputs from geomorphometric parameters. *Remote Sens. Environ.* **2010**, *114*, 1378–1387. [CrossRef]
69. Malenovský, Z.; Rott, H.; Cihlar, J.; Schaepman, M.E.; García-Santos, G.; Fernandes, R.; Berger, M. Sentinels for science: Potential of Sentinel-1, -2, and -3 missions for scientific observations of ocean, cryosphere, and land. *Remote Sens. Environ.* **2012**, *120*, 91–101. [CrossRef]
70. Martone, M.; Bräutigam, B.; Rizzoli, P.; Gonzalez, C.; Bachmann, M.; Krieger, G. Coherence evaluation of TanDEM-X interferometric data. *ISPRS J. Photogramm. Remote Sens.* **2012**, *73*, 21–29. [CrossRef]

71. Hölbling, D.; Friedl, B.; Eisank, C.; Tsai, T.-T. An object-based method for mapping landslides on various optical satellite imagery-transferability and applicability across spatial resolutions. In Proceedings of the RSPSoc Annual Conference, Aberystwyth, UK, 2–5 September 2014; pp. 2–5.
72. Torres-Sánchez, J.; López-Granados, F.; Peña, J.M. An automatic object-based method for optimal thresholding in UAV images: Application for vegetation detection in herbaceous crops. *Comput. Electron. Agric.* **2015**, *114*, 43–52. [CrossRef]

Supplementary Materials: Decadal scale changes in glacier area in the Hohe Tauern National Park (Austria) determined by Object-Based Image Analysis

Benjamin Aubrey Robson, Daniel Hölbling, Christopher Nuth, Tazio Stozzi and Svein Olaf Dahl

Table S1. Measured Glacier Areas within the Hohe Tauern National Park. The datasets from 1969 and 1998 are from the Austrian Glacier Inventories. The datasets from 1985. 2003 and 2013 are from OBIA classifications.

Glacier ID	Glacier Name	Glacier Area					Total Change (1969–2013) (%)
		1969	1985	1998	2003	2013	
4018	Leiter Kees	0.47	0.33	0.38	0.05	0.13	−72
4020	Hohenwart Kees E	0.28	0.02	0.24	0.12	0.14	−49
4022	Schwerteck Kees E	0.09	0.07	0.08	0.05	0.05	−49
4023	Schwerteck Kees M	0.51	0.49	0.40	0.28	0.43	−15
4024	Schwerteck Kees W	0.43	0.38	0.26	0.02	0.17	−60
4025	Kellersberg Kees	0.18	0.16	0.12	0.03	0.11	−40
4026	Hofmas Kees	1.17	1.12	1.09	0.82	0.88	−25
4027	Pasterzen Kees	19.90	18.28	18.37	15.32	15.37	−23
4028	Wasserfallwinkel	1.98	1.96	1.86	1.62	1.55	−22
4030	Freiwand (Magnes) Kees	0.35	0.27	0.32	0.19	0.17	−51
4034	Grosser Fleiss Kees	0.40	0.24	0.35	0.17	0.15	−63
4036	Kleiner Fleiss Kees	1.27	1.12	0.96	0.77	0.85	−33
4037	Zirknitz Kees	0.10	0.11	0.11	0.03	0.07	−29
5008	Tischlerkar Kees M2	0.58	0.64	0.55	0.34	0.31	−46
5012		0.05	0.07	0.04	0.00	0.04	−21
5013	Grubenkar Kees	0.87	0.85	0.76	0.35	0.52	−40
5019	Sparaenger Kees E	0.07	0.08	0.05	0.00	0.03	−56
5021	Schlappereben Kees	0.79	0.75	0.68	0.07	0.62	−22
5025	Schareck Kees E	0.41	0.43	0.33	0.05	0.30	−27
5027	Schareck Kees W	0.20	0.20	0.16	0.03	0.12	−39
5028		0.10	0.07	0.07	0.00	0.04	−58
5030	Vogelmaier Ochsenkar Kees un.	1.28	1.21	1.11	0.61	0.62	−52
5031	Vogelmaier Ochsenkar Kees ob.	0.40	0.42	0.39	0.22	0.26	−34
5034	Pilatus Kees	0.47	0.30	0.47	0.13	0.13	−72
5035	Hocharn Kees S	0.31	0.35	0.27	0.07	0.17	−44
5036	Hocharn Kees N	0.75	1.05	0.74	0.47	0.50	−33
5037		0.15	0.15	0.11	0.00	0.07	−52
5038	Krummel Kees	1.03	1.09	0.93	0.53	0.68	−34
5039		0.22	0.26	0.21	0.10	0.17	−22
5040	Weissenbach Kees	1.24	1.40	0.87	0.36	0.52	−58
5043	Brekogel Kees	0.62	0.57	0.39	0.00	0.23	−63
5045	Spielma Kees E	0.39	0.37	0.27	0.19	0.22	−44
5046	Spielma Kees W	0.14	0.14	0.07	0.04	0.08	−42
5050	Fuscherkar Kees	1.27	0.14	0.89	0.47	0.81	−36

5051	Bockkar Kees	3.53	3.51	3.26	2.73	2.94	−17
5053	Hochgruber Kees	1.84	1.90	1.75	1.36	1.43	−22
5054	Teufelsmuehl Kees	0.77	0.76	0.60	0.47	0.61	−21
5055	Boggenei Kees	0.29	0.10	0.27	0.06	0.13	−57
5056	Sandboden Kees	0.77	0.76	0.72	0.23	0.79	3
5058	Walcher Kees	0.98	0.87	0.78	0.64	0.98	0
5061	Hirzbach Kees ob.	0.30	0.41	0.14	0.13	0.22	−28
5063	Brach Kees	0.27	0.18	0.22	0.06	0.11	−60
5066	Wielinger Kees	1.02	0.91	0.76	0.61	0.99	−2
5067	Foschez Kees	0.23	0.19	0.15	0.07	0.14	−37
5068	Kaindl Kees	0.45	0.48	0.38	0.32	0.51	13
5069	Oberer Klockerin Kees	0.31	0.28	0.18	0.12	0.26	−17
5070	Klockerin Kees	0.58	0.18	0.48	0.00	0.08	−86
5071	Baerenkopf Kees	2.32	2.27	2.12	1.86	2.26	−3
5072	Schwarzkoepfl Kees	0.71	0.63	0.63	0.03	0.23	−67
5073	Karlinger Kees	4.41	3.98	3.78	2.66	2.99	−32
5091	Unterer Riffl Kees	1.02	1.01	0.88	0.59	0.69	−32
5094	Oedenwinkel Kees	2.26	1.77	2.06	1.38	1.52	−33
5097	Soblick Kees	1.76	1.57	1.50	1.13	0.93	−47
5113	Abreder Kees	0.22	0.20	0.14	0.04	0.06	−73
5114	Kratzenberg Kees	0.36	0.42	0.31	0.11	0.15	−58
5115	Watzfeld Kees S	0.18	0.15	0.09	0.06	0.07	−62
5116	Watzfeld Kees N	0.55	0.46	0.35	0.22	0.20	−63
5117	Habach Kees	3.57	3.69	3.29	2.21	2.12	−41
5118	Suedliches Leiterkeesl	0.26	0.24	0.23	0.15	0.16	−40
5121		0.35	0.35	0.27	0.11	0.24	−31
5123	Untersulzbach Kees	3.96	3.75	3.72	2.97	3.01	−24
5124	Untersulzbach Kees W	0.26	0.27	0.24	0.20	0.17	−32
5125	Kaeferfeld Kees	2.79	2.86	2.49	1.92	1.78	−36
5127		0.22	0.22	0.18	0.09	0.14	−38
5128		0.49	0.54	0.44	0.25	0.29	−41
5129	Obersulzbach Kees	12.17	11.96	11.01	9.49	8.96	−26
5130	Oestliches Sotags Kees	2.69	2.86	2.45	2.04	1.84	−32
5131	Grosser Jaidbach Kees	1.05	1.09	0.93	0.71	0.60	−43
5132	Kleiner Jaidbach Kees	0.84	0.83	0.73	0.54	0.48	−42
5136	Westliches Jaidbach Kees	0.78	0.73	0.71	0.55	0.49	−37
5137	Schliefer Kees N	0.19	1.15	0.16	0.04	0.07	−63
5138	Schliefer Kees M	0.07	0.06	0.06	0.02	0.05	−29
5139	Schliefer Kees S	0.09	0.09	0.08	0.03	0.06	−37
5140	Westliches Sotags Kees	0.67	0.70	0.49	0.22	0.30	−56
5141	Krimmler Kees	5.50	5.16	4.88	3.60	3.39	−38
5150	Seekar Kees N	0.20	0.20	0.18	0.09	0.13	−37
5152	Keeskar Kees	0.98	0.94	0.88	0.61	0.54	−44
5153		0.11	0.96	0.09	0.02	0.06	−52
5154	Rainbach Kees	0.89	0.87	0.82	0.42	0.44	−51
5156	Weisskar Kees S	0.33	0.30	0.31	0.20	0.18	−46
5157	Weisskar Kees N	0.29	0.23	0.24	0.12	0.13	−54
5158	Waldbergkar Kees	0.23	0.19	0.15	0.05	0.09	−63
6033	Welitz Kees S	1.04	1.19	0.95	0.89	0.73	−30
6034	Welitz Kees M	0.57	0.85	0.52	0.46	0.33	−42
6039	Althaus Kees	0.78	0.88	0.69	0.45	0.42	−45
6040	Umbal Kees	5.20	5.01	4.73	4.06	4.13	−20

6042	Gubach Kees S	0.25	0.20	0.17	0.04	0.11	−54
6044	Malham Kees N	0.67	0.69	0.50	0.23	0.48	−29
6045	Simony Kees	2.91	2.81	2.56	1.88	1.61	−45
6046	Maurer Kees W	1.48	1.50	1.41	1.34	1.27	−14
6048	Maurer Kees M	2.39	2.59	2.12	1.62	1.92	−20
6049	Maurer Kees E	0.87	0.94	0.73	0.55	0.60	−31
6052	Dorfer Kees	4.55	4.13	3.80	2.79	1.08	−76
6053	Rainer Kees	3.63	4.01	3.51	3.39	3.36	−7
6054	Mullwitz Kees	3.52	3.61	3.24	3.01	2.95	−16
6055	Garaneber Kees N	0.54	0.46	0.38	0.27	0.28	−48
6056	Garaneber Kees S	0.61	0.46	0.36	0.15	0.19	−68
6058	Nill Kees	0.25	0.16	0.16	0.00	0.12	−49
6063	Mailfrosnitz Kees	1.11	0.50	0.56	0.20	0.18	−84
6064	Mailfrosnitz Kees N	0.14	0.08	0.06	0.00	0.08	−45
6065	Hohe Achsel	0.10	0.08	0.08	0.00	0.08	−21
6066	Frosnitz Kees	2.95	2.85	2.73	2.19	1.98	−33
6067	Kristallwand Kees	0.36	0.37	0.27	0.18	0.17	−53
6073	Knorr Kees E	0.26	0.17	0.15	0.07	0.11	−58
6074	Knorr Kees W	0.19	0.09	0.14	0.05	0.06	−70
6075	Karles Kees	0.60	0.61	0.48	0.33	0.32	−46
6077	Schlaten Kees	9.68	9.59	9.32	7.88	7.74	−20
6078	Viltragen Kees	2.47	2.43	2.13	1.64	1.57	−36
6079		0.26	0.29	0.21	1.62	0.15	−42
6080		0.18	0.19	0.14	0.00	0.16	−11
6081	Noerdlicher Viltragen Kees	1.30	1.36	1.14	0.75	0.84	−36
6082		0.11	0.12	0.09	0.05	0.14	33
6083		0.10	0.17	0.11	0.00	0.09	−13
6084	Gschloess Kees W	0.09	0.11	0.05	0.00	0.04	−57
6085	Gschloess Kees E	0.10	0.10	0.09	0.03	0.07	−23
6088	Daber Kees N	0.38	0.50	0.37	0.18	0.30	−19
6092	Praegrat Kees	1.00	1.00	0.90	0.65	0.54	−46
6095	Muntanitz Kees	0.49	0.46	0.40	0.15	0.25	−50
6096		0.19	0.10	0.10	0.03	0.06	−67
6097	Backtroeger Kees	0.41	0.37	0.27	0.20	0.23	−43
6098	Gradoetz Kees	1.19	0.92	0.73	0.52	0.54	−55
6099	Loames Kees S	0.36	0.24	0.24	0.05	0.12	−66
6100	Loames Kees N	0.30	0.26	0.24	0.13	0.13	−58
6102	Kalser Tauern Kees S	0.22	0.20	0.18	0.11	0.11	−52
6104	Hinterer Kasten Kees ob.	0.06	0.05	0.06	0.00	0.05	−16
6105	Hinterer Kasten Kees un.	0.08	0.04	0.07	0.00	0.06	−28
6106	Vorderer Kasten Kees	0.56	0.42	0.50	0.24	0.24	−57
6107	Laperwitz Kees	2.23	2.32	2.18	1.81	1.80	−19
6108	Fruschnitz Kees	2.82	2.92	2.69	2.53	2.70	−4
6109		0.08	0.08	0.05	0.00	0.04	−45
6110	Teischnitz Kees	2.10	2.03	1.93	1.65	1.68	−20
6112	Koednitz Kees	1.41	1.40	1.37	0.94	1.02	−27
9001	Wildkar Kees	0.40	0.30	0.26	0.13	0.17	−58
9002	Wildgerlos Kees E	0.63	0.40	0.39	0.24	0.24	−62
9003	Wildgerlos Kees M	2.10	1.96	1.98	1.42	1.41	−33
21007	Westlicher Tripp Kees	0.67	0.66	0.63	0.31	0.42	−37
21011	Hochalm Kees	3.14	3.14	2.90	2.33	2.53	−19

21012	Findlkar Kees	0.74	0.77	0.43	0.07	0.30	−59
21014	Grosselend Kees	2.92	2.91	2.47	0.88	1.83	−37
21015	Kaelberspitz Kees	0.83	0.69	0.60	0.12	0.29	−65
21016	Plessnitz Kees un.	0.25	0.23	0.12	0.00	0.07	−71
21018	Plessnitz Kees mi. S	0.20	0.18	0.18	0.00	0.14	−29
21021	Schwarzhorn Kees	0.09	0.09	0.07	0.00	0.07	−21
21022	Kleinelend Kees	3.04	3.41	2.82	2.14	2.36	−22
21023	Tischlerspitz Kees	0.48	0.43	0.42	0.16	0.21	−56
TOTAL		181	175	160	118	124	−33

Table S2. Total change in glacier area between 1969 and 2013 by different elevation classes.

Mean Elevation (m)	Glacier Area (km²)		Change in Area (km²)	Change in Area (%)
	1969	**2013**		
<2600	6.12	2.89	−3.2	−53
2600–2700	11.33	6.75	−4.6	−40
2700–2800	47.09	30.64	−16.5	−35
2800–2900	43.87	31.12	−12.8	−29
2900–3000	39.13	26.60	−12.5	−32
3000–3100	17.60	12.78	−4.8	−27
>3100	10.61	9.39	−1.2	−12

Table S3. Total change in glacier area between 1969 and 2013 by different size classes.

Glacier Size (km²)	Glacier Area (km²)		Change in Area (km²)	Change in Area (%)
	1969	**2013**		
<0.5	19.26	8.66	−10.6	−55
0.5–1	21.02	12.09	−8.9	−42
1–2.5	41.36	26.92	−14.4	−35
2.5–5	47.12	36.58	−10.5	−22
5.0–10.0	20.38	15.26	−5.1	−25
>10	32.07	24.33	−7.7	−24

Table S4. Total change in glacier area between 1969 and 2013 by aspect.

Aspect	Glacier Area (km²)		Change in Area (%)
	1969	**2013**	
N	0	0	0
NNE	0.26	0.17	−32
ENE	6.11	4.09	−33
E	32.78	22.16	−32
ESE	43.38	31.28	−28
SSE	13.78	6.69	−51
S	9.82	5.77	−41
SSW	37.45	28.48	−24
WSW	17.41	12.65	−27
W	14.24	8.56	−40
WNW	0.59	0.25	−57
NWN	0.58	0.31	−46

Table S5. Measured amount of supraglacial debris within the Hohe Tauern'National Park compared with the total glacier (clean ice and debris covered ice) area.

Glacier ID	1985 Debris	1985 Total Glacier	2003 Debris	Debris Area Change 1985–2003 (%)	2003 Total Glacier	Total Area Change 1985–2003 (%)	2013 Debris	Debris Area Change 2003–2013 (%)	2013 Total Glacier	Total Area Change 2003–2013 (%)	Debris Area Change 1985–2013 (%)	Total Area Change 1985–2013 (%)
6077	0.58	9.59	0.50	−14	7.88	−18	0.81	61	0.90	−3	−100	−28
5091	0.25	1.01	0.44	76	0.59	−42	0.36	−18	0.41	−30	22	−16
5094	0.47	1.77	0.47	1	1.38	−22	0.27	−43	0.86	−38	−42	−52
4027	0.86	18.28	0.65	−25	15.32	−16	1.06	63	15.37	0	45	−59
5129	0.39	11.96	0.07	−81	9.49	−21	0.00	−100	8.63	−9	39	−20
Total	*3.37*	*42.23*	*2.15*	*−36*	*34.66*	*−19*	*3.38*	*57*	*32.93*	*−5*	*0*	−23

Table S6. Comparison between the 2003 OBIA classification outlines (OBIA_2003) and the 2003 glacier outlines submitted to GLIMS (by Paul *et al.* (2011 (2003 GLIMS)). as well as a comparison between the 2013 OBIA classification outlines and the 2013 manually corrected outlines (2013_Man).

Glacier ID	Glacier Name	OBIA_ 2003 (km^2)	2003 GLIMS (km^2)	Accuracy (%)	OBIA_2013 (km^2)	2013_Man (km^2)	Accuracy (%)
4018	Leiter Kees	0.05	0.15	34	0.16	0.13	84
4020	Hohenwart Kees E	0.12	0.12	96	0.10	0.14	72
4022	Schwerteck Kees E	0.05	0.04	76	0.02	0.05	51
4023	Schwerteck Kees M	0.28	0.28	99	0.47	0.43	92
4024	Schwerteck Kees W	0.02	0.04	45	0.14	0.17	80
4025	Kellersberg Kees	0.03	0.03	92	0.11	0.11	99
4026	Hofmas Kees	0.82	0.91	90	0.85	0.88	97
4027	Pasterzen Kees	15.32	17.79	86	15.37	15.37	100
4028	Wasserfallwinkel	1.62	1.62	100	1.52	1.55	98
4030	Freiwand (Magnes) Kees	0.19	0.25	76	0.14	0.17	78
4034	Grosser Fleiss Kees	0.17	0.14	84	0.14	0.15	98
4036	Kleiner Fleiss Kees	0.77	0.80	96	0.85	0.85	100
4037	Zirknitz Kees	0.03	0.03	100	0.04	0.07	62
5008	Tischlerkar Kees M2	0.34	0.37	93	0.28	0.31	91
5012					0.04	0.04	95
5013	Grubenkar Kees	0.35	0.37	94	0.51	0.52	99
5019	Sparaenger Kees E				0.02	0.03	55
5021	Schlappereben Kees	0.07	0.07	100	0.56	0.62	91
5025	Schareck Kees E	0.05	0.15	36	0.32	0.30	92
5027	Schareck Kees W	0.03	0.03	100	0.08	0.12	68
5028					0.03	0.04	74
5030	Vogelmaier Ochsenkar Kees un.	0.61	0.71	85	0.61	0.62	99
5031	Vogelmaier Ochsenkar Kees ob.	0.22	0.24	91	0.32	0.26	81
5034	Pilatus Kees	0.13	0.13	96	0.13	0.13	99
5035	Hocharn Kees S	0.07	0.08	86	0.17	0.17	96
5036	Hocharn Kees N	0.47	0.46	99	0.50	0.50	99
5037					0.05	0.07	74
5038	Krummel Kees	0.53	0.51	98	0.59	0.68	87
5039		0.10	0.12	82	0.14	0.17	84
5040	Weissenbach Kees	0.36	0.31	85	0.50	0.52	96
5043	Brekogel Kees	0.00	0.04	0	0.21	0.23	90
5045	Spielma Kees E	0.19	0.16	79	0.18	0.22	82
5046	Spielma Kees W	0.04	0.03	56	0.05	0.08	59
5050	Fuscherkar Kees	0.47	0.51	91	0.73	0.81	90
5051	Bockkar Kees	2.73	2.74	100	2.79	2.94	95
5053	Hochgruber Kees	1.36	1.40	97	1.43	1.43	100
5054	Teufelsmuehl Kees	0.47	0.52	91	0.67	0.61	89
5055	Boggenei Kees	0.06	0.07	77	0.08	0.13	63
5056	Sandboden Kees	0.23	0.26	88	0.68	0.79	86
5058	Walcher Kees	0.64	0.65	100	0.83	0.98	84
5061	Hirzbach Kees ob.	0.13	0.13	94	0.11	0.22	50
5063	Brach Kees	0.06	0.08	79	0.11	0.11	99
5066	Wielinger Kees	0.61	0.57	92	0.77	0.99	77
5067	Foschez Kees	0.07	0.07	99	0.09	0.14	64
5068	Kaindl Kees	0.32	0.31	97	0.50	0.51	97
5069	Oberer Klockerin	0.12	0.14	84	0.19	0.26	74

	Kees						
5070	Klockerin Kees				0.03	0.08	38
5071	Baerenkopf Kees	1.86	1.74	93	2.39	2.26	94
5072	Schwarzkoepfl Kees	0.03	0.53	6	0.16	0.23	70
5073	Karlinger Kees	2.66	2.87	92	3.04	2.99	98
5091	Unterer Riffl Kees	0.59	0.71	83	0.41	0.69	60
5094	Oedenwinkel Kees	1.38	1.37	99	0.86	1.52	56
5097	Soblick Kees	1.13	1.19	95	0.82	0.93	88
5113	Abreder Kees	0.04	0.06	65	0.05	0.06	86
5114	Kratzenberg Kees	0.11	0.13	82	0.17	0.15	87
5115	Watzfeld Kees S	0.06	0.07	75	0.05	0.07	75
5116	Watzfeld Kees N	0.22	0.26	84	0.14	0.20	70
5117	Habach Kees	2.21	2.41	92	2.05	2.12	97
5118	Suedliches Leiterkeesl	0.15	0.14	93	0.10	0.16	60
5121		0.11	0.11	99	0.26	0.24	94
5123	Untersulzbach Kees	2.97	2.74	92	2.85	3.01	95
5124	Untersulzbach Kees W	0.20	0.20	100	0.15	0.17	89
5125	Kaeferfeld Kees	1.92	1.91	100	1.69	1.78	95
5127		0.09	0.13	67	0.17	0.14	75
5128		0.25	0.27	91	0.29	0.29	98
5129	Obersulzbach Kees	9.49	10.02	95	8.63	8.96	96
5130	Oestliches Sotags Kees	2.04	2.09	98	1.69	1.84	92
5131	Grosser Jaidbach Kees	0.71	0.72	99	0.54	0.60	89
5132	Kleiner Jaidbach Kees	0.54	0.56	95	0.42	0.48	87
5136	Westliches Jaidbach Kees	0.55	0.58	94	0.45	0.49	92
5137	Schliefer Kees N	0.04	0.06	64	0.09	0.07	67
5138	Schliefer Kees M	0.02	0.02	96	0.06	0.05	66
5139	Schliefer Kees S	0.03	0.04	76	0.06	0.06	85
5140	Westliches Sotags Kees	0.22	0.24	95	0.35	0.30	81
5141	Krimmler Kees	3.60	4.05	89	3.27	3.39	97
5150	Seekar Kees N	0.09	0.09	93	0.13	0.13	100
5152	Keeskar Kees	0.61	0.64	96	0.41	0.54	76
5153		0.02	0.03	78	0.05	0.06	95
5154	Rainbach Kees	0.42	0.52	81	0.44	0.44	99
5156	Weisskar Kees S	0.20	0.24	83	0.15	0.18	82
5157	Weisskar Kees N	0.12	0.12	100	0.12	0.13	90
5158	Waldbergkar Kees	0.05	0.06	83	0.09	0.09	95
6033	Welitz Kees S	0.89	0.82	91	0.73	0.73	100
6034	Welitz Kees M	0.46	0.42	92	0.36	0.33	93
6039	Althaus Kees	0.45	0.47	96	0.34	0.42	81
6040	Umbal Kees	4.06	4.26	95	3.97	4.13	96
6042	Gubach Kees S	0.04	0.05	86	0.10	0.11	85
6044	Malham Kees N	0.23	0.22	92	0.30	0.48	63
6045	Simony Kees	1.88	1.96	96	1.91	1.61	81
6046	Maurer Kees W	1.34	1.26	94	1.33	1.27	95
6048	Maurer Kees M	1.62	1.56	96	2.04	1.92	94
6049	Maurer Kees E	0.55	0.53	97	0.65	0.60	91
6052	Dorfer Kees	2.79	2.85	98	2.85	1.08	−64
6053	Rainer Kees	3.39	3.24	95	3.24	3.36	97

6054	Mullwitz Kees	3.01	2.94	98	2.82	2.95	95
6055	Garaneber Kees N	0.27	0.29	95	0.28	0.28	99
6056	Garaneber Kees S	0.15	0.14	93	0.15	0.19	76
6058	Nill Kees	0.00	0.05	0	0.14	0.12	88
6063	Mailfrosnitz Kees	0.20	0.22	91	0.15	0.18	83
6064	Mailfrosnitz Kees N				0.06	0.08	85
6065	Hohe Achsel				0.07	0.08	92
6066	Frosnitz Kees	2.19	2.16	99	1.88	1.98	95
6067	Kristallwand Kees	0.18	0.21	86	0.19	0.17	90
6073	Knorr Kees E	0.07	0.09	82	0.10	0.11	90
6074	Knorr Kees W	0.05	0.05	99	0.05	0.06	80
6075	Karles Kees	0.33	0.32	98	0.33	0.32	97
6077	Schlaten Kees	7.88	8.28	95	7.67	7.74	99
6078	Viltragen Kees	1.64	2.19	75	1.67	1.57	93
6080		0.00	0.01	0	0.15	0.15	98
6081	Noerdlicher Viltragen Kees	0.75	0.82	92	0.18	0.16	86
6082		0.05	0.06	76	0.87	0.84	96
6083		0.00	0.02	0	0.09	0.14	67
6084	Gschloess Kees W				0.09	0.09	97
6085	Gschloess Kees E	0.03	0.03	97	0.04	0.04	91
6088	Daber Kees N	0.18	0.18	97	0.08	0.07	95
6092	Praegrat Kees	0.65	0.63	96	0.31	0.30	98
6095	Muntanitz Kees	0.15	0.22	70	0.47	0.54	87
6096		0.03	0.04	74	0.23	0.25	91
6097	Backtroeger Kees	0.20	0.18	91	0.05	0.06	86
6098	Gradoetz Kees	0.52	0.50	98	0.21	0.23	92
6099	Loames Kees S	0.05	0.06	80	0.51	0.54	95
6100	Loames Kees N	0.13	0.14	99	0.09	0.12	71
6102	Kalser Tauern Kees S	0.11	0.12	92	0.10	0.13	77
6104	Hinterer Kasten Kees ob.	0.00	0.01	0	0.28	0.11	−65
6105	Hinterer Kasten Kees un.				0.06	0.05	88
6106	Vorderer Kasten Kees	0.24	0.25	97	0.05	0.06	84
6107	Laperwitz Kees	1.81	1.71	94	0.21	0.24	89
6108	Fruschnitz Kees	2.53	2.57	98	1.66	1.80	92
6109					2.65	2.70	98
6110	Teischnitz Kees	1.65	1.64	99	0.04	0.04	88
6112	Koednitz Kees	0.94	1.00	94	1.66	1.68	99
9001	Wildkar Kees	0.13	0.13	100	0.90	1.02	88
9002	Wildgerlos Kees E	0.24	0.27	90	0.15	0.17	90
9003	Wildgerlos Kees M	1.42	1.56	91	0.24	0.24	99
21007	Westlicher Tripp Kees	0.31	0.32	98	1.54	1.41	91
21011	Hochalm Kees	2.33	2.34	100	0.42	0.42	99
21012	Findlkar Kees	0.07	0.09	80	2.37	2.53	94
21014	Grosselend Kees	0.88	1.57	56	0.24	0.30	79
21015	Kaelberspitz Kees	0.12	0.17	67	1.64	1.83	89
21016	Plessnitz Kees un.				0.26	0.29	89
21018	Plessnitz Kees mi. S				0.06	0.07	78
21021	Schwarzhorn Kees	0.00	0.02	0	0.13	0.14	91
21022	Kleinelend Kees	2.14	2.28	94	0.06	0.07	86
21023	Tischlerspitz Kees	0.16	0.16	100	2.23	2.36	95
4018	Leiter Kees	0.05	0.15	34	0.16	0.13	84
TOTAL		116.45	124.05	94	120.54	123.60	98

Table S7. Transient snowline elevation for glaciers larger than 0.2 km² for 1985. 2003 and 2013.

Glacier ID	Transient Snowline Elevation (m.)			Total Change 1985–2013 (m)
	1985	**2003**	**2013**	
6106	2808	2961	2846	−38
5121	2900		2914	−14
6095	2940		2962	−22
6055	3080		3114	−34
5128	3001	3075	3023	−22
5140	2869	2984	2934	−65
21012	2780		2877	−97
6088	2677		2765	−88
6034	3155	3170	3073	81
21007	2740	3149	3021	−282
6039	3000	3092	3046	−46
4023	3028	2943	3063	−36
5154	2841	2980	2960	−119
5136	2914	2965	2933	−19
6092	2858	2974	2890	−32
5152	2789		2897	−107
6049	2910	3096	3016	−106
5054	3111	3186	3171	−60
5091	3042		3015	27
6033	3065	3213	3155	−90
5056	2941	2847	2919	22
6081	2731	2857	2780	−50
4026	3049	3329	3205	−156
5097	2682	2927	2836	−154
5058	2750	2749	2907	−158
5066	3087	3048	3046	41
6112	3120	3251	3182	−62
6052	2893	3111	3036	−143
6046	2930	3101	3079	−149
9003	2768	2832	2852	−84
5053	2896	3106	3053	−157
5094	2724	3045	2971	−248
4028	2853	2965	2888	−36
6078	2793		2979	−186
6045	2836	3144	3072	−236
6110	3223	3236	3188	34
5125	2851	2899	2924	−74
6107	2936	3178	3097	−161
21014	2811		2870	−59
5130	2827	3037	2934	−107
6048	2917	3073	3026	−109
6066	2879	3120	3000	−121
5117	2793	3011	2906	−113
5071	3051	3074	3058	−7
21022	2770	2918	2910	−140
21011	2893	3065	3004	−112
6108	3125	3277	3245	−119

5051	2969	3055	3003	−34
6054	2973	3202	3042	−70
5073	2917	3078	3007	−90
5123	2952	3139	3164	−212
6053	2996	3262	3242	−246
5141	2918		3002	−84
6040	3004	3231	3124	−120
6077	2846	3178	3089	−243
5129	2879	3092	2924	−45
4027	2941	3132	3041	−100
Mean	**2913**	**3071**	**3005**	**−92**

Table S8. Transient snowline elevation for glaciers larger than 0.2 km² by aspect.

Aspect	**Transient Snowline Elevation (m.)**			**Total Change in Transient Snowline Elevation (m)**	**Total Change in Transient Snowline Elevation (%)**
	1985	**2003**	**2013**		
N					
NNE	2774	2859		−85	100
ENE	2848	2897	2915	−67	−2
E	2823	2988	2945	−122	−4
ESE	2887	3055	3020	−133	−5
SSE	2811	3015	2923	−112	−4
S	2910	3086	2967	−57	−2
SSW	2900	3113	3022	−122	−4
WSW	2861	3090	3006	−145	−5
W	2878	2965	2942	−64	−2
WNW	2711				
NNW	2814				
Range	**189**	**231**	**108**		

Paper III

Camping by Thulagi Glacier, 4000 m a.s.l. Photo: Pål Ringkjøb Nielsen

Decadal Scale Glacier Surface Lowering and Stagnation in the Manaslu Region of Nepal

Benjamin Aubrey Robson[1*], Christopher Nuth[2], Pål Ringkjøb Nielsen[1], Luc Girod[2] Marijn Hendrickx [3] and Svein Olaf Dahl[1]

1 Department of Geography, University of Bergen, Fosswinckelsgate 6, Bergen 5007, Norway

2 Department of Geosciences, University of Oslo, Postboks 1047 Blindern, Oslo 0316, Norway

3 Department of Geography, Ghent University, Krijgslaan 281 S8, 9000 Ghent, Belgium

Keywords: Himalayas, Debris-covered glacier, geodetic mass balance, glacier area change, velocity, corona.

Abstract

Despite ongoing mass losses over recent decades, many Himalayan debris-covered glaciers have had stationary termini and only modest changes in area. Here, we calculate changes in glacier area with rates of velocity and volume change for the glaciers in the Manaslu Region of Nepal between 1970, 2000, 2005 and 2013. Between 2001 and 2013 the glacier area decreased by 8.2% (-0.68% a^{-1}), simultaneously, the glaciers lowered by -0.21 ± 0.08 m a^{-1} and had a slightly negative geodetic mass balance of -0.05 ± 016 m w.e.a^{-1} although mass balances ranged from -2.49 ± 2.24 to +0.27 ± 0.30 m w.e. a^{-1}. Generally, the uppermost portions of the glaciers (> ~5635 m a.s.l.) have been gaining mass, while the lowermost portions have downwasted at a mean rate of 0.35 ± 0.03 m a^{-1} between 2000 and 2013. Three glaciers were investigated in more detail with a 1970 Corona DEM. The geodetic mass balance between 1970 and 2013 was -0.24 ± 0.12 m w.e. a^{-1} which became more negative (-0.51 ± 0.12 m w.e. a^{-1}) between 2005 and 2013 with rates of surface lowering over debris-covered ice increasing by 168% between 1970 – 2000 and 2005 - 2013. Simultaneously, the glacier velocities have decreased by a mean of -16.8% between 1999 and 2013. Over decadal scales the rates of change of glacier area and velocity are similar, while a weak relationship exists between trends in glacier volume and velocity. Our analysis demonstrates that the glaciers of the Manaslu Region have been simultaneously reducing in area, stagnating, and downwasting. Furthermore, the debris-covered tongues of 12% of the glaciers have remained relatively stationary (<1% change in area), we therefore suggest that future change assessment for Himalayan debris-covered glaciers include glacier volume or velocity results in addition to glacier area measurements.

***Corresponding author:** Benjamin Aubrey Robson, Department of Geography, University of Bergen, Fosswinkelsgate 6, N-5007, Bergen, Norway.

Email address: benjamin.robson@uib.no

1. Introduction

The Himalayas contain the largest concentration of ice outside of the polar areas. Glacial meltwater has many implications for the regional population such as irrigation and hydroelectric power production (Immerzeel et al., 2010, Bolch et al., 2012), and hazards such as glacial lake outburst floods (GLOFs) which have killed more than 6300 people in Central Asia since the 1500s and threaten hydro-electric power generation, tourism, and transport infrastructure (Richardson and Reynolds, 2000, Schwanghart et al., 2014, Carrivick and Tweed, 2016).

Existing *in-situ* data in the Himalayas is extremely limited and tends to be biased towards small to medium sized and debris-free glaciers (Gardelle et al., 2013). A high level of uncertainty therefore exists when interpreting regional trends in Himalayan glaciers. Remote Sensing data allows systematic monitoring of glaciers worldwide over decadal scales, and has permitted large scale investigations of glacier area (Bajracharya et al., 2014a, Nuimura et al., 2014, Robson et al., 2015), glacier velocities (Heid and Kääb, 2012b, Dehecq et al., 2015) and glacier volume (or geodetic mass balance) (Bolch et al., 2011, Gardelle et al., 2012, Kääb et al., 2012). Trends in Himalayan glacier ice have been found to be heterogeneous and vary profusely from one region to another (Scherler et al., 2011, Kääb et al., 2012, Kääb et al., 2015).

A significant number of glaciers in the Himalayas are covered by supraglacial debris. The effects of debris-cover on glacier mass balance are poorly known, and can act to either retard or exacerbate glacier melting depending on debris thickness, composition and distribution (Reznichenko et al., 2010, Zhang et al., 2011). In many cases, the terminus positions of debris-covered glaciers have remained relatively stationary over the previous decades despite significant glacier down-wasting and mass loss (Scherler et al., 2011, Benn et al., 2012, Nagai et al., 2013). This implies that other glacier parameters are needed to fully quantify glacier changes.

2. Objectives

The objectives of this paper are two-fold. Firstly, there is a need to assess how rates of glacier area change relate to glacier volume and velocity for debris-covered glaciers in the Himalayas, and whether glacier terminus position or area change are appropriate parameters to measure. Secondly, this paper investigates decadal scale glacier changes in the Manaslu Region of Nepal, a previously undocumented region in the Himalayas. This information will be used to better understand the heterogeneous response of Himalayan glaciers to climate across the mountain chain.

2.1 Study Area

We conducted our study in the Manaslu Region of Nepal (Figure 1). Most studies addressing decadal scale geodetic mass balances of Himalayan glaciers have done so in the Karakoram in the west and the Everest Region in the east, with select studies in the Pamir mountains, Indian Himalaya and Bhutan Himalaya. We therefore chose to study the glaciers in the vicinity of Mount Manaslu in the Central Himalayas to help further our understanding of the heterogeneity of Himalayan glacier response. The study area contains an assortment of clean, debris-covered, stagnant and lake-terminating ice. We restricted our analysis to 36 glaciers that were mostly covered by the SRTM (Shuttle Radar Topographic Mission) DEM. The Manaslu Region covers ~2350 km^2 of which 34% is covered by glaciers. Our study area extends across the Nepali-Tibetan border, which is also the mountain divide between the humid, monsoon-driven Himalayas and the arid Tibetan plateau (Benn and Owen, 1998, Maussion et al., 2014). While the glaciers north of the topographic divide are predominantly clean glaciers, those south of the divide are covered by thick supraglacial debris. This difference in debris-cover is attributed to stronger diurnal freeze-thaw cycles found south of the topographic divide, where winter temperatures fluctuate more around freezing point (Nagai et al., 2013).

The glaciers in the study area are typically 0.5–1 km in width and 5–15 km in length with areas that vary from 5.6 km^2 to 32.0 km^2. Mean annual temperatures range between 26.7°C and 12.8°C and the mean precipitation in the region is estimated to be ~1000 mm a year at Larke Samdo weather station, (84°38E, 28°39N 3650 m a.s.l; shown on Figure 1) (Department of Hydrology and Meteorology (Government of Nepal), 2014). The Central Himalayas receive 80% of annual precipitation during the Monsoon season when rates of glacier accumulation and ablation are simultaneously at their highest (Ageta and Higuchi, 1984, Benn and Owen, 1998). The glaciers situated on the Tibetan Plateau receive less precipitation and as such respond primarily to variations in the ablation season temperature (Owen and Benn, 2005).

Of particular interest in the study area is Thulagi Glacier (GLIMS ID: G084538E28524N) (shown in Figure 1B) which is approximately 27 km^2 in size and extends from ~ 4100 to 7500 m a.s.l. As Thulagi Glacier has melted, a moraine-dammed lake situated at the glacier terminus has grown which is now 0.9 km^2 in size. Pant and Reynolds (2000) found that the moraine damming the lake contained significant amounts of dead ice. Calving events from the glacier or downwasting of the moraine dam could have potentially caused a breach of the ice cored moraine and a GLOF (Richardson and Reynolds, 2000). A

2011 report by ICIMOD (International Centre for Integrated Mountain Development) identified Thulagi Glacier as one of the most potentially dangerous lakes in Nepal (Mool, 2011).

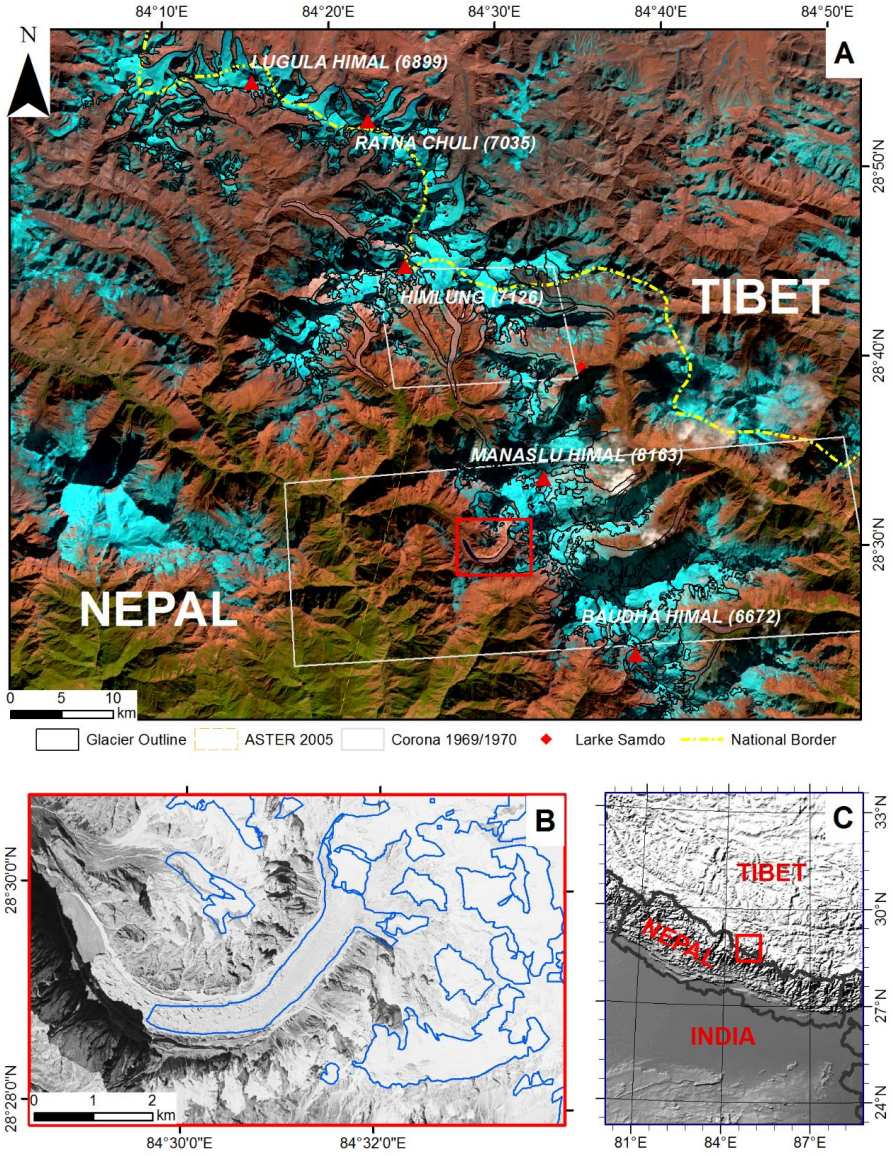

Figure 1: (A) Location of the glaciers studied (outlines derived from Robson et al., (2015) within the Manaslu Region (28ºN, 84ºE), and (C) the location of the Manaslu Region within Nepal. Thulagi Glacier (B) previously terminated in Dona Lake (shown on the 1970 Corona image). Note that the 2013 SETSM DEM covers the entire study area and is therefore not shown. Larke Samdo weather station is shown as a red diamond. Background image: Rapideye image (20th November 2012) overlaying Landsat 8 (26th December 2013).

Table 1: The data used in this study and the purpose of each data source.

Scene ID	Date of Acquisition	Sensor	Resolution	Bands used	Purpose
LC81420402014284LGN00	10/10/2014	Landsat 8	30 (15 pan)	Panchromatic	Velocity
LC81420402013281LGN00	8/10/2013	Landsat 8	30 (15 pan)	Panchromatic	Velocity
LT51420402005291BKT00	18/10/2005	Landsat 5	30	SWIR1, NIR, Red	Area
LE71420402001304SGS00	31/10/2001	Landsat	30 (15 pan)	SWIR1, NIR, Red	Area
LE71420402000350SGS00	15/12/2000	Landsat 7	30 (15 pan)	Panchromatic	Velocity
LE71420401999283SGS00	10/10/1999	Landsat	30 (15 pan)	Panchromatic	Velocity
LE71420401999283SGS00	10/10/1994	Landsat 7	30 (15 pan)	Panchromatic	Velocity
LT51420401994357ISP00	23/12/1994	Landsat 5	30	SWIR1, NIR, Red	Velocity & Area
LT51420401993354ISP00	1/12/1993	Landsat 5	30	SWIR1	Velocity
WV02_20131125_103001002A5FE600	25/11/2013	Worldview 2	8	Panchromatic	Volume changes
WV01_20140119_102001002B106000_	19/1/2014	Worldview 1	8	Panchromatic	Volume changes
WV01_20131116_10200100250FF100	16/11/2013	Worldview 1	8	Panchromatic	Volume changes
WV01_20131116_10200100250E5100	16/11/2013	Worldview 1	8	Panchromatic	Volume changes
WV02_20131125_10300100298E5400	25/11/2013	Worldview 2	8	Panchromatic	Volume changes
WV02_20131117_1030010029470C00	17/11/2013	Worldview 2	8	Panchromatic	Volume changes
AST_L1A_00311042005050442	11/03/2005	ASTER	15	3N/3B	Volume changes
N28_E084_1ARC_V2	02/2000	SRTM	30	Elevation	Volume changes
DS1112-1007DF180	19/11/1970	Corona KH-4B	1.8	Panchromatic	Volume changes & Area
DS1112-1007DA185	19/11/1970	Corona KH-4B	1.8	Panchromatic	Volume changes & Area
DS1044-1086DA051_S1	08/11/1967	Corona KH-4B	1.8	Panchromatic	Area
DS1044-1086DA051_S2	08/11/1967	Corona KH-4B	1.8	Panchromatic	Area

3. Data and Methods

Four DEMs were compared in order to determine the change in surface elevation. The most recent DEM is the 8 m resolution SETSM (Surface Extraction with TIN-based Search-space Minimization) DEM from 2013. The SETSM DEM was generated automatically from Worldview imagery by Ohio State University to aid humanitarian efforts following the April 2015 Nepal earthquake (Noh and Howat, 2015b, Noh and Howat, 2015a). The DEM has a reported accuracy of ± 3.5 m for the Worldview 2 DEMs and ± 4.0 m for the Worldview 1 DEMs (Noh and Howat, 2015b). An ASTER DEM from 2005 was generated from the nadir and back-looking near-infrared bands with the free opensource software MicMac. The procedure used the RPC generation and jitter compensation methods presented in Girod et al. (2015) to output a more precise DEM than the AST14DMO product distributed by NASA. We also used the 30 m SRTM1 DEM from February 2000, although the coverage of the dataset was not complete, in particular the accumulation zones of many of the glaciers lacked elevation data.

Lastly, two sets of Corona stereopairs were available that covered parts of the Manaslu Region. The first stereopair was from 1967 and covered Ponkar Glacier. Some portions of the ice were obscured by cloud in these images. The Corona images covering Ponkar Glacier were therefore only used for measuring the changes in glacier area and not glacier volume. The second Corona stereopair covered Thulagi,

Punggen and Hinang glaciers and was from 1970. This image was cloud free and contained sufficient image contrast to generate a DEM.

All the Corona imagery was processed in ERDAS Imagine 2015. The Ponkar Corona image was processed with 28 Ground Control Points (GCPs), and 359 tie points (mostly automatically generated). The Thulagi Corona image was processed with 75 GCPs and 1837 tie points. Orthomosaics from both datasets were exported at 2 m resolution, while the DEM from the Thulagi Corona image was exported at 8 m resolution using the eATE (enhanced Automatic Terrain Extraction) tool. All the DEMs were registered to UTM zone 45 N.

3.2 Pre-processing

A combination of correlation masks and manual interpretation using the hillshade models was used to clean the DEMs. The DEMs were then set to the spatial resolution of the lowest DEM (30 m) using a median *block statistics* operation within ArcMap 10.3 following Paul (2008) and Gardelle et al. (2013), who suggested that coarser resolution DEMs cannot fully represent the elevation for areas with high curvature (such as ridges or mountain peaks) leading to co-registration problems.

3.2.1. Planimetric DEM co-registration

We used the method outlined by Nuth and Kääb (2011) to linearly coregister the DEMs by minimising elevation biases on stable terrain. This method aims to minimise the residuals by fitting the elevation bias (dH) divided against the tangent of the slope (tanα) against the aspect (ψ), as shown in Eq (1)

$$\frac{dh}{\tan\alpha} = a.\cos(b - \psi) + c \quad (1)$$

where *a* and *b* are the magnitude and direction of the co-registration shift, respectively, and *c* is the mean elevation bias between the DEMs divided by the mean surface slope. The co-registration process was iterated until the improvement of the residual standard deviation was less than 2%. The co-registration shifts are shown in Table 4. Figure 2 shows a graph of slope normalised elevation biases before and after planimetric co-registration.

3.2.2 Along track and across track elevation bias correction

A sixth-order polynomial was fitted to the elevation biases over stable terrain to account for both along- and across-track biases associated with Corona data (Figure 3) and a second order polynomial for the ASTER elevation biases.

The mean surface lowering and total change in volume were then determined. Pixels were masked out that had (a) surface changes of more than 500 m or (b) elevation differences of greater than three standard deviations of the stable terrain elevation bias (after Gardelle et al. (2013)). Following Bolch et al. (2011) a spline interpolation was used to fill data gaps that were smaller than 10 pixels. The change in mass was calculated by assuming a density of 850 kgm^{-3} following Huss (2013). *Sorge's Law* was assumed to hold true – that the density does not vary with depth (Bader, 1954).

3.2.3 Radar penetration correction

The SRTM dataset was acquired in C-band which can penetrate into snow and ice by several metres (Rignot et al., 2001). Various estimates have been made of the magnitude of this penetration in the Himalayas, ranging from 1.4 – 3.4 m (Gardelle et al., 2013) to 8 -10 m (Kääb et al., 2012, Kääb et al., 2015). In this study we opted to use the uniform value of 1.5 m over the entire accumulation zone which Pellicciotti et al. (2015) calculated for the Langtang valley in the Central Himalayas.

3.3 Area changes

Four Landsat images that approximately corresponded with the DEMs were used to assess the areal glacier change. The outlines created by Robson et al. (2015) for 2013 were used as a baseline. These outlines had been created semi-automatically using a combination of Landsat 8 imagery, a DEM and SAR Coherence data within an Object Based Image Analysis (OBIA) classification with additional manual corrections applied. We compared these to outlines from 1967/1970 (henceforth referred to as 1970) generated with the Corona imagery, and 2001 and 2005 which were generated from Landsat imagery. Noticeable breaks in morphology, vegetation, exposed ice, or collapses in terminal moraines were all used as indicators when mapping the debris-covered ice.

3.4 Glacier Velocity

Prominent features on the debris-covered glaciers were tracked between sets of successive satellite images in order to determine the surface velocity. Features were matched using cross-correlation on orientation images (CCF-O). Oriented images allow the gradients in pixel values to be used instead of the raw values, thereby reducing the influence of differences in scene illumination and has been shown by Heid and Kääb (2012a) to outperform other image matching methods in a Himalayan setting.

Landsat images from 2013/2014, 1999/2000 and 1993/1994 (Table 1) were used for determining glacier velocities. The free software *CIAS*, developed by the University of Oslo, was used for feature tracking (Kääb and Vollmer, 2000). The image pairs were referenced together within CIAS using a Helmert Transformation. Between 15 and 20 points on stable terrain were used to register the images together. Landsat 5 and 7 images were registered with RMSEs typically of 10-12 m, while Landsat 8 images were registered with RMSEs typically of less than 5 m.

Displacements were filtered by direction and magnitude. A 3x3 moving window process was then used to remove displacement vectors that varied by more than 20% in magnitude or direction to the mean values. Some manual filtering was needed for removing matches associated with snow, shadow or mass movements.

Glacier centrelines were calculated automatically using the method of Kienholz et al. (2014) based on outlines from the RGI (Randolf Glacier Inventory) and the SRTM that had been void filled with the 1:50,000 Finnmap topographic maps of Nepal (available pre-processed online (De Ferranti, 2012)). The

centrelines were manually edited to adapt them to the older satellite imagery and the mean velocity was extracted along the centrelines.

3.5 Uncertainty assessment

3.5.1 – Glacier outline accuracy

When the 2013 outlines were compared to manually delineated outlines, an accuracy of 91% was determined (Robson et al., 2015). We have no reference data in which to determine accuracies for these delineations, however Paul et al. (2013) estimated that the errors relating to the creation of glacier outlines are < 5% when working with clean ice, but errors of up to 30% can arise due to debris-covered ice, stagnant ice and shadows. In the absence of reference data, we cannot speculate on the accuracy of these manual delineations other than assuming they are of an accuracy approximately equal to the 2013 outlines.

3.5.2 – Glacier volume accuracy

The accuracy of the elevation changes was assessed by determining both the stochastic errors and the systematic errors (or biases). The systematic errors ($\vec{Z}$) between the DEMs was estimated by triangulating the DEM co-registration residuals (after Nuth et al. (2012)). The z residual (Table 4) shows the vertical biases between the DEMs but is most likely an overestimate as these triangulations include only the linear residuals and not the nonlinear adjustments made to the Corona and ASTER DEMs.

Nevertheless, the z triangulations are < ± ~15 m for the entire time series which is less than the magnitude of total downwasting over the 43-year period for many glaciers. The DEM with the highest systematic bias is the ASTER DEM, which can also be seen in higher standard deviations and DEM differencing uncertainties (Table 2). The Corona DEM has a standard deviations of 23.9 m against the SETSM DEM. Given the large time period between these datasets, and the image distortions associated with Corona data, these deviations are acceptable, although ~5 m higher than the standard deviations found by Bolch et al. (2011) or (Pieczonka et al., 2013).

The stochastic errors were quantified by comparing elevations over non-glacier terrain. We consider the 2013 SETSM DEM as a reference for the uncertainty analysis as it has the most spatial coverage. Elevation differences were calculated for 2638 randomly chosen points over non-glacier terrain which had slopes of less than 30°. Extreme values (> ± 100 m) were not considered. The standard error (SE) was calculated which relies on the standard deviation over stable terrain (SD_{STABLE}) and the number of independent pixels included in the DEM differencing (n):

$$SE = \frac{SD_{STABLE}}{\sqrt{n}} \quad (2)$$

where *n* considers the original number of pixels(N_{tot}), the pixel size (PS) and spatial autocorrelation (d):

$$n = \frac{N_{tot}.PS}{2d} \quad (3)$$

We used a value of 400 m for the spatial correlation distance for the SETSM DEM and 600 m for all other DEMs based on the work of others (Bolch et al., 2011, King et al., 2016). The standard error (SE) and the z-residual from the triangulation of the DEM co-registrations ($\vec{Z}$) was combined using the sum of root mean squares to calculate the DEM differencing uncertainty (e):

$$e = \sqrt{SE^2 + \vec{Z}^2} \tag{4}$$

The value of *e* was used in estimating error budgets. For DEM differences that included the SRTM, ± 1.5 m was added for the clean-ice components of the glaciers.

Table 2: The mean deviation , standard deviation and DEM differencing uncertainty (e), over stable (non-glacier) terrain from a sample of random points.

SETSM → SRTM			SETSM → ASTER			ASTER → SRTM			SRTM → Corona			SETSM → Corona		
Mean deviation (m)	StDev (m)	e (m)	Mean deviation (m)	StDev (m)	e (m)	Mean deviation (m)	StDev (m)	e (m)	Mean deviation (m)	StDev (m)	e (m)	Mean deviation (m)	StDev (m)	e (m)
2.1	8.9	0.7	-5.9	44.7	7.7	5.3	18.6	14.8	2.7	41.4	10.5	0.41	23.9	2.4

Table 3: The co-registration shifts between the different DEMs that was necessary before DEM differencing. The second half of the table shows the triangulated residuals between the different DEMs. The residuals represent the systematic accuracy between the datasets (A = Corona, B = SRTM, C = ASTER, D = SETSM). All the residuals are in metres.

Vector notation	Dx	Dy	Dz
$\overrightarrow{AB}$	-2.6	20.7	7.7
$\overrightarrow{AD}$	-13.8	21.1	-2.4
$\overrightarrow{BC}$	9.6	-17.4	14,8
$\overrightarrow{CD}$	32	-15.9	10.5
$\overrightarrow{AB} + \overrightarrow{BD} - \overrightarrow{AD}$	38.1	23.9	8.1
$\overrightarrow{AC} + \overrightarrow{CD} - \overrightarrow{AD}$	79.4	-22.8	13.6
$\overrightarrow{AB} + \overrightarrow{BC} - \overrightarrow{AC}$	-45.8	-10.9	-7.8
$\overrightarrow{BC} + \overrightarrow{CD} - \overrightarrow{BD}$	-4.5	-57-6	-2.3
$\overrightarrow{AB} + \overrightarrow{BC} - \overrightarrow{CD} - \overrightarrow{AD}$	-30.4	-1.9	-15.2

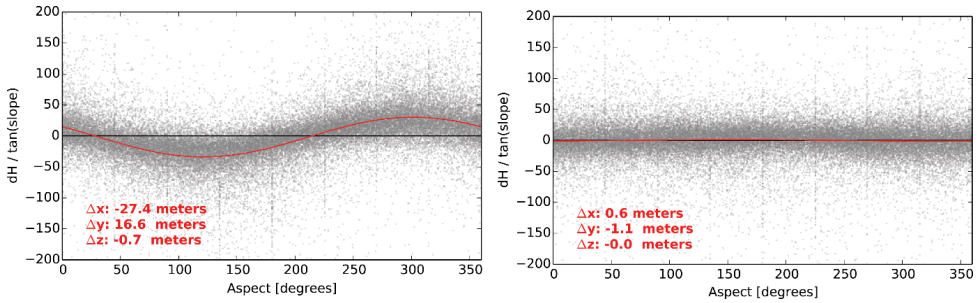

Figure 2: Plots of slope normalised terrain elevation differences between the 2013 SETSM DEM and the 2000 SRTM DEM over stable (non-glacier) terrain before co-registration (left) and after four iterations of co-registration (right). The co-registration shifts that were applied are shown in red.

Table 4: Mean and standard deviations of displacements on stable terrain for the velocity measurements.

2013/2014		1999/2000		1993/1994	
Mean	Standard Deviation	Mean	Standard Deviation	Mean	Standard Deviation
2.0	8.2	16.0	3.2	5.5	5.6

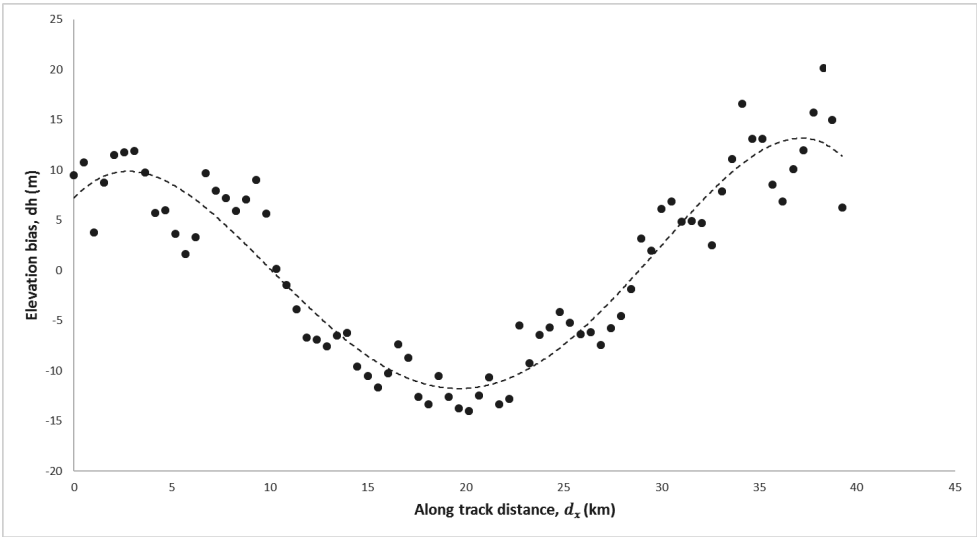

Figure 3: Elevation biases (dh) against along track ($\boldsymbol{d_x}$) distances over stable (non-glacier) terrain between the Corona and SETSM DEMs. A noticeable along track bias is observable. A sixth order polynomial was fitted to the trend and used to remove the bias.

3.5.3 Glacier velocity accuracy

The uncertainty of the velocity measurements was determined by measuring displacements over terrain that is assumed to be stable (Table 3). We restricted our error assessment to displacements on the terrain within 500 m of the terminus of Ponkar Glacier which was gently sloping, and shadow and snow free in all images. In all cases the standard deviations are <9 m, smaller than the 15 m pixel size for the 2013/2014 and 1999/2000 imagery, and 30 m for the 1993/1994 images. The only results which are not significant are for the glaciers that appear to be largely stagnant (for example Baudha Himal Glacier (G084684E28407N) and Northern Fukang Glacier (G084425E28837N).

4. Results

4.1 Glacier Area

The glacier area was measured for 36 glaciers for the years 2001 and 2013 (Table S1). Eight of these glaciers also had their area measured for the year 1970 with a total area of 200.7 km^2. Between 1970 and 2001 the glacier area decreased by -0.05% a^{-1}, and a further -1.3% a^{-1} between 2001 and 2005 followed by a -0.4% a^{-1} reduction between 2005 and 2013. In total this represented a 14.4% (-0.33% a^{-1}) reduction in glacier area between 1970 and 2013. When all glaciers were examined, a change of 8.2% (-0.68% a^{-1}) was found between 2001 and 2013, leaving 386.4 km^2 of glacier ice in the study area in 2013. Despite being situated at higher elevations, the clean ice glaciers in Tibet and the clean-ice components of debris-covered glaciers lost a greater proportion of area than the debris-covered glaciers (-0.58% a^{-1} and -0.80% a^{-1} respectively as opposed to -0.09% a^{-1}) between 2001 and 2013 and over half of the glaciers (52%) underwent an increase in debris-cover. The terminus position of many of the debris-covered tongues remained relatively stationary with 12% of the glaciers having area changes of <1%, with glacier area loss predominately occurring at the glacier margins and clean ice situated near the ELA. Some debris-covered glaciers however underwent strong retreats. Thulagi glacier lost a significant portion of its debris-covered tongue and retreated ~1.4 km onto land between 1970 and 2013. Similarly, the large eastern flowing debris-covered glaciers (Punggeon Glacier; G084595E28536N and Hinang Glacier; G084640E28489N) underwent terminus retreat over the same time period.

4.2 Glacier Volume

The largest spatial coverage of volume changes was obtained between 2000 and 2013 by comparing the SRTM and SETSM DEMs (Figure 4). There are however large gaps in data over the accumulation zones of many of the glaciers which will affect the clean ice results. In total, the 36 glaciers in the region lost 0.33 ± 1.2 km^3 of ice between 2001 and 2013 (Table S2), which equates to a mean surface lowering or -0.21 ± 00.8 m a^{-1}. The debris-covered portions of the glaciers, located in the ablation zones, lost significantly more mass (0.95 ± 0.1 km^3) equivalent to -0.35 ± 0.03 m a^{-1}. Over the whole study area, the geodetic mass balance is only slightly negative (-0.05 ± 0.16m w.e. a^{-1}), although the region contains a high degree of heterogeneity, with geodetic mass balances ranging from -2.49 ± 2.24 to +0.27 ± 0.30 m w.e. a^{-1}.

Higher downwasting rates occurred between 2005 and 2013 (-0.51 ± 0.48 m a^{-1}) (Table S3) while the geodetic mass balance also became more negative (-0.27 ± 0.55 m w.e. a^{-1}) and even more so between 2000 and 2005 (-1.30 ± 1.63 m a^{-1}).

The Corona DEM covered the three glaciers of most importance in the Manaslu Region. Rates of glacier downwasting have remained relatively stable over the 43-year period, from -0.49 ± 0.02 m a^{-1} between 1970 and 2000 compared to -0.51 ± 0.48 m a^{-1} between 2005 and 2013. The rates of loss over debris-covered ice increased by 26% from -0.65 ± 1.48 m a^{-1} between 2000 – 2005 to -0.82 ± 0.48 m a^{-1} between

2005 and 2013, and by 168% between 1970 – 2000 and 2005 – 2013 for the glaciers covered by the Corona DEM from -0.40 ± 0.18 m a^{-1} to -1.07 ± 48 m a^{-1}. The mean geodetic balance for the three glaciers between 1970 and 2013 was -0.24 ± 0.12 m w.e. a^{-1} and -0.51± 0.12 m w.e. a^{-1} between 2005 and 2013.

4.3 Glacier velocity

In general, the glaciers flowed fastest towards the transition from clean ice, and slowest towards the glacier termini (Figures 5 and 8). There is a large variation in glacier speed, Ponkar Glacier (ID: G084456E28737N) and Thulagi Glacier (G084595E28536N) flowed at mean velocities in 2013/2014 of 47 ± 8.2 and 41 ± 8.2 m a^{-1}, respectively, while Baudha Himal Glacier (G084684E28407N) and Northern Fukang Glacier (G084425E28837N) have mostly stagnant debris tongues with mean velocities of < 3 m a^{-1}.

When the mean velocities for the whole region are considered, the velocity varies only slightly between 1993/1994 and 1999/2000 (31 ± 5.6 and 27 ± 3.2 m a^{-1} respectively). Overall the studied glaciers decreased in velocity by a mean of 16.8% (-1.2% a^{-1}) between 1999/2000 and 2013/2014, and 25.3% (-1.3% a^{-1}) between 1993/1994 and 2013/2014.

There is a large variety in rates of glacier change. Some glaciers have slowed dramatically, Kechakyu Khola Glacier (G084456E28737N), Suti Glacier (G084350E28675N) and Himal Chuli Glacier (G084684E28407N) have all slowed by -2.2% a^{-1} , -2.8% a^{-1} and -2.3% a^{-1} respectively between 1993/1994 and 2013/2014. Other glaciers are depicted at having stagnated more, however these are glaciers that are flowing at such slow rates (< 3 m a^{-1}) that these changes in velocity are of a small magnitude. Thulagi and Ponkar glaciers are depicted at having undergone slight accelerations in glacier velocity between 1993/1994 and 2013/2014 of 0.5% a^{-1} and 0.7% a^{-1} respectively, however if the velocities are examined only between 1999/2000 and 2013/2014 then Ponkar Glacier decreased in velocity by -0.8 % a^{-1} while Thulagi glacier accelerated by 2.1% a^{-1}.

Some general patterns can be extracted from the velocity data. The lowermost portions of the debris-tongues can be said to typically undergo less deceleration in glacier velocity than the more active parts of the glacier found higher up (Figure 7). Some glaciers (for example G084456E28737N Eastern; Figure 6C) have stagnant glacier tongues with low (< 10 ms^{-1}) velocities. The steeper sections of ice, such as the tributaries found high up on the debris-covered tongues also slowed more than the flatter sections of the glacier (Figure 6). When traverse-profiles are considered (Figure 7) it can be seen towards the glacier terminus the deceleration in velocity becomes more pronounced towards the glacier centreline.

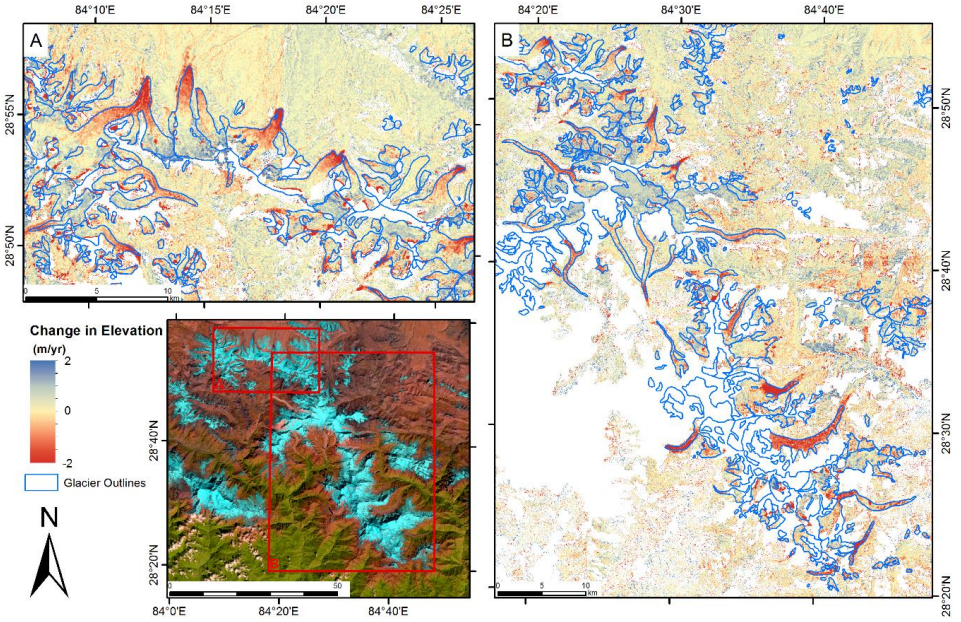

Figure 4: Change in surface elevation for glaciers in the Manaslu Region between 2000 and 2013. Background: Landsat 8 (26th December 2013).

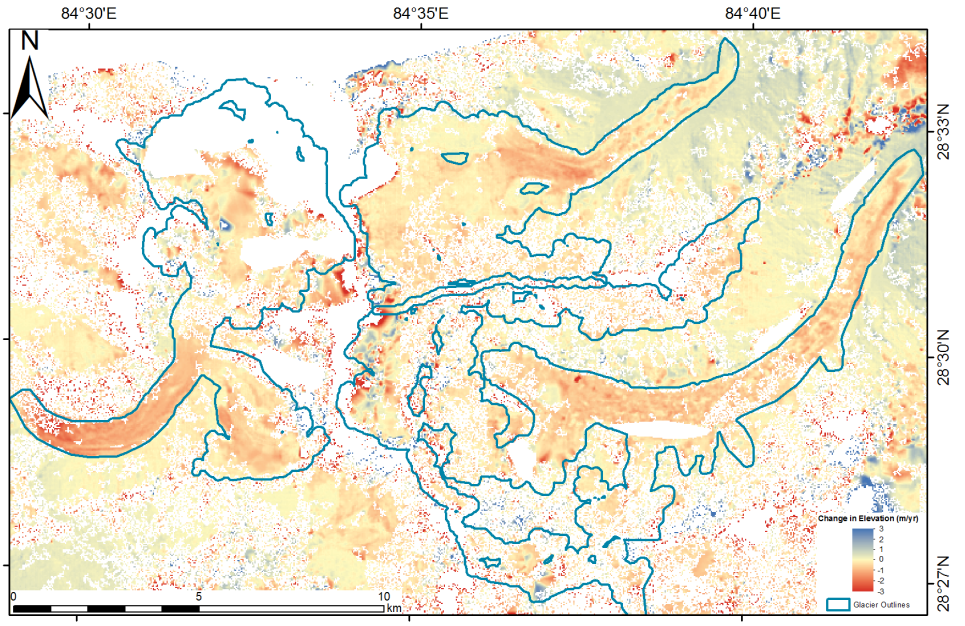

Figure 5: Mean annual Change in surface elevation for Thulagi, Punggeon and Hinang Glaciers, between 1970 and 2013.

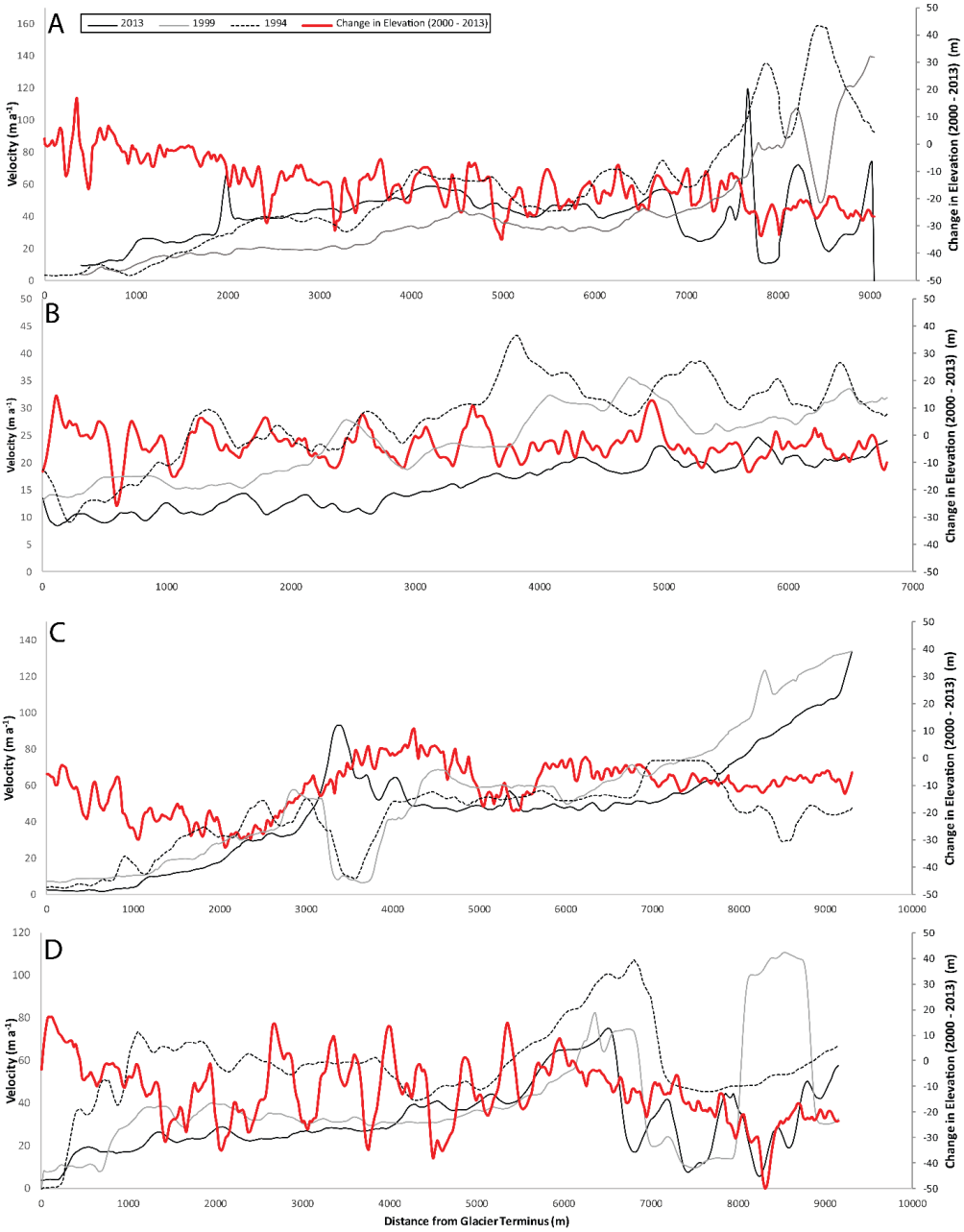

Figure 6: Velocity and change in elevation profiles from G084350E28675N (A) G084456E28737N W (B) G084456E28737NE (C) and G084684E28407N (D).

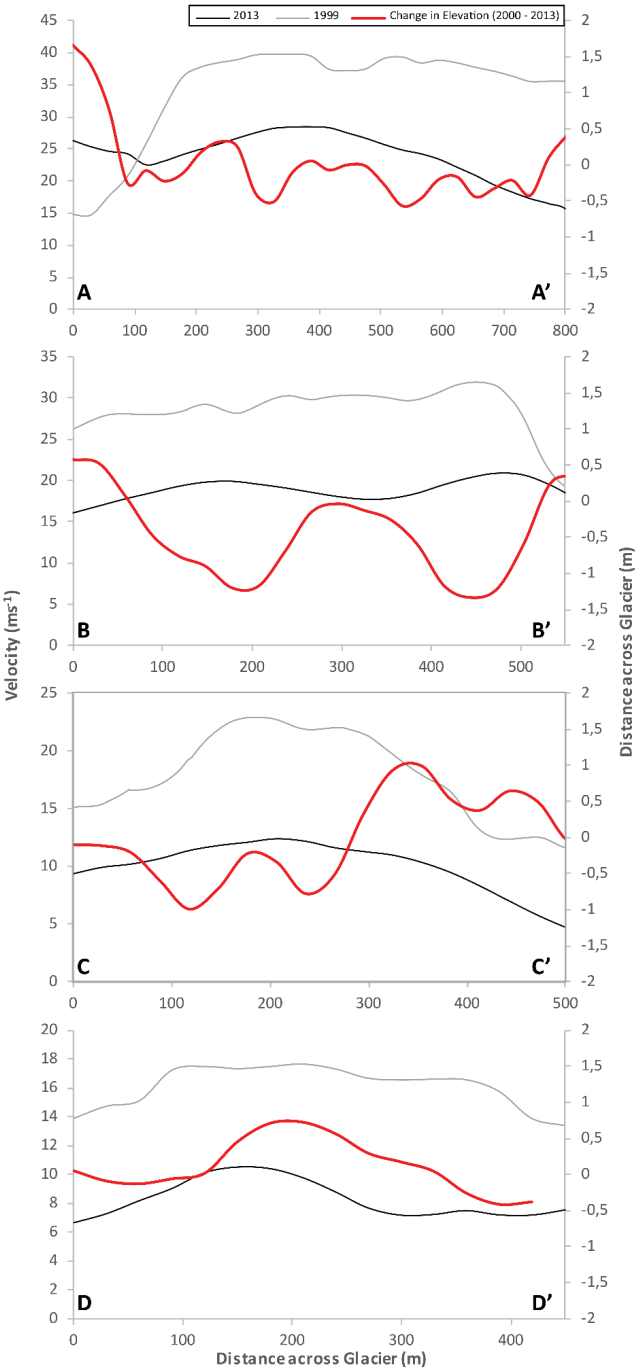

Figure 7: Longitudinal velocity profiles of Kechakya Khola Glacier (G084456E28737N). Profile A-A' occurs at the transition from clean ice to debris covered ice, while profiles B-B', C-C' and D-D' occur progressively further down-glacier where the ice flows slower and becomes more stagnant. The locations of the profiles are shown on Figure 7.

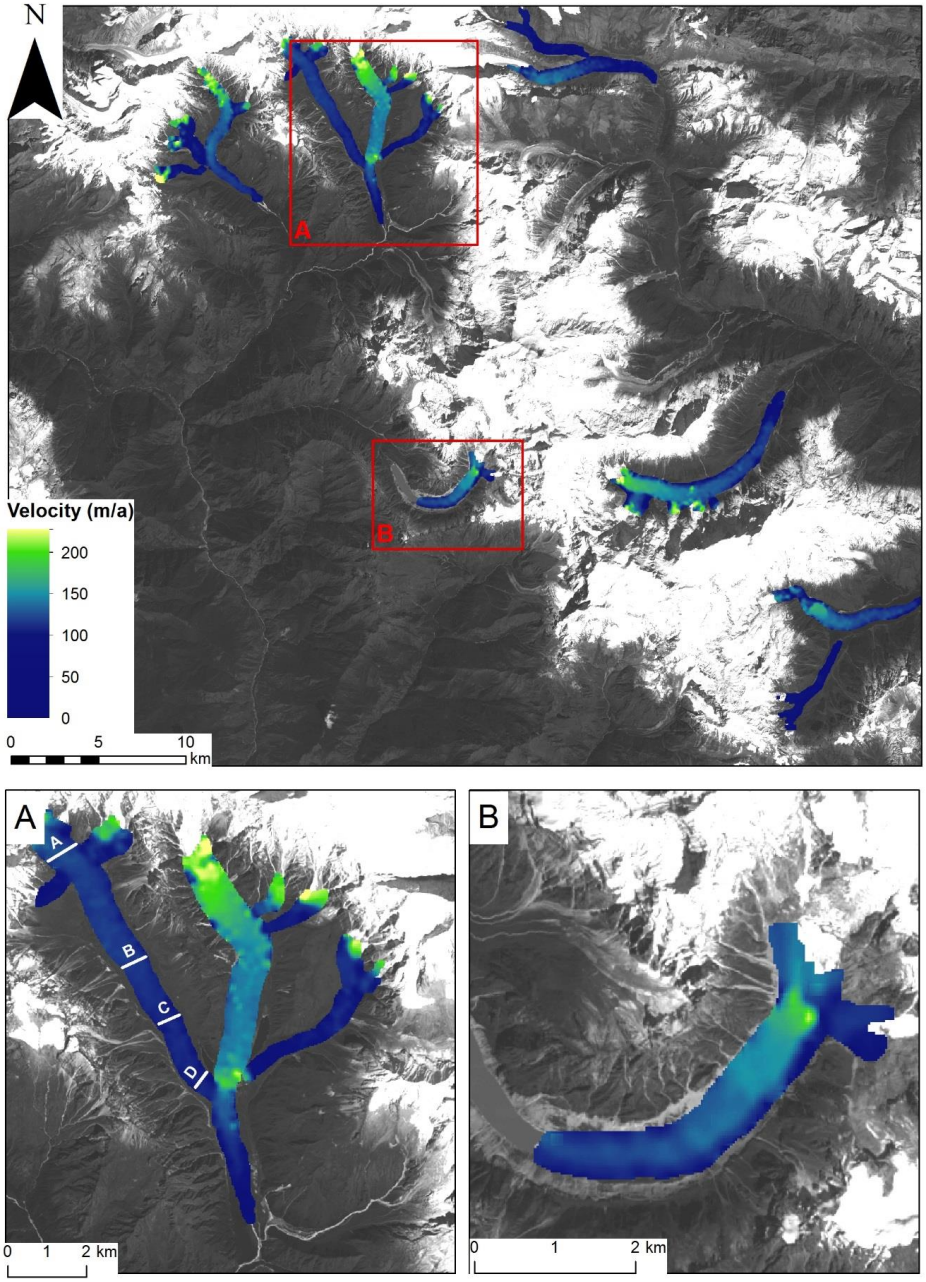

Figure 8: Annual surface velocity for the glaciers in the Manaslu Region for the year 2013/2014. Subsets are shown for (A) Ponkar Glacier and (B) Thulagi Glacier. Background: Landsat 8 (26th December 2013)

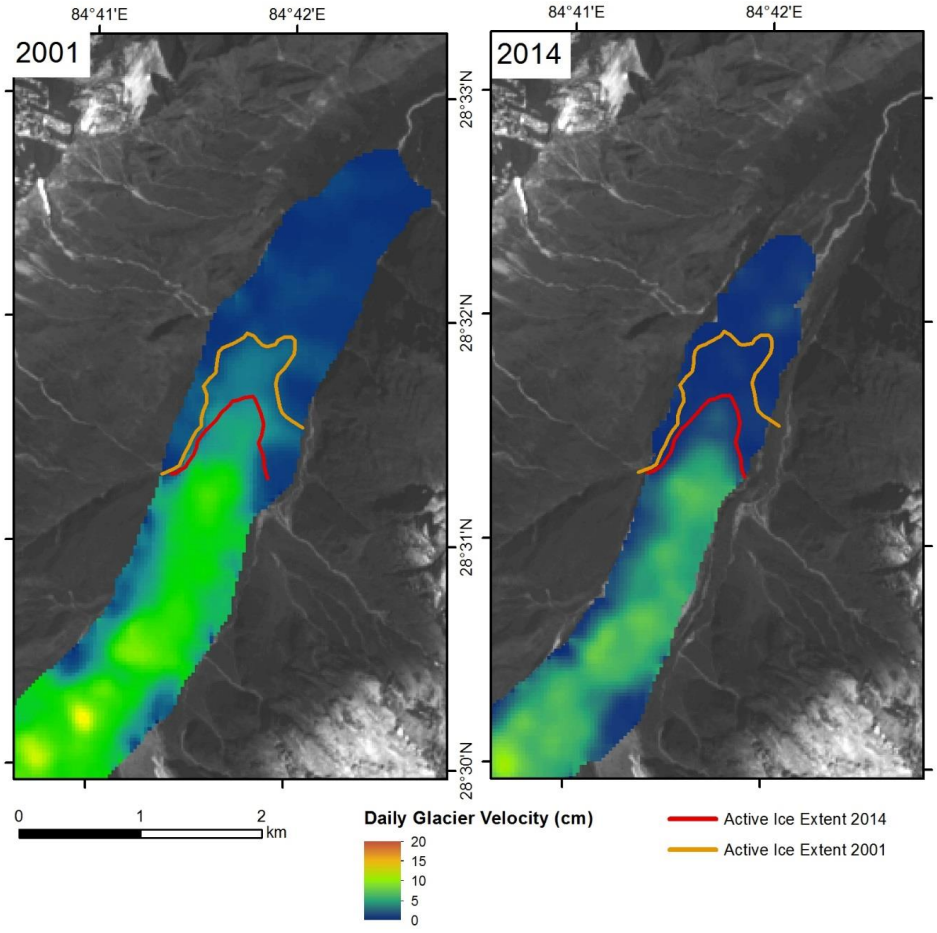

Figure 9: A comparison of ice velocities at Hinang Glacier (G084689E28511N) between 2000/2001 and 2013/2014. Despite no obvious changes in the extent of the debris-covered glaciers, the terminus has become noticeably more stagnant. Background: Landsat 8 (26th December 2013).

5. Discussion of results

Our results show a heterogeneity of glacier change across the Manaslu Region. We should point out that a lack of data in the accumulation zones from the SRTM could introduce problems when using rates of surface lowering in the ablation zones as a means of assessing glacier change in such a heterogeneous area as the Himalayas. This is because small changes in surface lowering over the ablation zones could be compensated by varying amounts of accumulation higher up the glacier. Our regional averages are however in many cases distinct enough to infer changes to glacier health.

Our results indicate the greatest rates of glacier downwasting occurred between 2000 and 2005 (-1.30 ± 1.63 m a^{-1}) however given the uncertainty surrounding radar penetration in the SRTM DEM and the noise in the ASTER DEM, these results are not significant. We can state however that rates of downwasting between 1970 – 2000 are in line with those between 2000 and 2013, with increased rates occurring between 2005 and 2013. The geodetic mass balance for the three glaciers covered by the Corona DEM is also seen as becoming increasingly more negative. Unfortunately, the lack of coverage over the accumulation zones of these glaciers by the SRTM meant that the geodetic mass balance could only be compared between 1970 – 2013 and 2005 – 2013. A similar trend is visible with glacier velocity, with little change occurring between 1993 and 1999, followed by a reduction in mean glacier velocity by 2013. We interpret our results to show an increased rate of mass loss and stagnation between 2005 and 2013 compared with previous decades.

A clear relationship exists ($R^2 = 0.90$) between elevation and surface lowering over the entire study area, with glaciers thickening above ~5635 m a.s.l. The lower lying portions of the glaciers lost the most mass, although many glaciers were stagnant towards the lowermost 1 – 2 km of the glacier termini (Figure 6C). The clean ice glaciers situated in Tibet shows a clear, linear response to a change in elevation (Figure 10: line A). The same trend is visible in the clean ice components of the debris-covered ice (Figure 10: line C), the shallower gradient could reflect the more important role that monsoonal precipitation plays in glacier mass balance for the glaciers south of the topographic divide compared to those on the Tibetan plateau.

The debris-covered ice shows a response that is more complex than the clean ice (Figure 10: line B). The gradient of the line is approximately equal to that the clean ice, however three noticeable deviations in the melt rate occur (Figure 10: 1-3). Two noticeable decreases in glacier melting occur at ~3500 and ~4400 - 4800 m.a.sl. and an increase in melt rates between ~3600 – 4100 m a.s.l.. We interpret the first of these (Figure 10: 1) to where the build-up of debris transported down-glacier becomes sufficient to offset glacier melting. A similar peak was found by Benn et al. (2012) when glacier mass balance was modelled for Ngozumpa Glacier in the Everest Region. The second reduction in glacier melt rates (Figure 10:3) occurs at the transition from steep clean ice (40°) to more gently sloped debris-covered ice (20°), an area where avalanche material becomes entrained as supraglacial debris. As the gradient of the

glacier decreases, supraglacial debris accumulates, thereby insulating the underlying ice from surface temperatures until glacier flow transports and re-distributes the debris.

We speculate that the area of increased glacier melt between 3500 and 4100 m a.s.l. (Figure 10: 2) relates to where the surface slope becomes gentler and the glacier velocity decreases towards the snout are favourable for both supraglacial lake formation and the presence of exposed ice. Although many of these features are too small to detect on satellite imagery, some supraglacial lakes are visible on a 5 m RapidEye image from 2012 (Figure 11). Additionally, exposed ice was visible towards the snout of Ponkar Glacier during fieldwork in 2013 (Figure 11). Such processes were also found to increase glacier downwasting in the Everest region and in Langtang valley (Nuimura et al., 2012, Immerzeel et al., 2014).

When just the glaciers that had velocities measured (excluding the two near-stagnant glaciers - G084516E28729N and G084695E28384N) are examined, it can be seen that the total area and the mean glacier velocity have been reducing at approximately the same rate (-0.9% a^{-1} and -0.8% a^{-1} respectively) between 2000/2001 and 2013 (Table 7). The same glaciers lowered by a mean of -0.59 ± 0.08 m a^{-1}. There is no relationship between a change in area and the mean surface change (R^2 = 0.002) or glacier area change and velocity change (R^2 = 0.22). A weak relationship (R^2 = 0.47) exists between glacier velocity change and mean surface lowering. Both the glacier area and mean surface lowering show increased rates of glacier losses between 2005-2000 compared with 2013-2005 and 2013-2000. Our analysis is limited by the number of glaciers that it was possible to determine changes in glacier area, velocity, and volume.

Table 7: A comparison in the rates of change of glacier area, velocity, and volume for 7 glaciers that had records of glacier area, velocity, and volume between 2000/2001, 2005 and 2013.

	2013 – 2005	2005 – 2000	**2013 – 2000**
Glacier Area	-0.6 % a^{-1}	-1.3% a^{-1}	**-0.8% a^{-1}**
Glacier Velocity			**-0.9% a^{-1}**
Mean Surface Lowering	-0.48 ± 0.48 ma^{-1}	-1.02 ± 1.63 ma^{-1}	**-0.59 ± 0.08 ma^{-1}**

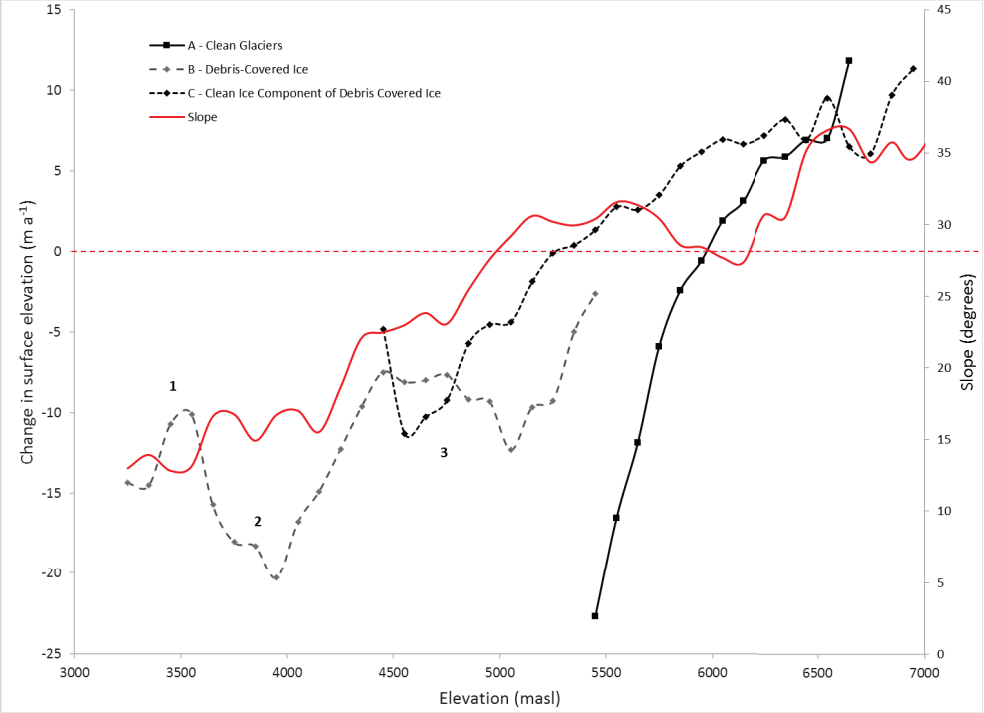

Figure 10: A relationship exists between elevation and the magnitude of glacier elevation change. Different responses to elevation are visible for the clean glaciers on the Tibetan Plateau (line A) the debris-covered components of the glaciers (line B) and clean ice components of the glaciers (line C) of the glaciers south of the topographic divide. Three deviations in the melt rate of debris-covered ice (1-3) are visible which are described in the text.

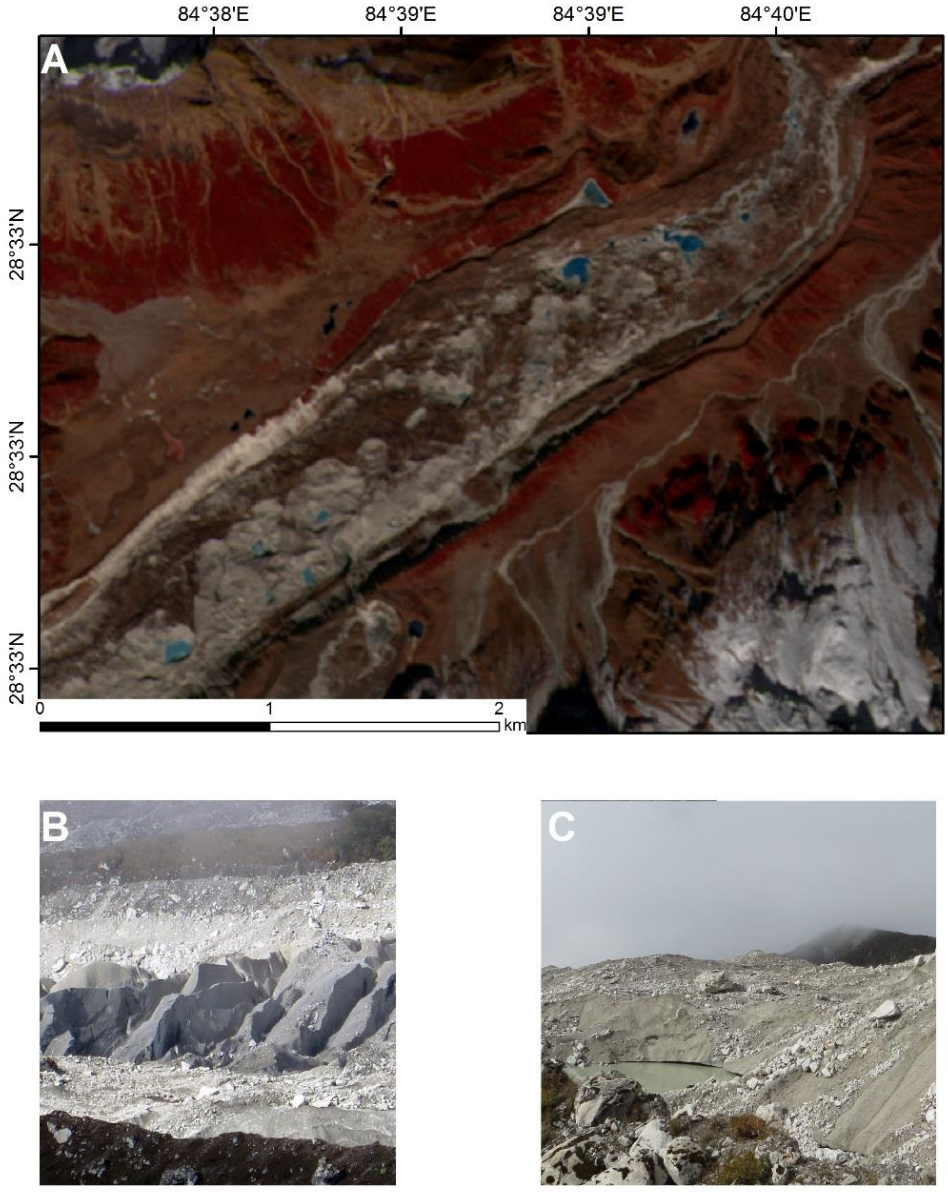

Figure 11: The lower stretches of the debris-covered tongues contained supraglacial lakes, as shown on a RapidEye image (20th November 2012) of Punggeon Glacier (**A**). Exposed ice (**B**) and supraglacial lakes (**C**) were visislbe on Ponkar Glacier during fieldwork in 2013.

When Thulagi glacier was studied in more detail it could be observed that in 1970 and 2001 the glacier still terminated in Dona Lake, however between 2001 and 2005 the glacier retreated onto land. The glacier lake has expanded from 0.50 km^2 in 1970 to 0.93 km^2 in 2013. During this time the glacier downwasted at a mean rate of -24.2 ± 6.8 m (-0.56 ± 0.03 m a^{-1}), the highest rates in the Manaslu Region. The rates of downwasting over debris-covered glacier increased from -0.76 ± 0.18 m a^{-1} between 1970 and 2000 to -0.89 ± 0.48 m a^{-1} between 2005 and 2013. The glacier underwent an acceleration in velocity of 9.4% between 1993 and 2013. We speculate that the rapid terminus retreat onto land over this time period caused the glacier to have a smaller ablation area allowing mass to build up in the accumulation area. This surplus mass could have then caused an increase in velocity. Thulagi glacier now terminates on land reducing the threat of a sudden breach of the moraine dam, however our results show that rates of downwasting have been increasing. Between 1970 and 2013 the debris-covered portion of Thulagi glacier lowered by -42.5 ± 6.8 m (-0.99 ± 0.03 m a^{-1}), although parts of the terminus dropped by up to 70 m as visible from field photographs (Figure 5). This indicates that Dona Lake is likely to continue to expand in the coming years. Ongoing monitoring of Dona Lake is therefore important.

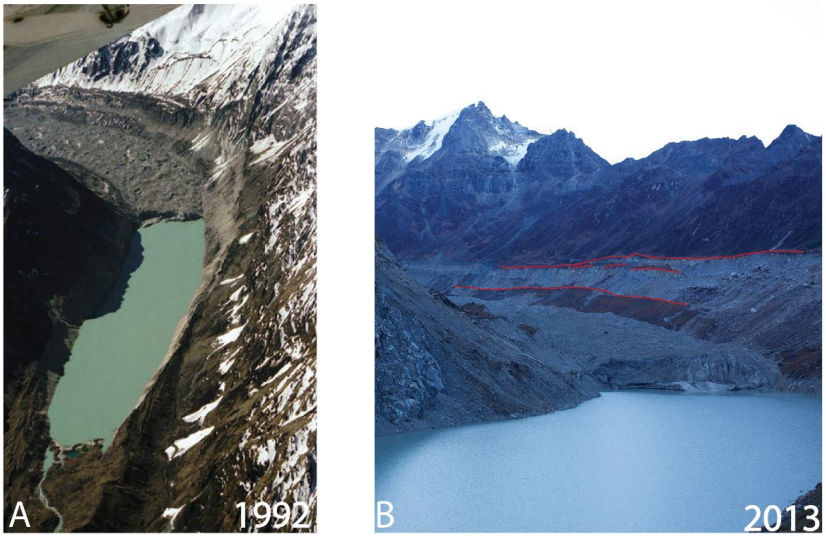

Figure 12: **A** shows Thulagi Glacier as seen from the air in 1992 Note that at this time the glacier terminated into Dona Lake. (Photograph: Hiroji Fushimi). **B** shows the glacier in 2013 taken from approximately 1 km from the terminus (Photo: Pål Ringkjøb Nielsen). The glacier is now terminating on land and no longer calving. The red lines show trimlines and fracture lines from previous glacier extents.

5.2 Discussion of Uncertainties

We calculated the DEM differencing uncertainties in terms of stochastic error and systematic error. The stochastic error was based on the standard error and the mean elevation difference on stable terrain. Magnusson et al. (2016) used a LiDAR derived DEM with multi-temporal aerial photographic DEMs to assess geodetic mass balance uncertainties and showed how standard methods neglect the spatial dependence of DEM errors, and as such typically overestimate uncertainties by between 2-4 times the actual uncertainty. We did not have access to such a precise and accurate DEM so it was not possible to perform a rigorous error assessment. It should therefore be considered that our uncertainty analysis is most likely too conservative.

Even with our conservative error estimation, 64% of our surface lowering results are significant as well as 8 of the 10 regional averages. Only 30% of our geodetic mass balance results however were significant, with only the regional average from 1970 – 2013 being significant. As stated by Gardelle et al. (2013), the largest component of the uncertainty is the estimation of the SRTM penetration. Values range from 1-10 m (Gardelle et al., 2013, Kääb et al., 2015, Berthier et al., 2016) which is considerably greater than the stochastic error. Additionally, there are other factors that were assumed such as a constant density of 850 kgm^{-3} across the entire glacier and that the glacier had a constant density profile, which could lead to additional errors.

In the absence of a more rigorous method, we estimated uncertainties for our velocity results based on ± one standard deviation. This assumes that no displacements have occurred on non-glacier terrain. Rockfalls and movements are common in the High Himalayas meaning our uncertainty estimates are most likely overestimates. Nevertheless, 94% of our velocity measurements are significant, in addition to all three regional averages.

5.3 Comparison with other work

In recent years, studies looking at the change in volume of Himalayan glaciers have become more common (Gardelle et al., 2012, Gardelle et al., 2013, Shangguan et al., 2015), although the number using declassified data such as Corona or Hexagon still number relatively few. Due to the differing climatic regimes across the Himalayas, it is not appropriate to compare our results with those from the Indian Himalaya, the Tien Shan, or the Karakoram. We therefore restrict our comparisons to the Central Himalayas and the Everest Region. Downwasting rates of -0.32 ± 0.08 m a^{-1} were calculated in the Everest Region between 1970 and 2007 (Bolch et al., 2011). This is less negative than our result of -0.45 ± 0.03 m a^{-1} between 1970 and 2013. It is worth pointing out that such differences could be due to the years of acquisition. It is probable that between 2007 and 2013 the glaciers experienced a continued and perhaps accelerating rate of mass loss (Bolch et al., 2012). The evidence also suggests that the three glaciers covered by the Corona DEM are not fully representative of the Manaslu Region with rates of glacier change being more negative than the regional average.

When looking at shorter time periods, Kääb et al. (2012) found a mean annual surface lowering of -0.21 ± 0.05 m a^{-1} over the entire Hindu Kush Himalaya Region between 2003 and 2008, with some regions losing as much as -0.66 m a^{-1}. The losses we found between 2000 and 2013 of -0.21 m a^{-1} therefore compare well with the regional average. Our results of geodetic mass balance between 2000 and 2013 (-0.05 ± 0.16 m.w.e.a $^{-1}$) is more positive than the results found by Gardelle et al. (2013) for western Nepal (−0.32 ± 0.13 m w.e.a $^{-1}$) or the Everest region (−0.26 ± 0.13 m w.e.a^{-1}) over roughly the same time period. Bolch et al. (2011) found a more negative mass balance of −0.79 ± 0.52 m w.e.a $^{-1}$ between 2002 and 2009 in the Everest Region. Our geodetic mass balance between 2005 and 2013 (-0.51 ± 0.12 m w.e.a^{-1}) is more comparable to these findings. Our mean geodetic mass balance between 1970 and 2013 (-0.24 ± 0.12 m w.e.a^{-1}) compares well with values reported for the Langtang valley between 1974 and 1999 (–0.32 ± 0.18 m w.e.a^{-1}) (Pellicciotti et al., 2015) as well as the Everest Region from 1970 to 2007 (−0.32 ± 0.08) (Bolch et al., 2011).

We found that an altitude of approximately 5635 m to represent the transition from areas losing mass and gaining mass. If this is taken as an estimate of the ELA then this is in broad agreement with the estimate of ~5600 m for the central Himalayas reported by (Bolch et al., 2012) and for Western Nepal of 5590 ± 138 m by Gardelle et al. (2013).

When it comes to velocity, Quincey et al. (2009) found that the debris-covered glaciers in the Everest region flowed at ~20 m a^{-1}, which is broadly in agreement of our mean result of 23 m a^{-1} in 2014. Kääb (2005) found that the debris-covered glaciers in Bhutan were flowing at higher rates of between 20 and 50 m a^{-1}. Towards the glacier terminus the glacier velocities drop off to almost northing over stagnant ice, something that has been observed also in Khumbu (Bolch et al., 2008).There is less work concerning changes in glacier velocity over time, and the work that does exist often find contradictory results of how glacier velocity has varied. Heid and Kääb (2012b) attribute negative mass balances to widespread reductions in glacier velocity globally, including a 43% reduction in velocity in the Pamir mountains between 2001 and 2010. Haritashya et al. (2015) found reductions in glacier velocity of Khumbu glacier between 2003 and 2008 of “between 10 and 20%” while Bhattacharya et al. (2016) found a 6.7% decrease from 1996 to 2013 in the Indian Himalaya. The reduction we measured of 16.8% between 1999 and 2013 fits in-between these values.

5.4 Future work

A clear trend of ongoing glacier stagnation is occurring on many of the debris-covered tongues. Future automated or semi-automated glacier change analysis should attempt to include volume or velocity products to compliment glacier area change assessments. The Landsat 8 and Sentinel-2 sensors contain less sensor noise than the previous optical missions and can therefore be used for large area glacier velocity mapping (Fahnestock et al., 2015, Kääb et al., 2016). The high precision of this imagery could help automate future image matching and glacier velocity determination, although automated or semi-automated methods for filtering displacements need to be improved and implemented.

Maurer and Rupper (2015) developed an approach that fully automatically processes declassified Hexagon satellite imagery (from the same mission program as Corona) and applied it to determining glacier volume change in the Bhutanese Himalayas. If such methods could be combined with automated DEM co-registration (e.g. Nuth and Kääb (2011)) and global or regional elevation datasets such as the SRTM (Schiefer et al., 2007), SETSM (Noh and Howat, 2015b), ALOS Global DEM (Shangguan et al., 2015), ICESAT (Moholdt et al., 2010, Kääb et al., 2012) or TerraSAR World DEM (Jaber et al., 2014) data then there is a large potential for regional scale volume change analysis in the future.

6. Conclusion

Our study shows a varied glacier response to climate in the Manaslu region of Nepal. Twelve percent of glaciers had an area change of <1% between 2001 and 2013 and the debris-covered area increased for 52% of the glaciers. When a subset of glaciers had trends in area, velocity, and volume compared however, the rates of reduction in glacier area and glacier velocity were near-identical, while glacier surface lowering showed strong mass losses. This shows that although glacier area change provides a straightforward measure for assessing glacier change, the glaciers in the Himalayas may be stagnating and downwasting despite relatively stationary glacier termini and modest reductions in area for some glaciers. Surface lowerings, geodetic mass balances and rates of glacier shrinkage have become more negative over the last decades with increased rates of loss between 2000 and 2005. Ice above approximately 5635 m a.s.l. has thickened slightly. Furthermore, our results add to the consensus of a heterogeneous yet clear trend of glacier downwasting across the Himalayas, with the changes in Manaslu region being in line with regional averages. Future work should make use of the high temporal resolution of a combination of Landsat 8 and Sentinel 2 to investigate seasonal changes to glacier velocity, and compare trends in glacier area, velocity, and volume over a larger sample of glaciers.

Acknowledgements

The authors would like to thank Asha Badadur Rai (www.adventurousnepal.com) and his family for organising all the logistics and practicalities of our fieldwork trekking around the Manaslu Conservation Area in both 2013 and 2014 and making us very welcome in Nepal. Thanks to Christian Kienholz who generated the centrelines for the glaciers. The authors are grateful to Owen King and Max Koller who read through this manuscript. Thanks also to the colleagues at the Department of Geography, University of Bergen and the Department of GeoScience, University of Oslo for their useful feedback and support during the writing process of this paper. We are grateful to ResClim and Melzer for funding that supported this work. Thanks to NASA and the USGS for the provision of Landsat, ASTER, Corona and SRTM Data and to Ian Howat for the SETSM data.

References

AGETA, Y. & HIGUCHI, K. 1984. Estimation of Mass Balance Components of a Summer-Accumulation Type Glacier in the Nepal Himalaya. *Geografiska Annaler. Series A, Physical Geography,* 66**,** 249-255.

BADER, H. 1954. Sorge's Law of densification of snow on high polar glaciers. *J. Glaciol,* 2**,** 319-323.

BAJRACHARYA, S. R., MAHARJAN, S. B. & SHRESTHA, F. 2014a. The status and decadal change of glaciers in Bhutan from the 1980s to 2010 based on satellite data. *Annals of Glaciology,* 55**,** 159-166.

BAJRACHARYA, S. R., MAHARJAN, S. B., SHRESTHA, F., BAJRACHARYA, O. R. & BAIDYA, S. 2014b. *Glacier Status in Nepal and Decadal Change from 1980 to 2010 Based on Landsat Data*.

BENN, D. I., BOLCH, T., HANDS, K., GULLEY, J., LUCKMAN, A., NICHOLSON, L. I., QUINCEY, D., THOMPSON, S., TOUMI, R. & WISEMAN, S. 2012. Response of debris-covered glaciers in the Mount Everest region to recent warming, and implications for outburst flood hazards. *Earth-Science Reviews,* 114**,** 156-174.

BENN, D. I. & OWEN, L. A. 1998. The role of the Indian summer monsoon and the mid-latitude westerlies in Himalayan glaciation: review and speculative discussion. *Journal of the Geological Society,* 155**,** 353-363.

BERTHIER, E., CABOT, V., VINCENT, C. & SIX, D. 2016. Decadal region-wide and glacier-wide mass balances derived from multi-temporal ASTER satellite digital elevation models. Validation over the Mont-Blanc area. *Frontiers in Earth Science,* 4**,** 63.

BHATTACHARYA, A., BOLCH, T., MUKHERJESS, K., PIECZONKA, T., KROPACEK, J. & BUCHROITHNER, M. 2016. Overall recession and mass budget of Gangotri Glacier, Garhwal Himalayas, from 1965-2015 using remote sensing data. *Journal of Glaciology*.

BOLCH, T., BUCHROITHNER, M. F., PETERS, J., BAESSLER, M. & BAJRACHARYA, S. 2008. Identification of glacier motion and potentially dangerous glacial lakes in the Mt. Everest region/Nepal using spaceborne imagery. *Natural Hazards and Earth System Sciences,* 8**,** 1329-1340.

BOLCH, T., KULKARNI, A., KAAB, A., HUGGEL, C., PAUL, F., COGLEY, J. G., FREY, H., KARGEL, J. S., FUJITA, K., SCHEEL, M., BAJRACHARYA, S. & STOFFEL, M. 2012. The State and Fate of Himalayan Glaciers. *Science,* 336**,** 310-314.

BOLCH, T., MENOUNOS, B. & WHEATE, R. 2010. Landsat-based inventory of glaciers in western Canada, 1985-2005. *Remote Sensing of Environment,* 114**,** 127-137.

BOLCH, T., PIECZONKA, T. & BENN, D. 2011. Multi-decadal mass loss of glaciers in the Everest area (Nepal Himalaya) derived from stereo imagery. *The Cryosphere,* 5**,** 349-358.

CARRIVICK, J. L. & TWEED, F. S. 2016. A global assessment of the societal impacts of glacier outburst floods. *Global and Planetary Change,* 144**,** 1-16.

DE FERRANTI, J. 2012. *Viewfinder panorama DEMs* [Online]. Available: http://www.viewfinderpanoramas.org/.

DEHECQ, A., GOURMELEN, N. & TROUVE, E. 2015. Deriving large-scale glacier velocities from a complete satellite archive: Application to the Pamir–Karakoram–Himalaya. *Remote Sensing of Environment,* 162**,** 55-66.

DEPARTMENT OF HYDROLOGY AND METEOROLOGY (GOVERNMENT OF NEPAL). 2014. *Interpolated 12 km temperature and rainfall mean annual data (1970–2010)* [Online]. Kathmandu, Nepal. Available: http://dhm.gov.np/dpc.

FAHNESTOCK, M., SCAMBOS, T., MOON, T., GARDNER, A., HARAN, T. & KLINGER, M. 2015. Rapid large-area mapping of ice flow using Landsat 8. *Remote Sensing of Environment*.

GARDELLE, J., BERTHIER, E. & ARNAUD, Y. 2012. Slight mass gain of Karakoram glaciers in the early twenty-first century. *Nature geoscience,* 5**,** 322-325.

GARDELLE, J., BERTHIER, E., ARNAUD, Y. & KAAB, A. 2013. Region-wide glacier mass balances over the Pamir-Karakoram-Himalaya during 1999-2011. *Cryosphere,* 7**,** 1263-1286.

GIROD, L., NUTH, C. & KÄÄB, A. 2015. Improvement of DEM generation from ASTER images using satellite jitter estimation and open source implementation. *The International Archives of Photogrammetry, Remote Sensing and Spatial Information Sciences,* 40**,** 249.

HARITASHYA, U. K., PLEASANTS, M. S. & COPLAND, L. 2015. Assessment of the Evolution in Velocity of Two Debris-Covered Valley Glaciers in Nepal and New Zealand. *Geografiska Annaler: Series A, Physical Geography,* 97**,** 737-751.

HEID, T. & KÄÄB, A. 2012a. Evaluation of existing image matching methods for deriving glacier surface displacements globally from optical satellite imagery. *Remote Sensing of Environment,* 118**,** 339-355.

HEID, T. & KÄÄB, A. 2012b. Repeat optical satellite images reveal widespread and long term decrease in land-terminating glacier speeds. *The Cryosphere,* 6**,** 467-478.

HUSS, M. 2013. Density assumptions for converting geodetic glacier volume change to mass change. *The Cryosphere,* 7**,** 877-887.

IMMERZEEL, W. W., KRAAIJENBRINK, P. D. A., SHEA, J. M., SHRESTHA, A. B., PELLICCIOTTI, F., BIERKENS, M. F. P. & DE JONG, S. M. 2014. High-resolution monitoring of Himalayan glacier dynamics using unmanned aerial vehicles. *Remote Sensing of Environment,* 150**,** 93-103.

IMMERZEEL, W. W., VAN BEEK, L. P. H. & BIERKENS, M. F. P. 2010. Climate Change Will Affect the Asian Water Towers. *Science,* 328**,** 1382-1385.

JABER, W. A., FLORICIOIU, D. & ROTT, H. Glacier dynamics of the Northern Patagonia Icefield derived from SRTM, TanDEM-X and TerraSAR-X data. Geoscience and Remote Sensing Symposium (IGARSS), 2014 IEEE International, 13-18 July 2014 2014. 4018-4021.

KIENHOLZ, C., RICH, J., ARENDT, A. & HOCK, R. 2014. A new method for deriving glacier centerlines applied to glaciers in Alaska and northwest Canada. *The Cryosphere,* 8**,** 503-519.

KING, O., QUINCEY, D. J., CARRIVICK, J. L. & ROWAN, A. V. 2016. Spatial variability in mass change of glaciers in the Everest region, central Himalaya, between 2000 and 2015. *The Cryosphere Discuss.,* 2016**,** 1-35.

KÄÄB, A. 2005. Combination of SRTM3 and repeat ASTER data for deriving alpine glacier flow velocities in the Bhutan Himalaya. *Remote Sensing of Environment,* 94**,** 463-474.

KÄÄB, A., BERTHIER, E., NUTH, C., GARDELLE, J. & ARNAUD, Y. 2012. Contrasting patterns of early twenty-first-century glacier mass change in the Himalayas. *Nature,* 488**,** 495-498.

KÄÄB, A., TREICHLER, D., NUTH, C. & BERTHIER, E. 2015. Brief Communication: Contending estimates of 2003–2008 glacier mass balance over the Pamir–Karakoram–Himalaya. *The Cryosphere,* 9**,** 557-564.

KÄÄB, A. & VOLLMER, M. 2000. Surface geometry, thickness changes and flow fields on creeping mountain permafrost: Automatic extraction by digital image analysis. *Permafrost and Periglacial Processes,* 11**,** 315-326.

KÄÄB, A., WINSVOLD, H. S., ALTENA, B., NUTH, C., NAGLER, T. & WUITE, J. 2016. Glacier Remote Sensing Using Sentinel-2. Part I: Radiometric and Geometric Performance, and Application to Ice Velocity. *Remote Sensing,* 8.

MAGNUSSON, E., BELART, J. M. C., PALSSON, F., AGUSTSSON, H. & CROCHET, P. 2016. Geodetic mass balance record with rigorous uncertainty estimates deduced from aerial photographs and lidar data - Case study from Drangajokull ice cap, NW Iceland. *Cryosphere,* 10**,** 159-177.

MAURER, J. & RUPPER, S. 2015. Tapping into the Hexagon spy imagery database: A new automated pipeline for geomorphic change detection. *ISPRS Journal of Photogrammetry and Remote Sensing,* 108**,** 113-127.

MAUSSION, F., SCHERER, D., MÖLG, T., COLLIER, E., CURIO, J. & FINKELNBURG, R. 2014. precipitation seasonality and variability over the Tibetan Plateau as resolved by the High Asia Reanalysis*. *Journal of Climate,* 27**,** 1910-1927.

MOHOLDT, G., NUTH, C., HAGEN, J. O. & KOHLER, J. 2010. Recent elevation changes of Svalbard glaciers derived from ICESat laser altimetry. *Remote Sensing of Environment,* 114**,** 2756-2767.

MOOL, P. K. 2011. *Glacial lakes and glacial lake outburst floods in Nepal*, International Centre for Integrated Mountain Development.

NAGAI, H., FUJITA, K., NUIMURA, T. & SAKAI, A. 2013. Southwest-facing slopes control the formation of debris-covered glaciers in the Bhutan Himalaya. *Cryosphere,* 7**,** 1303-1314.

NOH, M.-J. & HOWAT, I. M. 2015a. *Advice for use of the SETSM 20m and 100m Posting Digital Elevation Model Mosaics Covering Nepal and Environs* [Online]. Ohio State University, USA. Available: http://repository.agic.umn.edu/elevation/dem/SETSM/Nepal/Nepal_PreEvent_SETSM_DEM_Mosaic_README.pdf.

NOH, M.-J. & HOWAT, I. M. 2015b. Automated stereo-photogrammetric DEM generation at high latitudes: Surface Extraction with TIN-based Search-space Minimization (SETSM) validation and demonstration over glaciated regions. *GIScience & Remote Sensing,* 52**,** 198-217.

NUIMURA, T., FUJITA, K., YAMAGUCHI, S. & SHARMA, R. R. 2012. Elevation changes of glaciers revealed by multitemporal digital elevation models calibrated by GPS survey in the Khumbu region, Nepal Himalaya, 1992–2008. *Journal of Glaciology,* 58**,** 648-656.

NUIMURA, T., SAKAI, A., TANIGUCHI, K., NAGAI, H., LAMSAL, D., TSUTAKI, S., KOZAWA, A., HOSHINA, Y., TAKENAKA, S. & OMIYA, S. 2014. The GAMDAM Glacier Inventory: a quality controlled inventory of Asian glaciers. *The Cryosphere Discussions,* 8**,** 2799-2829.

NUTH, C. & KÄÄB, A. 2011. Co-registration and bias corrections of satellite elevation data sets for quantifying glacier thickness change. *The Cryosphere,* 5**,** 271.

NUTH, C., SCHULER, T. V., KOHLER, J., ALTENA, B. & HAGEN, J. O. 2012. Estimating the long-term calving flux of Kronebreen, Svalbard, from geodetic elevation changes and mass-balance modelling. *Journal of Glaciology,* 58**,** 119-133.

OWEN, L. A. & BENN, D. I. 2005. Equilibrium-line altitudes of the Last Glacial Maximum for the Himalaya and Tibet: an assessment and evaluation of results. *Quaternary International,* 138–139**,** 55-78.

PANT, S. R. & REYNOLDS, J. M. 2000. Application of electrical imaging techniques for the investigation of natural dams: an example from the Thulagi Glacier Lake, Nepal. *Journal of the Nepal Geological Society,* 22**,** 211-218.

PAUL, F. 2008. Calculation of glacier elevation changes with SRTM: is there an elevation-dependent bias? *Journal of Glaciology,* 54**,** 945-946.

PAUL, F., ARNAUD, Y., RANZI, R. & ROTT, H. 2014. European Alps. *In:* KARGEL, J. S., LEONARD, G. J., BISHOP, M. P., KÄÄB, A. & RAUP, B. H. (eds.) *Global Land Ice Measurements from Space.* Springer Berlin Heidelberg.

PAUL, F., BARRAND, N. E., BAUMANN, S., BERTHIER, E., BOLCH, T., CASEY, K., FREY, H., JOSHI, S. P., KONOVALOV, V., BRIS, R. L., MÖLG, N., NOSENKO, G., NUTH, C., POPE, A., RACOVITEANU, A., RASTNER, P., RAUP, B., SCHARRER, K., STEFFEN, S. & WINSVOLD, S. 2013. On the accuracy of glacier outlines derived from remote-sensing data. *Annals of Glaciology,* 54**,** 171-182.

PELLICCIOTTI, F., STEPHAN, C., MILES, E., HERREID, S., IMMERZEEL, W. W. & BOLCH, T. 2015. Mass-balance changes of the debris-covered glaciers in the Langtang Himal, Nepal, from 1974 to 1999. *Journal of Glaciology,* 61**,** 373-386.

PIECZONKA, T., BOLCH, T., JUNFENG, W. & SHIYIN, L. 2013. Heterogeneous mass loss of glaciers in the Aksu-Tarim Catchment (Central Tien Shan) revealed by 1976 KH-9 Hexagon and 2009 SPOT-5 stereo imagery. *Remote Sensing of Environment,* 130**,** 233-244.

QUINCEY, D., LUCKMAN, A. & BENN, D. 2009. Quantification of Everest region glacier velocities between 1992 and 2002, using satellite radar interferometry and feature tracking. *Journal of Glaciology,* 55**,** 596-606.

REZNICHENKO, N., DAVIES, T., SHULMEISTER, J. & MCSAVENEY, M. 2010. Effects of debris on ice-surface melting rates: an experimental study. *Journal of Glaciology,* 56**,** 384-394.

RICHARDSON, S. D. & REYNOLDS, J. M. 2000. An overview of glacial hazards in the Himalayas. *Quaternary International,* 65–66**,** 31-47.

RIGNOT, E., ECHELMEYER, K. & KRABILL, W. 2001. Penetration depth of interferometric synthetic-aperture radar signals in snow and ice. *Geophysical Research Letters,* 28**,** 3501-3504.

ROBSON, B. A., NUTH, C., DAHL, S. O., HÖLBLING, D., STROZZI, T. & NIELSEN, P. R. 2015. Automated classification of debris-covered glaciers combining optical, SAR and topographic data in an object-based environment. *Remote Sensing of Environment,* 170**,** 372-387.

SCHERLER, D., BOOKHAGEN, B. & STRECKER, M. R. 2011. Spatially variable response of Himalayan glaciers to climate change affected by debris cover. *Nature Geoscience,* 4**,** 156-159.

SCHIEFER, E., MENOUNOS, B. & WHEATE, R. 2007. Recent volume loss of British Columbian glaciers, Canada. *Geophysical Research Letters,* 34.

SCHWANGHART, W., WORNI, R., HUGGEL, C., STOFFEL, M. & KORUP, O. 21st century Himalayan hydropower: Growing exposure to glacial lake outburst floods? EGU General Assembly Conference Abstracts, 2014. 15824.

SHANGGUAN, D., BOLCH, T., DING, Y., KRÖHNERT, M., PIECZONKA, T., WETZEL, H.-U. & LIU, S. 2015. Mass changes of Southern and Northern Inylchek Glacier, Central Tian Shan, Kagyzstan, during∼ 1975 and 2007 derived from remote sensing data. *The Cryosphere,* 9**,** 703-717.

ZHANG, Y., FUJITA, K., LIU, S., LIU, Q. & NUIMURA, T. 2011. Distribution of debris thickness and its effect on ice melt at Hailuogou glacier, southeastern Tibetan Plateau, using in situ surveys and ASTER imagery. *Journal of Glaciology,* 57**,** 1147-1157.

Table S1: Glacier area for glaciers in the Manaslu Region between 1969/1970. 2001. 2005 and 2013. The areas are shown for clean ice (C). debris-covered ice (D) and total glacier area (T).

GLIMS ID	2013 (km^2)			2005 (km^2)			2001 (km^2)			1967/1970 (km^2)			% a^{-1} Change 1970 - 2013			% a^{-1} Change 2001 - 2013		
	C	**D**	**T**	**C**	**D**	**T**	**C**	**D**	**T**	**C**	**D**	**T**	**C**	**D**	**T**	**C**	**D**	**T**
G084254E28913N	13.7		13.7	14.0		14.0	14.2		14.2							-0.3		-0.3
G084461E28797N	15.1		15.1	15.2		15.2	15.4		15.4							-0.1		-0.1
G084482E28758N	9.4		9.4	9.8		9.8	10.2		10.2							-0.6		-0.6
G084289E28902N	9.4		9.4	9.8		9.8	10.1		10.1							-0.5		-0.5
G084132E28911NW	19.7		19.7	22.7		22.7	22.7		22.7							-1.1		-1.1
G084132E28911NE	4.5		4.5	5.3		5.3	5.4		5.4							-1.4		-1.4
G084388E28888N	0.3		0.3	0.4		0.4	0.5		0.5							-3.5		-3.5
G084394E28877N	4.1		4.1	4.1		4.1	4.1		4.1							-0.1		-0.1
G084374E28888N	1.3		1.3	1.4		1.4	1.6		1.6							-1.5		-1.5
G084323E28882N	16.6		16.6	17.0		17.0	17.3		17.3							-0.3		-0.3
G084417E28869N	6.0		6.0	6.2		6.2	6.3		6.3							-0.3		-0.3
G084451E28832N	1.9		1.9	1.9		1.9	2.0		2.0							-0.3		-0.3
G084424E28839N	7.6		7.6	7.8		7.8	7.8		7.8							-0.2		-0.2
G084430E28788N	17.1	1.9	19.0	13.0	2.0	15.0	16.0	2.2	18.1							0.6	-0.9	0.4
G084365E28759N	24.8	5.6	30.4	22.6	6.4	29.0	28.0	6.2	34.2							-1.0	-0.7	-0.9
G084516E28729N	10.7	2.3	13.0	11.2	2.8	13.9	11.7	2.7	14.4							-0.7	-1.2	-0.8
G084459E28695N	24.2	7.2	31.3	25.6	7.1	32.7	25.9	7.2	33.1	26.9	6.9	33.8	-0.2	0.1	-0.2	-0.5	-0.1	-0.4
G084381E28716N	12.6	1.5	14.2	13.0	2.2	15.2	13.0	2.3	15.3							-0.2	-2.8	-0.6
G084502E28714N	10.0	3.8	13.7	10.2	4.0	14.1	10.2	3.9	14.2							-0.2	-0.3	-0.2
G084534E28677N	1.5		1.5	1.0		1.0	1.4		1.4							0.7		0.7
G084354E28669N	12.5	8.4	20.9	13.5	1.0	14.4	13.0	6.9	19.8							-0.3	1.9	0.4
G084539E28644N	4.5	2.7	7.2	4.7	2.5	7.2	4.5	2.6	7.2							-0.1	0.3	0.1
G084550E28613N	7.0	2.9	10.0	7.4	2.5	9.9	7.0	2.9	9.9							0.0	0.1	0.0
G084319E28640N	2.6	0.6	3.2	2.3	0.6	2.9	2.3	0.6	2.9							1.1	0.0	0.9
G084587E28578N	14.3		14.3	16.1		16.1	16.1		16.1							-1.0		-1.0
G084499E28581N	1.8	2.6	4.4	3.1	1.7	4.8	2.1	2.7	4.8							-1.2	-0.2	-0.6
G084584E28535N	12.7	7.5	20.2	17.4	5.6	23.0	15.8	7.2	23.0	19.8	5.6	25.4	-0.8	0.8	-0.5	-1.6	0.3	-1.0
G084549E28515N	22.4	2.7	25.0	23.8	2.7	26.6	26.7	2.9	29.6	23.5	4.0	27.5	-0.1	-0.8	-0.2	-1.3	-0.6	-1.3
G084689E28511N	16.6	14.3	30.9	24.7	11.6	36.3	27.1	12.8	39.9	26.0	13.4	39.4	-0.8	0.2	-0.5	-3.2	1.0	-1.9
G084589E28460N	2.1	2.3	4.4	2.5	2.0	4.6	3.8	1.6	5.4							-3.6	3.5	-1.5

GLIMS ID	2013 (km^2)			2005 (km^2)			2001 (km^2)			1967/1970 (km^2)			% a^{-1} Change 1970 - 2013			% a^{-1} Change 2001 - 2013		
	C	D	T	C	D	T	C	D	T	C	D	T	C	D	T	C	D	T
G084708E28469N	11.2	1.1	12.3	12.9	0.5	13.4	13.2	0.4	13.5	13.5	0.2	13.8	-0.4	8.2	-0.2	-1.2	17.2	-0.7
G084610E28423N	11.6	0.5	12.1	11.7	0.9	12.6	12.7	0.5	13.3							-0.7	-0.1	-0.7
G084759E28427N	30.1	6.6	36.6	31.7	5.8	37.6	31.4	6.0	37.4	34.2	5.6	39.8	-0.3	0.4	-0.2	-0.4	0.8	-0.2
G084655E28393N	6.9	0.4	7.3	7.1	0.5	7.6	6.8	0.3	7.1							0.1	2.4	0.2
G084695E28384N	6.1	3.2	9.3	6.4	2.4	8.8	6.5	2.7	9.2							-0.5	1.5	0.1
G084524E28591N	4.2		4.2	4.3		4.3	4.2		4.2							0.0		0.0
G084551E28439N	1.5	1.8	3.3	1.5	2.0	3.6	1.7	2.2	3.9	2.6	1.0	3.6	-1.0	1.8	-0.2	-1.1	-1.7	-1.4
G084496E28676N	2.5	2.0	4.5	2.8	1.7	4.5	2.8	1.7	4.5	3.0	1.8	4.8	-0.4	0.3	-0.1	-1.0	1.8	0.0
G084425E28700N	5.5	2.0	7.5	6.2	6.1	12.3	6.1	6.4	12.5	5.6	7.1	12.7	-0.1	-1.7	-0.1	-0.8	-5.7	-3.3
Total (visible on Corona)	**126.6**	**45.1**	**171.7**	**146.8**	**43.2**	**190.0**	**150.6**	**46.8**	**197.5**	**155.0**	**45.6**	**200.7**	**-0.4**	**0.0**	**-0.3**	**-1.3**	-0.3	-1.1
Total	**386.4**	**84.0**	**470.4**	**412.3**	**74.6**	**486.9**	**427.5**	**84.9**	**512.4**	**155.0**	**45.6**	**200.7**	**-0.4**	**0.0**	**-0.3**	**-0.8**	-0.1	-0.7

Table S2: Mean surface lowerings for total glacier area (when available) and over debris-covered ice. The geodetic mass balance was calculated when there was sufficient coverage from the DEMs.

GLIMS Glacier ID		**2013 – 2000**			**2013 - 2005**			**2005 - 2000**		**2000 - 1970**			**2013 - 1970**		
	Name (if available)	Mean annual change (m a^{-1})	Mean annual change debris (m a^{-1})	Annual geodetic mass balance (m w.e. a^{-1})	Mean annual change (m a^{-1})	Mean annual change debris (m a^{-1})	Annual geodetic mass balance (m w.e. a^{-1})	Mean annual change (m a^{-1})	Mean annual change debris (m a^{-1})	Mean annual change (m a^{-1})	Mean annual change debris (m a^{-1})	Annual geodetic mass balance (m w.e. a^{-1})	Mean annual change (m a^{-1})	Mean annual change debris (m a^{-1})	Annual geodetic mass balance (m w.e. a^{-1})
G084254E28913N		0.09 ±0.08		0.08 ±0.29											
G084461E28797N		-0.04 ±0.08		-0.04 ±0.31											
G084482E28758N		-0.08 ±0.08		-0.07 ±0.29	-1.07 ±0.48		-0.13 ±0.13								
G084289E28902N		-0.36 ±0.08		-0.28 ±0.23											
G084132E28911N W		-0.03 ±0.08		-0.03 ±0.31				-1.18 ±1.63							
G084132E28911NE		0.09 ±0.08		0.09 ±0.29											
G084394E28877N		0.29 ±0.08		0.27 ±0.30											
G084374E28888N		0.29 ±0.08		0.19 ±0.22											
G084323E28882N		-0.06 ±0.08		-0.03 ±0.15											
G084417E28869N		0.01 ±0.08		0.01 ±0.27											
G084451E28832N		0.19 ±0.08		0.14 ±0.24											
G084424E28839N		0.00 ±0.08		0.00 ±0.29											
G084430E28788N		0.31 ±0.08	-0.66 ±0.03	0.20 ±0.17											
G084365E28759N		0.21 ±0.08	-0.86 ±0.03	0.12 ±0.19											
G084516E28729N		0.08 ±0.08	-0.35 ±0.03	0.05 ±0.23	-1.20 ±0.48	-1.41 ±0.48	-1.03 ±0.42	-2.03 ±1.63	-1.37 ±1.85						
G084459E28695N	Ponkar	0.22 ±0.08	-0.45 ±0.03	0.14 ±0.19	-1.26 ±0.48	-1.00 ±0.48	-0.57 1.11	-2.75 ±1.63	-1.26 ±1.85						
G084381E28716N		0.19 ±0.08	-0.28 ±0.03	0.10 ±0.17				-1.20 ±1.63							
G084502E28714N	Fukang	-0.24 ±0.08		-0.18 ±0.35	-0.93 ±0.48		-0.91 ±0.93								
G084534E28677N		0.15 ±0.08	-0.78 ±0.03				-0.78 ±0.22								
G084354E28669N	Suti Glacier	-0.64 ±0.08	-0.95 ±0.03	0.17 ±0.37	-0.27 ±0.48	-1.10 ±0.48		-0.93 ±1.63	0.12 ±1.85						
G084539E28644N	Larkya	-0.25 ±0.08	-0.53 ±0.03	-0.16 ±0.35	-1.04 ±0.48	-0.99 ±0.48	-0.98 ±0.55								
G084550E28613N	Syacha	-0.57 ±0.08	-0.86 ±0.03		-0.93 ±0.48	-1.50 ±0.48	-1.05 ±1.75								
G084587E28578N	Manaslu	-0.22 ±0.08		-0.67 ±1.47	-0.35 ±0.48		-1.78 ±1.57	-2.21 ±1.63	-0.92 ±1.48						
G084499E28581N	Changli	-0.38 ±0.08	-0.53 ±0.03	-0.08 ±0.05	-0.32 ±0.48	-0.65 ±0.48	-0.11 ±2.10	-1.63 ±1.63	-1.29 ±1.48						

GLIMS Glacier ID		2013 – 2000			2013 - 2005			2005 - 2000			2000 - 1970		2013 - 1970		
	Name (if available)	Mean annual change (m a^{-1})	Mean annual change debris (m a^{-1})	Annual geodetic mass balance (m w.e. a^{-1})	Mean annual change (m a^{-1})	Mean annual change debris (m a^{-1})	Annual geodetic mass balance (m w.e. a^{-1})	Mean annual change (m a^{-1})	Mean annual change debris (m a^{-1})	Mean annual change (m a^{-1})	Mean annual change debris (m a^{-1})	Annual geodetic mass balance (m w.e. a^{-1})	Mean annual change (m a^{-1})	Mean annual change debris (m a^{-1})	Annual geodetic mass balance (m w.e. a^{-1})
G084584E28535N	Punggen	-0.86 ±0.08	-1.54 ±0.03		-0.69 ±0.48	-1.28 ±0.48	-2.77 ±1.21	-1.74 ±1.63	-0.10 ±1.48	-0.51 ±0.23	-0.18 ±0.18		-0.35 ±0.03	-0.41 ±0.03	-0.20 ±0.13
G084549E28515N	Thulagi		-2.06 ±0.03		-0.43 ±0.48	-0.89 ±0.48	-0.39 ±4.97		0.57 ±1.48	-0.67 ±0.23	-0.76 ±0.18		-0.56 ±0.03	-0.99 ±0.03	-0.26 ± 0.10
G084689E28511N	Hinang		-1.67 ±0.03		-0.62 ±0.48	-1.03 ±0.48	-0.81 ±1.63		0.17 ±1.48	-0.31 ±0.23	-0.25 ±0.18		-0.55 ±0.03	-0.55 ±0.03	-0.25 ± 0.12
G084589E28460N		-0.81 ±0.08	-0.99 ±0.03	-0.06 ±0.04	0.12 ±0.48	-0.07 ±0.48	0.01 ±0.19	-0.48 ±1.63	-0.25 ±1.48						
G084708E28469N		-0.08 ±0.08	-1.30 ±0.03	-0.07 ±0.44	0.11 ±0.48	-0.73 ±0.48	0.24 ±0.29	-0.52 ±1.63	-0.91 ±1.48						
G084610E28423N		-1.00 ±0.08	-0.77 ±0.03	-0.14 ±0.04	-0.41 ±0.48	-0.42 ±0.48	-0.23 ±2.37	-0.37 ±1.63	-1.51 ±1.48						
G084759E28427N	Himal Chuli	-0.88 ±0.08	-1.23 ±0.03	-0.85 ±0.35	-0.14 ±0.48	-0.68 ±0.48	-0.38 ±0.63	-1.98 ±1.63	-0.87 ±1.48						
G084655E28393N		-0.90 ±0.08	-0.89 ±0.03		-0.28 ±0.48	-0.27 ±0.48	-0.05 ±0.28	-0.98 ±1.63	-1.06 ±1.48						
G084695E28384N	Bhauda Himal	-1.18 ±0.08	-2.00 ±0.03		-0.27 ±0.48	-1.27 ±0.48	-0.33 ±1.04	-1.51 ±1.63	-0.36 ±1.48						
G084524E28591N		0.16 ±0.08		0.06 ±0.13	-0.32 ±0.48	-0.03 ±0.48	-0.24 ±1.04	-0.48 ±1.63							
G084551E28439N		-0.81 ±0.08	-0.88 ±0.03	-0.32 ±0.13	-0.10 ±0.48	-0.63 ±0.48	-0.07 ±0.33	-1.49 ±1.63	-0.40 ±1.48						
G084496E28676N	Salpudanda	-0.18 ±0.08		-0.16 ±0.62	-0.97 ±0.48		-1.31 ±0.10	-2.09 ±1.63							
G084425E28700N	Kechakyu Khola	-0.12 ±0.08	-0.27 ±0.03	-0.17 ±0.70	0.48 ±0.48		0.17 ±0.17	-0.55 ±1.63	-1.03 ±1.48						
Mean (clean ice component)		0.08 ±0.08			-0.45 ±0.48										
Mean (total)		-0.21 ±0.08	-0.35 ±0.03	-0.05 ±0.16	-0.51 ±0.48	-0.82 ±0.48	-0.27 ±0.55	-1.26 ±1.63	0.65 ±1.48	0.49 ±0.23	-0.40 ±0.18		-0.45 ±0.03	-0.65 ±0.03	-0.24 ± 0.12
Mean (visible on Corona)					-0.58 ±0.48	1.07 ±0.48	-0.51 ± 0.12			0.49 ±0.23	-0.40 ±0.18		-0.45 ±0.03	-0.65 ±0.03	-0.24 ± 0.12

Table S3: Mean centreline velocities and percentage changes for 11 glaciers in the Manaslu Region.

GLIMS Glacier ID	**Name (if available)**	**Mean centreline velocity (m a^{-1})**			**Change % a^{-1}**	
		2013/2014	**1999/2000**	**1993/1994**	**2013 – 1999**	**2013 - 1993**
G084354E28669NE		8.6 ±8.2	17.8 ±3.2	16.5 ±5.6	-3.7	-2.4
G084354E28669NW	Suti Glacier	38.2 ±8.2	40.0 ±3.2	53.8 ±5.6	-0.3	-1.4
G084425E28700N	Kechakyu	16.0 ±8.2	24.0 ±3.2	28.0 ±5.6	-2.4	-2.1
G084459E28695N	Ponkar	47.0 ±8.2	53.0 ±3.2	42.0 ±5.6	-0.8	0.6
G084496E28676N	Salpudanda	16.0 ±8.2	24.0 ±3.2	28.2 ±5.6	-2.4	-2.2
G084502E28714N	Fukang	47.0 ±8.2	52.6 ±3.2	41.7 ±5.6	-0.8	0.6
G084516E28729N	Fukang (North)	2.3 ±8.2	8.6 ±3.2	8.3 ±5.6	-5.2	-3.6
G084689E28511N	Hinang	37.2 ±8.2	40.9 ±3.2		-0.6	0.0
G084759E28427N	Himal Chuli	31.8 ±8.2	39.9 ±3.2	58.5 ±5.6	-1.4	-2.3
G084549E28515N	Thulagi	40.6 ±8.2	31.3 ±3.2	37.1 ±5.6	2.1	0.5
G084695E28384N	Bhauda Himal	2.0 ±8.2	12.6 ±3.2		-6.0	0.0
Mean		26.1 ±8.2	31.3 ±3.2	34.9 ±5.6	-1.2	-1.3